Magnetic order in functional iron oxides



Francis Chmiel

Hertford College

University of Oxford

A thesis submitted for the degree of

Doctor of Philosophy

2018

‘Adsiduus usus uni rei deditus et ingenium et artem saepe vincit.’

M. T. Cicero

Abstract

Developing our understanding of the magnetic order of iron oxides is essential if we are to devise novel, functional magnetic memory devices and sensors. In this thesis we report on the magnetic order of the newly synthesised Y-type hexaferrite $Ba_{0.5}Sr_{1.5}Mg_2Fe_{12}O_{22}$ (BSMFO) and on the remarkable domain morphology of the archetypal iron oxide α-Fe_2O_3.

The magnetic phase diagram of BSMFO is studied by lab based characterisation methods and synchrotron techniques. We reveal a series of metastable magnetic structures, characterised by a period commensurate with the crystallographic lattice. We confirm this system is polar below 100 K and exhibits the worlds largest magnetoelectric effect. We perform a Resonant X-ray Diffraction (RXD) experiment to study this effect and show that RXD is sensitive to the magnetic polarity of BSMFO, the order parameter which drives the large magnetoelectric effect observed in this system. Using RXD microdiffraction, we spatially resolve the magnetic polarity domain configuration of BSMFO for the first time. When complemented by dynamic polarisation analysis of the scattered X-ray beam, these results allow us to propose a microscopic mechanism describing the large magnetoelectric effect observed in BSMFO. The RXD techniques demonstrated in this thesis open up a previously unexplored avenue for effectively studying the field-induced phases of the Y-type hexaferrites.

The coupled domain structure of a α-Fe_2O_3/Co heterostructure is imaged using vector-mapped X-ray PhotoEmission Electron Microscopy. Our measurements reveal an unprecedented network of vortices in the antiferromagnetically ordered α-Fe_2O_3 layer which imprint, by exchange proximity, into the adjacent Co layer. This work represents the first observation of antiferromagnetic spin vortices in a laterally unconstrained system. These vortices are consistent with the Kibble-Zurek mechanism, originally conceived in the context of cosmology, which describes the formation (and preservation) of topological defects when cooling through a symmetry breaking phase transition. The topological nature of these vortices is exploited to control the domain configuration of our heterostructure by inducing mass vortex-antivortex annihilation. As well as being a suitable system to test the universality of the Kibble-Zurek mechanism, the network of vortices observed in this work have the potential to be incorporated into novel, highly efficient magnetic memory devices.

Acknowledgements

Firstly, I am grateful to my supervisor Paolo Radaelli, for giving me the opportunity to pursue my DPhil, his enthusiasm for science, and his invaluable guidance and supervision. Secondly, Roger Johnson has supervised many of the experiments presented in this thesis and I thank him for his indefatigable support, his friendship, and his aptitude for teaching the next generation of scientists. I am also indebted to the other members of the Oxide electronics group, past and present, who were always happy to lend a helping hand or discuss a new idea. Particular thanks must go to Noah Waterfield Price, who I thank for showing an eager interest in my work and for teaching me many of the concepts used throughout my studies, including the details of diffraction theory and the finer points of Python. My time in Oxford would have been less fruitful without his friendship. James Beilsten-Edmands introduced me to the magnetocurrent technique, was a keen teacher in my early years and I thank him for the friendship we shared.

I have been lucky to work with many other people during my time at Oxford, who I thank for their time in support of my work. Dharmalingam Prabhakaran provided me with a large number of excellent Y-type hexaferrite single crystals, without which this thesis would not of been possible. I thank Mohamed Cheddi for his time cutting and preparing single crystals prior to my experiments. I had fruitful collaborations, not included in this thesis, with Zhiping Wang and Henry Snaith and I thank them for including me in their work. Shilei Zhang, Alex Baker and Thorsten Hesjedal were generous with their time introducing me to oxide thin film growth and I thank them for this.

Much of this work in this thesis would not be possible without the excellent experimental facilities of the Diamond Light source, the ISIS neutron facility and the staff associated with these facilities. I thank the experimental team at I10 (P. Steadman, M. Sussmuth, R. Fan and D. Burn) for all their tireless efforts supporting my experiments. I thank A. Lamirand and the rest of the I06 team (S. Dhesi and F. Maccherozzi) for their time and enthusiasm throughout the PEEM experiments we performed together. The WISH team (P. Manuel, D. Khalayvin and F. Orlandi) consistently go beyond the call of duty to deliver experiments of exceptional quality and it was a pleasure to learn from them. I thank A. Bombardi for his support during the diffraction experiments on I16.

I spent two months visiting the University of Wisconsin-Madison, learning the details of oxide thin film growth. C. B. Eom and his group kindly

hosted me during this time and generously allowed me open-access to their excellent experimental facilities. I thank Josh Frederick for welcoming me into his home during my stay and the other members of the group for welcoming me so eagerly. T. Anderson kindly invited me to an authentic American thanksgiving.

I would also like to thank the broader Quantum Materials group who have helped me throughout my DPhil with discussions over tea or at a local pub. I wish the new students of the Oxide electronics group, Anurahda Vibhakar, Jiahao Chen and Laura Schade all the best with their future work.

Hertford college generously provided me with a travel grant to support the presentation of my research at March Meeting, 2018 in Los Angeles, for which I am grateful. Additionally, Hertford was my primary social base during my time at Oxford and here I met many people who I hope will remain life long friends. Bas Bavelaar and Jessica Bevan deserve an honourable mention for providing excellent life advice and sharing in many of my best times at Oxford. I thank Andy, Frankie, Guy, Helen, Jonny, Naomi, Rory, Steve and the other members of the MCR for making my time at Oxford all the more enjoyable. I thank Ben Crofts for sharing my early years as a physicist in training at Durham University and his continued friendship since. I thank all the other friends (Durham and Matravers alumni) who I have been lucky enough to stay in regular contact with during my DPhil. I am incredibly grateful for all the support my parents have given me throughout my education and beyond.

Finally I thank Sarah for her continued love and support during my university education and for her careful proof-reading of this thesis. It is with great sadness that I leave Oxford but will look back on fond memories of late nights spent in the company of friends in the Hertford MCR common room and later nights spent in windowless 'hutches' at various synchrotron sources.

Publication list

1. N. Waterfield Price, R. D. Johnson, W. Saenrang, F. Maccherozzi, S.S. Dhesi, A. Bombardi, **F. P. Chmiel**, C.-B. Eom, and P.G. Radaelli, *Physical Review Letters*, 117, 177601 (2016)

2. N. Waterfield Price, R. D. Johnson, W. Saenrang, A. Bombardi, **F. P. Chmiel**, C.-B. Eom, and P. G. Radaelli, *Physical Review Applied*, 8 (1), 014033 (2017)

3. Z. Wang, Q. Lin, **F. P. Chmiel**, N. Sakai, L. M. Herz and H. J. Snaith, *Nature Energy*, 2, 17134 (2017)

4. **F. P. Chmiel**, N. Waterfield Price, R. D. Johnson, A. D. Lamirand, J. Schad, G. van der Laan, D. T. Harris, J. Irwin, M. S. Rzchowski, C.-B. Eom and P. G. Radaelli, *Nature Materials*, 17, 581–585 (2018)

Pre-prints

1. N. Waterfield Price, A. M. Vibhakar, R. D. Johnson, J. Schad, W. Saenrang, A. Bombardi, **F. P. Chmiel**, C.B. Eom and P. G. Radaelli. *arXiv:1808.10666*

2. **F. P. Chmiel**, D. Prabhakaran, P. Steadman, N. Waterfield Price, R. Fan, P. G. Radaelli and R. D. Johnson. *In preparation*

Contents

1 Introduction **1**

1.1 Magnetic order in oxides 2

1.1.1 Long-range magnetic order 4

1.1.2 Magnetoelectricity 9

1.2 Domains 10

1.3 Plan of thesis 12

2 Experimental techniques **14**

2.1 Crystalline materials 14

2.1.1 Diffraction from crystalline materials 16

2.2 X-ray diffraction 18

2.2.1 Thomson scattering 19

2.2.2 Non-resonant magnetic scattering 22

2.2.3 Resonant magnetic scattering 23

2.2.4 X-ray instrumentation 26

2.3 Neutron diffraction 30

2.3.1 Nuclear scattering 30

2.3.2 Magnetic scattering 31

2.4 X-ray PhotoEmission Electron Microscopy 33

2.4.1 X-ray Magnetic Circular Dichroism 35

2.4.2 X-ray Magnetic Linear Dichroism 38

3 Magnetoelectric phase diagram of Y-type hexaferrite:

$Ba_{0.5}Sr_{1.5}Mg_2Fe_{12}O_{22}$ **40**

3.1 Introduction . . . 40

3.1.1 Y-type hexaferrites . . . 44

3.1.2 The block model . . . 45

3.1.3 $Ba_2Mg_2Fe_{12}O_{22}$ . . . 50

3.2 Experimental details . . . 54

3.2.1 Magnetometry . . . 54

3.2.2 Magnetocurrent measurements . . . 55

3.3 Results and discussion . . . 57

3.3.1 $Ba_{2-x}Sr_xMg_2Fe_{12}O_{22}$ . . . 57

3.3.2 Magnetic phase diagram of $Ba_{0.5}Sr_{1.5}Mg_2Fe_{12}O_{22}$ . . . 58

3.3.3 Magnetoelectric properties . . . 64

3.4 Conclusions . . . 69

4 Magnetic phase identification of $Ba_{0.5}Sr_{1.5}Mg_2Fe_{12}O_{22}$ by X-ray and neutron diffraction **70**

4.1 Introduction . . . 71

4.1.1 Magnetic fan structures of Y-type hexaferrites . . . 72

4.2 Experimental details . . . 76

4.2.1 I16: Non-resonant X-ray magnetic diffraction . . . 76

4.2.2 WISH: Neutron diffraction . . . 79

4.3 Results and discussion . . . 82

4.3.1 Zero-field phases . . . 82

4.3.2 Field-induced phases . . . 86

4.3.3 Phase co-existence . . . 92

4.4 Conclusions . . . 94

5 Magnetoelectric polarity switching in $Ba_{0.5}Sr_{1.5}Mg_2Fe_{12}O_{22}$ studied by resonant X-ray diffraction **96**

5.1 Introduction . . . 97

5.2 Experimental details . . . 104
5.2.1 Sample environment . . . 104
5.2.2 Sample preparation . . . 108
5.2.3 Resonant X-ray diffraction . . . 108
5.3 Results and discussion . . . 119
5.3.1 Zero-field properties . . . 119
5.3.2 Field induced phases . . . 124
5.3.3 Magnetic polarity memory . . . 129
5.4 Conclusions . . . 141

6 Observation of magnetic vortex pairs in an α-Fe_2O_3/Co heterostructure 143

6.1 Introduction . . . 144
6.1.1 Crystal and magnetic structure of α-Fe_2O_3 . . . 148
6.1.2 Imaging magnetic domains . . . 151
6.2 Experimental details . . . 154
6.2.1 Growth of α-Fe_2O_3/Co heterostructure . . . 154
6.2.2 X-ray PhotoEmission Electron Microscopy . . . 156
6.3 Results and discussion . . . 161
6.3.1 In-situ film characterisation . . . 161
6.3.2 XMLD-PEEM vector map of α-Fe_2O_3 . . . 163
6.3.3 Coupled domain structure of α-Fe_2O_3/Co heterostructure . . . 167
6.3.4 Vortex annihilation . . . 171
6.4 Conclusions . . . 173

7 Conclusions 175

A X-ray scattering calculations 178

B Defined constants 181

Bibliography 182

Definitions of abbreviations and acronyms

- AFM : Atomic Force Microscopy
- APD : Anti-Phase Boundary
- APPLE (undulator) : Advanced Planar Polarized Light Emitter
- BMFO : $Ba_2Mg_2Fe_{12}O_{22}$
- BSMFO : $Ba_{0.5}Sr_{1.5}Mg_2Fe_{12}O_{22}$
- DC : Direct Current
- FWHM : Full-Width-Half-Maximum
- HDD : Hard Drive Disk
- LC : Longitudinal Conical
- ME : Magnetoelectric
- MFM : Magnetic Force Microscopy
- MRAM : Magnetoresistive Random-Access Memory
- MOKE : Magneto-Optic Kerr Effect
- NRXD : Non-Resonant X-ray Diffraction
- PEEM : PhotoEmission Electron Microscopy
- PPMS : Physical Property Measurement System
- RF : Radio Frequency
- RXD : Resonant X-ray Diffraction
- SPELEEM : Spectroscopic PhotoEmission and Low Energy Electron Microscope
- SQUID : Superconducting Quantum Interference Device
- TEM : Transmission Electron Microscopy
- VSM : Vibrating Sample Magnetometer
- WF : Weak Ferromagnet
- WISH : Wide angle In a Single Histogram
- X-PEEM : X-ray PhotoEmission Electron Microscopy
- XMCD : X-ray Magnetic Circular Dichroism
- XMLD : X-ray Magnetic Linear Dichroism
- ZFC : Zero Field Cooled

1 | Introduction

Research into the quantum mechanical properties of crystalline materials has historically had a transformative effect on the technology we have at our disposal [1]. Our daily activities are now dominated by microelectronics which are underpinned by a fundamentally quantum mechanical understanding of a broad range of materials. Integrated circuits, recognised with the Nobel prize for Physics in the year 2000, form the core component of these electronics and rely on the use of semiconductors (typically Si) [2]. Data centres, storing the vast amounts of information we generate, heavily depend upon cost-effective hard-drive disks (HDDs) which store information in the magnetic state of a ferromagnetic material. As our demand for higher-density storage, smaller devices, and faster computation speed continues to grow, these technologies and their constituent materials must inevitably be replaced by more energy efficient materials offering enhanced functionality.

Currently, there are a vast number of magnetic systems offering potentially revolutionary applications [3–6]. Magnetoelectric materials, exhibiting coupling between the magnetic and electric order parameters, are one such candidate. From a technological perspective, interest in these materials is motivated by the ability to control magnetic order with electric fields. A functional magnetoelectric memory, one where information could be stored in the magnetic order and wrote/read electrically, could revolutionise data storage by offering a device without thermal loss: a significant improvement on conventional devices, which write and read information from magnetic hard drives using current generated magnetic fields [7].

The functional ability of more exotic forms of magnetic order has also become apparent [4, 8]. Notably, skyrmions (topologically protected spin configurations, first observed in 2009) [9], offer a route to completely novel logic or memory devices where skyrmions are constrained in a 'race track' and manipulated with small electrical currents [4]. Another route to all electrically operated magnetic memories is in the use of arrays of geometrically constrained magnetic vortices, nanodots where magnetic spins whirl around in a closed loop [10].

Underpinning these technologies, is the need to understand the fundamental magnetic properties of these materials at a range of length scales. In this thesis we focus on the properties of two functional magnetic iron oxides. Firstly, we study $Ba_{0.5}Sr_{1.5}Mg_2Fe_{12}O_{22}$, the system exhibiting the worlds largest magnetoelectric coefficient [11]. Our aim is to understand its complex magnetic orders and the magnetoelectric effects these drive. Secondly, we study the domain configuration of the archetypal antiferromagnet α-Fe_2O_3, which has a trivial collinear magnetic structure. Its collinear and well understood magnetic order allows us to develop a X-ray PhotoEmission Electron Microscopy vector mapping technique to image its magnetic domain structure. We find that the magnetic domains in this system arrange themselves in a topologically interesting way, never before observed in a geometrically unconfined antiferromagnet.

For the rest of this chapter we discuss the magnetic order observed in functional oxides relevant to this thesis and introduce the concept of magnetic domains, a particularly important concept because domains can alter the bulk properties of a material.

1.1 Magnetic order in oxides

In functional magnetic oxides, long-range magnetic order appears because of exchange interactions between neighbouring magnetic ions. Exchange is a consequence

of the quantum mechanical nature of an electron and arises because the quantum mechanical wavefunction of electrons (fermions) must be antisymmetric on particle exchange; that is they must obey the Pauli exclusion principle [12]. Considering a two electron system, with electrons at positions $\vec{r}_1$ and $\vec{r}_2$ (labelled a and b respectively), we can write the overall wavefunction of the system as,

$$\Psi_S = \frac{1}{\sqrt{2}}\overbrace{[\psi_a(\vec{r}_1)\psi_b(\vec{r}_2) + \psi_b(\vec{r}_2)\psi_a(\vec{r}_1)]}^{Spatial}\overbrace{\chi_S}^{Spin} \tag{1.1}$$

$$\Psi_T = \frac{1}{\sqrt{2}}[\psi_a(\vec{r}_1)\psi_b(\vec{r}_2) - \psi_b(\vec{r}_2)\psi_a(\vec{r}_1)]\chi_T, \tag{1.2}$$

for the antisymmetric spin singlet (χ_S), spatially symmetric state and for the symmetric spin triplet (χ_T), spatially anti-symmetric state respectively. ψ_i are the spatial wavefunctions of the individual electrons. Generally, there will be an energy difference between the spin singlet and triplet states which is parameterised by J, the exchange constant (or exchange integral) [13],

$$J = \frac{E_S - E_T}{2} = \int \psi_a^*(\vec{r}_1)\psi_b^*(\vec{r}_2)H\psi_b(\vec{r}_1)\psi_a(\vec{r}_2)\mathrm{d}\vec{r}_1\mathrm{d}\vec{r}_2. \tag{1.3}$$

This energy difference is then the pre-factor for the spin-dependent component of the Hamiltonian describing the interaction of a collection of electrons,

$$H_{exchange} = -\sum_{i,j} J_{ij}\vec{S}_i \cdot \vec{S}_j, \tag{1.4}$$

where J_{ij} is the exchange constant between the i^{th} and j^{th} spins. In the convention displayed here $J_{i,j} > 0$ favours ferromagnetic alignment of the i^{th} and j^{th} spin pairs and $J_{i,j} < 0$ an antiferromagnetic alignment of them. With knowledge of all relevant exchange interactions of a system it is possible to predict the ground state magnetic configuration. Considering multiple exchange interactions (such as nearest

and next-nearest neighbour) complex magnetic orders, such a helices and cycloids can be realised.

Superexchange

Direct exchange describes situations in which electrons on neighbouring ions interact via an exchange interaction, its strength depends strongly on the overlap of neighbouring electron orbitals. In transitional metal oxides the magnetic ions are spatially separated by oxygen ions and the spatial separation of the magnetic ions is generally too great for direct exchange to be effective (the orbital overlap decreases exponentially with distance) [14]. Despite this, ionic solids are still often magnetically ordered and a longer-range exchange must, therefore, be present to explain this ordering.

This mechanism is known as *superexchange*, where the exchange interaction between two magnetic ions is mediated by a non-magnetic ion. In iron oxides, a Fe $3d$ orbital may overlap with the $2p$ orbital of a neighbouring oxygen ion, which in turn can overlap with the $3d$ orbital of a different neighbouring Fe orbital, resulting in an effective exchange between the two Fe sites. The exchange arises because partial delocalisation of electrons across the bond can reduce their kinetic energy, as given by the uncertainty principle [15]. Similarily to direct exchange, the strength of the superexchange interaction depends on the orbital overlap of the $3d$ and $2p$ orbitals and the strength (and sign) of superexchange interactions, therefore, depend strongly on the Fe-O-Fe bond angle. This means superexchange interactions can be effectively tuned by inducing lattice deformations local to a bond, for example by site-specific elemental doping [16].

1.1.1 Long-range magnetic order

As discussed, long-range magnetic order in iron oxides is primarily a result of superexchange interactions. Competition between multiple exchange interactions can

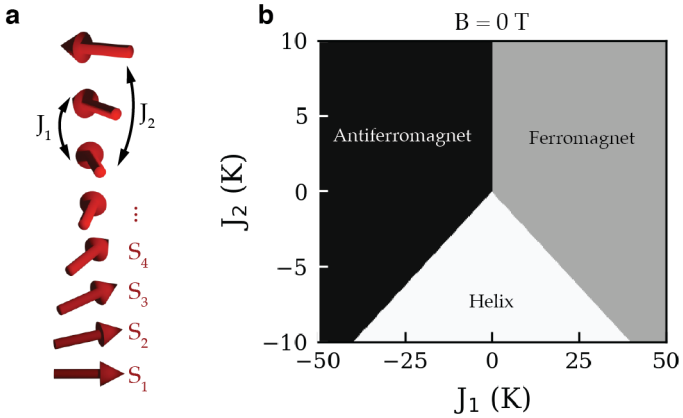


Figure 1.1: Magnetic order of a spin chain. **a,** Helical magnetic structure, with spins rotating in a plane perpendicular to the direction of propagation ($\vec{r}$). J_1 and J_2 denote nearest and next-nearest neighbour exchange interactions, respectively. All other interactions are assumed to be zero. **b,** Ground state of system (in zero applied field) as a function of J_1 and J_2. After S. Blundell [13].

stabilize a diverse range of magnetic orders. To gain a qualitative understanding of how exchange interactions can stabilize different magnetic orders we consider a 1D chain of spins, where moments lie in the plane orthogonal to their stacking direction (fig. 1.1 a). We consider only nearest (J_1) and next-nearest (J_2) neighbour exchange interactions and investigate how the strength and sign of these interactions can compete to form different magnetic orders. This discussion follows closely that presented in reference [13].

First we parametrise the spin Hamiltonian (eq. (1.4)) in a convenient way such that the energy of the spin system can be expressed as,

$$E = -2S^2[J_1 \cos(\phi_0) + J_2 \cos(2\phi_0)], \tag{1.5}$$

where ϕ_0 is the angle between neighbouring spins pairs (it is assumed this is the same between each pair). The minimum energy state ($\frac{\delta E}{\delta \phi_0}$) is obtained by differentiation,

$$[J_1 + 4J_2 \cos(\phi_0)] \sin(\phi_0) = 0, \tag{1.6}$$

which has two solutions, either $\sin(\phi_0) = 0$ or $[J_1 + 4J_2 \cos(\phi_0)] = 0$. The first

solution corresponds to collinear magnetic order: either ferromagnetic order ($\phi_0 = 0$, all spins parallel) or antiferromagnetic order ($\phi_0 = \pi$, neighbouring spins are anti-parallel). The latter solution corresponds to a helical structure, where the pitch (ϕ_0) of the helix is given by,

$$\phi_0 = \arccos\left(\frac{-J_1}{4J_2}\right). \tag{1.7}$$

Following S. Blundell, we calculate the lowest energy (ground state) magnetic order as a function of $J_{1,2}$, the results of which are shown in fig. 1.1 b. It is found that a non-collinear magnetic structure (a helix) is the ground state order only when the conditions: $J_2<0$ and $|J_1| < 4|J_2|$ are satisfied [13]. For other values of exchange constants the systems is either ferromagnetically or antiferromagnetically ordered (fig. 1.1 b).

In addition to these structures, magnetic anisotropies or additional interactions (such as the Dzyaloshinskii–Moriya interaction [17, 18]) can stabilize more complex spontaneous magnetic orders, such as cycloids (rotating magnetic structures where the plane of rotation contains the direction of propagation) and conical structures (a superposition of a ferromagnet and a helix or cycloid). These systems can still be understood by trivially extending the Hamiltonian to include the relevant anisotropies and exchanges constants [19].

Field induced phase transitions

As well as considering the spontaneous magnetic order of a system, we can also consider the changes in a system under the influence of an external magnetic field. The spin dependent Hamiltonian can be altered to include the additional Zeeman energy of the structure (describing the systems coupling to the applied magnetic field),

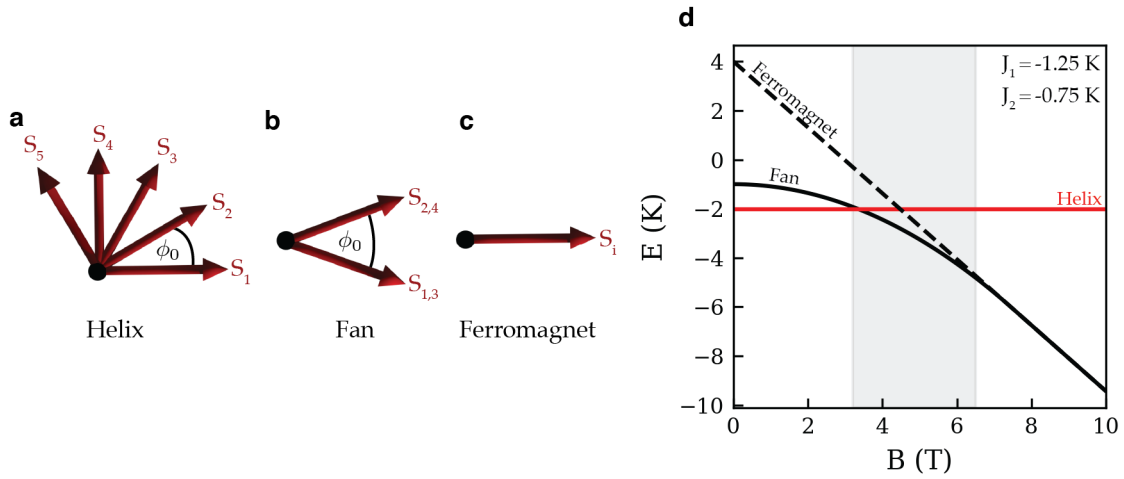


Figure 1.2: Energy of different magnetic orders in an applied magnetic field. a-c, Orthographic projection of different magnetic orders into the basal plane. Spins (red arrows) follow the labelling convention of fig. 1.1 a. **d,** Energy of each structure (a-c) as a function of applied magnetic field for given exchange constants (top right). For the fan structure (b) the value of ϕ_0 which minimizes the energy of the system is selected at each field value. The grey box highlights the field region where the fan structure is stable.

$$H = -\sum_{i,j} J_{ij}\vec{S}_i \cdot \vec{S}_j + g\mu_B \sum_j \vec{S}_j \cdot \vec{B}, \tag{1.8}$$

where $\vec{B}$ is the magnetic flux density, g the Landé g-factor and μ_B the Bohr magneton. As an example, relevant to the experimental studies presented in this thesis, we consider the 1D spin chain previously discussed (fig. 1.1 a) with nearest and next-nearest neighbour exchanges constants of $J_1 = -1.25$ K and $J_2 = -0.75$ K respectively. For these values, in the absence of an applied magnetic field ($\vec{B} = 0$) the system is helically ordered (fig. 1.1 b). The energy of a helix is independent of magnetic field (the average Zeeman energy of a spin is zero), but a ferromagnetic structure ($\phi_0 = 0$) can couple to a magnetic field to lower its energy, explicitly,

$$E_{ferro} = -2(J_1 + J_2) - 2\mu_B B, \tag{1.9}$$

therefore at some magnetic field magnitude (B) we expect the system to undergo a phase transition from the helical state (i.e., fig. 1.2 a) to a ferromagnetically ordered one (fig. 1.2 c).

Competition between exchange and the Zeeman energy can, in some circumstances, stabilize more complex, intermediate phases [19]. For example, consider the so-called 'fan' structure displayed in fig. 1.2 b, where spins are splayed about the applied magnetic field direction. The energy of this structure is given by,

$$E_{fan} = -2(J_1 \cos(\phi_0) + J_2) - 2\mu_B B \cos(2\phi_0), \tag{1.10}$$

where the 'fan-angle' (ϕ_0) is displayed in fig. 1.2 b. For certain values of J_1, J_2 and B this can have a lower energy than either a helical or ferromagnetic state and can therefore be experimentally realised.

The energy of the three discussed structures (fig. 1.2 a-c) are calculated as a function of applied magnetic field, graphically displayed in fig. 1.2 d. Clearly, in the low magnetic field limit, a helical structure is the ground state (solid red line) but at $\sim$2.65 T the fan structure (solid black line) becomes lower in energy, such that a phase transition to this metamagnetic state is expected. As the magnitude of the magnetic field is increased the energy of the fan state approaches the ferromagnetic one (dashed black line) such that ϕ_0 continuously decreases to zero: in the high magnetic field limit the system is ferromagnetically ordered.

This fictional spin model has demonstrated how competition between exchange interactions and the Zeeman energy can induce metamagnetic phase transitions between distinct magnetic orders. In the presence of multiple magnetic sites or an increased number of relevant exchange interactions even more complex intermediate states can be stabilized [19, 20]. The study of such metamagnetic structures is the subject of chapters 3 and 4 where we present the metamagnetic phase diagram of the Y-type hexaferrite $Ba_{0.5}Sr_{1.5}Mg_2Fe_{12}O_{22}$.

1.1.2 Magnetoelectricity

Magnetoelectric materials are those that exhibit coupling between the magnetic and electric order parameters and their respective conjugate fields. It was first experimentally realised in materials exhibiting the so-called linear magnetoelectric effect, [21] where magnetic field application induces an electric polarisation,

$$P_i = \alpha_{ij} H_j, \tag{1.11}$$

where α_{ij} is a 2^{nd} rank axial tensor characterising the strength of the effect [22]. More recently, the term magnetoelectric has come to encompass any material exhibiting coupling between the magnetic and electric order parameters. For example, in a composite material coupling a magnetostrictive material to a piezelectric one [23]. Of particular importance are materials where ferroelectricity, a net reversible electric polarisation, is driven by non-collinear magnetic order [24]. The electric polarisation induced by a pair of spins is described by the spin-current mechanism [25],[1]

$$\vec{P} \propto \hat{e}_{i,j} \times (\vec{S}_i \times \vec{S}_j), \tag{1.12}$$

where $S_{i,j}$ are neighbouring spins and $\hat{e}_{i,j}$ the unit vector joining them. Spin-driven ferroelectrics are of great interest because they typically exhibit significant coupling between the magnetic and electric orders. For example, the polarisation is anti-symmetric on exchange of the spins ($(\vec{S}_i \times \vec{S}_j) \rightarrow -(\vec{S}_j \times \vec{S}_i)$), which is equivalent to changing the sense of rotation of a magnetic structure, hinting at the coupling between the electric and magnetic orders.

[1] Other mechanisms exist for spin-induced ferroelectricity but this is the only one relevant to this thesis.

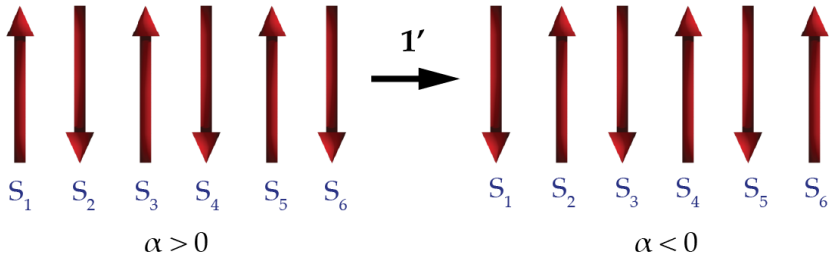


Figure 1.3: Temporal inversion domains of a fictional magnetoelectric antiferromagnet. At a transition from a magnetically disordered to a magnetically ordered state domains, related by temporal inversion, are expected to form.

1.2 Domains

Domains, macroscopic regions of crystal with different physical properties, naturally occur at symmetry breaking phase transitions. Each distinct domain is related to all other domains in the crystal by the symmetry elements (or combination of those) that are lost during the phase transition. For example, in a transition from a magnetically disordered state to a magnetically ordered one we expect, as a minimum, the formation of two domains related by temporal inversion (fig. 1.3).

Domains can have detrimental effects on the functional properties of a material. Consider, for example, a magnetoelectric (necessarily magnetically ordered) with an equal population of either time inversion domains (i.e., fig. 1.3). As the magnetoelectric tensor ($\alpha_{i,j}$) is time antisymmetric, its elements are opposite in sign between each domain. This means that on the application of magnetic fields, equal and opposite electric polarisation will be induced in each domain.

Functionally, it is therefore important to be able to *engineer* domain configurations as to maximize the functional properties of a material. This can be as simple as causing a domain re-population by application of appropriately large conjugate fields (see 'magnetoelectric poling' in the following) [26], or by more exotic means such as substrate engineering in epitaxial thin films or by utilizing a magnetic exchange proximity effect [26–28].

The study of domain structures underpin much of this thesis. In chapter 5 we discuss

how spatially resolved X-ray diffraction is sensitive to the magnetic polarity domains (related by temporal/spatial inversion) of the magnetoelectric, $Ba_{0.5}Sr_{1.5}Mg_2Fe_{12}O_{22}$.

Magnetoelectric poling

As an example of magnetic domain control, we consider time-inversion domains in a magnetoelectric at the onset of magnetoelectric order (i.e. at a relevant paramagnetic-antiferromagnet phase transition). For simplicity, we consider a diagonal magnetoelectric tensor ($\alpha_{11} = \alpha_{22} \neq \alpha_{33}$), as is the case in the archetypical magnetoelectric Cr_2O_3. Additionally we consider magnetic and electric fields applied (anti-)parallel to the z axis of the crystal such that only the α_{33} component is relevant [22]. The free energy of the system can therefore be described by,

$$F(E,H) = F_0 - \frac{1}{2}\epsilon_0\epsilon_r E_z^2 - \frac{1}{2}\mu_0\mu_r H_z^2 - \alpha_{33}E_z H_z + \dots \tag{1.13}$$

ignoring the constant term, the quantities are associated with electric and magnetic susceptibility and the (linear) magnetoelectric effect. Considering the two magnetoelectric domains related by temporal inversion ($\alpha_{33} > 0$ and $\alpha_{33} < 0$, see fig. 1.3), one domain ($\alpha_{33}>0$) will minimize the free energy for parallel configurations of E_z and H_z and the other ($\alpha_{33} < 0$) for anti-parallel configurations of E_z and H_z. This energetic imbalance can be used to favourably nucleate one domain at the magnetoelectric phase transition to effectively prepare a single time inversion domain [29].

Similar procedures can be used to pole ferromagnetic or ferroelectric materials by coupling to the spontaneous magnetisation or electric polarisation with their respective conjugate field. This principle is used throughout our experimental studies to prepare samples into monodomain states.

Novel domain topologies

Recently, it has become apparent that the domain morphologies of ordered media are

much richer than ever previously imagined. Topologies beyond the trivial, irregularly shaped and geometrically simple domains have been observed in several systems [30–32]. Notably, vortex domain structures, where multiple domains extend from a common vertex, have been observed in several systems and display topological protection: changes in domain morphology can only occur through the annihilation (or creation) of vortex/anti-vortex pairs. This protection can make certain domain morphologies particularly stable and could make the basis of a functional memory device, where information is stored robustly in a vortex state [10].

Such domain structures are the topic of chapter 6 where we discuss the magnetic domain morphology of a coupled α-Fe_2O_3/Co/Al heterostructure imaged using vector-mapped X-ray PhotoEmission Electron Microscopy, where an unprecedented network of antiferromagnetic vortex domains is observed.

1.3 Plan of thesis

In this thesis we present a set of experimental studies of the magnetic order of two functional iron oxides. We begin (chapter 2) by presenting an outline of the experimental techniques forming the foundation of these investigations, with a strong emphasis on the X-ray diffraction technique. Next, we discuss experimental studies of single crystal samples of $Ba_{0.5}Sr_{1.5}Mg_2Fe_{12}O_{22}$ (BSMFO), a magnetic material exhibiting the world's largest magnetoelectric coefficient [11]. In chapters 3 and 4 we study its magnetic order under the influence of external magnetic fields, using magnetometry to resolve its magnetic phase diagram. Magnetocurrent measurements and diffraction experiments of this system are discussed and allow us to classify the different magnetic orders of BSMFO. We use the results of these investigations as the basis of chapter 5, where we discuss the resonant X-ray diffraction technique and show it possesses a unique sensitivity to the magnetic polarity (sense of rotation) of the magnetoelectric phase of BSMFO. We utilize this sensitivity to spatially resolve the magnetic polarity of BSMFO as a function of applied magnetic field and use

these results to propose a microscopic model for the large magnetoelectric effect observed in BSMFO.

The final study presented in this thesis (chapter 6) is an X-ray PhotoEmission Electron Microscopy study of a magnetic heterostructure consisting of α-Fe_2O_3 (10 nm)/Co (1 nm) stack, a geometry suitable for application. We develop a novel vector-mapping technique to image the magnetic domain structure of each layer of the heterostructure and observe an unprecedented network of antiferromagnetic vortices in the α-Fe_2O_3 layer, these vortices are found to imprint into the adjacent Co layer. We discuss the topological properties of these vortices and demonstrate the system exhibits topological stability by inducing mass annihilation of the vortices by the application of a small magnetic field. We conclude by suggesting future studies which could build on this novel discovery.

2 | Experimental techniques

In this chapter we introduce the experimental techniques forming the foundation of this thesis. Magnetic X-ray and neutron diffraction are used to inform us about the long-range magnetic order of a system and allows us to interrogate the domain configuration of a material, with spatial resolutions approaching 5 µm. Moreover, X-ray diffraction is the technique of choice when it comes to characterising the crystallographic properties (i.e. phase purity and composition) of a sample prior to study at national facilities.

X-ray PhotoEmission Electron Microscopy (X-PEEM) is a technique which excels at imaging the real-space distribution of the (staggered) magnetisation at the surface of magnetically ordered systems, allowing the visualisation of magnetic domains occurring on sub-micron length-scales. It has the advantage of being sensitive to distinct elements and can therefore be used to image the individual layers of magnetic heterostructures.

2.1 Crystalline materials

This thesis focuses on systems exhibiting a long-range periodic array of atoms, generally referred to as crystals. The translational symmetry of such a periodic array means we can describe crystals as a convolution of a lattice (a series of points) and a basis, the set of atoms themselves repeated at each point on the lattice. The position of each lattice point can be described by a lattice vector,

$$\vec{R}_n = n_1\vec{a} + n_2\vec{b} + n_3\vec{c}, \tag{2.1}$$

s where $\vec{a}$, $\vec{b}$ and $\vec{c}$ are the basis vectors of this lattice. These basis vectors form a parallelepiped that define the repeat unit of the crystal (referred to as the unit cell) of volume,

$$V = \vec{a} \cdot (\vec{b} \times \vec{c}). \tag{2.2}$$

The unique set of atoms (the basis) which make up the crystal are then defined within this unit cell. Much of the physics of a crystal can be understood by considering just the atoms within a single unit cell, for example the magnetic moment density is invariant by translation of a lattice vector ($\vec{R}_n$).

The reciprocal lattice

The reciprocal lattice is a geometrical construct which provides a simple basis for understanding diffraction experiments. Its construction can be introduced in several ways, including considering the normals of planes of atoms, as a set of vectors which satisfy the Laue condition, or simply as a convenient basis to describe diffraction from ordered media. In the following we simply define the reciprocal lattice and its merits will become apparent when discussing diffraction in later sections. The reader is directed to other texts to gain a developed understanding [33–35].

The reciprocal lattice of a crystalline material is a set of points described by three lattice vectors: $\vec{a}^*$, $\vec{b}^*$ and $\vec{c}^*$ which are defined as follows,

$$\vec{a}^* = 2\pi\frac{\vec{b} \times \vec{c}}{\vec{a} \cdot (\vec{b} \times \vec{c})},\ \vec{b}^* = 2\pi\frac{\vec{c} \times \vec{a}}{\vec{a} \cdot (\vec{b} \times \vec{c})},\ \vec{c}^* = 2\pi\frac{\vec{a} \times \vec{b}}{\vec{a} \cdot (\vec{b} \times \vec{c})}, \tag{2.3}$$

where $\vec{a}, \vec{b}$ and $\vec{c}$ are the real-space lattice vectors. A general reciprocal lattice vector is denoted by $\vec{G} = h\vec{a}^* + k\vec{b}^* + l\vec{c}^*$ where h, k, l are integers. Not apparent from this

definition is that the reciprocal lattice vectors are perpendicular to crystallographic planes and are therefore intimately linked to diffraction by the coherent scattering of these atomic planes as described by Braggs law or the Laue condition [34].

2.1.1 Diffraction from crystalline materials

Within the context of this work, diffraction occurs when incident radiation (X-rays, neutrons, electrons) with wavevector $\vec{k}_i$ is scattered (outgoing wavevector $\vec{k}_f$) by a crystalline material. The spatial distribution of atoms within a crystal means constructive interference will only occur at certain positions for a given incident wavevector.

The diffraction process is characterised by a change in momentum,

$$\vec{Q} = \vec{k}_i - \vec{k}_f, \tag{2.4}$$

where $\vec{Q}$ is known as the momentum transfer or (more commonly) the scattering vector. The condition for constructive interference of the scattered X-rays or neutrons depends only on the translational symmetry of the crystalline lattice and is given by the Laue condition,

$$\vec{Q} \cdot \vec{R}_n = 2\pi n, \tag{2.5}$$

where n is an integer. Importantly, reciprocal lattice vectors exclusively satisfy this equation ($\vec{Q} = \vec{G}$) such that the scattering vector must coincide with a reciprocal lattice point for constructive interference to be observed.

This discussion has dealt with the geometric part of diffraction arising only from the crystallographic lattice. To calculate the predicted intensity of Bragg scattering we must consider the differential scattering cross section, which we express in terms of scattering amplitudes, which characterise the scattering strength from the individual

scattering centres (atoms). Denoting the total coherent scattering amplitude of the n^{th} atom as $f_n(\vec{Q})$ the coherent differential cross section is given by,

$$\left(\frac{d^2\sigma}{d\Omega dE_f}\right) = \left|\sum_n f_n(\vec{Q})e^{i\vec{Q}\cdot\vec{r}_n}\right|^2 \delta(E_f - E_i), \tag{2.6}$$

where r_n is the position of the n^{th} atom. We can make the simplification, $\vec{r}_n \rightarrow \vec{R}_n + \vec{d}_n$ where $\vec{R}_n$ is the (lattice) vector to the origin of the unit cell the n^{th} atom resides in and $\vec{d}_n$ the position of the atom with respect to the unit cell origin giving,

$$\left(\frac{d^2\sigma}{d\Omega}\right) = \left|\overbrace{\sum_j f_j(\vec{Q})e^{i\vec{Q}\cdot\vec{d}_j}}^{\text{Basis}}\overbrace{\sum_n e^{i\vec{Q}\cdot\vec{R}_n}}^{\text{Lattice}}\right|^2, \tag{2.7}$$

where the first summation (basis) is over a single unit cell and the second (lattice) runs over every lattice vector. The delta function, highlighting the elastic nature of the scattering, has been ignored as only elastic scattering is considered in this thesis. The lattice summation is only non-zero for values of $\vec{Q}\cdot\vec{R}_n$ equal to an integer multiple of 2π, as given by the Laue condition (eq. (2.5)) which is true when $\vec{Q}$ equals a reciprocal lattice vector ($\vec{G}$) therefore,

$$\left(\frac{d^2\sigma}{d\Omega}\right) = \left|N\sum_j f_j(\vec{Q})e^{i\vec{Q}\cdot\vec{d}_j}\delta(\vec{Q}-\vec{G})\right|^2, \tag{2.8}$$

where N is the number of unit cells in the scattering volume. This equation highlights that the intensity of a Bragg reflection can be calculated by considering a single unit cell only.

In the following we will discuss the form of the scattering amplitude ($f(\vec{Q})$) for X-ray diffraction and express it in a basis convenient for experimentation.

2.2 X-ray diffraction

X-ray diffraction from a crystal (copper sulphate) was first observed in 1912 by Max von Laue [36]. The potential of X-ray diffraction was quickly realised (von Laue was awarded the 1914 Nobel prize in physics for his discovery [37]) and it underpinned many of the great breakthroughs of crystallography over the next decades [38, 39]. More recently, the advent of synchrotron technology has made even more novel studies possible. While historical magnetic X-ray diffraction experiments (utilizing X-ray tubes) required significant effort and infeasibly long measurement times, the order of magnitudes larger incident flux offered by synchrotron facilities has made it routine to study the magnetic order of crystals by X-ray diffraction [40, 41]. In this section we introduce the different scattering amplitudes relevant to the X-ray diffraction experiments presented in this thesis.

Coherent scattering amplitude

The total coherent X-ray scattering amplitude of an isolated magnetic ion can be expressed as [42],

$$f(\vec{Q}) = f_0(\vec{Q}) + f^{mag}(\vec{Q}) + \overbrace{f'(\hbar\omega) + if''(\hbar\omega)}^{f^{RES}}, \tag{2.9}$$

where $f_0(\vec{Q})$ is the Thomson scattering amplitude (scattering from electron charge density), $f^{mag}(\vec{Q})$ the (non-resonant) magnetic X-ray scattering and the $f'(\hbar\omega) + if''(\hbar\omega)$ terms denote the $\vec{Q}$-independent 'anomalous' scattering amplitudes, which are collected into a single scattering amplitude f^{RES}, highlighting that these amplitudes are only relevant when on or near to 'resonance' (incident photon energy near to an absorption edge of the material).

In the following we will discuss each of these terms and the order they are sensitive to.

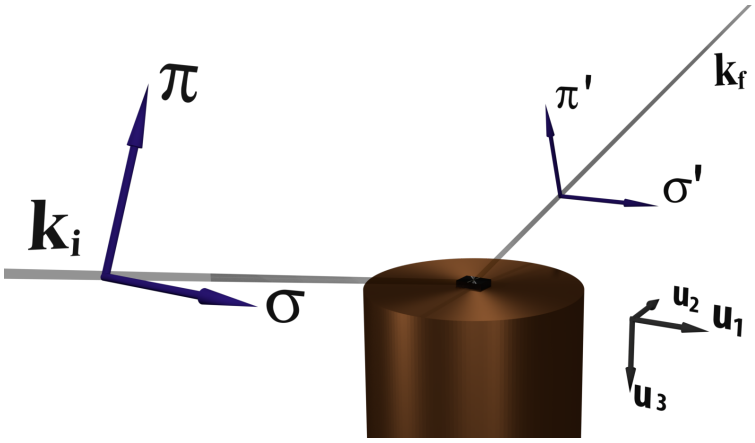


Figure 2.1: Geometry of a X-ray scattering experiment. X-rays are incident (wavevector $\vec{k}_i$) on a sample (black cuboid) and scatter coherently in the direction described by $\vec{k}_f$. σ and π denote the basis of orthogonal linear polarisation states used throughout our scattering calculations. $\hat{u}_i$ denotes the Cartesian basis used to describe crystallographic and magnetic structures.

2.2.1 Thomson scattering

Thomson scattering describes the coherent scattering from a crystalline material as a result of the interaction between the incident photon and the electron charge. The Thomson scattering amplitude can be calculated using classic electromagnetic theory [43, 44], treating the electron (perturbed by an electric field) as an electric dipole oscillator or by using non-relativistic perturbation theory [41]. The scattering amplitude is given by,

$$f_0(\vec{Q}) = r_0 f_D f_{atom}(\vec{Q}) \left| \hat{\epsilon} \cdot \hat{\epsilon}' \right| \tag{2.10}$$

where $r_0 = e^2/(mc^2)$ is the Thomson scattering length and f_D is the Debye-Waller factor, characterising the effect of the thermal motion of the atoms [45, 46]. The scattering power of a single atom is denoted by $f_{atom}(\vec{Q})$ (discussed in the following) and $\hat{\epsilon} \cdot \hat{\epsilon}'$ is the polarisation factor, which describes the polarisation of the scattered X-ray beam for a given incident polarisation state.

For a scattering experiment it is convenient to express this factor in a basis of two orthogonal linear polarisation states: σ (perpendicular to the scattering plane) and

π (parallel to the scattering plane) states, as outlined graphically in fig. 2.1. In this basis the polarisation factor is given by [41],

$$\begin{aligned}\hat{\epsilon}\cdot\hat{\epsilon}' &= \begin{pmatrix} \epsilon_\sigma \to \epsilon'_\sigma & \epsilon_\pi \to \epsilon'_\sigma \\ \epsilon_\sigma \to \epsilon'_\pi & \epsilon_\pi \to \epsilon'_\pi \end{pmatrix} \\ &= \begin{pmatrix} 1 & 0 \\ 0 & \cos(2\theta) \end{pmatrix}. \end{aligned} \tag{2.11}$$

The merits of expressing scattering amplitudes in this basis becomes apparent when performing scattering experiments at synchrotron facilities, where incident X-ray polarisation state can be easily controlled. This basis allows for quick visual inspection of the effect any scattering process has on the polarisation state of the scattered X-rays, notably Thomson scattering (eq. (2.11)) does not rotate the polarisation of incident X-rays during the scattering process (off-diagonal elements are zero).

Atomic form factor

The atomic form factor, $f_{atom}(\vec{Q})$, describes the X-ray scattering amplitude from the electron cloud of an isolated atom. It is defined as the ratio of the scattering amplitude of an X-ray beam by an atom compared to the scattering from a single isolated electron. It can be shown to be equal to the Fourier transform of the electron density,

$$f_{atom}(\vec{Q}) = \int \rho(\vec{r}) e^{i\vec{Q}\cdot\vec{r}} dV, \tag{2.12}$$

where $\rho(\vec{r})$ is the electron density, $\vec{r}$ the position vector relative to the centre of the atom and $\vec{Q}$ the scattering vector [43, 44].

Qualitatively, this equation shows that for broad real space electron distributions f_{atom} is narrower and so scatters weakly at higher $|\vec{Q}|$. Physically, the dependence

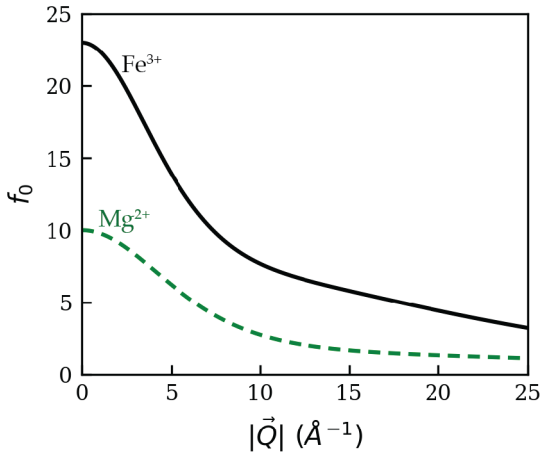


Figure 2.2: Atomic form factor as a function of $|\vec{Q}|$. Solid black line displays the atomic for factor for Fe^{3+} and the dashed green line for Mg^{2+}. For small $|\vec{Q}|$ f_0 tends to Z (number of bound electrons) and reduces with increasing $|\vec{Q}|$.

of the form factor on $|\vec{Q}|$ arises because scattering originating from the different electrons of an atom will possess (slightly) different path lengths and will therefore de-constructively interfere. This interference is more severe at large $|\vec{Q}|$ as the path-length differences increase. Analytically the form factor can be approximated as a sum of Gaussians [47],

$$f_{atom}(\vec{Q}) = \sum_{i=1}^{4} a_i e^{(-b_i \frac{|\vec{Q}|}{4\pi}^2)} + c, \tag{2.13}$$

valid for $|\vec{Q}| < 25$ Å^{-1}, where the constants are tabulated in reference [47]. Figure 2.2 displays this function evaluated for Fe^{3+} and Mg^{2+} ions (relevant to chapter 3), where at low $|\vec{Q}|$ we see the form factor tends to Z (the number of electrons in the ion). Light elements therefore scatter X-rays weakly and we note that X-ray diffraction is poor at differentiating between elements of similar atomic number. Fe^{3+} and Mg^{2+} ions, as shown in fig. 2.2, possess a sufficiently different number of electrons that moderate contrast can be achieved between these two elements.

2.2.2 Non-resonant magnetic scattering

The non-resonant magnetic scattering effects are encompassed in $f^{mag}(\vec{Q})$ in eq. (2.9). The form of $f^{mag}(\vec{Q})$ has been discussed by several authors and non-relativistic perturbation theory must be utilized to understand its form [48,49]. It was first derived in a convenient form by Blume and Gibbs [41,49], and was found to depend on the atomic orbital and spin magnetic densities,

$$f^{mag}(\vec{Q}) = ir_0\frac{\hbar\omega}{mc^2}f_D\big[\frac{1}{2}\vec{l}\cdot\vec{A} + \vec{s}\cdot\vec{B}\big], \tag{2.14}$$

where $\vec{l}$ and $\vec{s}$ are the orbital and spin moment of the magnetic ion. $\vec{A}$ and $\vec{B}$ are the polarisation vectors defined, in the previously introduced basis of orthogonal polarisation states, as,

$$\begin{aligned}\vec{A} &= \frac{|\vec{Q}|^2}{2|\vec{k}|^2}\begin{pmatrix} 0 & -(\hat{k}_i + \hat{k}_f) \\ \hat{k}_i + \hat{k}_f & 2\hat{k}_i \times \hat{k}_f \end{pmatrix}, \\ \vec{B} &= \begin{pmatrix} \hat{k}_i \times \hat{k}_f & -\hat{k}_f(1 - \hat{k}_i \cdot \hat{k}_f) \\ \hat{k}_i(1 - \hat{k}_i \cdot \hat{k}_f) & \hat{k}_i \times \hat{k}_f \end{pmatrix}. \end{aligned} \tag{2.15}$$

Formulating $\vec{A}$ and $\vec{B}$ in this way allows $f^{mag}(\vec{Q})$ to be expressed in this basis,

$$f^{mag}(\vec{Q}) = \\ ir_0\frac{\hbar\omega}{mc^2}f_D\begin{bmatrix} \sin(2\theta)s_2 & -2\sin^2(\theta)[\cos(\theta)(l_1+s_1) - \sin(\theta)s_3] \\ 2\sin^2(\theta)[\cos(\theta)(l_1+s_1) + \sin(\theta)s_3] & \sin(2\theta)\big[2\sin^2(\theta)l_2 + s_2\big] \end{bmatrix}, \tag{2.16}$$

where θ is the scattering (Bragg) angle and $\vec{s} = [s_1, s_2, s_3]$ and $\vec{l} = [l_1, l_2, l_3]$. The

constant prefactor ($\frac{r_0\hbar\omega}{mc^2}$) of non-resonant magnetic scattering gives an indication of its strength relative to Thomson scattering: it is approximately 10^{-6} weaker in transition metal oxides (one also has to consider that fewer electrons contribute to magnetic scattering process compared to charge scattering) [50]. Its weak nature means that measurement of non-resonant magnetic scattering can generally be performed only at synchrotron sources with high incident photon flux. An advantage of performing an X-ray diffraction experiment at synchrotron facilities is the four different polarisation channels (eq. (2.16)) can be easily measured. As eq. (2.16) shows, this can be used to identify the orbital and spin contributions to the scattering cross section or isolate magnetic scattering from scattering of charge origin (by measuring only scattering processes which rotate the polarisation of the scattered X-rays). The non-resonant scattering experiment discussed in this thesis is performed on an orbitally quenched system (d^5 valence electron configuration) such that $\vec{l} = 0$ and we only have to consider scattering from spin densities.

2.2.3 Resonant magnetic scattering

The resonant scattering process (outlined in fig. 2.3) occurs when the energy of incident photons are tuned to an atomic transition of the magnetic species under study. At this energy, incident photons are absorbed by electrons causing them to undergo a virtual transition from the ground state to empty valence states. Upon de-excitation they emit ('scattered') photons of the same energy as the absorbed photon, an elastic scattering event.

The resonant process can cause a dramatic increase in the (magnetic) scattering cross section: in Ho a ∼50-fold increase in the magnetic scattering was observed near to the L_3 absorption edge (8.067 keV), corresponding to an electric dipole allowed transition from a $2p$ core state to a $5d$ valence state. As the $5d$ valence state is magnetically polarised the scattering process is sensitive to the magnetic order in this band as a result of the exclusion principle [51].

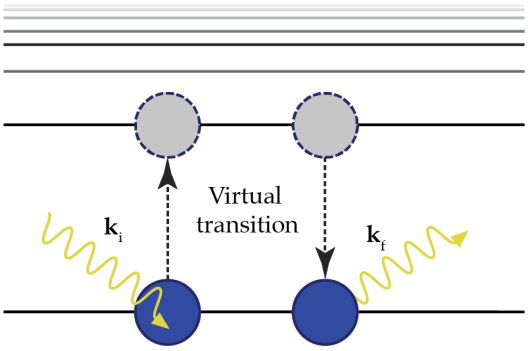


Figure 2.3: Mechanism of resonant scattering process. The incident X-ray energy is tuned to be equal to the energy difference between two atomic levels, allowing an electron to be make a virtual transition to the higher energy (unoccupied) state. It radiates the 'scattered' photon on de-excitation to the ground state

In the following we derive the form of the resonant scattering amplitude (f^{RES}). While different electric and magnetic multipole transitions contribute to the resonant scattering process, we consider contributions which are a result of electric dipole (E1) transitions ($\Delta l = \pm 1$) only, such that $f^{RES} \rightarrow f^{RES}_{E1}$, as these transitions are dominant and the only processes relevant to the work presented in this thesis. Additional contributions (electric quadrupole and magnetic dipole) which maybe relevant in different systems have been discussed in the following references [42, 52].

For the electric dipole resonance in a magnetic ion the resonant X-ray component of the scattering amplitude is given by,

$$f^{RES}_{E1} = \frac{4\pi}{|\vec{k_i}|} f_D \sum_{M=-1,0,1} [\hat{\epsilon}'^* \cdot \mathbf{Y}^{(e)}_{1M}(\hat{k}_f) \mathbf{Y}^{(e)*}_{1M}(\hat{k}_i) \cdot \hat{\epsilon}] F^{(e)}_{1M}(\omega), \tag{2.17}$$

where $\mathbf{Y}^{(e)}_{1M}(\hat{k})$ are vector spherical harmonics, f_D is the Debye-Waller factor and F_{1M} (a constant for fixed energy) determines the strength of the resonance and depends on the atomic properties of the system [42]. The polarisation state of the incident (scattered) photon is denoted by $\hat{\epsilon}$ ($\hat{\epsilon}'$).

If the system consists of a magnetic ion (of moment $\vec{z}_j$) the three terms can be written as,

$$[\hat{\epsilon}'^* \cdot \mathbf{Y}_{1\pm1}(\hat{k}_f) \mathbf{Y}^*_{1\pm1}(\hat{k}_i) \cdot \hat{\epsilon}] = \frac{3}{16\pi} [\hat{\epsilon}' \cdot \hat{\epsilon} \mp i(\hat{\epsilon}' \times \hat{\epsilon}') \cdot \hat{z}_n - (\hat{\epsilon}' \cdot \hat{z}_n)(\hat{\epsilon} \cdot \hat{z}_n)], \tag{2.18}$$

for $M = \pm 1$ and,

$$[\hat{\epsilon}'^{*} \cdot \mathbf{Y}_{10}(\hat{k}_f)\mathbf{Y}^{*}_{10}(\hat{k}_i) \cdot \hat{\epsilon}] = \frac{3}{8\pi}[\hat{\epsilon}' \cdot \hat{z}_n)(\hat{\epsilon} \cdot \hat{z}_n)], \tag{2.19}$$

for $M = 0$, where $\hat{z}_n$ is the unit vector describing the moment of the n^{th} magnetic ion [53]. Therefore, using eq. (2.17), the resonant scattering amplitude for electric dipole contributions can be expressed as,

$$f^{RES}_{E1} = (\hat{\epsilon} \cdot \hat{\epsilon}')F^{(0)} - i(\hat{\epsilon}' \times \hat{\epsilon}) \cdot \hat{z}_n F^{(1)} + (\hat{\epsilon}' \cdot \hat{z}_n)(\hat{\epsilon} \cdot \hat{z}_n)F^{(2)}, \tag{2.20}$$

with,

$$F^{(0)} = \frac{3}{4k}[F_{11} + F_{1-1}], \tag{2.21}$$

$$F^{(1)} = \frac{3}{4k}[F_{11} - F_{1-1}], \tag{2.22}$$

$$F^{(2)} = \frac{3}{4k}[2F_{10} - F_{11} - F_{1-1}]. \tag{2.23}$$

The first term ($\propto F^{(0)}$) in eq. (2.20) is independent of magnetic moment and possesses the same polarisation dependence as Thomson scattering, it therefore contributes an additional ('anomalous') intensity to Bragg reflections. The second term ($\propto F^{(1)}$) is linear in moment and, for an incommensurate structure, produces first order magnetic satellites. The final term ($\propto F^{(2)}$) is quadratic in moment and produces second order magnetic satellites and a (small) contribution to Bragg reflections. In the incommensurate case, because terms $\propto F^{(2)}$ are significantly weaker they are often ignored. Much of this thesis is concerned with scattering from magnetic structures commensurate with the crystallographic lattice and, as we shall explain in chapter 5, terms of different orders ($F^{(i)}$) in the resonant scattering amplitude terms can interfere in this case.

The coherent scattering amplitude has been re-expressed by Hill and McMorrow [52] in the basis of orthogonal linear polarisation states (σ and π) previously used to

express the non-resonant scattering amplitudes,

$$
\begin{aligned}
f_{E1}^{RES} = F^{(0)} & \begin{pmatrix} 1 & 0 \\ 0 & \cos(2\theta) \end{pmatrix} \\
& + iF^{(1)} \begin{pmatrix} 0 & z_1\cos(\theta) - z_3\sin(\theta) \\ -z_1\cos(\theta) - z_3\sin(\theta) & z_2\sin(2\theta) \end{pmatrix} \\
& + F^{(2)} \begin{pmatrix} z_2^2 & -z_2(z_1\sin(\theta) - z_3\cos(\theta)) \\ z_2(z_1\sin(\theta) + z_3\cos(\theta)) & -\cos^2(\theta)(z_1^2\tan^2(\theta) + z_3^2) \end{pmatrix},
\end{aligned} \tag{2.24}
$$

where θ is the Bragg angle of the observed reflection and z_j the components of the unit vector describing the moment of the n^{th} site. We use this form of the coherent scattering amplitude explicitly in chapter 5 to calculate the resonant scattering intensity from a magnetically ordered system.

2.2.4 X-ray instrumentation

In the following we discuss the instrumentation which allows us to measure the different contributions to the coherent scattering amplitude (eq. (2.9)). First, we introduce the lab-based X-ray diffractometer (the Rigaku SmartLab) used extensively to characterise our samples prior to synchrotron studies. Because incident X-rays in this instrument are sourced by a Cu X-ray tube, the incident photon flux is relatively low and their energy is not coincident with any elemental absorption edge of the samples studied in this thesis. The Rigaku SmartLab is therefore effectively sensitive to scattering of charge origin only, $f_0(\vec{Q})$ terms in eq. (2.9), and is suitable for characterising the crystallographic properties of our samples.

More developed studies are performed at Diamond Light Source, a synchrotron source based in Oxfordshire, UK. Compared to a lab source, photon fluxes at synchrotron sources are orders of magnitude greater meaning that, as well as $f_0(\vec{Q})$

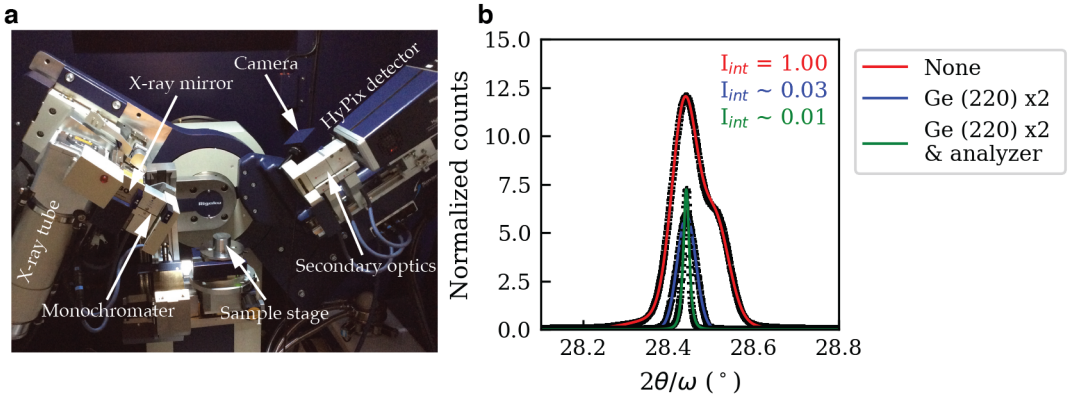


Figure 2.4: The Rigaku SmartLab four-circle diffractometer. a, Photograph of the Rigaku SmartLab, within the safety enclosure, outlining the various optical components. **b,** $2\theta/\omega$ scan of the (111) reflection of a Si single crystal measured using different monochromator and analyser configurations of the Rigaku SmartLab. Crosses show the measured intensity and solid (red, green, blue) lines fits of a Lorentzian profile to each data set. The Ge (220)×2 configurations have been arbitrarily scaled by a factor of 10 for clarification. The inset text (I_{int}) displays the integrated intensity of the (111) reflection measured with different optical components (colour).

terms, it can also measure the weaker $f^{mag}(\vec{Q})$ terms in the coherent scattering amplitude, yielding sensitivity to the spin and orbital magnetic order of a system. Additionally, the incident X-ray energy can be finely controlled at synchrotron sources [40], such that they can be tuned to an absorption edge of a magnetic ion. At (or near to) these energies f^{RES} terms become relevant and yield another avenue to probe the magnetic order of a material.

Lab source: the Rigaku SmartLab

The SmartLab is a high-resolution four circle diffractometer with X-rays sourced by a 3 kW Cu ($\lambda \approx 1.54$ Å) X-ray tube. The incident X-ray beam can be conditioned with various interchangeable optical components, outlined in fig. 2.4 a, making the SmartLab suitable for a diverse range of applications. Single crystal Ge monochromators, added to the incident beam path, better define the incident wavelength and improve $|\vec{Q}|$ resolution, but at the cost of reduced total flux. Soller slits can be added to minimize beam divergence perpendicular to the scattering plane and a range of beam masks and collimators can be used to reduce the beam footprint ($\approx$ 2 x 10 mm^2) to approximately 50 µm in diameter. Samples can be mounted onto a

XY-translation stage and a camera, mounted on the detector arm of the instrument, allows accurate alignment of the incident X-ray beam to user-defined regions of the sample with 50 µm accuracy.

Scattered X-rays are measured by a HyPix 2D detector constructed of a 7.75 cm by 3.85 cm pixel array of 100 µm wide semiconductor chips. Figure 2.4 displays the detector being used as a point detector ('0D mode'), required for the highest resolution. The stage can also be used as an area detector for fast data collection. In 0D mode secondary optics, including motorized slits and Ge single crystal analysers, can be added to improve the instrumental resolution.

Figure 2.4 b displays $2\theta/\omega$ scans of the (111) reflection of a Si single crystal, measured using a range of optical components. Si crystals are of sufficient quality such that they can be considered as 'perfect' crystals, the measurement of their Bragg reflections therefore give an indication of the instrumental resolution function at a given 2θ. In the lowest resolution setting (red line in fig. 2.4 b), the incident beam has not been monochromatized and two distinct reflections, corresponding to the Cu Kα_1 and Kα_2 multiplet structure of the X-ray tube, are observed. Ge single crystal monochromators can be added to remove the Kα_2 line from the incident spectrum, although with a $\sim$30-fold reduction in total flux (blue line in fig. 2.4 b). The instrumental resolution can be improved further by inclusion of a post-scatter analyser crystal as shown by the green line in fig. 2.4 b. The resolution of each monochromator varies significantly as a function of θ and each optical device must be appropriately selected for each experiment [54]. For example, low-resolution configurations are suitable when either accurate d-spacing information is not required or when studying samples with a small scattering volume, such as in polycrystalline thin films often used in the development of perovskite solar cells [55]. Conversely, optics providing a high-resolution set-up are suitable for single crystal diffraction studies or for X-ray reflectively measurements of 'thick' films (on the order of 100 nm's thick).

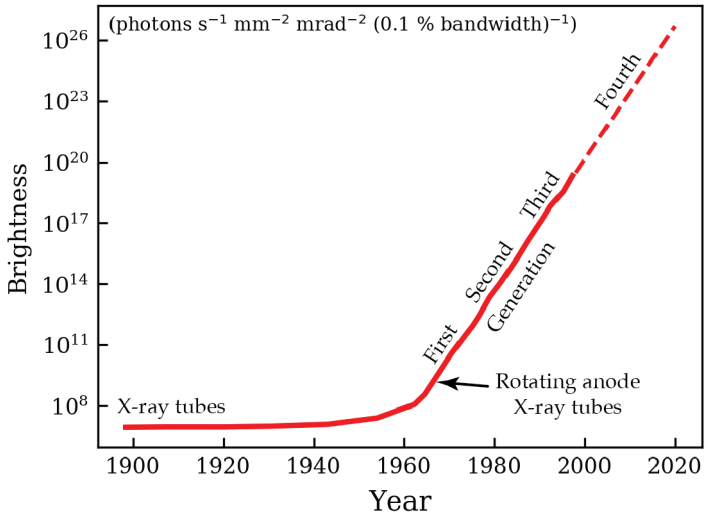


Figure 2.5: Intensity of X-ray sources as a function of time. The approximate brilliance of first (synchrotrons developed for particle physics, used parasitically for solid state research), second (purpose built synchrotrons for solid state research, primarily utilizing bending magnets) and third (synchrotrons using wigglers and undulators as insertion devices) generation machines are indicated by text. The dashed red line denotes projected improvements in brilliance as a result of the introduction of free electron lasers. Units for the y-axis are displayed in the top inset text. Adapted from [40].

Synchrotron source: Diamond Light Source

Compared to laboratory X-ray sources synchrotrons produce photon beams many orders of magnitude more brilliant (fig. 2.5) and offer control of the incident X-ray energy and polarisation. These properties mean a unique range of experiments can be performed at synchrotron facilities.

Synchrotrons operate by accelerating a beam of electrons (or other charged particle) up to relativistic speeds and storing them in a storage ring. In this ring bending magnets force the electrons to follow a circular path (by use of the Lorentz force), causing them to emit Bremsstrahlung (X-ray) radiation. Early (first generation, fig. 2.5) synchrotrons were designed for particle physics experiments and the Bremsstrahlung radiation was parasitically used for diffraction experiments from condensed matter. Synchrotrons purpose built for scattering experiments (second and third generation) began to increase the incident photon flux by utilizing insertion devices (IDs, wigglers and undulators) into the synchrotron storage ring. IDs consist of alternating arrays of north and south pole magnets, forcing the electrons

to emit X-rays as they following a highly oscillatory path. Undulators, compared to wigglers, produce radiation of much higher flux and at a fundamental wavelength, determined by the period of the magnet array. Wigglers can be considered as a dense series of independent bending magnets, producing a high net flux but at a broad spectrum of wavelengths. Synchrotrons have proven essential in the continued development of crystallography and in the study of long-range magnetic order, they are now of interest to a broad range of disciplines [40, 56]. For further information on synchrotron radiation and the components of a synchrotron facility please see reference [57].

2.3 Neutron diffraction

In this section we introduce the concept of Neutron diffraction. Developed later than X-ray diffraction it can be understood using many of the tools previously introduced. However, owing to its different interactions with matter compared to X-rays it can yield complementary information to a X-ray diffraction experiment. The interested reader is directed to the following notable references for additional information [58–60].

2.3.1 Nuclear scattering

Neutrons scatter from the nucleus of an atom, interacting via the strong nuclear force. The interaction strength is less systematic than that of the interaction of X-rays with electrons (approximately proportional to Z), and varies unpredictably across the periodic table [61].

Considering only an elastic scattering process, in an analogous way to the X-ray atomic form factor, the atomic scattering length is determined by performing an integral of the scattering potential of a nucleus,

$$f^{nuc}(\vec{Q}) = \frac{m}{2\pi\hbar^2}\int_V V(\vec{r})e^{\vec{Q}\cdot\vec{r}}dV, \tag{2.25}$$

where m is the neutron mass, $\vec{r}$ a position vector defined with respect to the centre of the nucleus and $V(\vec{r})$ the scattering potential of the nucleus. By assuming that the scattering potential is zero outside some radius (r_0) and a constant value (a) for radii below r_0, a definite integral can be obtained [62]. Additionally, we can take advantage of the large neutron wavelength ($\sim$2 Å) compared to the nuclear radius ($\sim$2 fm) to treat the scattering as point-like, such that $|Qr_0| << 1$. In this case, the atomic scattering length is therefore $\vec{Q}$ *independent* and given by,

$$f^{nuc} = \frac{mV}{2\pi\hbar^2}(\frac{4\pi r_0^3}{3}). \tag{2.26}$$

The atomic scattering lengths (for thermal neutrons) are tabulated in reference [61]. Practically, the measured diffraction intensity is then calculated from the (elastic) coherent differential cross section previously defined (eq. (2.8)), such that,

$$\left(\frac{d^2\sigma}{d\Omega}\right) \propto \Big|\sum_n f^{nuc}e^{i\vec{Q}\cdot\vec{d}_n}\delta(\vec{Q}-\vec{G})\Big|^2. \tag{2.27}$$

The different interactions with an atom for neutrons and X-ray means their scattering can be used in complementary way. Notably, X-ray scattering is only weakly sensitive to small atoms (its scattering power is proportional to its number of electrons) but the neutron scattering length from such atoms is not necessarily small [61].

2.3.2 Magnetic scattering

As well as interacting with the nucleus of an atom, neutrons possess a magnetic dipole moment and therefore interact with unpaired moments in the outer shell electron orbitals, allowing coherent magnetic scattering. The interaction is a direct result of the neutrons magnetic moment interacting with the internal magnetic field

of an atom [58]. Considering this interaction the coherent (elastic) differential cross section for magnetic scattering by neutrons is given by,

$$\left(\frac{d^2\sigma}{d\Omega}\right) \propto \Big| \sum_n \vec{m}_{\perp,n} f_{m,n}(\vec{Q}) e^{i\vec{Q}\cdot\vec{r}_n} \Big|^2. \tag{2.28}$$

where $f_{m,n}(\vec{Q})$ is the magnetic form factor (discussed in the following). We have not explicitly included the Laue condition in this expression, but this will be discussed in chapter 4. $\vec{m}_{\perp,n}$ is the magnetisation interaction vector, which is given by,

$$\vec{m}_{\perp,n} = \vec{m}_n - (\vec{m}_n \cdot \hat{Q})\hat{Q}, \tag{2.29}$$

where $\vec{m}_n$ is the magnetic moment of the n^{th} atom. This interaction vectors highlights that neutrons are sensitive only to the component of the magnetisation orthogonal to the scattering vector ($\vec{Q}$). For an unpolarised neutron beam this magnetic contribution will simply add to the scattering of nuclear origin, but if a polarised neutron beam is used an interference term will also be present.

Magnetic form factor

In magnetic scattering of neutrons the point-like scattering approximation used to determine the nuclear scattering length is no longer valid [58]. We must therefore consider a $\vec{Q}$-dependant form factor analogous to the atomic form factor of X-ray scattering (eq. (2.12)). Due to the complex nature of the magnetic form factors derived from first principles [58], they are normally expressed as an analytical approximation within the dipole approximation (i.e. assuming the electron density is symmetrical), which is more than sufficient for most neutron scattering experiments. This approximation is given by,

$$f_m(Q) = < j_0(Q) > = Ae^{-as^2} + Be^{-bs^2} + Ce^{-cs^2} + D, \tag{2.30}$$

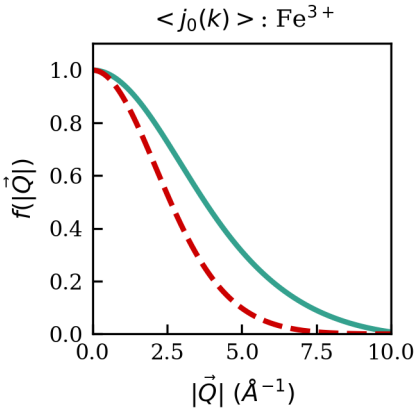


Figure 2.6: Magnetic form factor for Fe^{3+}. Solid blue line is the form factor calculated from the empirical equation (eq. (2.30)). Red dashed line is the square of the magnetic form factor.

where $j_0(Q)$ describes the radial distribution of the spin densities (the 0^{th} order spherical Bessel function) and $s = \frac{sin(\theta)}{\lambda}$ [63]. Constants (A, B, C, D) are tabulated in P. J. Brown [63]. We have assumed spin-only scattering (Landé g-factor, g=2).

Figure 2.6 displays this empirical approximation for an Fe^{3+} ion (L=0). It highlights the rapid reduction in the magnetic form factor with increasing $|\vec{Q}|$ and hence the corresponding reduction in the measured scattering intensity. Experimentally one preferentially measures low-$|\vec{Q}|$ magnetic scattering to maximize the observed intensity.

2.4 X-ray PhotoEmission Electron Microscopy

X-ray PhotoEmission Electron Microscopy (X-PEEM) utilizes a high-resolution electron microscope to image the photoemission from a sample under incident X-rays [64]. By spatially resolving the photoemission from a sample, one can indirectly probe the absorption properties of a material. Qualitatively, when an X-ray photon is absorbed by a material a core hole is generated and an electron from a higher energy level can decay via Auger emission to fill this hole.[1] The Auger (secondary) electrons produced in this cascade can escape from the sample if their energy exceeds

[1] Auger decay is dominate in low Z elements and fluorescence for heavier elements.

the materials work function, it is these secondary electrons measured by the electron microscope. As the number of secondary electrons emitted is proportional to the number of photoabsorption events, the photoemission measured by an electron microscope gives a reliable measure of the absorption coefficient of a material [65].

The applicability of X-PEEM to the study of magnetic functional oxides becomes apparent when one considers that magnetic order can result in anisotropic photoabsorption, a result of the X-ray Magnetic Circular Dichroism (XMCD) or X-ray Magnetic Linear Dichroism (XMLD) effects [66,67]. Empirically, these effects are the preferential absorption of X-ray photons of a given polarisation state. For example, XMCD represents the preferential absorption of either right circularly or left circularly polarised X-rays. When used in conjunction with an electron microscope, the XMCD and XMLD effects allow the imaging of ferromagnetic and antiferromagnetic domains respectively [68, 69].

Because electrons generated in the bulk of the sample have a high chance of being captured, X-PEEM is a surface sensitive technique; penetration depths are of the order of a few nanometres [64]. Additionally, by virtue of the effect being largest at elemental absorption edges it is elemental sensitive. This has made X-PEEM an invaluable tool in the study of magnetic heterostructures used in next generation spintronic devices, such as spin valves [70, 71]. In these devices an antiferromagnet is coupled to an adjacent ferromagnetic layer and the magnetic domain structures of both layers can be imaged by using complementary XMCD and XMLD techniques. In the following we will discuss the origin of XMCD and XMLD in a way which highlights its similarities to resonant X-ray diffraction [50]. In chapter 6 we use X-PEEM to image the domain structure of a coupled $\alpha-Fe_2O_3/Co$ heterostructure.

Absorption coefficient

In this section we consider the absorption of X-rays by a material which, by use of the optical theorem [50], can be shown to be proportional to the imaginary component

of the forward scattering amplitude. Following S. W. Lovesey and S. P. Collins [50], we begin by considering an X-ray beam of intensity I_0, incident on a thin foil. On passing through the foil the transmitted intensity (I) of the X-ray beam will be diminished, as described by,

$$I = I_0 e^{-\gamma t}, \tag{2.31}$$

where t is the thickness of material the photon beam has passed through and γ the materials absorption coefficient, which depends on the polarisation properties of the X-ray beam and the materials properties. By using the optical theorem, it can be shown to be proportional to the imaginary component of the forward scattering amplitude,

$$\gamma = \frac{4\pi n_0}{q} \mathrm{Im}\Big(f(\vec{Q} = 0) \Big) \tag{2.32}$$

where n_0 is the density of scatterers. We are interested in magnetisation and polarisation dependent contributions to the absorption coefficient, arising from the XMCD and XMLD effects. In X-PEEM one can measure the absorption coefficient (γ) indirectly by recording the total photoemission from a sample and noting that it is proportional to the total photoabsorption [65]. As we will show, measurement of the absorption coefficient in such a way can resolve the direction of magnetisation at the surface of a material.

2.4.1 X-ray Magnetic Circular Dichroism

The X-ray Magnetic Circular Dichroism (XMCD) effect is the difference in photoabsorption for right circularly polarised and left circularly polarised X-rays, the difference in absorption yields information about the spin and orbital magnetisations. Owing to the signal being finite only at and (to a lesser extent) above energies

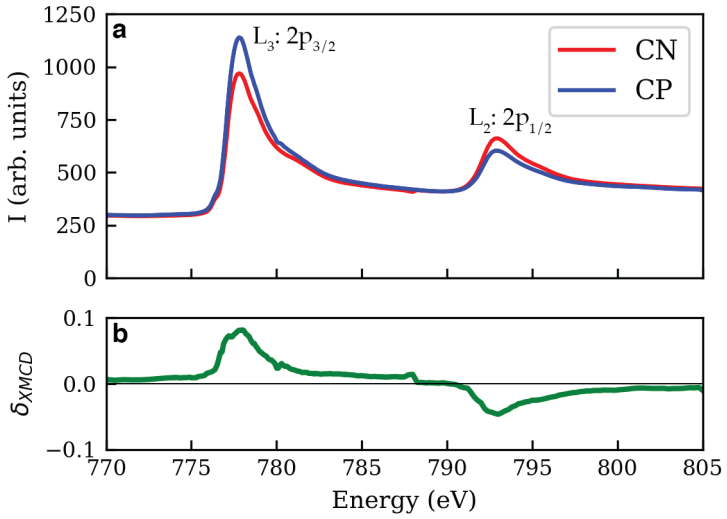


Figure 2.7: Measured X-ray absorption spectra of Co thin film with circularly polarised incident X-rays. a, X-ray absorption spectra, indirectly measured by recording the net photoemission, for a Co thin film in an arbitrary location on its surface for (red) negative circularly and (blue) positive circularly polarised incident X-rays. It is proportional to the absorption coefficient (γ) of the material. **b,** Calculated circular dichroism, proportional to the XMCD effect.

corresponding to absorption edges, XMCD is elemental sensitive.

The XMCD effect arises as a result of the conservation of angular momentum. As the X-ray photon is annihilated in the absorption process its angular momentum (opposite in sign for circular positive and negative polarised X-rays) must be transferred to the sample. Therefore different atomic transitions will be allowed for each incident polarisation as given by selection rules, which can yield a preferential absorption of either circular polarisation of X-rays (see for example, the discussion in J. Als-Nielsen and D. McMorrow) [72]. In the following we derive the form of the XMCD effect.

To emphasise the similarity in origin between XMCD and resonant X-ray scattering we follow the example by S. W. Lovesey and S. P. Collins in using the optical theorem to relate the coherent scattering amplitude to the absorption coefficient, for further details the reader is referred to this work [50]. We begin by taking the resonant magnetic scattering amplitude (f^{RES}, eq. (2.20)) up to first order in the magnetisation projection (i.e., ignoring the weaker $F^{(2)}$ terms). Only this term is

considered in the coherent scattering amplitude as it dominates on resonance and can yield sensitivity to the magnetic order. We are concerned with forward scattering only, such that $\hat{\epsilon} = \hat{\epsilon}'$ and we use the result [50],

$$\hat{\epsilon} \times \hat{\epsilon}' = i\vec{k}P_2, \tag{2.33}$$

where P_2 is the Stokes parameter (see appendix A) which describes the mean helicity of the photon beam. We can then make use of the optical theorem (eq. (2.32)) and our derived form of the resonant scattering amplitude (eq. (2.20)) to derive,

$$\begin{aligned} \gamma &= Im(F^{(0)}) - (\hat{z} \cdot \vec{k})P_2 Im(F^{(1)}), \\ \gamma &= \gamma_0 + \underbrace{\Delta\gamma P_2 \cos(\theta)}_{\delta_{XMCD}} \end{aligned} \tag{2.34}$$

where θ is the angle between the X-ray helicity and the local moment direction ($\hat{z}$). The absorption coefficient consists of two components: γ_0, a component independent of the polarisation properties of the X-ray beam and a term $\propto \Delta\gamma$, which depends on the samples magnetisation and the incident X-ray polarisation, this second term is the XMCD effect.

In X-PEEM literature it is more common to express the XMCD effect of the material in an equivalent form,

$$\delta_{XMCD} \propto \langle \vec{M} \rangle \cdot \hat{\sigma}, \tag{2.35}$$

where $\langle \vec{M} \rangle$ is the thermal average of the local magnetisation and $\hat{\sigma} = \sigma\hat{k}$ denotes the helicity of the incident X-rays ($\sigma = \pm 1$) and is parallel to the incident X-ray wavevector [73]. δ_{XMCD} is the measured XMCD signal (i.e., fig. 2.7 b), which is isolated by measuring with incident light of both helicities ($P_2 = \pm 1$) and subtracting

the invariant component of the absorption coefficient (γ_0). This is the form used in chapter 6 to image the ferromagnetic domains of a Co thin film.

2.4.2 X-ray Magnetic Linear Dichroism

In all but a few special cases (see the discussion in chapter 6) XMCD-PEEM is insensitive to the magnetic order of antiferromagnetic materials, owing to their compensated nature, $\langle M \rangle = 0$. However, X-ray Magnetic Linear Dichroism (XMLD), defined as the preferential absorption of one of two orthogonal linear X-ray polarisation states [72]. yields a similar sensitivity to the axis of magnetisation and so can be used (in conjugation with a photoemission microscope) to image the domain configuration of antiferromagnets [69, 74].

In a similar way to XMCD, the linear-polarisation dependent absorption rates can be obtained by using the resonant X-ray scattering amplitude (f^{RES}, eq. (2.20)), but now considering all terms in f^{RES}. Taking eq. (2.20) and noting that absorption is determined by the forward scattering amplitude ($\vec{k}_i = \vec{k}_f$) with no change in the polarisation ($\hat{\epsilon} = \hat{\epsilon}'$) and using that, for linearly polarised incident X-rays, $\hat{\epsilon} \times \hat{\epsilon}' = 0$, the forward scattering length can be expressed as,

$$f^{RES}(\vec{Q} = 0) = F^{(0)} + (\hat{\epsilon} \cdot \hat{z})^2 F^{(2)}, \tag{2.36}$$

which, by use of the optical theorem, gives a linear absorption coefficient,

$$\begin{aligned} \gamma &= \frac{4n_0}{k}[Im(F^{(0)}) + (\hat{\epsilon} \cdot \hat{z})^2 Im(F^{(2)})], \\ &= \gamma_0 + \underbrace{\Delta\gamma_l(\hat{\epsilon} \cdot \hat{z})^2}_{\delta_{XMLD}}. \end{aligned} \tag{2.37}$$

In this situation the XMCD effect is vanishing (it requires the X-ray beam to have a

net helicity) and the highest order term which depends on the photon polarisation is the XMLD effect, proportional to the square of the projection of the magnetisation on the photon polarisation direction ($\hat{\epsilon}$). Again, it is more common to emphasise the dependence of the materials absorption properties on the magnetisation, such that [69, 75],

$$\delta_{XMLD} = A + B(3\cos^2(\theta) - 1)\langle \vec{M}^2 \rangle, \tag{2.38}$$

where $\langle \vec{M}^2 \rangle$ is the thermal average of the square of the local magnetisation, A and B are constants, and θ the angle between the incident X-ray polarisation (ϵ).

Experimentally, one measures this by measuring the photoemission (proportional to the absorption coefficient) of the sample with two orthogonal linear polarisation states, one in a plane containing the magnetisation ($\hat{z}_n$) and another orthogonal to this plane, an easily achieved experimental geometry in thin films. We then compute the quantity defined as,

$$\delta = \frac{I_{LH} - I_{LV}}{I_{LH} + I_{LV}} \approx \frac{\Delta\gamma_l(\hat{\epsilon} \cdot \hat{z})^2}{2\gamma_0}, \tag{2.39}$$

where I_{LH} and I_{LV} denote X-rays with linear horizontal and vertical incident polarisation respectively. We have used the fact that the XMLD contribution is small compared to the polarisation independent term and now $\hat{\epsilon}$ denotes the polarisation vector in the plane containing $\hat{z}$. This measurement is proportional to the XMLD effect.

As we shall see in chapter 6 measurement of this quantity yields sensitivity to the axis of the magnetisation and by rotation of the polarisation of the incident light this axis can be experimentally determined.

3 | Magnetoelectric phase diagram of Y-type hexaferrite: $Ba_{0.5}Sr_{1.5}Mg_2Fe_{12}O_{22}$

In this chapter we introduce the Y-type hexaferrite $Ba_2Mg_2Fe_{12}O_{22}$ (BMFO) [76–80]. It exhibits large magnetoelectric effects (of spin-current origin [25, 77]) but is functionally limited by its low helical ordering temperature of 195 K. Here we show that this ordering temperature can be increased above room temperature via Sr doping of the Ba sites. We study the magnetoelectric phase diagram of the most promising compound in this series, $Ba_{0.5}Sr_{1.5}Mg_2Fe_{12}O_{22}$, by a combination of magnetocurrent measurements and magnetometry, revealing the existence of several metamagnetic phases, one of which is electrically polar.

This phase diagram is further characterised by X-ray and neutron diffraction in chapter 4.

3.1 Introduction

Magnetoelectric (ME) materials, those that exhibit coupling between the magnetic and electric order parameters, have attracted much interest due to their potential incorporation into low-power magnetic memories, where magnetic domains are controlled by electric fields [81, 82]. ME materials were originally defined as single-

phase materials which exhibited the *linear* magnetoelectric effect, the induction of an electric polarisation (magnetisation) with application of a magnetic (electric) field ($P_i = \alpha_{i,j} H_j$) [83]. [1] More recently the term 'magnetoelectric' has come to encompass all materials exhibiting coupling between the magnetic and electric orders, for example in composite magnetoelectrics where piezoelectric and magnetostrictive materials are grown as a heterostructure [23, 85–87].

Useful ME materials must be functional at room temperature, suitable for growth by epitaxial film methods and exhibit sufficiently large ME effects to allow the electrical writing (and ideally reading) of magnetic 'bits'. Many notable ME materials are multiferroics, systems which exhibit two or more spontaneous ferroic orders. For our purposes, we are interested in multiferroic materials which are magnetically ordered and electrically polar (i.e., ferroelectric) [88].

Systems where ferroelectricity is induced by spontaneous magnetic order (so-called type-II multiferroics) promise the largest ME coupling and have, appropriately, received significant attention [89]. The best known type-II multiferriocs are transition metal oxides, such as $TbMnO_3$, in which an incommensurate non-collinear ordering of the Mn^{3+} spins break inversion symmetry, inducing an electric polarisation of approximately $\sim$800 $\mu C\,m^{-2}$ which can be controlled by a magnetic field [86, 90]. The primary restriction of these magnetically induced ferroelectrics is that the required magnetic orders are generally only stable at very low temperatures ($\sim$50 K) [24]. The notable exception to this are a class of materials known as hexaferrites,[2] which exhibit a diverse range of magnetic orders at temperatures well in excess of 300 K [91].

The name 'hexaferrite' reflects the hexagonal lattice of their unit cells and that Fe (in coordination with oxygen environments) is their main magnetic constituent. They were first discovered in the magnetic mineral 'magnetoplumbite' ($PbFe_{12}O_{19}$) in

[1] The linear ME effect was first experimentally demonstrated in the archetypal magnetoelectric Cr_2O_3 in 1960 [21, 84].

[2] Formally the hexaferrites are not multiferroic because their polar magnetic orders are not *spontaneous*. They are often classified as 'field-induced' multiferroics or magnetically induced magnetoelectrics, the reasons for which will become apparent in the following.

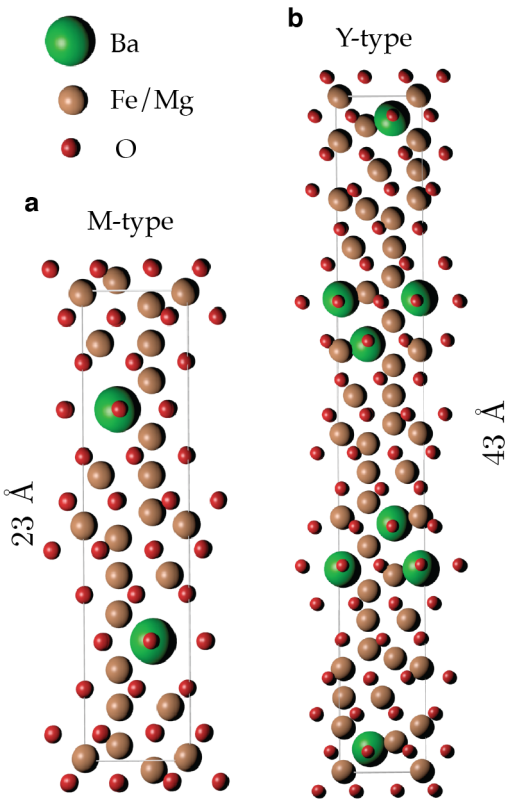


Figure 3.1: Crystal structure of M and Y-type hexaferrites. a, M-type ($BaFe_{12}O_{19}$) and **b,** Y-type ($Ba_2Mg_2Fe_{12}O_{22}$) hexaferrites. Green spheres represent Ba sites, brown Fe/Mg sites and red oxygen. The c lattice parameters are ∼23 Å and ∼43 Å respectively. Both structures are orthographic projections in the (0,1,0) plane and are not to scale.

1925 [92], and were quickly utilized, finding use as permanent magnets, in magnetic recording media, and in microwave applications, owning to their excellent dielectric and (ferri-)magnetic properties [93, 94]. Their crystallographic and magnetic properties have been extensively reviewed and here, after a brief introduction, we will focus on their ME properties and the associated magnetic orders [14, 91, 95].

Structurally, the hexaferrites are a class of layered materials composed of different stacking sequences of the same three basic crystallographic blocks: S (spinel) $Me^{2+}Fe_4O_8$, where Me denotes a divalent metal ion, R $[(Ba,Sr)Fe_6O_{11}]^{-2}$ and T blocks $[(Ba,Sr)_2Fe_8O_{14}]$ [14]. The stacking of these three blocks in different sequences and orientations allow a large number of hexaferrites, with similar magnetic properties, to be stabilized. The stacking sequences of the six most common hexaferrites, identified by a single upper case letter (M, W, Y, Z, X or U), are displayed in table 3.1. Beyond the six outlined here, a large number of hexaferrites have been identified, with the unit cells getting appropriately larger as the number of stacked units increase. In fact the hexaferrites have claim to the largest known unit cell

Type	Formula	Stacking sequence	c (Å)	Space group
M	(Ba,Sr)$Fe_{12}O_{19}$	RSR^*S^*	∼23	$P6_3/mmc$
W	(Ba,Sr)$Me_2Fe_{16}O_{27}$	$RS_2R^*S_2^*$	∼33	$P6_3/mmc$
Y	(Ba,Sr)$_2Me_2Fe_{12}O_{22}$	TST'S'T"S"	∼43	$R\bar{3}m$
Z	(Ba,Sr)$_3Me_2Fe_{24}O_{41}$	$RSTSR^*S^*T^*S^*$	∼52	$P6_3/mmc$
X	(Ba,Sr)$_2Me_2Fe_{28}O_{46}$	$(RSR^*S_2^*)_3$	∼84	$R\bar{3}m$
U	(Ba,Sr)$_4Me_2Fe_{36}O_{60}$	$(RSR^*S^*TS^*)_3$	∼113	$R\bar{3}m$

Table 3.1: Stacking sequence and properties of the six main hexaferrites. Asteriks denotes a 180° rotation of the block about the stacking direction and apostrophes a 120° rotation. Me denotes a divalent metal ion. After T. Kimura 2012 [91].

volume ($V \approx 14,000$ Å^3) of any inorganic system [96].

To date, four classes of hexaferrites (M, Y, Z and U) are confirmed magnetoelectrics and here we review their key properties [77, 97–99].

M-type hexaferrites (doped $BaFe_{12}O_{19}$) have promising dielectric properties (they are excellent insulators) but they have not yet been observed to exhibit ME effects at room temperature [97]. They are easily grown as epitaxial thin-films and if their ME functionalites could be improved, they would make promising candidates for future devices [100].

Room temperature magnetoelectric effects (in a hexaferrite) were famously demonstrated for the first time in polycrystalline samples of the Z-type hexaferrite $Ba_3Co_2Fe_{24}O_{41}$, where a magnetically induced electric polarisation ($|\vec{P}| \sim 10\ \mu C\,m^{-2}$) was found to exist at room temperature [98]. While excellent insulators, single-phase Z-type hexaferrites are extremely difficult to grow and epitaxial growth of Z-type hexaferrites has yet to be achieved, severely limiting their functionally.

ME effects of the U-type hexaferrites are extremely small ($|\vec{P}| \approx 0.1\ \mu C\,m^{-2}$) and are unlikely to be functionally useful [99], particularity as growth of single-phase U-type hexaferrites is more even more challenging than that of the Z-types.

Arguably, of the magnetoelectric hexaferrites, Y-types offer the most promising avenue to application: they exhibit large magnetoelectric effects, even observed at room-temperature [11, 101]. Importantly, they can be grown as single-phase

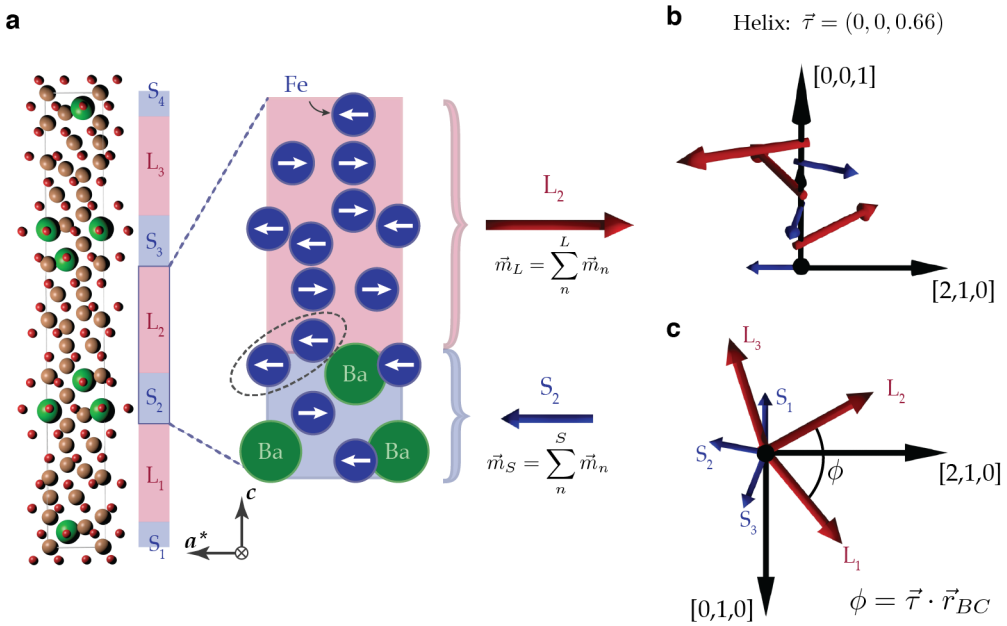


Figure 3.2: The magnetic block model of the Y-type hexaferrites. a, Crystallographic unit cell and outline of the magnetic structure within the block model. The unit cell is divided into six spin blocks (either large, L_i, or small, S_i, blocks) centred at $\vec{r}_{BC} = [0, 0, r_z]$ with $r_z = \{0, \frac{1}{6}, \frac{2}{6}, \frac{3}{6}, \frac{4}{6}, \frac{5}{6}\}$, within which all Fe moments are assumed to be collinear. Magnetic structures are then described by six 'pseudo' spins (L_i or S_j) at the centres of these blocks (with magnitude equal to the net moment of each block). **b-c,** Visualisation of a helical structure ($\vec{\tau} = (0, 0, 0.66)$) within the (six-spin) block model where b is a perspective view of the structure and c, an orthographic projection into the *ab*-plane.

epitaxial thin films, meaning prototype devices could be constructed [102]. We therefore, choose to study the Y-type hexaferrites for their functional potential. In this chapter we begin by discussing the general magnetic properties of the Y-type hexaferrites and in the remainder study the ME phase diagram of one of the most promising Y-type hexaferrites, $Ba_{0.5}Sr_{1.5}Mg_2Fe_{12}O_{22}$.

3.1.1 Y-type hexaferrites

Y-type hexaferrites have the general formula $A_2Me_2Fe_{12}O_{22}$, where A is an alkaline earth metal (typically a mix of Ba^{2+} and Sr^{2+}) and crystallize in space group 166 ($R\bar{3}m$) [96]. Conventionally, they are described in the hexagonal setting of the unit cell with lattice parameters $a = b \approx 5.8$ Å and $c \approx 43.5$ Å, displayed in fig. 3.2 a. Transition metal ions (Me^{2+}/Fe^{3+}) are in mixed tetrahedral / octahedral coor-

dination and the distribution of Me^{2+} ions over these sites is strongly dependent on the choice of divalent metal ion [103]. Furthermore, the choice of divalent metal ion (Me^{2+}) greatly influences the physical properties of the Y-type hexaferrites, tuning both their dielectric and magnetic properties [104]. A large number of compositions have therefore been studied, including Ni, Cu, Al, Zn, Co, Mg and Zr metal ions, primarily in attempts to maximize the magnetic ordering temperatures and minimize the critical magnetic fields required to stablize the polar magnetic phases [103, 105–110].

Across all the compositions, the common feature of ME effects in Y-types is that they arise as a result of non-collinear magnetic order. Because of the giant unit cells of the Y-type hexaferrites, as a matter of convenience, these magnetic structures have historically been described under the so-called 'block approximation'. In this model, rather than considering all 42 Fe sites in the unit cell (6 unique, labelled Fe1 $\rightarrow$ Fe6 in the following) one divides the unit cell into a sequence of two distinct magnetic blocks, within which strong nearest neighbour exchange between Fe moments is assumed to maintain a collinear (antiferromagnetic) arrangement of spins within a block. The magnetic structure is then described by the net behaviour of these blocks and is visualised by a set of 'pseudo' spins (L_i or S_j, fig. 3.2) positioned at the block centres (see fig. 3.2 a). As the block approximation is used exclusively throughout the literature to describe the magnetic structures of the Y-type hexaferrites, we will explicitly describe the construction of the block model in a way which will prove useful for calculating the magnetic scattering cross section from these structures in later chapters.

3.1.2 The block model

Throughout this thesis, for ease of visualisation, whenever we depict a magnetic structure we will display only the six pseudo spins of the block model, but calculate the scattering from a full unit cell (42 spins) orientated as described in the following.

In this section we describe the block model in detail, starting with the ferrimagnetic structure (common to all Y-type hexaferrites) and conclude with the block description of the incommensurate helical structure.

Constructing the block model

Crystallographically, the unit cell is divided into a set of magnetic blocks: 3 'L' (large moment) and 3 'S' (small moment) blocks, see for example fig. 3.2 a. These blocks are centred at $\vec{r}_{BC} = [0, 0, z_i]$ where z_i is equal to $\{\frac{1}{6}, \frac{3}{6}, \frac{5}{6}\}$ for the L blocks and $\{0, \frac{2}{6}, \frac{4}{6}\}$ for the S blocks, their vertical extent ($\| z$) is approximately 0.216 and 0.117 (in fractional coordinates) respectively. Within each block, spins are assumed to be collinear but antiferromagnetically aligned along c (zoomed region in fig. 3.2 a).

Site	Wyckoff letter	x	y	z	$\phi_{\pi,n}$	Block
Fe1	6*c*	0	0	0.3765	π	S
Fe2	6*c*	0	0	0.1523	π	L
Fe3	6*c*	0	0	0.0656	π	L
Fe4	3*b*	0	0	0.5	0	L
Fe5	18*h*	0.5038	0.4962	0.1096	0	L
Fe6	3*a*	0	0	0	0	S

Table 3.2: Site specific phases ($\phi_{\pi,n}$) in the block model, used to introduce AFM order within the blocks. Atomic positions are approximate and from A. Collomb, *et al.* [111].

We describe magnetic structures within the propagation vector formalism, where the collection of moments describing the magnetic structure are expanded in a Fourier decomposition,

$$\vec{m}_n = \sum_j \left(\vec{S}_{j,n} e^{-i\vec{\tau}_j \cdot \vec{r}_n - i\phi_n} + \vec{S}^*_{j,n} e^{i\vec{\tau}_j \cdot \vec{r}_n + i\phi_n} \right), \tag{3.1}$$

where $\vec{r}_n$ is the position vector of the n^{th} spin, $\vec{S}_{j,n}$ the Fourier coefficient of the j^{th} propagation vector ($\vec{\tau}_j$) for the n^{th} spin and ϕ_n a site specific phase. The sum runs over each propagation vector of the structure. To generate the collinear arrangement of spins within each block we use a 'correction' phase (ϕ_n in eq. (3.1)) generally,

$$\phi_n \rightarrow \phi_{n,j} = \vec{\tau}_j \cdot \vec{r}_{BC} - \vec{\tau}_j \cdot \vec{r}_n + i\phi_{\pi,n}, \tag{3.2}$$

where $\vec{r}_{BC}$ is the position vector of the block centre the n^{th} spin resides in and $\phi_{\pi,n} = \{0, \pi\}$ a site specific phase (defined for each site in table 3.2), used to introduce antiferromagnetic alignment within the blocks.[3] In the following we present examples of construction of the magnetic structures of the Y-type hexaferrites, in the absence of a magnetic field, within the block approximation.

Ferrimagnetic structure

The ferrimagnetic structure ($\vec{\tau} = (0, 0, 0)$) provides a clear example of the antiferromagnetic alignment within the blocks. The magnetic moment of each site is given by,

$$\vec{m}_n = \frac{m_{\text{Fe}}}{2}(e^{i\phi_{\pi,n}} + e^{-i\phi_{\pi,n}})\hat{x}, \tag{3.3}$$

where we have assumed that a magnetic field is applied parallel to $\hat{x}$ and m_{Fe} is the magnitude of the site moment, site specific phases ($\phi_{\pi,n}$) are displayed in table 3.2. All Fe sites in the unit cell therefore have a magnetic moment equal to $\vec{m} = \pm m_{\text{Fe}}\hat{x}$, where the sign is determined by the value of $\phi_{\pi,n}$ (see zoomed region of fig. 3.2 a). Assuming equal magnitude moments for each site and performing the relevant summation, the net moments of L and S blocks are 3m_{Fe} and m_{Fe} respectively.

Helical structure

A helical structure is characterised by a single, incommensurate propagation vector, $\vec{\tau}_0 = (0, 0, \tau_z)$. We can describe a helical modulation by two $\frac{\pi}{2}$ out-of-phase orthogonal components in the plane perpendicular to $\vec{\tau}_0$,

[3] ϕ_n could be implicitly included in $\vec{S}_{j,n}$, but we explicitly include it to emphasise how the block nature of the magnetic structure is produced.

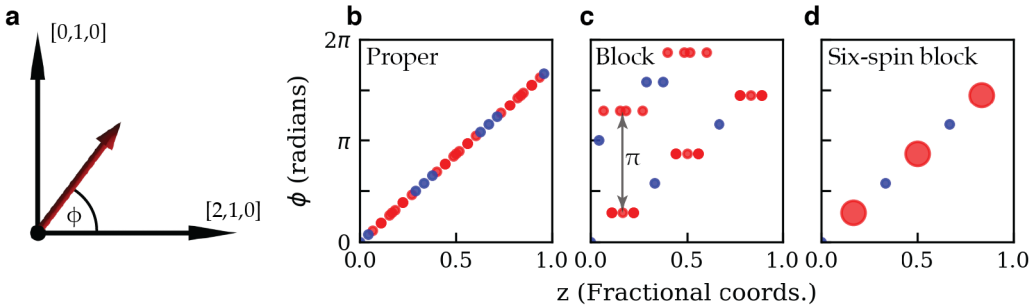


Figure 3.3: Construction of a block helix. **a,** Definition of ϕ, angle between (arbitrarily chosen) [2,1,0] axis and the direction of given moment in the *ab* plane. **b,** Phase angle (ϕ) of all Fe moments in the unit cell of a Y-type hexaferrite for a proper helix as a function of their z position. **c,** Phase angle within the block model, where all moments within a block are collinear (i.e., phase difference of either 0 or π between members of a block). **d,** Phase angles for six 'pseudo' spin block model. Red points represent L block moments and blue S block moments. Data point diameters are proportional to the net moment of the (pseudo) spin site.

$$\vec{m}_n = m_{\mathrm{Fe}} \cos(\vec{\tau}_0 \cdot \vec{r}_n + i\phi_{n,0})\hat{x} + m_{\mathrm{Fe}} \sin(\vec{\tau}_0 \cdot \vec{r}_n + i\phi_{n,0})\hat{y}, \tag{3.4}$$

where to make a 'block' helix we have introduced our previously defined 'correction' phase ($\phi_{n,0}$, eq. (3.2)), which makes all spins within a block collinear, the effect of this correction phase is outlined in fig. 3.3 where the 'phase' of each site in a block helix is compared to that of a proper helix. Using the euler formula to write $\vec{m}_n$ as a sum of exponentials,

$$\vec{m}_n = \frac{m_{\mathrm{Fe}}}{2}\left\{e^{\vec{\tau}_0 \cdot \vec{r}_n + i\phi_{n,0}}(\hat{x} - i\hat{y}) + e^{-(\vec{\tau}_0 \cdot \vec{r}_n + i\phi_{n,0})}(\hat{x} + i\hat{y})\right\}. \tag{3.5}$$

Thus comparing eq. (3.1) and eq. (3.5) we note, that for a helix, $\vec{S}_{helix} = \frac{m_{\mathrm{Fe}}}{2}[1, i, 0]$. The graphical representation of a helical structure, within the block model, is shown in fig. 3.2 b and c. A large number of Y-type hexaferrites exhibit some form of incommensurate magnetic order in zero applied magnetic field, while not directly ME themselves, they are often connected to the ME phases by application of a magnetic field in the *ab* plane of the sample.

Origins of the block model

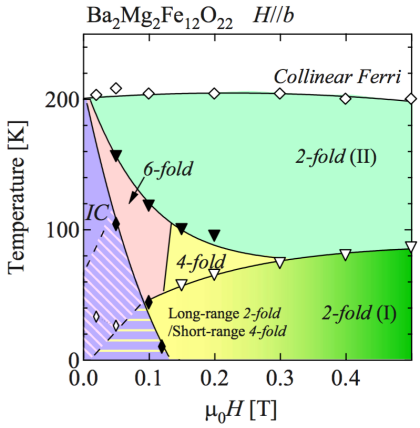


Figure 3.4: Magnetic phase diagram of $Ba_2Mg_2Fe_{12}O_{22}$ for $\vec{H} \parallel b$. Above 200 K BMFO exhibits a collinear ferrimagnetic order, below which (in the absence of an applied magnetic field) the system orders as an incommensurate (IC) planar helix. Application of a small magnetic field ($\sim$0.1 T) in the plane of the helix induces a series of 'fan' structures, some of which are confirmed to be ferroelectric. Hatched areas represented regions of phase-coexistence. Reprinted with permission from H. Sagayama *et al.* [78]. Copyright 2009 by the American Physical Society.

The block model was first used to describe the field-induced phases of the Y-type hexaferrite $Ba_{1-x}Sr_xZn_2Fe_{12}O_{22}$ in 1985 [112]. This work divided the unit cell into the, now well known, large (L) and small (S) spin blocks by considering the relative strength of the superexchange interactions within the unit cell. Intrablock interactions are generally strong and interblock interactions (across the L/S block interface) are weak [112]. The 'block' approximation was shown to well describe the zero field structures [16, 19, 112], and qualitatively describes the physics of the field-induced phases. To date, however, no study has been able to test the details of the field-induced phases to determine how far they deviate from the block model. The success of the block model to accurately describe the polarisation characteristics of the Y-type hexaferrites and qualitatively describe the diffraction data has made the block model the exclusive way of describing the magnetic structures of the Y-type hexaferrites.

3.1.3 $Ba_2Mg_2Fe_{12}O_{22}$

$Ba_2Mg_2Fe_{12}O_{22}$ (BMFO) was the first hexaferrite where large magnetoelectric effects were demonstrated using small (∼0.1 T) magnetic fields: previous to this discovery magnetic fields in an excess of 1 T were required to induce magnetoelectric phases [77, 113]. Its magnetic phase diagram, as determined by magnetometry and neutron diffraction, is displayed in fig. 3.4 [78]. Between 553 K and 200 K it is ferrimagnetically ordered, below which (in zero applied magnetic field) it forms an incommensurate ($\vec{\tau}_0 \approx (0, 0, 0.62)$) block helix structure [14,78,80]. The helical phase stabilizes as a result of competition between three superexchange interactions near to the L/S block interface [16]. The weakest interaction (dashed ellipse in fig. 3.2) plays a dominate role and altering its strength is expected to change the ordering temperature (T_H) of the helical phase [16]. On further cooling (∼50 K) neutron diffraction has indicated a transition to a longitudinal conical (LC) structure where moments cant out of the *ab* plane, such that there is a net ferrimagnetic moment parallel to *c*. The mechanism for the formation of the longitudinal conical structure is still not fully understood [80, 103, 114].

Application of magnetic fields orthogonal to *c* in either of these phases can stabilize metastable 'fan' structures (see for example fig. 3.5), a magnetic order ubiquitous to the hexaferrites [78,91]. Magnetic fan structures are characterised by moments which lie in the *ab* plane and feature modulations commensurate with the crystallographic unit cell. They are identified by their longest period modulation (i.e., 2, 4 and 6 fan as shown in fig. 3.5 a, b, c, respectively). At temperatures exceeding ∼50 K in the low-field regions BMFO is in either a 4 or 6 fan state (solid yellow and pink regions in fig. 3.4), evident by a unique set of propagation vectors (see fig. 3.5), measured by neutron diffraction [78]. On increasing the magnitude of the applied field these high order fan structures are converted into 2-fan structures (green regions in fig. 3.4, labelled 2-fan (I) and 2-fan (II)). On removal of the magnetic field, BMFO exhibits significant phase co-existence (see dashed lines in fig. 3.4). In these regions,

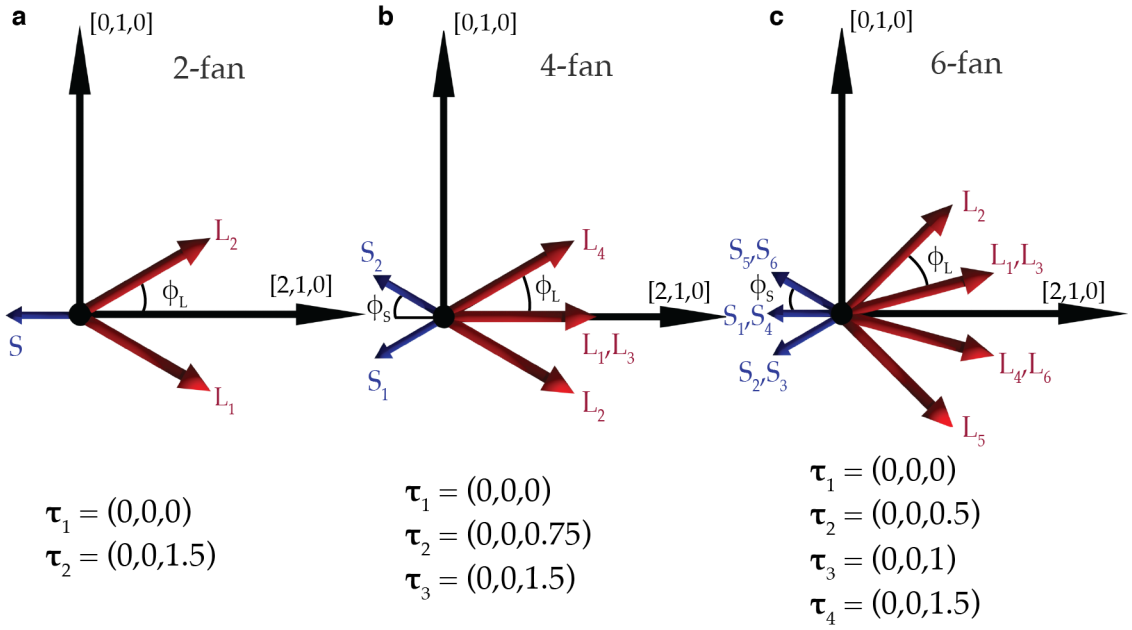


Figure 3.5: Planar magnetic fan structures of $Ba_2Mg_2Fe_{12}O_{22}$. Orthographic view of planar fan structures of the Y-type hexaferrites within the block model. **a,** A planar 2-fan structure. **b,** 4-fan **c,** 6-fan structure, none of which are polar. Red arrows represent L block moments and blue arrows S blocks, the labelling convention follows that of fig. 3.2. In the above graphics it is assumed that magnetic fields are applied parallel to [2,1,0]. Fan angles of the L and S blocks are denoted by ϕ_L and ϕ_S respectively. Magnetic fans are characterised by moments which lie in the *ab* plane and are commensurately modulated.

multiple fan structures (6-fan and 2-fan) are observed to co-exist with the zero-field incommensurate helical structures [78]. All of the *planar* fan structures displayed in fig. 3.5 preserve inversion symmetry and cannot, therefore, be magnetoelectric.

Despite this, S. Ishiwata *et. al* measured an appreciable polarisation ($|\vec{P}| = 80$ $\mu C\,m^2$), coincident with the 2-fan (I) phase, orthogonal to the direction of the magnetic field applied to stablize this phase [77,80]. This observation required an amendment to the planar 2-fan model to be made, such that it was polar in a way consistent with the orientation of the electric polarisation with respect to the applied magnetic field. The model imposed (hereafter referred to as the canted 2-fan model) is displayed in fig. 3.6 a and b: the S blocks (blue arrows) cant out of the *ab* plane and feature an antiferromagnetic alignment along *c*. Conveniently, the structure can now be considered as a superposition of a ferrimagnetic structure and a commensurate cycloid, where the cycloidal modulation can induce an electric polarisation by the spin current mechanism, familiar to many type-II multiferroics [25].

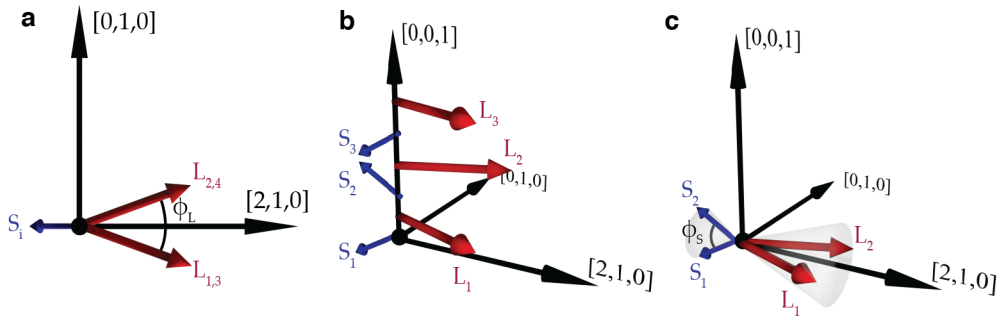


Figure 3.6: Proposed polar structure of $Ba_2Mg_2Fe_{12}O_{22}$, the canted 2-fan. a, Projection of the structure in the *ab* plane. **b,** Perspective view of model in six spin-block model. **c,** Magnetic structure presented as a transverse conical structure, a common representation, emphasising the polar nature of the structure. While the magnetic structures presented in fig. 3.5 are all contained in the *ab* plane, in this structure the S blocks cant out of this plane such that the structure has a cycloidal component, capable of inducing electric polarisation by the spin-current mechanism.

The canted 2-fan magnetic structure was used to describe both the (confirmed magnetoelectric) 2-fan (I) and the (proposed magnetoelectric) 2-fan (II) phases (fig. 3.4). The difference between the two phases was suggested to be a 90° coherent rotation of the magnetic structure about the applied field direction ([2,1,0] in fig. 3.6) such that the L block (red arrows) spins lie in the *ab* plane in the 2-fan (I) state and the S block moments (blue arrows) lie in the *ab* plane for the 2-fan (II) phase. The consequence of this is that the magnetic polarity (or sense of rotation) of the magnetic structure is preserved at the boundary of these two phases [80].

We note that it is typical in the literature to visualise the canted 2-fan as a transverse conical structure, see for example fig. 3.6 c, as this emphasises the magnetic origin of the electric polarisation. We use this graphical representation throughout this thesis for ease of visualisation.

Description of canted 2-fans

Canted 2-fans (believed to describe the 2-fold (I) and 2-fold (II) phases in fig. 3.4) describe magnetic structures where both S and L blocks have both $\vec{\tau}_1 = (0,0,0)$ and $\vec{\tau}_2 = (0,0,1.5)$ modulations in orthogonal directions. The $\vec{\tau}_1$ modulations are described by:

$$\begin{aligned} &\text{L blocks: } \vec{m}_{n,1} = m_{\text{Fe}} \cos(\phi_L) \cos(\phi_{\pi,n}) \hat{x} \\ &\text{S blocks: } \vec{m}_{n,1} = m_{\text{Fe}} \cos(\phi_S) \cos(\phi_{\pi,n}) \hat{x} \end{aligned} \tag{3.6}$$

where $\cos(\phi_N)$ (as defined in fig. 3.6) is the fan-angle of the respective block. Similarly, the $\vec{\tau}_2$ components are described by,

$$\begin{aligned} &\text{L blocks: } \vec{m}_{n,2} = m_{\text{Fe}} \sin(\phi_L) \sin(\vec{\tau}_2 \cdot \vec{r}_n + \phi_{n,2}) \hat{y} \\ &\text{S blocks: } \vec{m}_{n,2} = m_{\text{Fe}} \sin(\phi_S) \cos(\vec{\tau}_2 \cdot \vec{r}_n + \phi_{n,2}) \hat{z} \end{aligned} \tag{3.7}$$

which by writing in terms of a sum of exponentials and comparing to eq. (3.1) we see that for the S blocks $\vec{S}_1 = \frac{m_{\text{Fe}}}{2} \cos(\phi_S)[1,0,0]$ and $\vec{S}_2 = \frac{m_{\text{Fe}}}{2} \sin(\phi_S)[0,0,1]$ and for the L blocks $\vec{S}_1 = \frac{m_{\text{Fe}}}{2} \cos(\phi_L)[1,0,0]$ and $\vec{S}_2 = \frac{m_{\text{Fe}}}{2} \sin(\phi_L)[0,i,0]$. To recover the description of a planar 2-fan (fig. 3.5 a) one simply sets $\phi_S = 0$. The formulations of the 4- and 6-fan structures are shown in chapter 4.

Magnetoelectric properties of the canted 2-fan structure

Several authors have measured magnetoelectric effects in BMFO where, owing to the poor insulating properties of all previously grown samples, only the low temperature 2-fan (I) phase is confirmed to be polar [11, 76, 77]. In this state, the electric polarisation is observed to be orthogonal to the applied magnetic field (which defines the 'cone' axis), consistent with it arising from the the spin-current mechanism (the inverse Dzyaloshinskii-Moriya interaction) [18,25,115], where the induced polarisation is equal to,

$$\vec{P} \propto \hat{e}_{i,j} \times (\vec{S}_i \times \vec{S}_j), \tag{3.8}$$

$\hat{e}_{i,j}$ is the unit vector joining the i^{th} and j^{th} spin and $S_{i,j}$ denote their respective magnitudes.

A result consistent across all previous electric polarisation measurements performed

on BMFO is that the polarisation is coupled to the applied magnetic field: for a mono-domain polar state, if the applied field is inverted the electric polarisation also (losslessly) changes sign, even in the absence of any electrical bias [11, 76, 77]. Such coupling is not a given for electric polarisation of spin-current origin and is of significant functional interest [113].

In this chapter we demonstrate that this polar 'memory' effect exists in our material and dedicate chapter 5 to study the microscopic mechanisms of the electric polarisation reversal.

3.2 Experimental details

Single crystals were grown[4] using a flux method as described by Momozawa *et al.* [103]. Structural characterisation of samples were performed using a Rigaku SmartLab diffractometer or an Oxford Diffraction Supernova. Crystals were found to grow as large crystallite 'plates' ($\sim 4 \times 4 \times 1$ mm^3) with the c axis surface normal to the largest face. Samples with a low degree of mosaicity and high phase purity were selected for subsequent measurements.

3.2.1 Magnetometry

Magnetisation measurements were performed using a Quantum Design MPMS-3 (SQUID - VSM). In this system the sample is mounted at the centre of a set of pick up coils and oscillated at 14 Hz through the extent of the coils. The current in the coils (and hence magnetic flux) is measured as a function of sample position during the oscillations by a shielded detection coil and SQUID. The measured moment is extracted by the Quantum Design Multi-Vu software by fitting this signal on the assumption of a point-like sample. Compared to DC magnetometry, the high

[4] I am indebted to Dr. D. Prabhakaran who provided all hexaferrite single crystals used in the experimental work presented in this thesis.

frequency of oscillation is a distinct advantage of a vibrating sample magnetometer (VSM) as it allows significantly faster data collection and improved sensitivity.

Samples were mounted on a (low-background) quartz rod with either the $[2, 1, 0]$ or $[0, 0, 1]$ direction mounted parallel to the applied magnetic field. All measurements were undertaken after a zero-field cool (ZFC) to the (initial) measurement temperature from 400 K and the magnetic moment was subsequently recorded either as a function of magnetic field or temperature.

For construction of the magnetic phase diagram of $Ba_{0.5}Sr_{1.5}Mg_2Fe_{12}O_{22}$ (section 3.3.2) a single crystal of mass 0.386(2) mg was mechanically cleaved from a larger sample used for the subsequent diffraction and magnetocurrent measurements. The magnetic moment as a function of applied magnetic field (- 7 T $\rightarrow$ 7 T) was recorded at seventeen temperatures between 10 K and 400 K. Prior to each measurement the sample was warmed to 400 K and zero field cooled back to the measurement temperature.

3.2.2 Magnetocurrent measurements

Magnetocurrent measurements are an invaluable characterisation tool for studying magnetoelectric effects, being the primary confirmation of the polar nature of many proposed magnetoelectrics.[5] The sample environment is provided by a Quantum Design Physical Property Measurement System (PPMS), capable of sample temperatures between $\approx$ 5 K and 360 K and applying magnetic fields up to 12 T. The sample is connected in series with a DC high voltage supply and a current-to-voltage amplifier (IV amplifier), both sharing a common ground (see fig. 3.7 a). The IV amplifier is protected by connecting it in parallel with a pair of back-to-to back zener diodes, such that if the circuit was to short (for example, during unexpected sample breakdown) the maximum voltage applied across the IV amplifier is limited.

[5]Magnetocurrent measurements are relevant only when an electrical polarisation is coupled to an applied magnetic field.

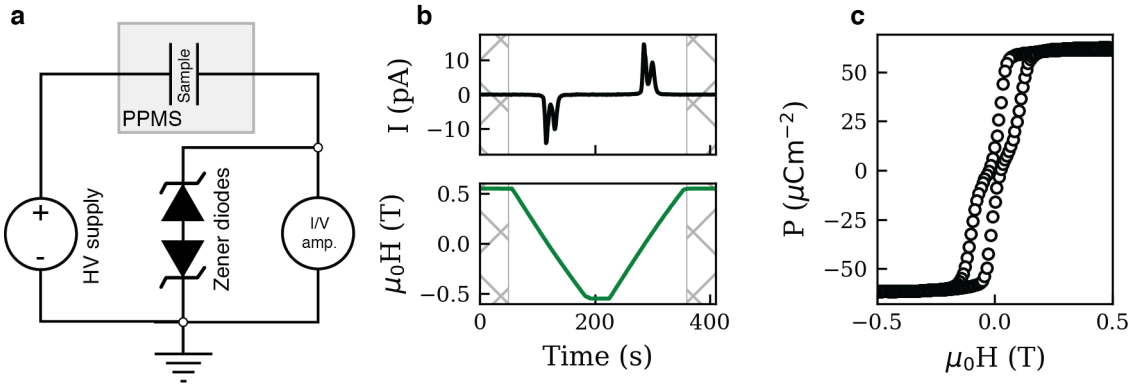


Figure 3.7: Magnetocurrent experimental details and example data. **a,** Measurement circuit diagram. **b,** Example data, the top panel shows the displacement current and bottom panel the applied magnetic field. Hatched regions outline pre- and post-measurement regions used in estimating the background. **c,** Electric polarisation field dependence constructed from example data in b.

The time, sample temperature, applied magnetic field and current flowing through the sample are logged simultaneously on a set of Keithley multimeters, connected to a control PC. Before the measurement the sample is electrically poled to prime it into a single (polar) domain state. Practically this is performed by applying a poling electric field while traversing a non-polar/polar phase transition as a function of magnetic field (or temperature). Once poled, the electric field is removed and the sample electrodes shorted for several minutes, the current ($I(t)$) is then recorded as the magnetic field is swept at a constant rate (nominally 5 mT s^{-1}). Any change in the electric polarisation results in a current flow as electrons move to screen (increasing polarisation) or reduce screening (decreasing polarisation) of the surface charge of the sample, see for example fig. 3.7 b). Working in the time domain, a polynomial background is subtracted from $I(t)$, whose form is determined by measuring the current for a minimum of 60 seconds prior to and after performing the measurement, see for example hatched regions in fig. 3.7 b. The relative change in electric polarisation is then calculated by integrating the recorded displacement current,

$$P = \frac{\int I dt}{A}, \tag{3.9}$$

where A is the area of the sample electrode. This can then trivially be plotted as a function of magnetic field (fig. 3.7 c).

Measurements presented in this chapter were performed on a single crystal polished into a cuboid of dimensions $4 \times 1 \times 1$ mm^3 - with the longest axis parallel to the [2,1,0] direction. Electrodes were made with silver paste on the (largest) b faces. Measurements were performed at a series of temperatures and after various magnetoelectric annealing procedures.

3.3 Results and discussion

3.3.1 $Ba_{2-x}Sr_xMg_2Fe_{12}O_{22}$

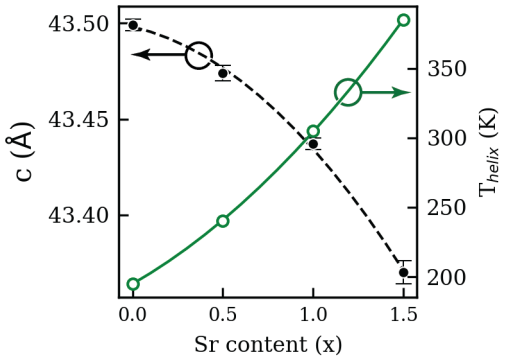


Figure 3.8: Measured c lattice parameter and helical ordering temperatures for $Ba_{2-x}Sr_xMg_2Fe_{12}O_{22}$ single crystals as a function of nominal Sr content. Solid black circles correspond to the measured c lattice parameter (left axis) and hollow green circles the helical ordering temperature (right axis), measured on warming in a magnetic field of 0.01 T applied parallel to [2,1,0].

Here we discuss the effect of Sr substitution on $Ba_2Mg_2Fe_{12}O_{22}$. Doping of the Ba^{2+} sites with smaller Sr^{2+} has long been known to alter the observed magnetic orders of the Y-type hexaferrites [112], however, until recently Sr-substituted BMFO has not been studied [11]. Figure 3.8 displays the c lattice parameter (measured by X-ray diffraction) and the helical ordering temperature, as determined by magnetometry, of $Ba_{2-x}Sr_xMg_2Fe_{12}O_{22}$ single crystals. The maximal Sr content studied was $x = 1.5$:

because of the smaller radius of Sr^{2+} compared to Ba^{2+} it can not fully substitute onto the Ba sites so a mixed composition must be used [116].

We observe that as the Sr content is increased the c lattice parameter decreases, confirming successful substitution, at maximal doping the lattice has contracted by ∼0.3 %. Conversely, the helical ordering temperature (see fig. 3.10 for an example of the raw data) increases dramatically as the Sr content is increased, exceeding 380 K for $Ba_{0.5}Sr_{1.5}Mg_2Fe_{12}O_{22}$. The mechanism behind the large increase in helical ordering temperature in our system can be understood as that described by Utsumi *et. al* for $BaSrZn_2Fe_{12}O_{22}$: the smaller Sr atom causes a local lattice deformation, strengthening one of the three superexchange interactions responsible for the formation of the helical phase. The net result is an increase of the helical ordering temperature [16].

3.3.2 Magnetic phase diagram of $Ba_{0.5}Sr_{1.5}Mg_2Fe_{12}O_{22}$

The high ordering temperature of the non-collinear phase of $Ba_{2-x}Sr_xMg_2Fe_{12}O_{22}$ meets the minimum requirement for room-temperature magnetoelectric effects. Motivated by this result we study the magnetoelectric phase diagram of the Y-type hexaferrite with the highest ordering temperature: $Ba_{0.5}Sr_{1.5}Mg_2Fe_{12}O_{22}$, subsequently referred to as BSMFO.

X-ray characterisation of crystal

A single crystal ($4 \times 1 \times 1$ mm^3) was selected and characterised by lab-based X-ray diffraction. It was used (unless explicitly expressed otherwise) for all measurements presented in this chapter. Initially a small, ∼50 µm section was mechanically removed from the crystal and mounted into a Oxford Diffraction Supernova. This uses a Mo ($\lambda = 0.7107$ Å) X-ray source and measures the intensity of ∼98 % of reflections accessible on the surface of the Ewald sphere, shown as black points in fig. 3.9 a. Rietveld refinement was used to refine the crystallographic properties of the sample

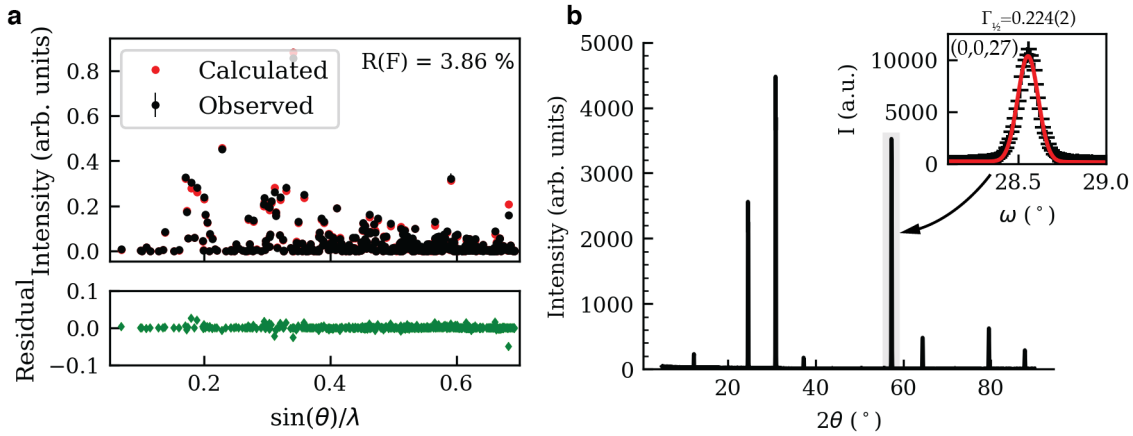


Figure 3.9: X-ray characterisation of a BSMFO single crystal. **a,** Results of Rietveld refinement (see main text), performed on an Oxford Diffraction Supernova ($\lambda = 0.7107$ Å). Black points indicate the observed intensity of each reflection and red points the calculated intensity. **b,** (0,0,l) scan performed on Rigaku SmartLab diffractometer ($\lambda = 1.54056$ Å). Inset displays a rocking curve (constant $|\vec{Q}|$) scan of the (0,0,27) reflection where the width ($\Gamma_{\frac{1}{2}}$) of the reflection is limited by the samples mosaicity. Black crosses are measured data points and the solid red line a Gaussian fit to the data.

within space group $R\bar{3}m$, the resulting predicted intensities ($R_F = 3.86$ %) are indicated by red points in fig. 3.9 a. The measured lattice parameters were $a = 5.8569(2)$ Å and $c = 43.352(2)$ Å and all atomic positions, anisotropic thermal parameters and a global scale factor were allowed to freely refine. Relative site occupancies (i.e., Ba/Sr and Fe/Mg) were allowed to refine while maintaining a full site occupancy: the refined stoichiometry of the crystal was $Ba_{0.65}Sr_{1.35}Mg_{1.428}Fe_{12.572}O_{22}$. The reduced Sr and Mg ratios, compared to the nominal amount, is understandable due to the increased volatility of these elements compared to Ba and Fe respectively. For example, Mg is significantly smaller than Fe and can diffuse from the bulk of the crystal during growth, forming MgO or $MgFe_2O_4$ at either the surface of the crystal or at inclusions. Occupancies of the oxygen sites were not refined due to the low sensitivity of X-rays ($Z = 8$) to oxygen.

Overall, the measured intensities (fig. 3.9 a) are clearly consistent with those expected for BSMFO, demonstrating that our crystal is suitable for investigation. The bulk of the crystal, used to construct the magnetic phase diagram, was also characterised using a Rigaku SmartLab diffractometer. Compared to the Supernova, sensitive to only a ∼50 µm region of the crystal, the SmartLab can measure a

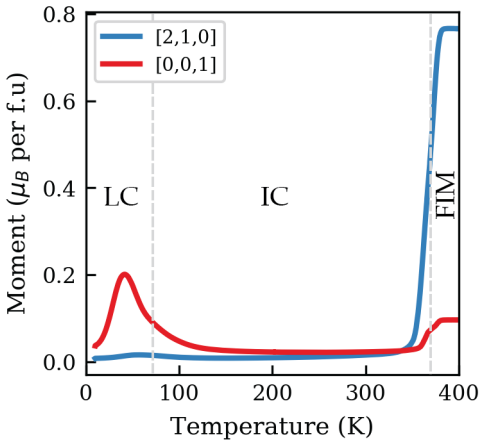


Figure 3.10: Magnetic moment as a function of temperature for a $Ba_{0.5}Sr_{1.5}Mg_2Fe_{12}O_{22}$ single crystal. Magnetic moment measured on warming from 10 K in an applied magnetic field of 10 mT parallel to [2,1,0] (solid blue line) or [0,0,1] (solid red line). The easy plane anisotropy is apparent by comparing the induced moment in the ferrimagnetic (FIM) phase. Prior to each measurement the sample was zero field cooled from 400 K to the initial measurement temperature, at which the measuring field was applied.

$\sim$1 mm^2 area but in a restricted reciprocal space volume. A scan along the (0,0,l) axis of our single crystal is shown in fig. 3.9 b. All reflections expected along this axis ($\vec{Q} = (0, 0, 3n)$), with the exception of the (0,0,9) for which $|F(\vec{Q})|^2 \approx 0.0$ for X-rays, are observed. There are some (vanishingly small) reflections not indexable within the space group of BSMFO that likely arise from impurity phases in the crystal, making up less than 1 % of the crystal. A rocking curve of the (0,0,27) reflection ($2\theta \approx 57.3°$) exhibits a FWHM of 0.224(2)°. The width is limited by the mosaicity of the sample and is sufficiently narrow to consider the crystal well-ordered and of high-quality.

Magnetic phase diagram

Figure 3.10 displays the low-field (10 mT) susceptibility of a BSMFO single crystal measured on warming, following a zero field cool to 10 K. For magnetic fields applied parallel to [2,1,0] (solid blue lines in fig. 3.10) we observe three distinct regions: at temperatures exceeding $\sim$350 K the sample is highly susceptible to magnetic fields and at low temperatures it has a small susceptibility, although there is a slight

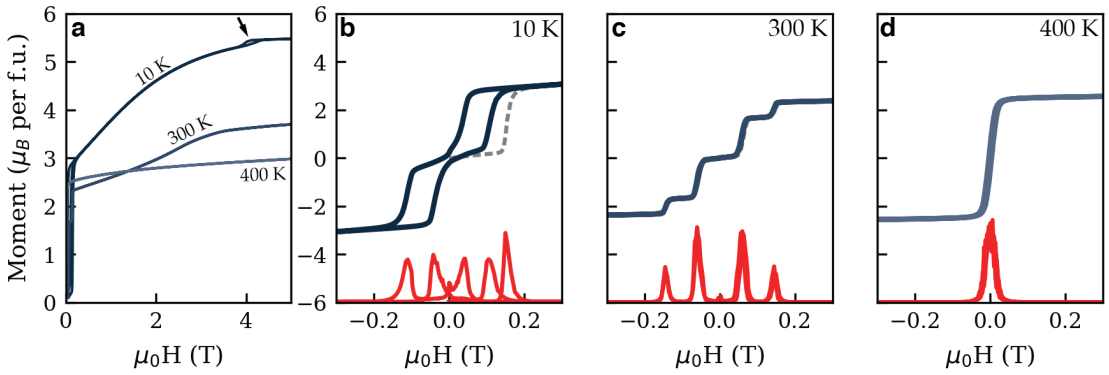


Figure 3.11: Magnetisation as a function of magnetic field applied parallel to [2,1,0]. a, Up to 5 T and **b-d,** between ± 0.3 T at 10 K, 300 K and 400 K respectively. Prior to each measurement, the sample was ZFC from 400 K to the measurement temperature. The virgin field sweep is shown by a dashed grey line (i.e., b). Solid red lines display the (arbitrarily scaled) differential of the magnetisation, highlighting transitions between adjacent magnetic orders.

increase at temperatures below 100 K. For fields applied parallel to [0,0,1] (solid red line of fig. 3.10) the susceptibility of the high temperature phase is reduced and, notably, there is a large increase in susceptibility below 100 K. With the exception of the increased helimagnetic ordering temperature, this data completely reflects the observed behaviour in BMFO [78]: at high temperatures we observe an *ab* plane ferrimagnet which evolves into an incommensurate helix at approximately 385 K. This phase persists to approximately 100 K, below which the helix cants out of the basal plane forming a longitudinal conical (LC) structure, evident by the increased moment measured along [0,0,1] [80, 114].

To construct the $H - T$ magnetic phase diagram of BSMFO, we isothermally measure the magnetisation of BSMFO for fields applied parallel to [2,1,0], the primary direction of interest because fields within the *ab* plane are expected to induce magnetoelectric phases [91]. The magnetisation curves of BSMFO are recorded at a series of temperatures after a zero field cooling procedure, see for example fig. 3.11 a. Clearly, under the application of small magnetic fields (fig. 3.11 b, c, d) the system undergoes a series metamagnetic phase transitions. For example, at 300 K (fig. 3.11 c) three distinct susceptibilities are observed below 0.3 T.

At temperatures below ∼100 K, a dramatic field hysteresis is observed (fig. 3.11

b), indicating a first order transition from the zero field state (LC) to the field-induced fan phases. At higher fields (fig. 3.11 a) the magnetisation varies smoothly with increasing field, until approximately 4 T where further hysteretic behaviour is observed (black arrow in fig. 3.11 a). Above this transition the field susceptibility is only weakly dependenton the applied magnetic field, consistent with this phase being ferrimagnetically ordered above ∼4 T [80].

We present the full magnetic phase diagram by constructing a false colour magnetic phase map, fig. 3.12, of the measured magnetic moment. This is constructed by using the positive field regions of magnetisation curves recorded in 25 K steps from 25 K to 400 K (and an additional 10 K data set), i.e., fig. 3.11 b-d. The measured magnetic moment is then interpolated onto a uniformly spaced grid of field and temperature. This is performed for the initial increasing magnetic field sweep (fig. 3.12 a) and the first decreasing field sweep (fig. 3.12 b) to investigate field hysteresis.

The end results (fig. 3.12 a and b) highlight the five distinct regions we observe. At temperatures exceeding ∼385 K the susceptibility varies smoothly, consistent with the ferrimagnetic structure of BMFO. Below this, four distinct regions are observed, labelled A-D in the following. By comparing the qualitive features of our phase diagram with the known phase diagram of BMFO (fig. 3.4) we can hypothesise on the identity of each phase [20, 78, 80].

As discussed, in small applied fields, (i.e., lightest broad regions in fig. 3.12, phase A), we observe a low-susceptibility state consistent with the block helix state (IC phase in fig. 3.4) which cants out of the *ab* plane at low temperatures to form a longitudinal conical structure. Under field application at temperatures exceeding ∼120 K two additional regions (B and C) of discrete susceptibility are observed, behaviour indicative of magnetic fan structures which are generally stable only in a small field range [20]. By comparing the shape of the phase boundaries to that observed in BMFO (fig. 3.4) we can predict that the light 'band' at the centre of the phase diagram (phase B) consists of higher order fan structures (4 and 6

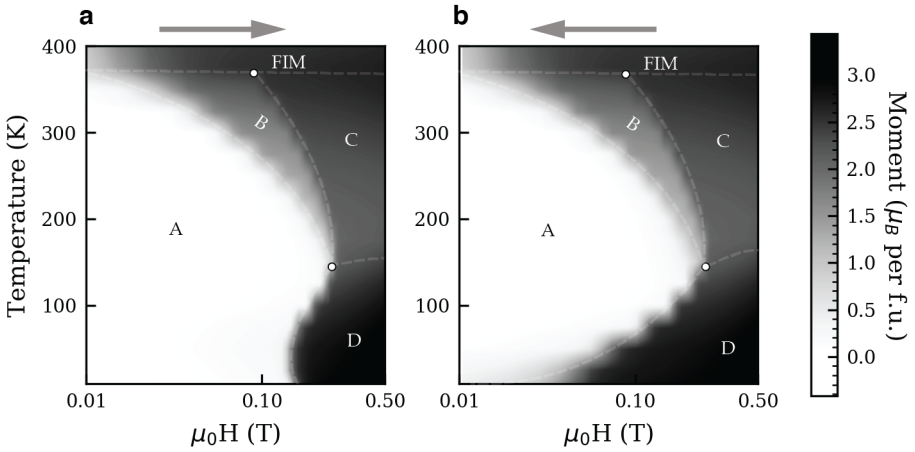


Figure 3.12: Low-field magnetic phase diagram of $Ba_{0.5}Sr_{1.5}Mg_2Fe_{12}O_{22}$ with magnetic field applied parallel to [2,1,0]. **a,** Phase diagram during virgin magnetic field sweep (i.e., dashed grey line in fig. 3.11 b). **b,** Phase diagram constructed from first decreasing field sweep. Color displays the measured magnetic moment. Phase diagrams are constructed from measurements at 17 temperatures, where the sample was ZFC from 400 K to each measurement temperature. The magnetic moment is linearly interpolated across the parameter space, jagged features are an artefact of this interpolation. The high field phases persist up to ∼4T, where the samples becomes ferrimagnetic.

fan, fig. 3.5) and the high field region (phase C) is a 2-fan (2-fan (II) in fig. 3.4) which continuously transforms into a ferrimagnetic structure as the applied field is increased.

At low temperatures (< 120 K) phase B vanishes and the first order transition at ∼0.2 T is apparent from comparison between fig. 3.12 a and b, where field hysteresis is observed. The high field fan phase below 120 K (darkest shade in fig. 3.12, phase D) is continuously connected to the high temperature one. The corresponding phase in BMFO would be the 2-fan (I) phase (fig. 3.4), such that this region of our phase diagram is expected to be polar in the same way as BMFO. S. Ishiwata *et al.* proposed that both the 2-fan (I) and 2-fan (II) phases were polar (i.e., they are canted 2-fans, fig. 3.6) and related to each other by a coherent, 90° rotation about the direction of the applied field direction, preserving the electric polarisation ($\vec{P}$) at the transition between phases C and D.

We can begin to interrogate our phase classification by investigating the magneto-electric properties of our BSMFO single crystal.

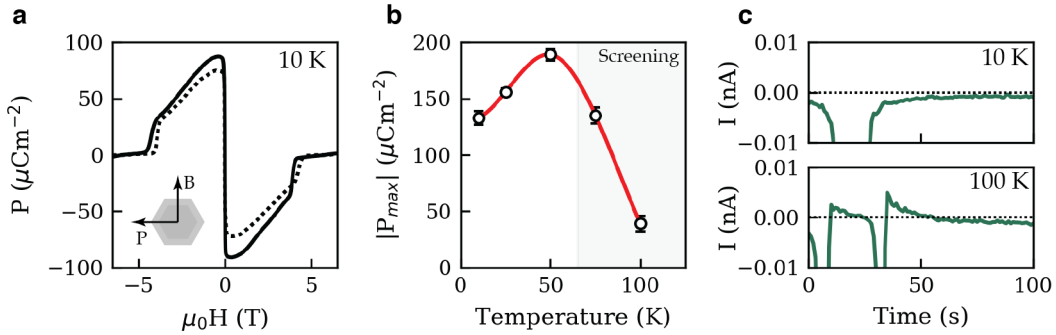


Figure 3.13: Polarisation of $Ba_{0.5}Sr_{1.5}Mg_2Fe_{12}O_{22}$ as function of temperature. **a,** Electric polarisation at 10 K, parallel to [0,1,0], on decreasing (solid line) magnetic field from 6.5 T and subsequently increasing field (dashed line) from -6.5 T. **b,** Maximum electric polarisation as function of temperature. Shaded grey region highlights temperatures where screening of the electric polarisation, an artefact of the imperfect insulating nature of the sample, inhibits reliable measurement. **c,** Displacement current after polarisation switching at 10 K (top panel) and 100 K (bottom panel). The effect of screening - manifested as a current flow of opposite polarity to the displacement current - is apparent at 100 K. In all cases magnetic fields are applied parallel to [2,1,0], such that an electric polarisation is induced orthogonal to this direction, parallel to [0,1,0].

3.3.3 Magnetoelectric properties

Figure 3.13 summarises the basic ME properties of BSMFO measured using the magnetocurrent measurement technique described in section 3.2.2. The low field helical phases of $Ba_{0.5}Sr_{1.5}Mg_2Fe_{12}O_{22}$ (lightest regions in fig. 3.12) are non-polar but, at temperatures below 100 K, a large displacement current is measured concurrent with the magnetic transitions observed by magnetometry. At 10 K the maximum magnitude of the electric polarisation is ∼135 μC m^{-2} (achieved with optimal magntoelectric poling), consistent in magnitude for other polar materials of spin-current origin [91]. This confirms that phase D is, as expected, polar.

It is worth noting that the measured polarisation in BSMFO single crystals, fig. 3.13 a), display an anomalous history dependence: on transition from the *polar* fan state to the *non-polar* ferrimagnetic state all memory of the polar state should be lost, such that on re-entry to the polar state one does not observe any appreciable polarisation. Converse to this expectation, ∼80 % of the electric polarisation is preserved. This behaviour has been observed in several other multiferroics and is attributed to the presence of polar nanoregions or multiferroic domain walls persisting in the

ferrimagnetic state with memory of the previous polar state. These regions then act as nucleation sites for the growth of polar domains on re-entry to the polar phase [117–119]. While of little technological interest, particularly in the hexaferrites (magnetic fields exceeding 4 T are required to observe this effect), it is worth emphasising its existence as it means the system cannot (necessarily) be effectively magnetoelectrically poled from the ferrimagnetic state. For example, when poling from a non-polar to polar state the measured polarisation should be symmetric in the poling field (E_p) used ($|\vec{P}(E_p)| = |\vec{P}(-E_p)|$), however after an initial 200 $\mathrm{V\,mm^{-1}}$ poling procedure we measure a large asymmetry in the magnitude of the polarisation ($|P(E_p)| > |P(-E_p)|$) when we apply poling fields of opposite polarity. To counteract this effect, when relevant, all our measurements were performed after thermal cycling of the sample to room temperature, in zero applied magnetic field, which was confirmed to remove any memory of the previous polar phase.

On warming, the magnitude of the electric polarisation was found to increase (fig. 3.13 b) to a maximum of $\sim$200 $\mu\mathrm{C\,m^{-2}}$ at 50 K, above which the polarisation decreases quite rapidly. At high temperatures, the insulating properties of our single crystals diminish and performing reliable magnetocurrent measurements becomes impossible. In a imperfect insulator, mobile charge carriers within the sample move to screen the spontaneous polarisation, manifested as a current flow of opposite polarity to the displacement current, see for example the comparison between a 10 K measurement (where the sample is an ideal insulator) and a 100 K (the sample is a poor insulator) measurement shown in fig. 3.13 c.

At temperatures exceeding 100 K the conductivity of the sample is sufficiently large to prevent direct confirmation of the (non-) polar nature of the high temperature phases (B and C). Despite this, even considering the reduced polarisation due to screening by mobile charge carriers, the maximum polarisation does indeed appear to decrease in magnitude on warming above $\sim$50 K, suggesting the approach to a non-polar phase - contrary to the suggestion that the high temperature field -induced phase (C) is polar [80].

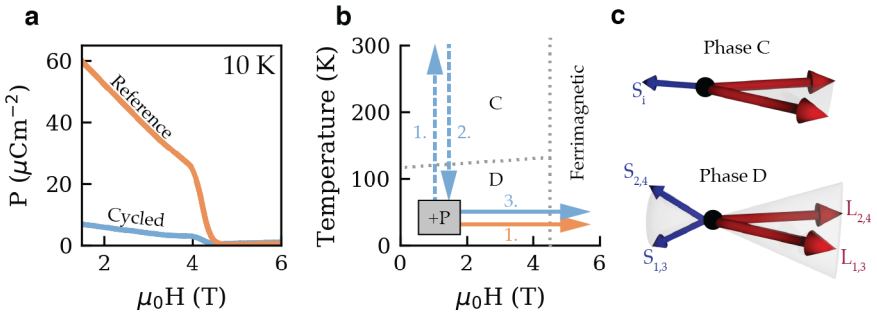


Figure 3.14: Polarisation memory in the high-field phase. **a,** Polarisation as a function of magnetic field, as poled (orange line) and after thermal cycling (solid blue line) to 300 K in a magnetic field of 1.5 T. **b** Graphic outlining the measurement procedure. Prior to each measurement the sample was prepared into a single polar state by poling with a -200 V mm^{-1} electric field while sweeping from 6.5 T (ferrimagnetic state) to 1.5T (polar fan). **c,** Phase classification considering the lack of polarisation memory at the C/D phase boundary. Phase C is a planar fan (all spins contained in the *ab* plane and Phase D is a canted 2-fan, with an additional antiferromagnetic modulation of the S block spins along *c*.

Polar nature of phase C

The field induced phases (C and D) are consistent with those previously observed in BMFO [78, 80]. We were able to confirm that phase D in BSMFO was polar and while a magnetocurrent measurement in phase C was impossible due to the poor insulating nature of our sample, we can test if phases C and D are related by the coherent rotation described by S. Ishiwata *et. al* which, if true, would preserve the electric polarisation at the transition [80]

We prepared a BSMFO single crystal into a polar monodomain (by appropriate magnetoelectric poling) at 10 K in phase D. In fixed magnetic field (1.5 T) we then thermally cycled the sample to 300 K (phase C) and back to 10 K. Here we measured the polar properties of the sample: this procedure is outlined graphically in fig. 3.14.

The results of this measurement are displayed in fig. 3.14 a. The solid orange line is a reference measurement in phase D (i.e., identical magnetoelectric poling procedure but no thermal cycling) and the solid blue line is a measurement performed following the thermal cycle. Both measurements were performed in zero electrical bias. Following the thermal cycling, the measured electric polarisation is reduced by ∼87%: in disagreement with the suggestion that the two phases are related by

a coherent rotation. If the phase classification suggested by S. Ishiwata *et. al* was true, we would expect no reduction in the measured electrical polarisation after this process [80].

We must, therefore, consider a phase classification which explains the absence of appreciable polarisation memory at the C/D boundary. Drawing on our knowledge of the zero field magnetic phase (it is a planar helix at high temperatures and a longitudinal conical structures at low temperatures) and the confirmed polar nature of phase D, the most likely interpretation is that the high temperature phase (lighter colour in fig. 3.12, phase C) is a *planar* 2-fan (non-polar) and the low temperature phase (phase D) is a *canted* 2-fan (polar), at odds to the belief that both phases C and D in BMFO are polar [78, 80].

Zero-field memory

One of the most striking ME effects in BMFO is the remarkable result that the electric polarisation of the canted 2-fan state can be inverted, without loss, by changing the direction of the applied magnetic field [11, 77]. Here we consider this effect in our BSMFO single crystals.

Figure 3.15 displays the electric polarisation of BSMFO, measured as a function of applied magnetic field, at a range of temperatures. All measurements began in a single polar domain - obtained by applying a 200 $\mathrm{V\,mm^{-1}}$ poling field while isothermally sweeping from the helical state to the initial measurement field, 0.5 T. The biasing electric field was then removed and the magnetic field subsequently swept between -0.5T and 0.5T multiple times (denoted by dashed grey lines in fig. 3.15).

We found that the electric polarisation was coupled to the sign of the applied magnetic field (fig. 3.15 a). Ten sequential field inversions were tested and, within our experimental resolution, no measurable decrease in $|\vec{P}|$ was observed (fig. 3.15 c) during the field oscillations. This affect was observed between 10 K and 100 K but

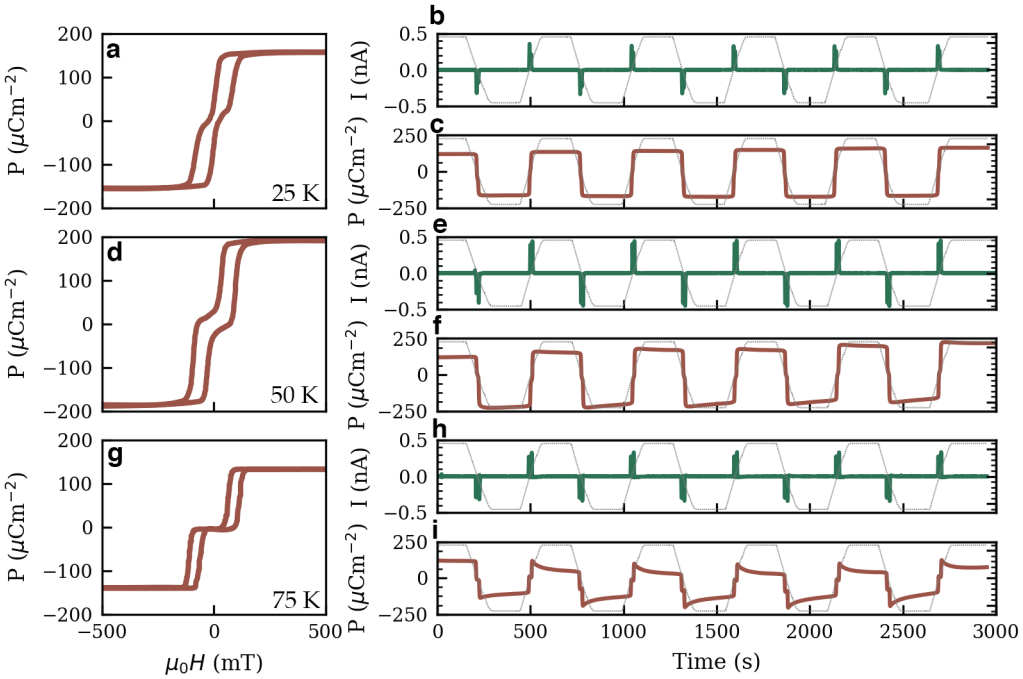


Figure 3.15: Low-field polarisation memory in $Ba_{0.5}Sr_{1.5}Mg_2Fe_{12}O_{22}$. a, b and c Electric polarisation as a function of applied magnetic field at 25 K in the low field region. **b,** Displacement current (top panel) and polarisation (bottom panel) as the magnetic field is alternately swept at 10 mT s^{-1} between ± 500 mT, dashed grey lines indicate the applied magnetic field. **d,e and f** and **g,h and i** are equivalent measurements at 50 K and 75 K respectively. The effects of the poor insulating properties of the sample become strikingly apparent at 75 K (i.e., see i). Prior to these measurements the sample was magnetoelectrically poled using an electric field of 200 V mm^{-1}, as described in the main text. Measurements were performed in the absence of electrical bias.

above ∼75 K (fig. 3.15 i) the poor insulating properties of the samples began to inhibit the measurement.

A mechanism of this electric polarisation reversal in BMFO was first proposed by S. Ishiwata *et al.* [77]. It relied on the direct coupling between the systems magnetic polarity (its sense of rotation, formally defined in chapter 5) and the electric polarisation, eq. (3.8). In this work it was proposed that when the magnetic field was inverted the canted 2-fan structure coherently rotated 180° around the [0,1,0] direction, the net result of which is to switch the structures sense of rotation (magnetic polarity), in turn driving a reversal of the electric polarisation. The reversal of the magnetic polarity, however has yet to be directly observed and studying the mechanisms of this electric polarisation memory is the subject of chapter 5.

3.4 Conclusions

We have confirmed that Sr doping of the Ba sites in BMFO increases the ordering temperature of the incommensurate helical phase. Building on this, we have characterised (for the first time) the magnetoelectric phase diagram of $Ba_{0.5}Sr_{1.5}Mg_2Fe_{12}O_{22}$ using lab-based techniques. Magnetometry indicates the presence of several metamagnetic states, which we identified the positions of the different phase boundaries for. By comparing the qualitative features of our data to literature we were able to predict the identity of each distinct magnetic phase. Contrary to current belief, our results appear to indicate that while the low temperature fan state (phase D) is polar, the high temperature 2-fan state (phase C) is a planar structure and therefore non-polar.

In chapter 4 we investigate this phase diagram further by performing a series of X-ray and neutron diffraction experiments. Following this, in chapter 5 we investigate the mechanisms of the electric polarisation memory demonstrated in this chapter (fig. 3.15) by ad resonant X-ray diffraction experiment.

4 | Magnetic phase identification of $Ba_{0.5}Sr_{1.5}Mg_2Fe_{12}O_{22}$ by X-ray and neutron diffraction

In chapter 3 we showed that $Ba_{0.5}Sr_{1.5}Mg_2Fe_{12}O_{22}$ exhibited a series of metamagnetic phases, one of which we confirmed to be polar (fig. 3.13). In this chapter, we discuss complementary X-ray and neutron diffraction experiments performed to identify each of these magnetic phases. We find that the zero field structure is an incommensurately modulated helical order and that application of magnetic fields ($\mu_0 H \gtrapprox 150$ mT) stabilizes metastable magnetic fan structures which are commensurately modulated with the crystal lattice, consistent with our expectations from chapter 3. Additionally, the persistence of the field-induced polar phase on removal of the applied magnetic field is investigated. Upon removal of the field the polar phase is found to co-exist with the incommensurate helical phase, suggesting it may be possible to indefinitely stabilize the polar phase in zero applied magnetic field.

Our results represent the first comprehensive study of the magnetic phase diagram of $Ba_{0.5}Sr_{1.5}Mg_2Fe_{12}O_{22}$ and will help guide future studies looking to utilize its functional potential.

4.1 Introduction

Y-type hexaferrites exhibit a diverse range of metamagnetic orders [91]. Magnetic fields, applied in their basal plane, transform the incommensurately modulated helical phases into commensurate fan structures [20, 77, 113, 120]. Many of these fan structures are magnetoelectric, with the electric polarisation being induced by the spin-current mechanism [25]. To be functionally useful, these metamagnetic states must exist in low applied magnetic fields and, preferentially, be stable in the absence of an applied magnetic field. In addition to this, the structure must be stable (and functional) at temperatures exceeding 300 K. In chapter 3 we showed that $Ba_{0.5}Sr_{1.5}Mg_2Fe_{12}O_{22}$ (BSMFO) has the potential to be one such compound. Magnetometry of a BSMFO single crystal identified the presence of several metamagnetic states, existing up to ∼390 K. We confirmed that one of these phases was polar and exhibited a giant magnetoelectric effect (fig. 3.15).

In chapter 3 we qualitatively compared the positions of the magnetic phase boundaries to those of $Ba_2Mg_2Fe_{12}O_{22}$ (BMFO, the parent compound of BSMFO) determined by single crystal neutron diffraction [78, 80], to predict the magnetic order of each phase. These previous works measured the positions of magnetic satellites, as a function of field and temperature, to identify the set of propagation vectors describing each phase. From these propagation vectors the magnetic structure of each phase, within the block model of the Y-type hexaferrites (see chapter 3), was then inferred. Additionally, these studies provided the first diffraction based evidence of the longitudinal conical structure [80], proposed to evolve at low temperatures in the absence of an applied field in BMFO. S. Ishiwata *et al.* tracked the intensity of the $(2, \bar{2}, 1)$ (sensitive to the ferrimagnetic component of the concial structure) as a function of temperature. An increase of the intensity of this reflection, coincident in temperature with the proposed helical to longitudinal conical transition, was indicative of its existence [80].

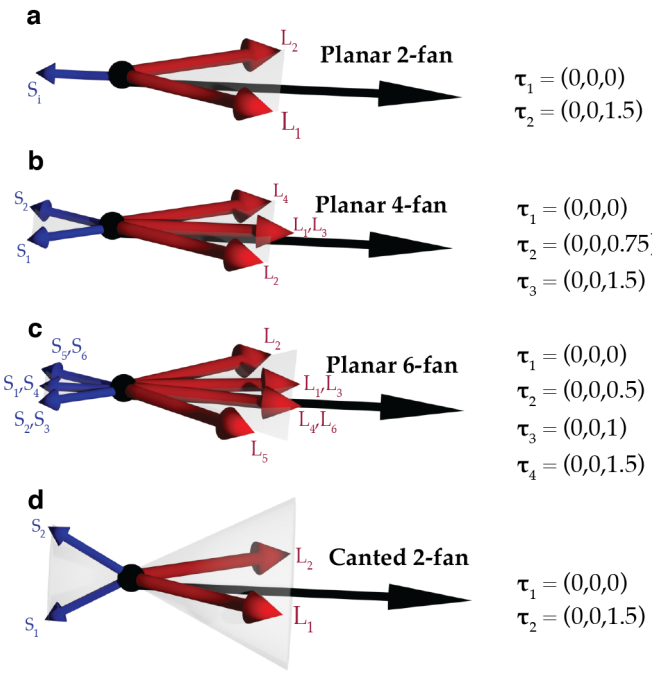


Figure 4.1: Fan structures of Y-type hexaferrites. a-c, Planar fan structures. L and S block moments are represented by red and blue arrows respectively. The labelling convention (S_i or L_j) indicate their stacking order along c and is defined in fig. 3.2. All of these planar fan structures are non-polar. **d,** Canted 2-fan magnetic structure. S block moments have canted out of the plane of the fan, this structure is polar. Solid black arrows represent the direction of the magnetic field required to stabilize the fan structures and the right column indicates the set of propagation vectors ($\vec{\tau_i}$) required to describe each respective fan.

In this chapter, we take advantage of the characteristic set of propagation vectors defining each of the fan structures (fig. 4.1) and the sensitivity of diffraction (via the Laue condition) to these propagation vectors to confirm the identity of each magnetic phases of BSMFO we identified by magnetometry. In the following we review the magnetic fan structures of the Y-type hexaferrites, within the block model, relevant to our phase diagram.

4.1.1 Magnetic fan structures of Y-type hexaferrites

The large crystallographic unit cells of the Y-type hexaferrites means, as a matter of convenience, their magnetic structures have been exclusively described in the so-called block model [80, 91, 107, 108]. In this model, introduced in chapter 3, the unit cell is divided into a sequence of two magnetic blocks, L (large moment) and

S (small moment) blocks, stacked along the c axis. Within each block Fe moments are assumed to be collinear (by virtue of strong superexchange between nearest neighbours within a block [16]) and are antiferromagnetically stacked along c. The magnetic structure is then described by a spin (L or S), located at the centre of each block, of magnitude equal to the net moment of the magnetic block: in BSMFO equal to $3m_{\mathrm{Fe}}$ and $1m_{\mathrm{Fe}}$ for the L and S blocks respectively (where m_{Fe} is the moment magnitude of a single Fe site). The net result is rather than having six independent sites (Fe1→Fe6) the magnetic structure can be described by just two 'sites', the L and S block moments (i.e., see fig. 4.1).

We describe magnetic structures using the propagation vector formalism, where the moment of each site is expanded in a Fourier series,

$$\vec{m}_n = \sum_j \vec{S}_{j,n} e^{-i\vec{\tau}_j \cdot \vec{r_n} - i\phi_n} + \vec{S}^*_{j,n} e^{i\vec{\tau}_j \cdot \vec{r_n} + i\phi_n}, \tag{4.1}$$

where $\vec{S}_{j,n}$ is the Fourier coefficient of the j^{th} propagation vector ($\vec{\tau_j}$) for the n^{th} site. ϕ_n is a site specific phase (defined in chapter 3), which can be included in the Fourier coefficient ($\vec{S}_{j,n}$) of the site but we explicitly include it to emphasise the block nature of the structure. Figure 4.1 displays the metamagnetic fan structures observed in BMFO (by neutron diffraction) described within the block model, where red arrows represent L block moments and blue arrows S block moments. Next to each graphic we display the set of propagation vectors required to describe each structure. In the following, we present the Fourier coefficients ($\vec{S}_{j,n}$) derived for these fan structures. The Fourier coefficients are defined in a Cartesian basis relevant to the experiments presented in this chapter: magnetic fields are applied parallel to $\hat{U}_2$ (see fig. 4.2 for an example).

Planar 2-fan

The planar 2-fan structure is described by two propagation vectors, $\vec{\tau}_1 = (0, 0, 0)$

and $\vec{\tau}_2 = (0, 0, 1.5)$ and the respective Fourier coefficients for sites in the L and S blocks respectively are,

L Blocks :

$$\vec{S}_{1,L} = \frac{m_{\mathrm{Fe}}}{2} \cos(\phi_L)[0, 1, 0], \tag{4.2}$$

$$\vec{S}_{2,L} = \frac{m_{\mathrm{Fe}}}{2} \sin(\phi_L)[i, 0, 0], \tag{4.3}$$

S Blocks :

$$\vec{S}_{1,S} = \frac{m_{\mathrm{Fe}}}{2}[0, 1, 0], \tag{4.4}$$

where m_{Fe} is the site moment and ϕ_L the fan angle of the L block, defined in fig. 3.5. In our definition all sites in a block (L or S) possess the same Fourier component, and only differ in their value of (ϕ_n). Visual inspection of the coefficients show that both the S and L blocks feature a $\vec{\tau}_1 = (0, 0, 0)$ modulation of the moments (ferrimagnetic) parallel to $\hat{U}_2$ and the L blocks feature an antiferromagnetic stacking ($\vec{\tau}_2 = (0, 0, 1.5)$), with moments (anti-)parallel to $\hat{U}_1$.

Planar 4-fan

Three propagation vectors are required to describe the planar 4-fan structure: $\vec{\tau}_1 = (0, 0, 0), \vec{\tau}_2 = (0, 0, 0.75), \vec{\tau}_3 = (0, 0, 1.5)$ with respective Fourier coefficients of,

L blocks :

$$\vec{S}_{1,L} = \frac{m_{\mathrm{Fe}}(1 + \cos(\phi_L))}{4}[0, 1, 0], \tag{4.5}$$

$$\vec{S}_{2,L} = \frac{\sqrt{2} m_{\mathrm{Fe}} e^{i\frac{\pi}{4}} \sin(\phi_L)}{2}[i, 0, 0], \tag{4.6}$$

$$\vec{S}_{3,L} = \frac{m_{\mathrm{Fe}}(1 - \cos(\phi_L))}{4}[0, i, 0], \tag{4.7}$$

S blocks :

$$\vec{S}_{1,S} = \frac{m_{\mathrm{Fe}}\cos(\phi_S)}{2}[0,1,0], \tag{4.8}$$

$$\vec{S}_{2,S} = \frac{\sqrt{2}m_{\mathrm{Fe}}e^{i\frac{\pi}{4}}\cos(\phi_S)}{2}[1,0,0], \tag{4.9}$$

$$\vec{S}_{3,S} = 0, \tag{4.10}$$

for the sites in the L and S blocks respectively. The fan angles are defined in fig. 3.5.

Planar 6-fan

The highest order fan observed in a Y-type hexaferrite is the 6-fan and is described by four propagation vectors, $\vec{\tau}_1 = (0,0,0), \vec{\tau}_2 = (0,0,0.5), \vec{\tau}_3 = (0,0,1), \vec{\tau}_4 = (0,0,1.5)$. The respective Fourier coefficients are,

L blocks :

$$\vec{S}_{1,L} = \frac{m_{\mathrm{Fe}}\cos(\frac{\phi_L}{2})(1+\cos(\phi_L))}{6}[0,1,0],$$

$$\vec{S}_{2,L} = \frac{2m_{\mathrm{Fe}}\sin(\frac{\phi_L}{2})(1+\cos(\phi_L))e^{-i\frac{\pi}{6}}}{3}[1,0,0],$$

$$\vec{S}_{3,L} = \frac{2m_{\mathrm{Fe}}\cos(\frac{\phi_L}{2})(1-\cos(\phi_L))e^{-i\frac{2\pi}{3}}}{3}[0,1,0],$$

$$\vec{S}_{4,L} = \frac{m_{\mathrm{Fe}}\cos(\frac{\phi_L}{2})(\cos(\phi_L)-\frac{1}{2})}{3}[i,0,0],$$

S blocks :

$$\vec{S}_{1,S} = \frac{m_{\mathrm{Fe}}\cos(\phi_S)}{2}[0,1,0],$$

$$\vec{S}_{2,S} = \frac{m_{\mathrm{Fe}}\sin(\phi_S)}{\sqrt{3}}[i,0,0],$$

$$\vec{S}_{3,S} = \frac{m_{\mathrm{Fe}}(1-\cos(\phi_S))}{2}[0,1,0],$$

for sites in the L and S block respectively.

Canted 2-fan

The canted 2-fan magnetic structure is similar to the planar 2-fan but S block moments now have an additional antiferromagnetic modulation parallel to [0,0,1] (fig. 4.1). It is described by two propagation vectors: $\vec{\tau}_1 = (0,0,0)$ and $\vec{\tau}_2 = (0,0,1.5)$ with respective Fourier coefficients of,

L Blocks :

$$\vec{S}_{1,L} = \frac{m_{\mathrm{Fe}}}{2}\cos(\phi_L)[0,1,0], \tag{4.11}$$

$$\vec{S}_{2,L} = \frac{m_{\mathrm{Fe}}}{2}\sin(\phi_L)[i,0,0], \tag{4.12}$$

S Blocks :

$$\vec{S}_{1,S} = \frac{m_{\mathrm{Fe}}}{2}\cos(\phi_S)[0,1,0], \tag{4.13}$$

$$\vec{S}_{2,S} = \frac{m_{\mathrm{Fe}}}{2}\sin(\phi_L)[0,0,1], \tag{4.14}$$

where m_{Fe} is the site moment and ϕ_i the fan angle of the respective block. Of the fan structures described (fig. 4.1) the canted 2-fan is the only polar structure.

4.2 Experimental details

In this section we introduce the non-resonant X-ray diffraction (NRXD) and neutron diffraction techniques discussed in this chapter. We utilize their different magnetic scattering cross sections (chapter 2) to provide complementary information about the system under study.

4.2.1 I16: Non-resonant X-ray magnetic diffraction

X-ray diffraction experiments were performed on the I16 beamline at Diamond Light Source, UK. A BSMFO single crystal was mounted on the copper cold finger of a helium cryostat at the centre of the pole pieces of an electromagnet (fig. 4.2).

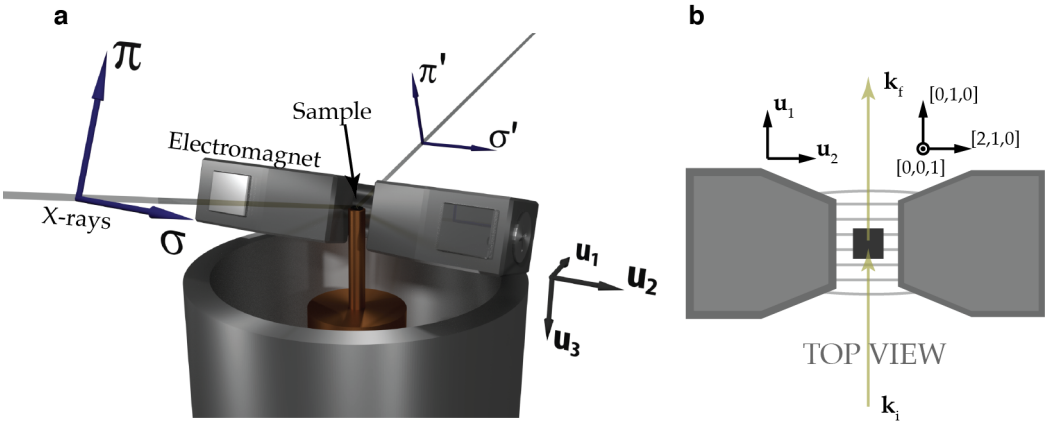


Figure 4.2: Geometry of the NRXD experiment performed on I16. a, Graphic of the electromagnetic showing the $\sigma - \pi$ basis. X-rays are incident on a sample which is at the centre of the pole pieces of an electromagnet. **b** Orthographic view of magnet, highlighting the orientation of the sample ([2,1,0] $\parallel \vec{B}$) with respect to the magnetic field.

The crystal was aligned such that the [0,0,1] direction was surface normal and the [0,1,0] direction was contained within the scattering plane. Using the electromagnet, magnetic fields (up to $\pm$ 200 mT) could be applied to the sample perpendicular to the scattering plane (parallel to $\hat{U}_2$ in fig. 4.2). Incident (σ-polarised) X-rays of energy 5.23 keV, off-resonance of any element in the sample, were used for the duration of the experiment.

We took advantage of the non-resonant magnetic component of the scattering amplitude ($f^{mag}(\vec{Q})$, eq. (2.9)) to gain sensitivity to the magnetic order of our BSMFO sample. In the absence of any polarisation analysis of the scattered X-ray beam, scattering of charge origin ($f_0(\vec{Q})$) was found to dominate the measured signal, such that magnetic scattering could not be observed (non-resonant magnetic scattering is weaker by a factor of $\sim \left[\frac{\hbar\omega}{mc^2}\right]^2$) [41].

Measurements of the magnetic contribution to the scattering cross section were therefore performed by taking advantage of the different polarisation characteristics of Thomson and the non-resonant magnetic scattering processes. While magnetic scattering can rotate the polarisation of linearly polarised incident light (eq. (2.16)), Thomson scattering does not (i.e., $f_0^{\sigma\pi'}(\vec{Q}) = 0$). Therefore, by measuring only scattering processes which rotate the polarisation of incident X-rays ($\sigma - \pi'$ or $\pi - \sigma'$

polarisation channels), we can isolate the (non-resonant) magnetic contribution to the scattering cross section. Measurements in the two non-rotated polarisation channels ($\sigma - \sigma'$ or $\pi - \pi'$) were not possible, because of the large Thomson background.[1]

For a given polarisation channel the intensity of a reflection is proportional to the square of the relevant component of the Fourier transform of the scattering amplitude (eq. (2.16)),

$$I \propto |\sum_n f_n^{mag}(|\vec{Q}|)e^{i\vec{Q}\cdot\vec{r}_n}|^2, \tag{4.15}$$

where f_n^{mag} is the (non-resonant) magnetic scattering amplitude and the sum runs over every atom in the crystal. For the $\sigma - \pi'$ polarisation channel the scattering intensity is given by,

$$I_{\sigma\pi'} \propto |\sum_n [-2\sin^2(\theta)\cos(\theta)m_{1,n} - 2\sin^3(\theta)m_{3,n}](|\vec{Q}|)e^{i\vec{Q}\cdot\vec{r}_n}|^2, \tag{4.16}$$

where we have assumed $\vec{L}$=0, the orbital angular momentum of Fe^{+3} is quenched ($3d^5$ ground state) and the spin moment of the n^{th} atom is given by $\vec{m}_n = [m_{1,n}, m_{2,n}, m_{3,n}]$, expressed in the Cartesian coordinate system displayed in fig. 4.2. This equation shows that our NRXD experiment is sensitive to components of the magnetic structure in the scattering plane ($\hat{U}_1\hat{U}_3$) only.

Identification of propagation vectors

As discussed in section 4.1 we have shown that any arbitrary magnetic structure can be expressed in the propagation vector formalism, where the magnetic moments are expanded in a Fourier series. Putting the Fourier decomposition of a general magnetic structure (eq. (3.1)) into the predicted scattering intensity for our experimental geometry (eq. (4.16)) we find,

[1] This restricts the components of the magnetic structure we are sensitive to (eq. (2.16)).

$$I_{\sigma\pi'} \propto \Bigg| \sum_n \sum_j \Bigg\{ -2\sin^2(\theta)\cos(\theta)[S_{1,j,n}e^{i(\vec{Q}-\vec{\tau}_j)\cdot\vec{r}_n} + S^*_{1,j,n}e^{i(\vec{Q}+\vec{\tau}_j)\cdot\vec{r}_n}] \\ -2\sin^3(\theta)[S_{3,j,n}e^{i(\vec{Q}-\vec{\tau}_j)\cdot\vec{r}_n} + S^*_{3,j,n}e^{i(\vec{Q}+\vec{\tau}_j)\cdot\vec{r}_n}] \Bigg\} \Bigg|^2, \tag{4.17}$$

where we have ignored site specific phases (ϕ_n) for clarity, as these do not affect the position of the magnetic scattering. The Fourier coefficient of the j^{th} propagation vector for the n^{th} site is given by $\vec{S}_{j,n} = [S_{1,j,n}, S_{2,j,n}, S_{3,j,n}]$. When the summation over all magnetic sites is performed, the intensity is non-zero *only* when $\vec{Q} = \vec{G} \pm \vec{\tau}_j$,[2] where $\vec{G}$ is a reciprocal lattice vector and $\vec{\tau}_j$ a magnetic propagation vector. Therefore, propagation vectors ($\vec{\tau}_j$) of a system can be identified by measuring the positions of the magnetic satellites with respect to the reciprocal lattice vectors ($\vec{G}$). Additionally, eq. (4.17) shows we are sensitive only to $\vec{S}_1$ or $\vec{S}_3$ components of the Fourier coefficients, which restricts the propagation vectors we are sensitive to (fig. 4.1), which can aid in the classification of each magnetic phase. For example, in our experimental geometry we are insensitive to the $\vec{\tau}_3 = (0, 0, 1.5)$ propagation vector of the planar 4-fan structure as it modulates moments exclusively along $\hat{U}_2$.

4.2.2 WISH: Neutron diffraction

Single crystal neutron diffraction experiments were performed on the WISH[3] instrument at the ISIS spallation source, UK. WISH is primarily designed for powder diffraction experiments, however, because the instrument is optimized to achieve high resolution at large d-spacings it is suitable for studying large unit cell single crystals, such as the Y-type hexaferrites [121].

A $4 \times 1 \times 1$ mm^3 ([0,0,1] perpendicular to the smallest face, [2,1,0] parallel to the

[2]This can be shown by taking advantage of the lattice periodicity, $\vec{r}_n \rightarrow \vec{R}_n + \vec{d}_j$, where $\vec{R}_n$ is the position the the unit cell origin the n^{th} spin resides in and $\vec{d}_n$ the position with respect to the unit cell origin. For further details see chapter 2.

[3]WISH is an acronym for 'Wide angle In a Single Histogram'

length of the crystal) BSMFO single crystal was inserted into a 9 T magnet such that magnetic fields could be applied parallel to the [2,1,0] direction. The crystal was aligned with the $(h, -2h, l)$ plane in the (horizontal) scattering plane of the WISH instrument. The temperature of the sample could be maintained between ∼25 K and 325 K. The geometry of our experiment is equivalent to our NRXD experiment previously discussed.

Time-of-flight neutron diffraction

WISH is a time-of-flight neutron diffractometer, where the flight time of the neutrons (over a path of known length) is recorded. The wavelength of the neutrons can be calculated using their flight time,

$$\lambda = \frac{h t_{tof}}{m_n L}, \tag{4.18}$$

where h is Planck's constant, t_{tof} the neutron flight time, m_n the neutron mass and L the flight path length, equal to ∼51 metres (it varies over the extent of the detector bank) at WISH. As the 2θ angle of diffracted neutrons is also recorded, Braggs law can be used to calculate the modulus of the scattering vector for any diffraction event.

Identification of propagation vectors

In the same way as NRXD, neutron diffraction can be used to identify the propagation vectors of a system. In this experiment we measure scattering exclusively along the $\vec{Q} = (0, 0, l)$ axis and describe the magnetic orders in the Cartesian basis outlined in fig. 4.2 (i.e., magnetic fields are applied parallel to $\hat{U}_2$).

For neutron scattering, the predicted magnetic differential cross section is described by eq. (2.8). The key difference between the neutron cross section and that of NRXD is that we need to calculate the magnetic interaction vector, given by,

$$\vec{m}_{\perp,n} = \vec{m}_n - \overbrace{(\vec{m}_n \cdot \hat{Q}) \cdot \hat{Q}}^{m_{\parallel}}, \tag{4.19}$$

where $\vec{m}$ is the moment of the n^{th} site. For our geometry (measuring along the $(0, 0, l)$ reciprocal axis) $\hat{Q}$ is equal to $\hat{Q} = [0, 0, 1]$.[4] Therefore, using our expression for the n^{th} magnetic moment in the propagation vector formalism (eq. (3.1)),

$$\vec{m}_{\parallel} = \sum_j S_{3,j,n} e^{-\vec{\tau}\cdot\vec{r}_n} + S^*_{3,j,n} e^{\vec{\tau}\cdot\vec{r}_n}, \tag{4.20}$$

where the Fourier coefficient of the j^{th} propagation vector is given by $\vec{S}_{j,n} = [S_{1,j,n}$, $S_{2,j,n}$, $S_{3,j,n}]$. Using this to calculate the magnetic interaction vector and inputting its form into the predicted differential scattering cross section (eq. (2.8), proportional to the scattering intensity), we get,

$$I = \sum_j \sum_n f_{m,n} \Big\{ (S_{1,j,n}\hat{U}_1 + S_{2,j,n}\hat{U}_2) e^{(\vec{Q}-\vec{\tau}_j)\cdot\vec{r}_n} + (S^*_{1,j,n}\hat{U}_1 + S^*_{2,j,n}\hat{U}_2) e^{(\vec{Q}+\vec{\tau}_j)\cdot\vec{r}_n} \Big\}. \tag{4.21}$$

In the same way as the NRXD case (eq. (4.17)), this will only be non zero when $\vec{Q} = \vec{G} \pm \vec{\tau}_j$, inspection of the positions of magnetic reflections is sufficient to identify propagation vectors of the system. Importantly, our sensitivity to each component of the magnetic structure is different for neutron diffraction compared to NRXD. For neutrons we are sensitive to components of the magnetic structure in the $\hat{U}_1\hat{U}_2$ plane. Therefore, when both techniques are used in conjunction we are sensitive to any possible propagation vector of the system.

[4] This is expressed in the Cartesian basis (displayed in fig. 4.2) and not in the reciprocal lattice.

4.3 Results and discussion

4.3.1 Zero-field phases

Our lab-based characterisation indicates that phase A, the phase stable in low magnetic fields (fig. 3.12) is a planar helix at temperatures exceeding ∼100 K and a longitudinal conical structure at temperatures below this. For both of these structures moments lie in the $(0, 0, l)$ plane and propagate along the [0,0,1] direction (eq. (3.4)). In the longitudinal conical structure the L and S blocks additionally cant ferrimagnetically ($\vec{\tau} = (0, 0, 0)$) out of the $(0, 0, l)$ plane. We are insensitive to this component in our diffraction experiments by virtue of our experimental geometry, but its existence is supported by the results of our magnetometry measurements (fig. 3.10).

We begin by discussing our neutron scattering results, recorded at room-temperature and in the absence of an applied magnetic field (Phase A). Figure 4.3 displays the neutron scattering intensity (black diamonds) measured along the (0,0,l) reciprocal axis, sensitive to components of the magnetic structure within this plane. As well as the nuclear reflections allowed by R-centering ($\vec{Q} = (0, 0, 3n)$), we observe pairs of magnetic reflections which index as $\vec{Q} = (0, 0, 3n \pm \tau_z)$ (dashed green lines).

The propagation vector was extracted by performing a Lebail fit to the data (solid red line), where intensities of each reflection freely refine, but their positions are determined by a single c lattice parameter, propagation vector ($\vec{\tau} = (0, 0, \pm\tau_z)$) and a zero l offset. Back-to-back exponentials (of arbitrary width parameters) are used to approximate the peak profiles [122].

The refined propagation vector and c lattice parameter are $\tau_z = (0, 0, 0.882(7))$ and 43.394(4) Å respectively, and clearly (red line in fig. 4.3) well describe the data, with all reflections being accounted for. This strongly suggests that the magnetic structure in zero field and at 300 K is a planar helix, consistent with the zero field

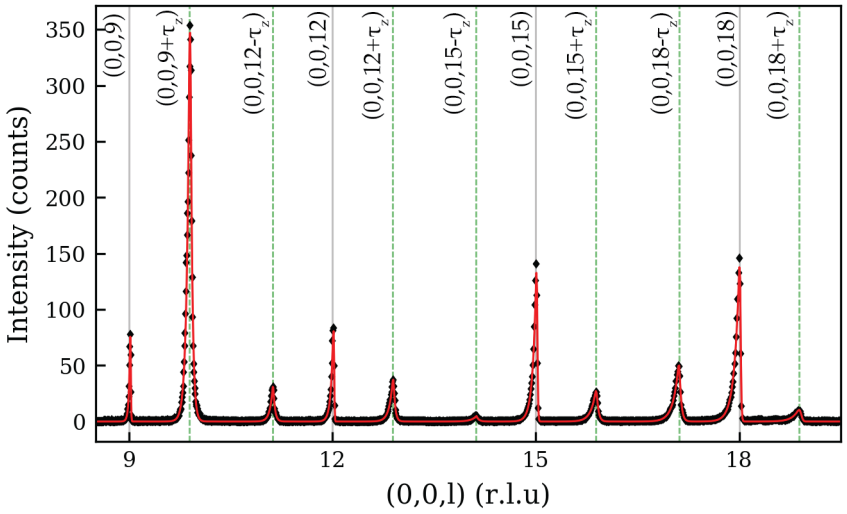


Figure 4.3: Neutron scattering intensity along the (0,0,l) axis of BSMFO single crystal. Solid points are the measured experimental data and the solid red line is a fit to the data, using back-to-back exponentials of arbitrary width parameters but with their centres appropriately tied. The relevant fit parameters were $c = 43.394(4)$ Å, $\vec{\tau}_z = (0, 0, 0.882(7))$ and, a zero offset $l_0 = 0.02$. Solid (vertical) grey lines show positions of the Bragg reflections $\vec{Q} \equiv \vec{G} = (0, 0, 3n)$ and dashed green lines the magnetic satellites $\vec{Q} = \vec{G} \pm \vec{\tau}_z$.

structures in similar Y-type hexaferrites [80, 112].

Next, we investigated the temperature dependence of the helical reflections using NRXD. Due to size restrictions, the experiment was performed on a different BSMFO single crystal, but from the same flux-grown batch. Its properties were confirmed (X-ray diffraction and magnetometry) to be qualitatively identical to the crystal used in the neutron diffraction experiment, although small differences in stoichiometry cannot be ruled out.

l-scans were performed, on warming, as a function of temperature about the (0,0,18) and (0,0,18-τ_z) reflections, displayed in fig. 4.4.[5] The position of the (0,0,18-τ_z) reflection (fig. 4.4 a) is clearly dependent on the sample temperature, indicating a variation of τ_z as the samples temperature is increased.

The measured propagation vector (τ_z), extracted by fitting a Lorentzian profile to the (0,0,18-$\vec{\tau}_z$) reflection, is plotted as a function of temperature in fig. 4.4 c. At

[5]These measurements were performed in the $\sigma - \pi'$ polarisation channel, and therefore we expect the intensity of the (0,0,18) reflection to be approximately zero. However, as the process of polarisation analysis is imperfect some charge scattering leak-through is always observed.

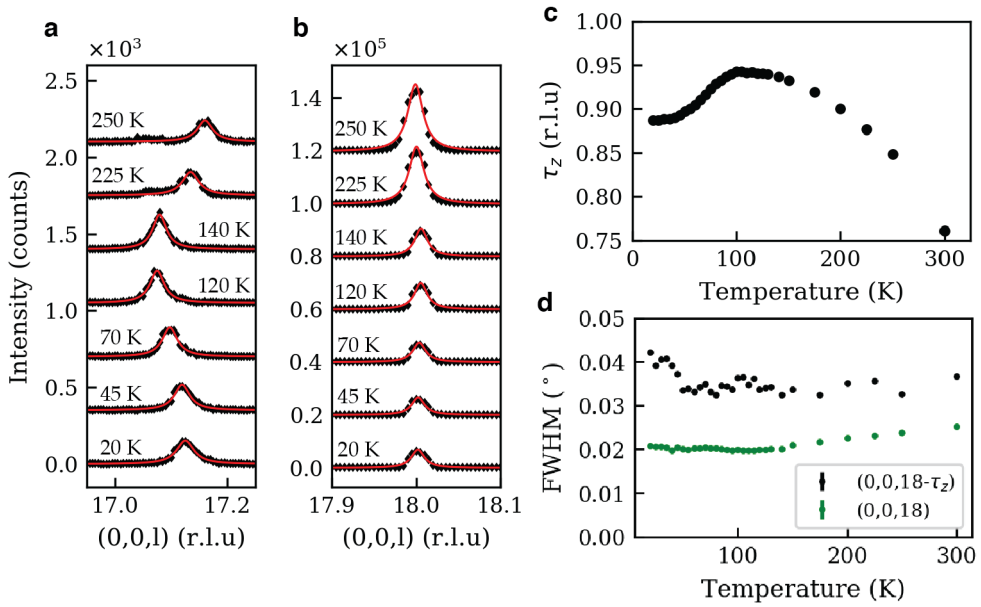


Figure 4.4: Temperature dependence of the helical magnetic reflection measured by NRXD in $\sigma - \pi'$. **a,** (0,0,18-τ_z) and, **b,** (0,0,18) reflections as function of temperature. The scans are arbitrarily displaced along the y-axis. **c,** Propagation vector of the zero field phase as a function of temperature. **d,** Full Width Half Maximum (FWHM) of both reflections as a function of temperature.

temperatures exceeding 100 K the magnitude of the propagation vector decreases on warming. This can be understood by considering a simple exchange model as presented in chapter 1 [20]. We consider three exchange interactions, nearest neighbour (between L and S blocks, J_{LS}) and next-nearest neighbour (between L blocks or S blocks, J_{LL} or J_{SS}) and calculate the energy of helical phase within the block model, eq. (1.4). Following the procedure from chapter 1 the pitch (ϕ_0) of the helical structure is given by,

$$\phi_0 = \arccos\left(\frac{J_{LS}S_LS_S}{4(J_{LL}S_L^2 + J_{SS}S_S^2)}\right), \tag{4.22}$$

where the propagation vector and the helix pitch are related by, $\phi_0 = \frac{\tau_z \pi}{3}$ and S_i is proportional to the block moment and defined in [20]. This equation suggests that for a decrease in propagation vector we would expect the numerator to decrease and, on the assumption of constant moment magnitudes, would correspond to a decrease in the J_{LS} exchange constant relative to J_{LL} and J_{SS}. It is therefore plausible that

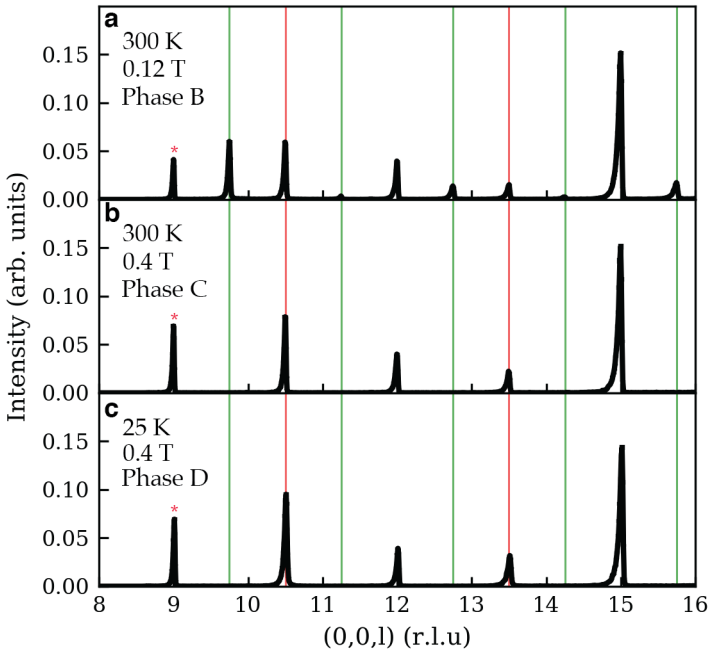


Figure 4.5: Measured neutron diffraction intensity along the (0,0,l) axis of BSMFO for different magnetic fields applied parallel to the [2,1,0] direction. a, At 300 K with a 0.12 T field applied. **b,** At 300 K with a 0.4 T field applied and **c,** with a 0.4 T applied at 25 K. Red solid lines show reflections at (0,0,3$n\pm$ 1.5) reciprocal positions and solid green lines those at (0,0,3$n\pm$ 0.75). The red asterisks highlights the (0,0,9) reflection where the $\vec{\tau} = (0, 0, 0)$ components of the magnetic structure are visible. Noticeably, only panel a has reflections which index as (0,0,3$n\pm$ 0.75).

the change in propagation vector could result from an increase of J_{LS} on cooling, possibly as a result of a local lattice deformation at the L/S block interface.

At temperatures below ∼100 K the propagation vector decreases on cooling, this change in trend is coincident with the proposed onset of the longitudinal conical structure. A similar temperature dependence was observed for $Ba_2Mg_2Fe_{12}O_{22}$ (BMFO) [80], where the helical propagation vector was observed to tend to a *commensurate* value ($\vec{\tau} = (0, 0, 1)$) at the transition between the two phases. It was suggested that the commensurate periodicity was a result of the magnetic structure 'locking' into the hexagonal anisotropy of BMFO, the net result of which was to cause the helical moments to cant out of the basal plane, forming the longitudinal conical structure. However, in our system the helical propagation vector is always *incommensurate* (errors are on the size of the data points in fig. 4.4 c), and this mechanism cannot be relevant.

Additionally, we plot the full-width-half maximum of the (0,0,18) (charge, solid green points) and (0,0,18-τ_z) (magnetic, solid black points) reflections (fig. 4.4 d). The magnetic reflection is broader, reflecting a reduced correlation length with respect to the crystal structure. If the magnetic structure was to commensurately lock-in with the lattice one would expect the width of the reflection to reduce. However, at low temperature we observe a broadening of the magnetic reflection, further supporting the case that the helical structure is always incommensurate.

4.3.2 Field-induced phases

Having characterised the zero field structure, we next discuss the field induced phases. Figure 4.5 displays the scattered intensity along the (0,0,l) reciprocal axis in the three proposed field-induced fan phases (B, C and D) measured by neutron diffraction, for a magnetic field applied parallel to [2,1,0]. As neutrons are sensitive only to components of the magnetic structure perpendicular to the scattering vector (eq. (2.29)), these reflections are sensitive to components of the magnetic structure in the $\hat{U}_1\hat{U}_2$-plane only.

We begin by discussing reflections allowed by the crystallographic space group $R\bar{3}m$ ($\vec{Q} = (0, 0, 3n)$). At these positions scattering of nuclear and magnetic origin (components with $\vec{\tau}$ = (0,0,0)) coincide. Reflections with $n > 4$ (we can observe a maximum n of approximately 16) are approximately invariant to changes in the applied field and temperature, as expected for reflections of pure nuclear origin at (relatively) low temperatures. At such high $|\vec{Q}|$, scattering of magnetic origin has been suppressed by the magnetic form factor (chapter 2) and is masked by the more brilliant nuclear scattering when they are coincident: $\vec{\tau}$ = (0,0,0) components of the magnetic structure are therefore only observed at low $|\vec{Q}|$. The lowest $|\vec{Q}|$ reflection measured along this axis, (0,0,9) reflections (red asterisks) in fig. 4.5, clearly has a magnetic contribution because, unlike other (0,0,3n) reflections, its intensity is strongly field and temperature dependent. This clearly indicates that phases B, C

and D all possess a $\vec{\tau} = (0,0,0)$ component of magnetic structure which is largest in the high-field phases, as expected for field induced fan structures (fig. 4.1).

Next, we discuss reflections which cannot be indexed in the crystallographic unit cell. At 300 K and with a magnetic field of 0.12 T applied to the sample (phase B, fig. 3.12) we observe additional satellite reflections which index as $(0,0,3n\pm 0.75)$ or $(0,0,3n\pm1.5)$, indicated by solid green and red lines in fig. 4.5 respectively. On isothermal increase of the applied magnetic field to 0.4 T (fig. 4.5 b) all $(0,0,3n\pm0.75)$ reflections vanish and the intensity of the $(0,0,3n\pm1.5)$ reflections increase, suggesting (as clear from magnetometry, fig. 3.12) a transition to a different magnetic structure (phase C). On cooling (in fixed magnetic field, fig. 4.5 c) into phase D there is no change in the number of reflections, but there is an increase in the scattering intensity of the $(0,0,3n\pm1.5)$ reflections.

As discussed, neutron diffraction is sensitive only to components of the magnetic structure orthogonal to the scattering vector, our measurements are therefore sensitive to propagation vectors describing components of the magnetic structure within the $\hat{U}_1\hat{U}_2$ plane only. To gain additional information on the magnetic structure we performed l-scans in each phase using NRXD. The measurements were performed in the $\sigma - \pi'$ polarisation channel, in comparison to neutron diffraction, NRXD performed in this polarisation channel is sensitive to components of the magnetic structure in the $\hat{U}_1\hat{U}_3$ plane only, as we have shown explicitly in eq. (4.17).

To aid in visualisation, we plot the l-scans as a false colour map (fig. 4.6), about the key magnetic reflections as a function of applied magnetic field. The positions of the phase transitions are compared to those observed with magnetometry.

At 300 K, in the low field regions we observe the helical phase (fig. 4.6 b). The value of the propagation vector (τ_z) in this phase changes as the magnetic field is increased, suggesting that the helix is perturbed by small magnetic fields at this temperature.

For magnetic fields between $\sim$65 mT and 150 mT, the incommensurate propagation

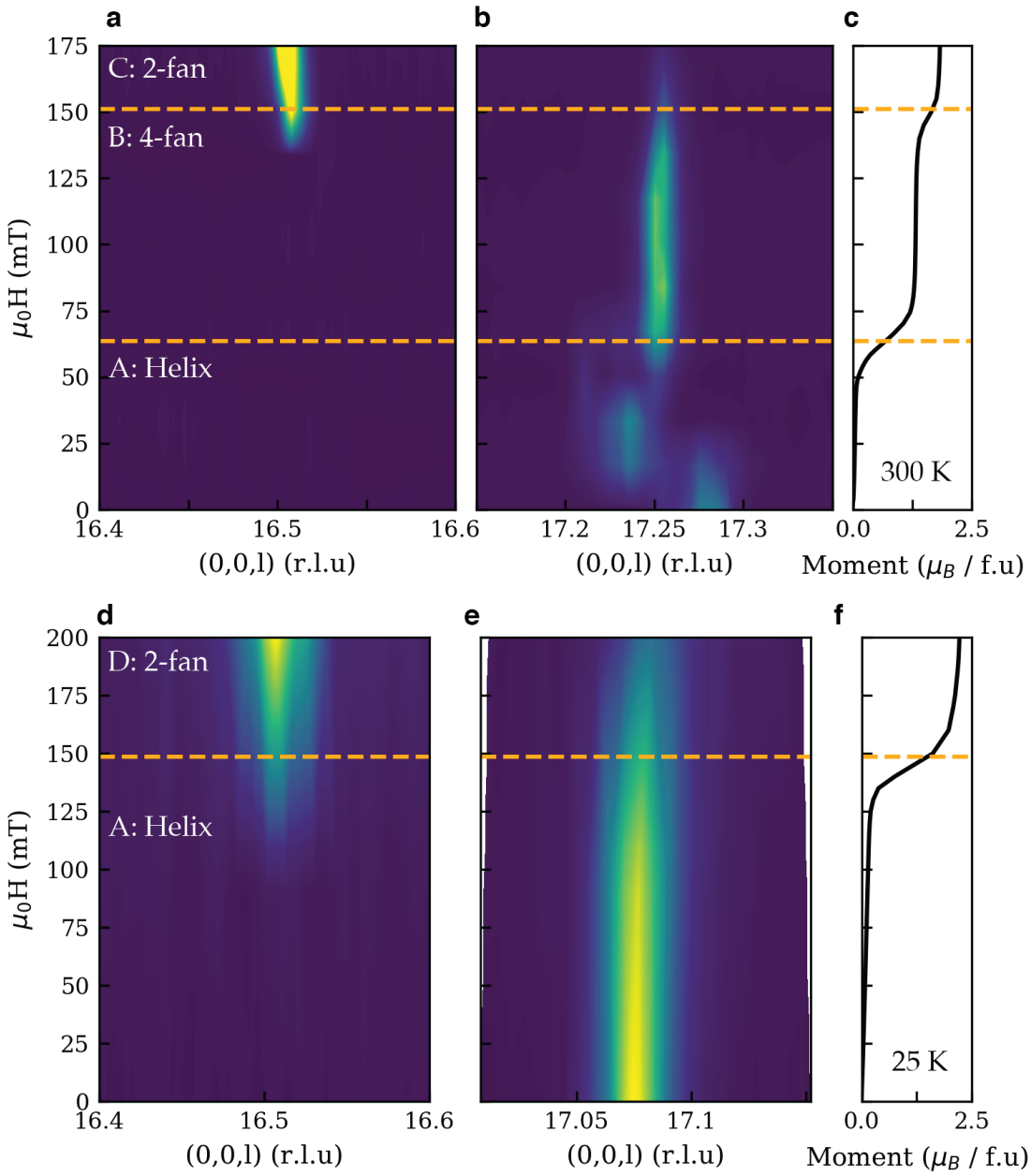


Figure 4.6: Field dependence of magnetic reflections observed with NRXD at a-c, 300 K and **d-f,** 25 K. Colour represents measured intensity on a linear scale, independent for each panel, and highlights the observed propagation vectors. c and f are the measured magnetic moment for an increasing field sweep, applied parallel to [2,1,0], after a ZFC from 400 K to 300 K and 25 K respectively. Dashed orange lines indicate approximate positions of phase boundaries. Phase labels (A, B, C, D) correspond to those introduced in fig. 3.12. All measurements were performed in the $\sigma - \pi'$ polarisation channel.

Phase	T (K)	μ_0H (T)	NRXD (0,0,l): $\sigma \rightarrow \pi'$	Neutrons (0,0,l)
A (Helix)	300	0	$(0, 0, \tau_z)$	$(0, 0, \tau_z)$
B (4-fan)	300	0.12	$(0, 0, 0.75)$	$(0, 0, 0)$, $(0, 0, 0.75)$, $(0, 0, 1.5)$
C (2-fan I)	300	0.4	$(0, 0, 1.5)$	$(0, 0, 0)$, $(0, 0, 1.5)$
D (2-fan II)	25	0.4	$(0, 0, 1.5)$	$(0, 0, 0)$, $(0, 0, 1.5)$

Table 4.1: Magnetic propagation vectors observed using NRXD and neutron diffraction in each region of BSMFOs phase diagram. The first three columns show the phase label, sample temperature and magnetic field respectively. The following columns show the observed propagation vectors. Differences arise both to the different sensitivities of each technique to the magnetic structure (see main text) and the distinct magnetic order of each phase.

vectors vanish and additional reflections of the form (0,0,3n±0.75), coincident with Phase B (dashed lines in fig. 4.6 a-c) are observed. Increasing the applied magnetic field further, such that the system is stable in Phase C, these reflections vanish and new reflections appears at (0,0,3n±1.5) positions.

At 25 K (fig. 4.6 d-f) there is no intermediate phase (no reflections of the form (0,0,3n±0.75) are observed) and only two propagation vectors are observed: in low magnetic fields (less than ∼100 mT) an incommensurate propagation vector ($\vec{\tau} \approx (0, 0, 0.925)$ is observed and at higher fields reflections of the form (0,0,3n±1.5) are observed. As the magnetic field magnitude is increased, the commensurate reflection (fig. 4.6 d) increases in intensity and the incommensurate magnetic reflection (fig. 4.6 e) decreases. At 200 mT (the highest achievable magnetic field with our set-up) only a weak incommensurate reflection is observed and it is expected to vanish in larger magnetic fields.

The set of propagation vectors observed with NRXD and neutron diffraction are summarised in table 4.1. In the following we discuss the set of observed propagation vectors and use them to identify each magnetic structure.

Phase B

Three propagation vectors were observed in total for Phase B (table 4.1), the set of which suggest that this phase is a planar 4-fan structure (fig. 4.1). We can interro-

gate this classification further by noting that in the non-resonant X-ray diffraction experiment only the $\vec{\tau}_2 = (0, 0, 0.75)$ satellite reflections are observed (fig. 4.6 a and b). This observation can be explained by considering that the expected intensity in the $\sigma - \pi'$ polarisation channel (eq. (4.17)) depends only on the S_1 and S_3 components of the Fourier coefficients. The Fourier coefficients of the planar 4-fan structure (eqs. (4.5) to (4.10)) all have $S_3 = 0$ and the only Fourier coefficients with $S_1 \neq 0$ are those corresponding to the $\vec{\tau}_2 = (0, 0, 0.75)$ propagation vector. Therefore for a planar 4-fan, magnetic satellites at positions $\vec{Q} = \vec{G} \pm \vec{\tau}_2$ are the only expected observable reflections in our NRXD experiment geometry(table 4.1).

Notably, by comparison with the phase diagram of BMFO [78], this phase is expected to be a planar 6-fan, but no evidence of this order was observed. If this phase was a 6-fan structure we would of observed a different set of propagation vectors with neutron scattering (fig. 4.5 a) and would of observed reflections resulting from the $\vec{\tau}_2 = (0,0,0.5)$ propagation vector in our NRXD experiment. Our results therefore suggest that Sr doping suppresses the 6-fan phase, in favour of the 4-fan phase. Although, we cannot rule out that the 6-fan phases exists in a small temperature range not studied in this experiment.

Phase C and D

Two propagation vectors (table 4.1, $\vec{\tau}_1 = (0, 0, 0)$ and $\vec{\tau}_2 = (0, 0, 1.5)$) were observed in both phases C and D, with identical polarisation properties. These structures are consistent with 2-fan structures (fig. 4.1), but from our diffraction experiments alone we are unable to discriminate between a planar 2-fan (fig. 4.1 a) and a canted 2-fan (fig. 4.1 d), because they possess qualitatively similar Fourier coefficients (eqs. (4.2) to (4.4) and (4.11) to (4.14)). Using diffraction, to discern them a full magnetic structure refinement must be performed. This has never been achieved for the field-induced phases of the Y-type hexaferrites, primarily a result of the large number of free parameters and the increased difficulty of performing a neutron diffraction experiment with an *in-situ* magnetic field.

To classify these phases we therefore draw on our previous lab-based characterisation (fig. 3.13), where we confirmed phase D to be polar and, phase C unlikely to be. Additionally, as the low-field, high temperatures phases are planar structures it plausible that phase C is *planar* 2-fan and, owing to its polar nature, phase D is a *canted* 2-fan structure. This classification also explains the lack of any appreciable polarisation memory across the phase C/D boundary (fig. 3.14), as a planar 2-fan has no memory of the polar state of the canted 2-fan phase.

Phase diagram summary

Our phase classifications are summarised in fig. 4.7, where we present the phase diagram (measured by magnetometry) and graphically display the different magnetic structures of each phase determined by our diffraction experiments.

In the low magnetic field regions (phase A) we observe magnetic structures characterised by an incommensurate propagation vector, consistent with the proposed helical classification of this phase. At high temperatures this structure appears to be a planar fan but magnetometry (chapter 3) and comparison with similar compounds [80], suggests that the helical phase transitions to a longitudinal conical structure (fig. 4.7 b). While our diffraction experiments are insensitive to the ferrimagnetic component of the longitudinal conical structure (it was not the phase of primary interest), a diffraction experiment could be designed to study it, for example a neutron powder or single crystal diffraction experiment could gain sensitivity to this component by measuring (nuclear and magnetic) reflections of the form $(h, k, 0) = 3n$ [80].

We have shown that magnetic field application in either of these phases induces transitions to commensurate, fan structures. At 300 K we observe phase B (light intermediate region in fig. 4.7 a) which our results suggest is a planar 4-fan structure (fig. 4.7 c). Increasing the magnitude of the applied magnetic field transforms this structure into the 2-fan phase (phase C). On cooling, in fixed magnetic field, we

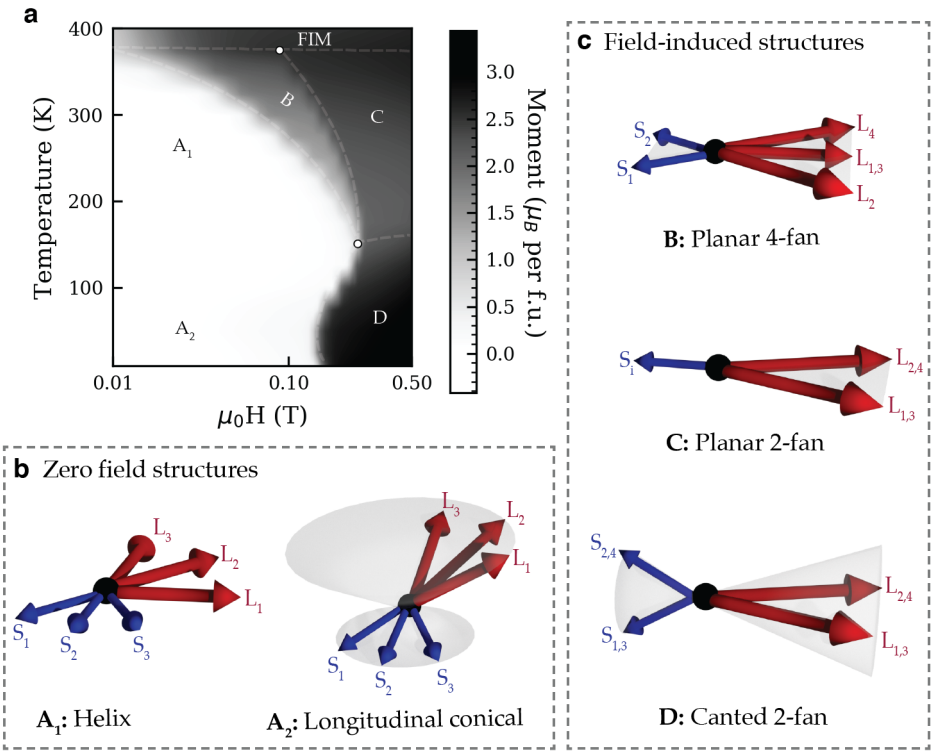


Figure 4.7: Summary of magnetic structures observed in BSMFO. a, Low-field magnetic phase diagram determined by magnetometry (see chapter 3). **b,** Proposed zero field magnetic structures within the block model and **c,** Field induced magnetic structures. Red arrows are L block and blue arrows S block moments.

observe no change in the number of observed propagation vectors but the polar nature of phase D suggests it is a canted 2-fan structure, which induces polarisation by virtue of its non-zero spin current [25].

4.3.3 Phase co-existence

Our lab based characterisation (fig. 3.12) indicated there was dramatic hysteresis between phases A and D at low temperatures, suggesting that the two phases may co-exist once the applied field is removed. Magnetic phase co-existence is a commonly noted feature of the phase diagram of the Y-type hexaferrites and has made magnetic phase classification significantly more challenging [20, 78].

To investigate this hysteresis, we first recorded the scattering intensity along the (0,0,l) axis after a zero field cool to 25 K using the WISH (neutron) diffractometer, displayed in fig. 4.8 a. The data is consistent with the helical state ($\vec{\tau}$ =

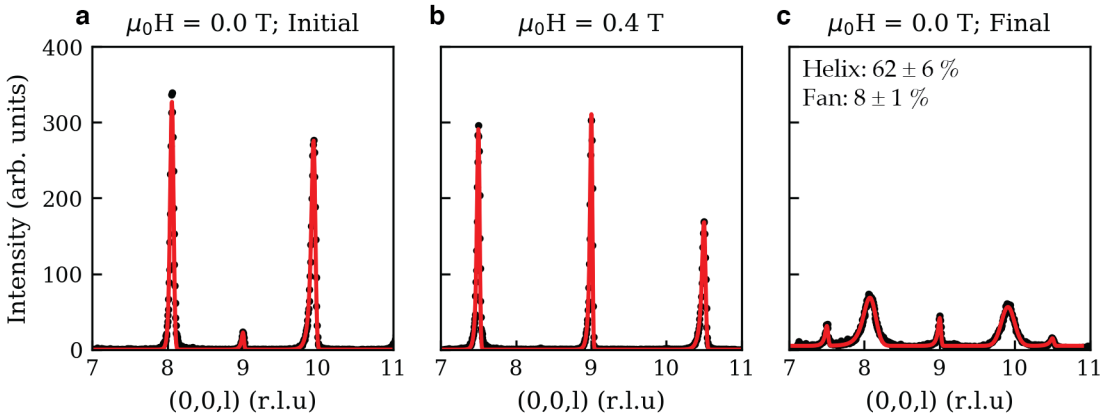


Figure 4.8: Scattering along (0,0,l) axis at key magnetic fields, measured at 25 K, following a zero field cool. **a,** Initial zero field cooled state, showing two incommensurate helical reflections and the (0,0,9) nuclear reflection. **b,** After application of 0.4 T magnetic field parallel to [2,1,0], all incommensurate reflections vanish but two commensurate (0,0,9±1.5) reflections have appeared, as expected for the canted 2-fan. **c,** Zero field state after isothermally removing the applied magnetic field. The sample is now in a mixed phase state, where the inset text highlights the predicted phase fractions, determined by comparing the integrated intensities of the single phase (a and b) and the mixed phase (c) reflections. Solid black points show experimental data (error bars are not shown for visual clarity, but are small). Solid red lines display Lebail fits to the experimental data where the profile functions are back-to-back exponentials [122].

$(0, 0, 0.944(2)))$ and exhibits a very low background. We are intensive to the ferromagnetic component of the longitudinal conical structure in this geometry and so only discuss the helical component in the following.

Following this measurement we applied a 0.4 T magnetic field. At this field magnitude the incommensurate reflections have vanished and two reflections at $(0, 0, 0.9 \pm 1.5)$ (fig. 4.8 b) are observed, consistent with the canted 2-fan phase (phase D). The applied magnetic field is then removed and the scattering recorded again in the zero field state. Previous magnetometry measurements of our sample (fig. 3.12) indicate that we expect significant field hysteresis at temperatures below ∼50 K and our measurement (fig. 4.8 c) supports this: reflections of the $(0, 0, 0.9 \pm 1.5)$ have greatly reduced in intensity and two incommensurate reflections (with the same propagation vector as the zero field cooled state) have returned, but are severely broadened. This suggests we have a mixed 2-fan and helical state, where the increased width of the incommensurate reflections suggests this phase has a reduced correlation length compared to the zero field case. This likely arises as a result of small 'nano-regions'

of the 2-fan disrupting the helical order. Additionally, the post-field sweep (fig. 4.8 c) has a noticeably larger background, which suggests additional disorder in the helical propagation vector may be present.

By comparing the integrated intensities of the high and initial zero field states to the mixed phase state we can estimate the phase fraction of the two orders. We assume the structure factor is independent of field (valid for the helix, but less so for the 2-fan). Comparing the intensities we find that 62(6)% of the sample is helical, 8(1)% in a canted 2-fan state and ∼30% unaccounted for. The helix is clearly the more dominate phase, but the 2-fan does make up an appreciable fraction of the sample. The unaccounted for intensity likely has two origins, firstly the 2-fan structure factor will be field-dependent and so direct comparison of the intensities is not entirely valid, likely meaning that more than 8% of the sample is in a 2-fan state. Secondly, some of the sample is likely disordered (perhaps at domain walls between the two phases) which accounts for the increased background intensity.

We also found the phase fractions to be sample dependent (not shown), but the broadening of the helical reflections to be consistent across all samples. This suggests that it may be possible to engineer the relative phase fractions and even stabilize the canted 2-fan state in zero applied magnetic field.

4.4 Conclusions

To conclude, we have used X-ray and neutron diffraction to study the metamagnetic phase diagram of Y-type hexaferrite $Ba_{0.5}Sr_{1.5}Mg_2Fe_{12}O_{22}$. We have shown that incommensurate helically modulated structures can be transformed into commensurate fan structures by the application of small (∼150 mT) magnetic fields. Our phase classifications were summarised in fig. 4.7 and our observations were largely consistent with the magnetic order observed in other isomorphic hexaferrites [78,80]. Our results show that BSMFO exhibits fan structures at temperatures exceeding 300

K and has significant functional potential. The phase diagram presented here will form the foundations of future studies looking to study the magnetic structures of the Y-type hexaferrites in greater detail.

Future Work

Additional diffraction based studies on BSMFO should focus on two features. Firstly, the longitudinal conical structure could be refined and confirmed by performing a neutron powder diffraction experiment. Secondly, refinement of the canted 2-fan magnetic structure (or any field-induced structure of a Y-type hexaferrite) has never been achieved. It is unlikely this could be achieved by performing a powder diffraction experiment, because a magnetic field applied along a distinct crystallographic direction is required to stabilize this phase. Any future experiments should be performed on a single wavelength neutron diffractometer on a single crystal system as this will maximize the chances of success.

5 | Magnetoelectric polarity switching in $Ba_{0.5}Sr_{1.5}Mg_2Fe_{12}O_{22}$ studied by resonant X-ray diffraction

Resonant X-ray Diffraction is a proven technique for studying the incommensurate phases of the Y-type hexaferrites: it is one of the few techniques which can resolve, with high spatial resolution, the chiral domain structure of the helical phases [123]. In spite of their obvious functional interest the polar, field-induced phases, however, have received little attention with this technique [89,91]. In this chapter we discuss a spatially resolved resonant X-ray diffraction experiment performed to study the field induced phases of $Ba_{0.5}Sr_{1.5}Mg_2Fe_{12}O_{22}$, we demonstrate that circular asymmetry measurements (difference in scattering for circular positive or negative incident X-rays) are sensitive to the magnetic order parameter of the polar phase (its magnetic polarity) and use this technique to investigate the giant magnetoelectric effect observed in this system [11]. A microscopic model is proposed to explain this effect: a rapid switching of the magnetic polarity drives a reversal of the electric polarisation. Analysis of the polarisation state of the scattered X-rays is performed reactively during the switching process, suggesting the magnetic polarity reversal occurs via a coherent rotation of the magnetic structure about the [0,0,1] direction, in contention with the currently accepted switching mechanism [77].

5.1 Introduction

In chapters 3 and 4 we studied the magnetic phase diagram of the Y-type hexaferrite $Ba_{0.5}Sr_{1.5}Mg_2Fe_{12}O_{22}$ (BSMFO) by non-resonant X-ray and neutron diffraction, magnetocurrent measurements, and magnetometry. Our results highlighted the existence of a spontaneous, incommensurate helical magnetic structure which could be transformed (by application of small magnetic fields) into a series of complex, metamagnetic fan structures - one of which, the so called canted 2-fan structure, we confirmed to be polar. This phase exhibited a giant magnetoelectric effect (demonstrated in fig. 3.15) of spin-current origin [25], synonymous with the magnetoelectric effect observed in its parent structure $Ba_2Mg_2Fe_{12}O_{22}$ (BMFO) [77]. The mechanisms of this magnetoelectric effect have never been directly studied and were originally inferred from bulk magnetocurrent measurements [77]. In this chapter we describe a novel resonant X-ray diffraction experiment that we have performed in order to study this effect and the magnetic orders driving it.

Resonant X-ray Diffraction (RXD) is an ideal experimental tool for studying the complex magnetic structures of the Y-type hexaferrites. It relies upon the large enhancement of the magnetic scattering cross section when the energy of incident X-rays are tuned to the Fe $L_{2,3}$ absorption edges, at which a $2p$ core electron is excited into a magnetically polarised $3d$ state [42]. The long wavelength X-rays (λ $\sim$17.5 Å) required for the Fe $L_{2,3}$ edges means the relevant scattering vectors ($|\vec{Q}| = \frac{4\pi \sin(\theta)}{\lambda}$) are extremely small: long-period structures are therefore required to observe any coherent scattering. The smallest accessible d-spacing at 710 eV (Fe L_3) is approximately 8.7 Å, representing a lower bound on the primitive unit cell of a system. The large unit cells of the Y-type hexaferrites (c $\sim$43 Å) makes them one of the few materials suitable for elastic resonant X-ray diffraction experiments at the transition metal L edges [124–126].

Following a seminal study in 2010 by A. Mulders *et. al*, where the sensitivity of RXD

to the chirality (sense of rotation) of the helical phase of $Ba_{0.8}Sr_{1.2}Zn_2Fe_{12}O_{22}$ was demonstrated, experimental focus has very much been on the zero field magnetic structures. Notably, the high-spatial resolution available at synchrotron sources has been exploited to spatially resolve the spin-chiral domain structure of the Y-type hexaferrites [123, 127, 128]. The chiral domains were found to form irregular morphologies on a sub-millimetre length scale and, in some cases, were even discovered to be coupled to a magnetic field [128].

Spatially resolved RXD, however, has never been applied to the field-induced polar phases. This is in part due to the commensurate nature of these structures, which introduces an added complication in understanding the resonant scattering cross section. Being commensurate, scattering of charge and magnetic origin can interfere more readily and terms proportional to $F^{(1)}$ and $F^{(2)}$ in the electric dipole scattering amplitude (see chapter 2) no longer scatter to unique positions in reciprocal space (as they do in the incommensurate case), meaning great care must be taken when interpreting a RXD experiment [50].

RXD experiments of the commensurate polar phases are worth pursing, despite its challenges, because it has the potential to yield information inaccessible to other (non-resonant) diffraction techniques. In the following chapter, by careful consideration of each term in the resonant scattering amplitude, we show how complementary information to bulk sensitive techniques (magnetometry, magnetocurrent measurements, and neutron diffraction) can be extracted from a RXD experiment. We show that the polar domain configuration of BSMFO can be indirectly measured in an analogous way to measurements resolving the chiral domain structure of the zero field phase. We use this method to study the giant magnetoelectric effect observed in BSMFO and exploit the polarisation dependence of RXD to propose a microscopic mechanism for this effect [11]. Our results represent the first comprehensive RXD study of the functional phases of a Y-type hexaferrite, a tool which will likely prove invaluable to understanding the microscopic magnetoelectric effects of functional hexaferrites. We begin by summarising the magnetic structures of BSMFO,

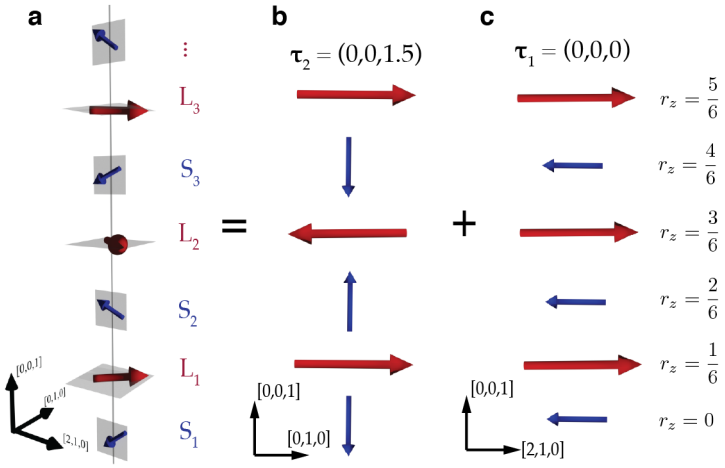


Figure 5.1: Canted 2-fan magnetic structure within the block model. **a,** The canted 2-fan magnetic structure where S spin blocks (blue) are labelled S_i and L spin blocks (red) are labelled L_j, following the convention of chapter 3. **b,c** Graphic demonstrating construction of canted 2-fan as a superposition of a commensurate cycloidal (b, $\vec{\tau}_2$) and a ferrimagnetic (c, $\vec{\tau}_1$) structure.

as relevant to this chapter, and review the magnetoelectric effects of interest.

Helical and canted 2-fan magnetic structures of $Ba_{0.5}Sr_{1.5}Mg_2Fe_{12}O_{22}$

In this section we recap the magnetic structures of BSMFO relevant to this chapter; a comprehensive description of these magnetic orders is presented in chapter 3.

As is standard in literature, we work under the magnetic block assumption [91]. In this model the structure is divided into a periodic series of magnetic blocks: L (large moment) and S (small moment) blocks. Within each block, Fe moments are assumed to be collinear and antiferromagnetically stacked along the [0,0,1] direction. Each magnetic block is then described by a single 'spin' (L_i or S_j) located at the block centre ($\vec{r}_{BC} = [0, 0, r_z]$, $r_z = \{0, \frac{1}{6}, \frac{2}{6}, \frac{3}{6}, \frac{4}{6}, \frac{5}{6}\}$) of magnitude equal to the net moment of the block ($3m_{Fe}$ for the L blocks and $1m_{Fe}$ for the S blocks). The full magnetic structure is then described by the set (L and S) of pseudo spins rather than the large number (42) of individual Fe sites; this construction is visualised in fig. 3.2.

In zero applied magnetic field and at temperatures below 100 K, BSMFO forms a longitudinal conical structure, where S and L blocks are helically modulated, with

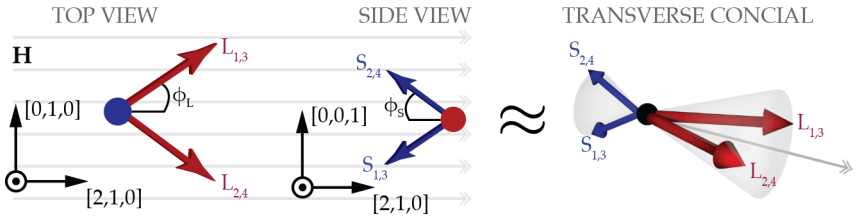


Figure 5.2: Transverse conical representation of the canted 2-fan. Left and centre panels shows projections the canted 2-fan structure in two planes (see fig. 5.1 for labelling convention of the spin blocks. $\phi_{L,S}$ denotes the fan angles of the blocks used in scattering calculations. Right panel: transverse conical representation of the magnetic structure, emphasising the cycloidal component of the structure. We will use this representation throughout as it makes transformations of the structure easier to visualise (i.e., compare to the extended structure in fig. 5.1 a).

a propagation vector equal to $\vec{\tau}_0 = (0, 0, \tau_z)$ where τ_z is temperature dependent and incommensurate, but features a small canting out of the (0,0,1) plane to form a net ferrimagnetic component (fig. 4.7 b).

Application of a magnetic field in this phase induces the (polar) canted 2-fan structure (fig. 5.1 a), which can be considered as a superposition of a ferrimagnetic structure (fig. 5.1 c) and a commensurate cycloidal structure (fig. 5.1 b), described by propagation vectors $\vec{\tau}_1 = (0, 0, 0)$ and $\vec{\tau}_2 = (0, 0, 1.5)$ respectively. Considering a magnetic field applied parallel to the [2,1,0] direction, L blocks lie exclusively in the (0,0,1) plane featuring a ferromagnetic alignment parallel to [2,1,0] (red spins in fig. 5.1 c) and an antiferromagnetic alignment of the spins parallel to [0,1,0] (red spins in fig. 5.1 b). S block moments, meanwhile, cant out of this plane featuring a ferromagnetic alignment anti-parallel to [2,1,0] (blue spins fig. 5.1 c) and an antiferromagnetic alignment of spins along [0,0,1] (blue spins in fig. 5.1 b). Considering the L and S block spins in unison, they are ferrimagnetically parallel to the [2,1,0] direction (i.e., fig. 5.1 c) and form a commensurate cycloid in the plane orthogonal to this direction (fig. 5.1 b).

It is common in literature to refer to the canted 2-fan structure as a commensurate transverse conical structure (see fig. 5.2) [76,77], as this emphasises the polar nature of the structure. Furthermore, this representation allows transformations of the structure (i.e., rotations) to be readily visualised, compared to considering a rotation

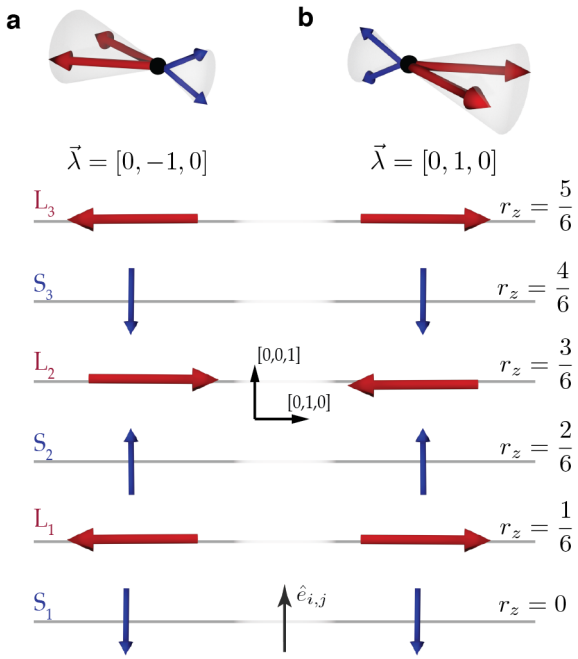


Figure 5.3: Magnetic polarity domains of the canted 2-fan structure. Projection of canted 2-fan structure in the plane perpendicular to applied magnetic field for each magnetic polarity domain, i.e., just the $\vec{\tau}_2 = (0, 0, 1.5)$ component of the structure. **a,** With $\vec{\lambda} = [0, -1, 0]$ and **b,** $\vec{\lambda} = [0, 1, 0]$. Red arrows represent L block spins and blue arrows S block spins.

of the extended structure.

Magnetic polarity and polarisation memory of $Ba_{0.5}Sr_{1.5}Mg_2Fe_{12}O_{22}$

The cycloidal component of the canted 2-fan structure can be characterised by an order parameter quadratic in the magnetic moment, $\vec{\lambda}$, known as the magnetic polarity, which defines both the sense and plane of rotation of the cycloid [129, 130]. Quantitatively, we define the magnetic polarity as,

$$\vec{\lambda} = \frac{\hat{e}_{i,j} \times (\vec{S}_i \times \vec{S}_j)}{|\vec{S}_i||\vec{S}_j|} \tag{5.1}$$

where $\vec{S}_{i,j}$ are the magnetic moments of adjacent spin (L, S) blocks and $\hat{e}_{i,j}$ is a unit vector parallel to the propagation vector of the commensurate cycloidal component ($\vec{\tau}_2$). The magnetic polarity for a canted 2-fan structure is shown in fig. 5.3, we observe (as apparent from eq. (5.1)) that $|\vec{\lambda}| = 1$ and can have two anti-parallel

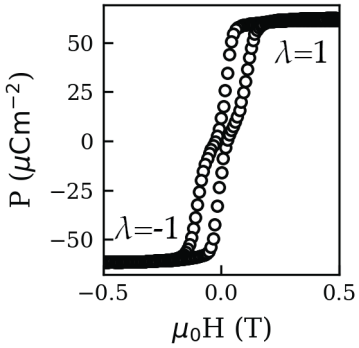


Figure 5.4: Electric polarisation of $Ba_{0.5}Sr_{1.5}Mg_2Fe_{12}O_{22}$ as a function of applied magnetic field. The electric polarisation is coupled to the sign of the applied magnetic field, such that the polarisation can be switched multiple times without any loss in magnitude, demonstrated in chapter 3.

configurations, $\vec{\lambda}$ = [0,-1,0] or $\vec{\lambda}$ = [0,1,0] (compare fig. 5.3 a and b). Magnetic polarity domains (breaking space inversion) are expected to form when entering the canted 2-fan state by magnetic field application as one undergoes a first order phase transition from the longitudinal conical state (i.e.,fig. 3.11 b).

Importantly, because $\vec{\lambda}$ breaks spatial inversion it can induce electric polarisation by a bilinear invariant coupling term in the free energy, $F \propto \vec{\lambda} \cdot \vec{P}$, such that to minimize the free energy of the system $\vec{P}$ and $\vec{\lambda}$ must be (anti) parallel. Visual inspection of eq. (5.1) shows this is equivalent ($\vec{P} \propto \vec{\lambda}$) to polarisation induced by the so called spin-current mechanism [25],

$$\vec{P} \propto \hat{e}_{i,j} \times (\vec{S}_i \times \vec{S}_j), \tag{5.2}$$

where $\vec{S}_{i,j}$ are the moments of adjacent magnetic sites and $\hat{e}_{i,j}$ the unit vector joining them. The defining characteristic of polarisation of spin-current origin is the orthogonal orientation of the polarisation with respect to the direction of propagation of the cycloidal magnetic structure.

In chapter 3 we measured the electric polarisation of the canted 2-fan phase, and here we summarise the key results (fig. 5.4). The electric polarisation in the canted 2-fan state is induced orthogonal to the applied magnetic field and can be reproducibly

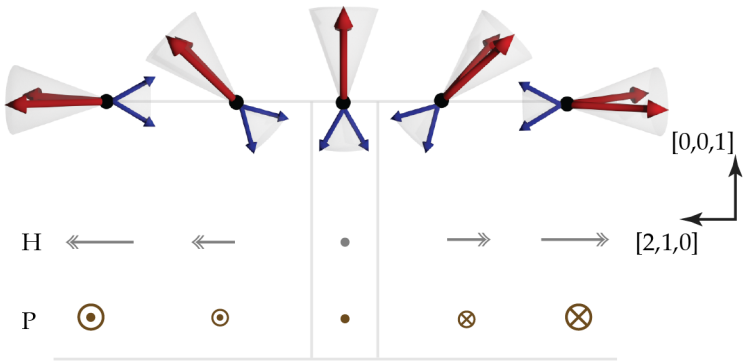


Figure 5.5: Zero field polarisation memory in $Ba_2Mg_2Fe_{12}O_{22}$. Mechanism of polarisation memory originally proposed by S. Ishiwata *et. al* to describe the polarisation memory in $Ba_2Mg_2Fe_{12}O_{22}$. The structure coherently rotates around the polarisation vector and information of the magnetic polarity of the field-induced phase is stored in the chirality of the longitudinal conical state in zero applied magnetic field. This structure subsequently rotates back to a 2-fan state with opposite magnetic polarity. After S. Ishiwata *et. al* [77].

switched ($\vec{P} \rightarrow -\vec{P}$) by inversion of the magnetic field. This magnetoelectric effect (magnetic field switching of $\vec{P}$) is the primary motivation for studying BSMFO as it represents the largest magnetoelectric effect to date and is rather unique: not all Y-type hexaferrites possess the property that $\vec{P}$ can be switched on inversion of the applied magnetic field without any 'memory' loss [11, 113].

A mechanism for the switching of the electric polarisation was first proposed by S. Ishiwata *et. al* by considering the effect that reducing the applied magnetic field has on the magnetic structure, outlined graphically in fig. 5.5 [77].[1] They proposed that the magnetic structure coherently rotates around [0,1,0] as the applied magnetic field is reduced, converting the magnetic polarity of the canted 2-fan structure to the *chirality* ($\sigma = \vec{\tau} \cdot (\vec{S}_i \times \vec{S}_j)$) of the zero field helical structure. In zero applied magnetic field the chiral domain structure is then expected to directly reflect the polarity domain structure of the field induced phase.

On subsequent application of a magnetic field anti-parallel to the initial field direction, the chirality is then converted back into a magnetic polarity by a coherent rotation of the magnetic structure, resulting in a reversal of $\vec{\lambda}$ (fig. 5.5): the switching

[1] This was originally proposed to explain the polarisation memory in BMFO, but we expect it to be relevant to BSMFO.

of $\vec{P}$ is driven by the reversal of $\vec{\lambda}$ as it can couple to magnetic field direction.

Despite the functional appeal of this magnetoelectric effect, there has been no study devoted to testing the mechanism of this memory, preferring instead to focus on optimizing the effect [11]. In this chapter, we show that circular asymmetry RXD is sensitive to the magnetic polarity of BSMFO and take advantage of this sensitivity to image the magnetic polarity domain structure of BSMFO as a function of applied magnetic field, confirming that $\vec{\lambda}$ switches on inversion of the magnetic field. Following this, we perform polarisation analysis of the scattered X-ray beam during the switching process and propose a new microscopic mechanism for the polarity reversal.

5.2 Experimental details

Resonant X-ray diffraction experiments were performed using the RASOR (Reflectivity and Advanced Scattering from Ordered Regimes) endstation installed on the I10 beamline at the Diamond Light Source, UK [131].

5.2.1 Sample environment

RASOR is a three circle diffractometer which is incorporated into a ultra-high vacuum (UHV) chamber, because soft X-rays are severely attenuated by air. The goniometer of the diffractometer provides full θ and 2θ motions and a small χ arc (orthogonal to the scattering plane) of $\pm$ 4°, used to compensate for sample misalignment. Samples are directly mounted onto the copper cold finger of a Janis SuperTran ST- 400 He flow cryostat, which can be translated $\pm$ 5 mm vertically and horizontally within the scattering plane and $\pm$ 20 mm orthogonal to this plane. The size of the incident X-ray beam can be controlled by a set of pin-hole apertures with dimensions of 10 µm, 20 µm or 50 µm. Coupled with the ability to translate the sample, these apertures allow the diffraction from the sample to be spatially

resolved.

The energy and polarisation of the incident X-ray beam is controlled by a pair of APPLE II undulators which can produce arbitrary linearly or circularly polarised incident X-rays between 500 and 1700 eV [132]. The undulators can be used in 'fast polarisation mode' where the incident polarisation state can be rapidly (10 Hz) switched between two states. We describe the polarisation state of X-rays in the $(\sigma - \pi)$ basis of orthogonal linear polarisation states, introduced in chapter 2 and visually represented in fig. 5.7. σ polarised X-rays are defined as being linearly polarised orthogonal to the scattering plane and π polarised X-rays within it.

The polarisation state of the diffracted beam can be analysed by performing a secondary scattering event on an analyser crystal and taking advantage of the polarisation dependence of Thomson scattering (see chapter 2): when scattering with $2\theta = 90°$ only X-rays polarised perpendicular to the scattering plane are transmitted. The scattering plane of the secondary scattering event can be rotated (denoted by η) to measure any arbitrary linear polarisation state of the scattered beam.

Reliable analysis of the polarisation state of the scattered beam requires an analyser crystal with a Bragg angle (θ, often referred to as the miscut angle θ_M) close to 45°. At hard X-ray energies, single crystals can be used, but there are no appropriate crystals with suitably large d-spacings for use as an analyser crystal at soft energies (i.e., 707 eV) and so multilayer materials must be used in reflection, where the d-spacing can be accurately tuned to scatter at $\theta \approx 45°$ at the required soft energy [133].

To test the analyser crystal used in this experiment we performed polarisation analysis of the direct X-ray beam with either σ or π polarised incident X-rays (fig. 5.6). The scattering plane of the analyser was rotated (η) about the X-ray beam and the measured scattering intensity fitted with the predicted intensity for each incident

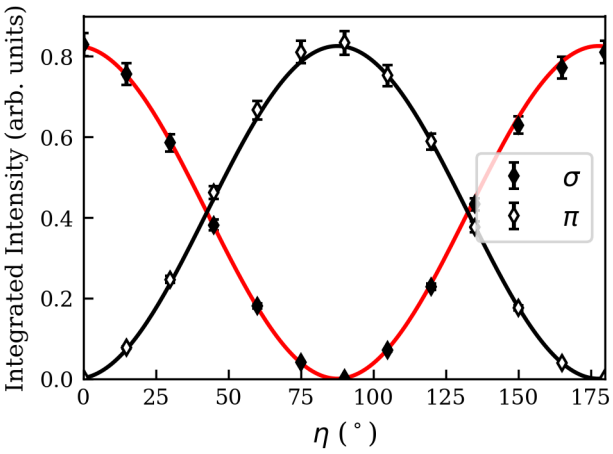


Figure 5.6: Polarisation analyser scan, measured on the main beam with incident X-rays of 707.48 eV. Data points are the integrated intensity of a rocking curve of the analyser crystal as a function of η, the analyser rotation angle about the diffracted beam. Solid points are with σ polarised incident X-rays and hollow ones with π incident. Solid lines are the refined theoretical intensities where only a global scale factor, θ_M and an analyser angle offset (η_0) are refined (see main text for details).

polarisation state (see appendix A for details),

$$I_\sigma = k(\cos^2(\eta + \eta_0) + \sin^2(\eta + \eta_0)\cos^2(2\theta_M)) \tag{5.3}$$

$$I_\pi = k(\sin^2(\eta + \eta_0) + \cos^2(\eta + \eta_0)\sin^2(2\theta_M)), \tag{5.4}$$

where k is a global constant, η the analyser angle, η_0 a zero offset of the η motor and θ_M the analyser miscut angle (nominally 45°). The measured scattering intensity and fits are shown in fig. 5.6. The refined miscut angle, θ_M, is 45.6 ±0.3° and the η_0 offset is 2.37±0.05°. The leak through of the analyser (i.e., measured signal with σ incident X-rays and the polarisation analyser set to measure in the π channel) is approximately 0.2%.

Our experiment required the application of magnetic fields, within the scattering plane, sufficient to stabilize the canted 2-fan phase (∼225 mT, as determined by our previous characterisation, see chapters 3 and 4) at temperatures between ∼25 K and 300 K. Furthermore, this environment must be stable for long durations (on the order of hours) to allow us to perform our scattering experiments. There was no specific solution for this in the RASOR diffractometer so we designed a bespoke

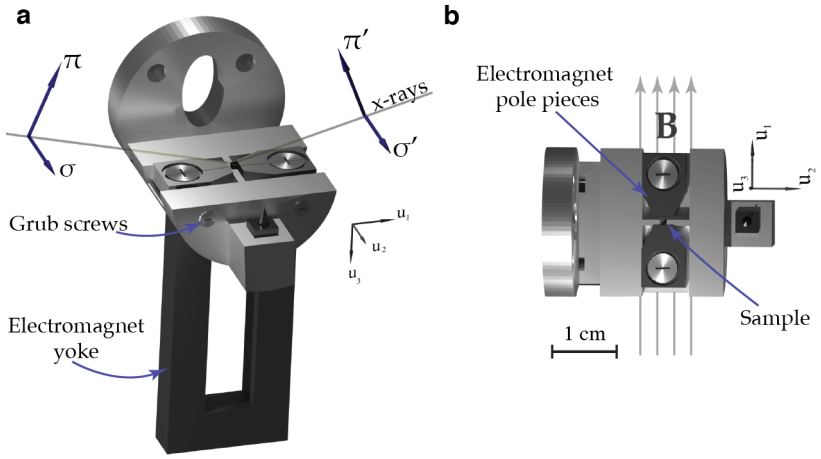


Figure 5.7: Design of RASOR electromagnet. **a,** Perspective view of scale model of electromagnet. It features an interchangeable yoke and pole pieces and a pin to assist with alignment. **b,** Orthographic projection of sample mounted on electromagnet, looking parallel to *c*. All features are to scale.

electromagnet for this experiment.[2]

The design of our electromagnet is displayed in fig. 5.7. The electromagnet is incorporated onto the RASOR sample stage which is directly connected to the cryostat cold finger. This is both for ease of construction and to allow for the electromagnetic windings to be cooled when operating at high current. The magnet features interchangeable, magnetically soft, iron pole pieces allowing the gap size of the electromagnet to be altered, to accommodate samples of different sizes. The minimum gap size is 1.2 mm. The pole pieces are connected to an iron yoke which is densely coiled with copper wires to allow control of the cores magnetisation by application of a current. The yoke (and therefore pole pieces) are fixed at a desired, sample-dependent height by a pair of grub screws (fig. 5.7). The magnetic field at the centre of the pole pieces was calibrated *ex-situ* to the diffraction chamber. Magnetic fields of approximately ± 300 mT could be achieved in the plane of the sample stage with an operating current of 1.5 A, exceeding the magnetic fields required by the design brief. The pole pieces can be removed from the sample mount such that measurements can be performed in true zero field.

[2]The magnet was designed by the author and constructed by M. Sussmuth.

5.2.2 Sample preparation

BSMFO single crystals were grown by the flux method, as previously discussed inchapter 3. Crystals were characterised by lab-based X-ray diffraction, magnetometry, and magnetocurrent measurements. A crystal with no visible impurities was chosen and mounted onto the sample stage with EPO-TEK H20E silver epoxy, which was subsequently cleaved in ambient conditions, yielding smooth c-surface normal faces. The cleaved sample was mounted into the diffraction chamber with the [2,1,0] direction anti-parallel to the incident beam direction ($\hat{U}_1$) and the [0,0,1] direction surface normal ($\hat{U}_3$), it was then pumped into UHV conditions.

5.2.3 Resonant X-ray diffraction

In this section, we calculate the resonant scattering amplitude for the incommensurate helical structure and the commensurate canted 2-fan magnetic structure of BSMFO within the block model.

This work closely follows Hill and McMorrow [52], but the interested reader may also find the following references of interest [41, 42, 50].

Considering only electric dipole transitions, the resonant scattering structure factor can be expressed in the $\sigma - \pi$ basis (see chapter 2 for details),

$$
\begin{aligned}
M^{RES}(\vec{Q}) &= \begin{pmatrix} M_{\sigma\sigma'} & M_{\pi\sigma'} \\ M_{\sigma\pi'} & M_{\pi\pi'} \end{pmatrix} \\
&\equiv \sum_n e^{i\vec{Q}\cdot\vec{r}_n} \Bigg\{ F^{(0)} \begin{pmatrix} 1 & 0 \\ 0 & \cos(2\theta) \end{pmatrix} \\
&+ iF^{(1)} \begin{pmatrix} 0 & m_1\cos(\theta) - m_3\sin(\theta) \\ -m_1\cos(\theta) - m_3\sin(\theta) & m_2\sin(2\theta) \end{pmatrix} \\
&+ F^{(2)} \begin{pmatrix} m_2^2 & -m_2(z_1\sin(\theta) - m_3\cos(\theta)) \\ m_2(m_1\sin(\theta) + m_3\cos(\theta)) & -\cos^2(\theta)(m_1^2\tan^2(\theta) + m_3^2) \end{pmatrix} \Bigg\},
\end{aligned}
\tag{5.5}
$$

where m_i are the components of the unit vector describing the magnetic moment of the n^{th} atom ($\hat{m}_n = [m_1, m_2, m_3]$), θ the Bragg angle of the scattering process and $F^{(j)}$ are (energy dependent) complex constants describing the strength of the resonant scattering process. These terms are referred to as '0^{th}','1^{st}' and '2^{nd}' order terms because (as we shall explicitly see) they give rise to n^{th} order magnetic satellites for an incommensurate magnetic structure. In this basis, diagonal elements of $M^{RES}(\vec{Q})$ represent scattering processes which do not rotate the polarisation state of scattered X-rays and off-diagonal elements are processes which rotate their plane of polarisation.

To calculate the scattering intensity of a magnetic structure we use the density matrix formalism, where for a given scattering vector, $\vec{Q}$, the scattering intensity is given by,

$$
I(\vec{Q}, \vec{P}, \eta) \propto Tr[D(\eta) \cdot M(\vec{Q}) \cdot \rho(\vec{P}) \cdot M(\vec{Q})^{\dagger}] \tag{5.6}
$$

where $D(\eta)$, $\rho(\vec{P})$ and $M(\vec{Q})$ are matrices describing the polarisation analyser, the incident beam polarisation and the resonant scattering amplitude. The individual

matrices are described in detail in appendix A. Further details on this formulism can be found in the following references [41, 134].

Circular asymmetry microdiffraction

The focus of this chapter is on employing circular asymmetry measurements, describing the difference in scattering for circular positive and negative incident polarised X-rays, to image the magnetic polarity domains of BSMFO as a function of applied magnetic field. Circular light can be expressed as the superposition of two orthogonal linear polarisation states, $\frac{\pi}{2}$ out-of-phase with each other. This allows us to express the scattering of circular light in the $\sigma - \pi$ basis of orthogonal linear polarisation states [72]. In this basis the density matrix describing the polarisation of circular light for a fully polarised beam is given by,

$$\rho_{+/-} = \frac{1}{2}\begin{pmatrix} 1 & \mp i \\ \pm i & 1 \end{pmatrix},$$

where $\rho_{+/-}$ denotes circular positive and negative incident X-rays respectively. We can calculate the diffraction intensity (eq. (5.6)) at any given $\vec{Q}$ under circularly polarised incident light,

$$\begin{aligned} I_{\pm} = \frac{1}{2}\big(&|M_{\sigma\sigma'}|^2 + |M_{\sigma\pi'}|^2 + |M_{\pi\sigma'}|^2 + |M_{\pi\pi'}|^2 \\ &\pm i[(M^*_{\sigma\pi'}M_{\pi\pi'} - M_{\sigma\pi'}M^*_{\pi\pi'}) + (M_{\pi\sigma'}M^*_{\sigma\sigma'} - M^*_{\pi\sigma'}M_{\sigma\sigma'})]\big), \end{aligned} \tag{5.7}$$

where $I_{\pm}$ denotes positive or negative circular incident X-rays respectively and M_{ij} are the components of the resonant scattering amplitude (eq. (5.5)). We assume no polarisation analysis of the scattered beam ($D(\eta) = \mathbb{1}$).

We then define the quantity, referred to as circular asymmetry,

$$\delta = \frac{I_+ - I_-}{I_+ + I_-}, \tag{5.8}$$

which can be determined experimentally by measuring a reflection with incident polarised light of both helicities ($I_\pm$). Alternatively, the circular asymmetry is sometimes defined as the ratio of the reflections intensity measured with either helicity, i.e., $\delta = \frac{I_+}{I_-}$ [123]. We preferentially use our definition as it naturally defines a bounded scale (it can only take values between ± 1), has a well defined zero and is independent of the relative scattering power of the probed region.

It is possible to express the predicted circular asymmetry in components of the magnetic scattering amplitude described in the basis of orthogonal linear polarisation states by using eqs. (5.7) and (5.8), assuming no post-scatter polarisation analysis,

$$\delta = \frac{-i[(M_{\sigma\sigma'}M^*_{\pi\sigma'} - M^*_{\sigma\sigma'}M_{\pi\sigma'}) + (M^*_{\pi\pi'}M_{\sigma\pi'} - M^*_{\sigma\pi'}M_{\pi\pi'})]}{|M_{\sigma\sigma'}|^2 + |M_{\sigma\pi'}|^2 + |M_{\pi\sigma'}|^2 + |M_{\pi\pi'}|^2}. \tag{5.9}$$

Visual inspection of eq. (5.9) can yield minimum requirements of the resonant scattering amplitude for a system to exhibit non-vanishing circular asymmetry: namely, $M^{RES}(\vec{Q})$ must contain both diagonal ($M_{\sigma\sigma'}$ or $M_{\pi\pi'}$) and off-diagonal elements ($M_{\sigma\pi'}$ and $M_{\pi\sigma'}$).

To spatially resolve the circular asymmetry of a reflection, we mask the incident X-ray beam with a 50 µm diameter aperture, set the diffractometer to the Bragg condition of the relevant reflection and measure its intensity as the X-ray beam is rastered (by translation of the sample in steps of 50 µm) across the sample. This procedure is performed for both positive and negative circularly incident polarised X-rays and the circular asymmetry (eq. (5.8)) is calculated at each position. The lateral resolution of this measurement is limited by the projection of the X-ray beam onto the sample surface, $\Delta \approx \frac{50}{\sin(\theta)}$, where θ is the Bragg angle of the relevant reflection. To maximize the spatial resolution of the measurement we measure the

circular asymmetry at the highest possible Bragg angle. For example, the beam footprint (assuming incident X-rays with energy equal to 707 eV) for scattering at the (0,0,1.5) and (0,0,4.5) reciprocal positions are approximately 165 µm and 55 µm respectively, we therefore focus our measurements on the (0,0,4.5) reflection.

In the next section, we will evaluate $M^{RES}(\vec{Q})$ for an incommensurate helix and a commensurate canted 2-fan structure, which can be used with the above formalism to calculate the expected circular asymmetry of each structure.

Resonant scattering from an incommensurate magnetic helix

Here we calculate the resonant scattering intensity of the zero field magnetic structure of BSMFO: an incommensurately modulated longitudinal conical structure, within the block approximation. We consider scattering arising only from the helical component of the structure (we are insensitive to the ferrimagnetic component) but the full calculations are outlined by J. Hill *et. al* [52]. Our calculations are performed within the block approximation (outlined in detail in chapter 3).

For a proper helix, with propagation vector $\vec{\tau} = (0, 0, \tau_z)$, the unit vector describing the magnetic moment of the n$^{\text{th}}$ atom is given by,

$$\hat{m}_n = \overbrace{\cos(\vec{\tau} \cdot \vec{r}_n + \phi_n)}^{m_1} \hat{\mathrm{U}}_1 + \overbrace{\gamma \sin(\vec{\tau} \cdot \vec{r}_n + \phi_n)}^{m_2} \hat{\mathrm{U}}_2 \tag{5.10}$$

described in the basis outlined in fig. 5.7, where $\vec{r}_n$ is the position of the n^{th} atom and ϕ_n a site specific phase, defined in chapter 3 for the block model. m_i highlights each component of the local magnetic moment (relevant for scattering calculations, eq. (5.5)). All moments lie in the $\hat{\mathrm{U}}_1\hat{\mathrm{U}}_2$ plane and propagate parallel to $\hat{\mathrm{U}}_3$ (this Cartesian basis is defined in fig. 5.7). The chirality (sense of rotation) of the magnetic structure is denoted by γ and is equal to ± 1.

Using eq. (5.5) we can write the $\sigma - \sigma'$ component of the structure factor as,

$$M_{\sigma\sigma'} = \sum_n e^{i\vec{Q}\cdot\vec{r}_n}(F^{(0)} + F^{(2)}m_2^2), \tag{5.11}$$

where we implicitly include both the Thompson and anomalous scattering in $F^{(0)}$ and sum over every atom in the crystal. Including the form of m_2 (eq. (5.10)) and expressing $\sin(\vec{\tau}\cdot\vec{r}_n + \phi_n)$ as the weighted sum of exponentials,

$$M_{\sigma\sigma'} = \sum_n (F^{(0)}e^{i\vec{Q}\cdot\vec{r}_n} - \frac{F^{(2)}}{4}(e^{i(\vec{Q}+2\vec{\tau})\cdot\vec{r}_n + i2\phi_n} + e^{i(\vec{Q}-2\vec{\tau})\cdot\vec{r}_n - i2\phi_n} - 2e^{i\vec{Q}\cdot\vec{r}_n})). \tag{5.12}$$

Next we can express the position of the n$^{\text{th}}$ atom as $\vec{r}_n = \vec{R}_n + \vec{d}_n$, where $\vec{R}_n$ is the position vector to the origin of the n^{th} unit cell and $\vec{d}_n$ the position of the atom with respect to the unit cell origin,

$$\begin{aligned} M_{\sigma\sigma'} = \sum_n \Big\{ & F^{(0)}e^{i\vec{Q}\cdot\vec{R}_n}e^{i\vec{Q}\cdot\vec{d}_n} \\ & - \frac{F^{(2)}}{4}\big(e^{i(\vec{Q}+2\vec{\tau})\cdot\vec{R}_n}e^{i(\vec{Q}+2\vec{\tau})\cdot\vec{d}_n}e^{i2\phi_n} \\ & + e^{i(\vec{Q}-2\vec{\tau})\cdot\vec{R}_n}e^{i(\vec{Q}-2\vec{\tau})\cdot\vec{d}_n}e^{-i2\phi_n} - 2e^{i\vec{Q}\cdot\vec{R}_n}e^{i\vec{Q}\cdot\vec{d}_n}\big)\Big\}. \end{aligned} \tag{5.13}$$

This expression will be non-vanishing only when $\vec{K}$ is discrete in exponentials of the form $e^{i\vec{K}\cdot\vec{R}_n}$, where $\vec{K} = \vec{Q}$ or $\vec{K} = \vec{Q} \pm 2\vec{\tau}$. This allows us to make the further simplification,

$$\begin{aligned} M_{\sigma\sigma'} = N\sum_n^{U.C} \Big\{ & (F^{(0)} - \frac{F^{(2)}}{2})e^{i\vec{Q}\cdot\vec{d}_n}\delta(\vec{Q} - \vec{G}) \\ & - \frac{F^{(2)}}{4}e^{i(\vec{Q}\pm 2\vec{\tau})\cdot\vec{d}_n \pm i2\phi_n}\delta(\vec{Q} - \vec{G} \pm 2\vec{\tau})\Big\}, \end{aligned} \tag{5.14}$$

where $\vec{G}$ is a reciprocal lattice vector ($\vec{G} = (0, 0, 3n)$ for our given experimental geometry) and the sum is now over a single unit cell only, N is the total number of unit cells in the scattering volume. This calculation shows that when scattering from a helical magnetic structure in the $\sigma - \sigma'$ channel, we expect to observe only 2$^{\text{nd}}$ order magnetic satellites (at positions $\vec{Q} \pm 2\vec{\tau}$), proportional to $|F^{(2)}|^2$, in addition to the Bragg scattering (dominated by the magnetisation independent, $F^{(0)}$, term).

We can use the same process to calculate the resonant dipole scattering amplitude for each linear polarisation channel,

$$\begin{aligned}
M_{\pi\sigma'} = N \sum_{n}^{U.C} \Bigg\{ & \frac{iF^{(1)} \cos\theta}{2} e^{i(\vec{Q}\pm\vec{\tau})\cdot\vec{d}_n \pm i\phi_n} \delta(\vec{Q} - \vec{G} \pm \vec{\tau}), \\
& - \frac{i\gamma F^{(2)} \sin(\theta)}{4} e^{i(\vec{Q}\pm 2\vec{\tau})\cdot\vec{d}_n \pm i2\phi_n} \delta(\vec{Q} - \vec{G} \pm 2\vec{\tau}) \Bigg\} \qquad (5.15) \\
M_{\sigma\pi'} = N \sum_{n}^{U.C} \Bigg\{ & \frac{-iF^{(1)} \cos\theta}{2} e^{i(\vec{Q}\pm\vec{\tau})\cdot\vec{d}_n \pm i\phi_n} \delta(\vec{Q} - \vec{G} \pm \vec{\tau}), \\
& + \frac{i\gamma F^{(2)} \sin(\theta)}{4} e^{i(\vec{Q}\pm 2\vec{\tau})\cdot\vec{d}_n \pm i2\phi_n} \delta(\vec{Q} - \vec{G} \pm 2\vec{\tau}) \Bigg\} \qquad (5.16) \\
M_{\pi\pi'} = N \sum_{n}^{U.C} \Bigg\{ & \Big(F^{(0)} \cos(2\theta) + \frac{F^{(2)}}{2} \cos^2(\theta) \tan^2(\theta)\Big) e^{i\vec{Q}\cdot\vec{d}_n} \delta(\vec{Q} - \vec{G}) \\
& \pm \frac{\gamma F^{(1)}}{2} e^{i(\vec{Q}\pm\vec{\tau})\cdot\vec{d}_n \pm i\phi_n} \sin(2\theta) \delta(\vec{Q} - \vec{G} \pm \vec{\tau}) \\
& - \frac{F^{(2)} \cos^2(\theta) \tan^2(\theta)}{4} e^{i(\vec{Q}\pm 2\vec{\tau})\cdot\vec{d}_n \pm i2\phi_n} \delta(\vec{Q} - \vec{G} \pm 2\tau) \Bigg\}. \qquad (5.17)
\end{aligned}$$

Clearly, $F^{(0)}$ terms only contribute to the Bragg reflections ($\vec{Q} = \vec{G}$), $F^{(1)}$ to first order magnetic satellites ($\vec{Q} = \vec{G} \pm \vec{\tau}$), and $F^{(2)}$ to second order satellites ($\vec{Q} = \vec{G} \pm 2\vec{\tau}$). Except for the contribution of the $F^{(2)}$ component to Bragg reflections in the $\sigma - \sigma'$ and $\pi - \pi'$ channels, there is no mixing of these terms in reciprocal space for a planar helix; for this reason $F^{(2)}$ terms can generally be ignored in the study of incommensurate structures [20, 135].

The expected intensity of each reflection can now be calculated through use of

eq. (5.6), for example in the $\pi - \pi'$ channel the intensity of the first order satellite, $\vec{Q} = \vec{G} + \vec{\tau}$, is given by,

$$I_{\pi\pi'} = \left| N \sum_{n}^{U.C} \frac{\gamma F^{(1)} \sin(2\theta) e^{i\vec{G}\cdot\vec{d}_n - i\phi_n}}{2} \right|^2. \tag{5.18}$$

We previously (eq. (5.9)) showed that the circular asymmetry of a given reflection can be expressed in terms of the resonant scattering amplitude in the basis of orthogonal linear polarisation states; we now use our calculated components ($M_{i,j}$) to calculate the predicted circular asymmetry, for the $\vec{Q} = (0, 0, 3)$ and $(0, 0, 3 \pm \tau)$ reflections of a magnetic helix.

For a planar helix the circular asymmetry of the (0,0,3) reflection is expected to be zero,

$$\delta_{(0,0,3)} = 0, \tag{5.19}$$

because there are no non-zero off-diagonal elements in the resonant scattering amplitude for $\vec{Q} = (0, 0, 3)$. Conversely, the circular asymmetry of the first order magnetic satellites is predicted to be of the form,

$$\delta_{(0,0,3\pm\tau)} = \frac{-2\gamma\zeta \sin(\theta)}{1 + 2\sin^2(\theta)}, \tag{5.20}$$

where $\gamma = \pm 1$ denotes the helix chirality and $\zeta = \pm 1$ the measured magnetic satellite ($\vec{Q} = \vec{G} \pm \vec{\tau}$). It is important to note that this asymmetry is valid for *any* planar helix (site specific phases vanish), is directly sensitive to the chirality (γ) of the helix and is opposite in sign for $\pm\tau$ satellites of a single reciprocal lattice point. This equation highlights the unique sensitivity of RXD to the chiral magnetic domain structure of helimagnets.

Resonant scattering from a commensurate canted 2-fan

Having calculated the resonant scattering intensity from the zero field structure of BSMFO we now discuss the resonant scattering from the field-induced canted 2-fan phase, which is commensurate with the crystal lattice. It is described by two propagation vectors, $\vec{\tau}_1 = (0, 0, 0)$ and $\vec{\tau}_2 = (0, 0, 1.5)$, and is displayed (within the block approximation) graphically in fig. 5.1. For a field applied along $\hat{\mathrm{U}}_1$, ignoring any anisotropy within the $\hat{\mathrm{U}}_1\hat{\mathrm{U}}_2$ plane, Fe sites located within the S blocks are described by,

$$\hat{m}_{S,n} = \overbrace{\nu_H \cos(\phi_S) e^{i\phi_{\pi,n}}}^{m_1} \hat{\mathrm{U}}_1 + \overbrace{\gamma_S \sin(\phi_S) \cos(\vec{\tau}_2 \cdot \vec{r}_n + \phi_n)}^{m_3} \hat{\mathrm{U}}_3, \tag{5.21}$$

and for sites within the L blocks,

$$\hat{m}_{L,n} = \overbrace{\nu_H \cos(\phi_L) e^{i\phi_{\pi,n}}}^{m_1} \hat{\mathrm{U}}_1 + \overbrace{\gamma_L \sin(\phi_L) \sin(\vec{\tau}_2 \cdot \vec{r}_n + \phi_n)}^{m_2} \hat{\mathrm{U}}_2, \tag{5.22}$$

where $\nu_H = \pm 1$ and defines the direction of the magnetic field (parallel or antiparallel to $\hat{\mathrm{U}}_1$) and $\gamma_{S,L} = \pm 1$ parametrises different magnetic polarity domains (i.e., compare fig. 5.3 a and b, for which $\gamma_S = 1$ for both, and $\gamma_L = 1$ and $\gamma_L = -1$ respectively). The magnetic polarity of the structure is equal to $\vec{\lambda} = \gamma_S\gamma_L[0, 1, 0]$. In the following the vector component of magnetic polarity is ignored, such that $\lambda = \gamma_S\gamma_L$.

In the same way as the incommensurate case we can now calculate the terms of the resonant scattering structure factor,

$$M_{\sigma\sigma'} = \sum_n F^{(0)} e^{i\vec{Q}\cdot\vec{d}_n}\delta(\vec{Q}-\vec{G}) + \sum_n^L \frac{-F^{(2)}\sin^2(\phi_L)}{4}\left(e^{i(\vec{Q}+2\vec{\tau}_2)\cdot\vec{d}_n+i2\phi_n} + e^{i(\vec{Q}-2\vec{\tau}_2)\cdot\vec{d}_n-i2\phi_n} - 2e^{i\vec{Q}\cdot\vec{d}_n}\right)\delta(\vec{Q}-\vec{G}), \tag{5.23}$$

$$\begin{aligned} M_{\pi\sigma'} = & -iF^{(1)}\left(\sum_n^L \nu_H\cos(\phi_L)e^{\vec{Q}\cdot\vec{d}_n+i\phi_{\pi,n}} + \sum_n^S \nu_H\cos(\phi_S)e^{\vec{Q}\cdot\vec{d}_n+i\phi_{\pi,n}}\right)\cos(\theta)\delta(\vec{Q}-\vec{G}), \\ & -\sum_n^S \frac{iF^{(1)}\gamma_S\sin(\phi_S)\sin(\theta)}{2}\left(e^{i(\vec{Q}+\vec{\tau}_2)\cdot\vec{d_n}+i\phi_n} + e^{i(\vec{Q}-\vec{\tau}_2)\cdot\vec{d_n}-i\phi_n}\right)\delta(\vec{Q}-\vec{G}\pm\vec{\tau}_2), \\ & -\sum_n^L \frac{iF^{(2)}\gamma_L\nu_H\cos(\phi_L)\sin(\phi_L)\sin(\theta)}{2}(e^{i(\vec{Q}+\vec{\tau}_2)\cdot\vec{d_n}+i(\phi_n+\phi_{\pi,n})} - e^{i(\vec{Q}-\vec{\tau}_2)\cdot\vec{d_n}-i(\phi_n-\phi_{\pi,n})})\delta(\vec{Q}-\vec{G}\pm\vec{\tau}_2), \end{aligned} \tag{5.24}$$

$$\begin{aligned} M_{\sigma\pi'} = & iF^{(1)}\left(\sum_n^L \nu_H\cos(\phi_L)e^{\vec{Q}\cdot\vec{d}_n+i\phi_{\pi,n}} + \sum_n^S \nu_H\cos(\phi_S)e^{\vec{Q}\cdot\vec{d}_n+i\phi_{\pi,n}}\right)\cos(\theta)\delta(\vec{Q}-\vec{G}), \\ & -\sum_n^S \frac{iF^{(1)}\gamma_S\sin(\phi_S)\sin(\theta)}{2}(e^{i(\vec{Q}+\vec{\tau}_2)\cdot\vec{d_n}+i\phi_n} + e^{i(\vec{Q}-\vec{\tau}_2)\cdot\vec{d}_n-i\phi_n})\delta(\vec{Q}-\vec{G}\pm\vec{\tau}_2)^* \\ & +\sum_n^L \frac{iF^{(2)}\gamma_L\nu_H\cos(\phi_L)\sin(\phi_L)\sin(\theta)}{2}(e^{i(\vec{Q}+\vec{\tau}_2)\cdot\vec{d_n}+i(\phi_n+\phi_{\pi,n})} - e^{i(\vec{Q}-\vec{\tau}_2)\cdot\vec{d}_n-i(\phi_n-\phi_{\pi,n})})\delta(\vec{Q}-\vec{G}\pm\vec{\tau}_2)^* \end{aligned} \tag{5.25}$$

$$\begin{aligned} M_{\pi\pi'} = & \left\{\sum_n F^{(0)}e^{i\vec{Q}\cdot\vec{d}_n}\cos(2\theta) - \sum_n^L \cos^2(\phi_L)e^{i\vec{Q}\cdot\vec{d}_n}F^{(2)}\tan^2(\theta)\cos^2(\theta)\right. \\ & \left. -\sum_n^S \cos^2(\phi_S)e^{i\vec{Q}\cdot\vec{d}_n}F^{(2)}\tan^2(\theta)\cos^2(\theta)\right\}\delta(\vec{Q}-\vec{G}) \\ & +\sum_n^S \frac{F^{(2)}\sin^2(\phi_S)}{2}(e^{i(\vec{Q}+2\vec{\tau})\cdot\vec{d}_n+i(\phi_n+\phi_{\pi,n})} + e^{i(\vec{Q}-2\vec{\tau})\cdot\vec{d}_n-i(\phi_n-\phi_{\pi,n})} + 2e^{i\vec{Q}\cdot\vec{d}_n})\cos(2\theta)\delta(\vec{Q}-\vec{G}) \\ & +\sum_L \frac{F^{(1)}\gamma_L\sin(\phi_L)}{2}(e^{i(\vec{Q}+\vec{\tau}_2)\cdot\vec{d}_n+i\phi_n} - e^{i(\vec{Q}-\vec{\tau}_2)\cdot\vec{d}_n-i\phi_n})\sin(2\theta)\delta(\vec{Q}-\vec{G}\pm\vec{\tau}_2) \end{aligned} \tag{5.26}$$

From visual inspection of the components of $M^{RES}(\vec{Q})$ we only expect to observe scattering at the $\vec{Q} = (0, 0, 3)$ and the $\vec{Q} = (0, 0, 3 \pm \vec{\tau}_2)$ reciprocal positions. Importantly, these calculations show that for a commensurate magnetic structure there is significantly more mixing of $F^{(1)}$ and $F^{(2)}$ terms at a given reciprocal position compared to the incommensurate case. Consider, for example, the $M_{\sigma\pi'}$ linear polarisation channel where both $F^{(1)}$ and $F^{(2)}$ terms (asterisks in eq. (5.26)) scatter to the same reciprocal position ($\delta(\vec{Q} \pm \vec{\tau}_2)$) as opposed to generating distinct first and second order satellites respectively. In general, including terms of $F^{(0)}$ or $F^{(1)}$ only, the $\vec{Q} = (0, 0, 3)$ will be sensitive to the ferrimagnetic ($\vec{\tau}_1 = (0, 0, 0)$) components of the magnetic structure and the $\vec{Q} = (0, 0, 3 \pm \vec{\tau}_2)$ to the cycloidal component ($\vec{\tau}_2 = (0, 0, 1.5)$) of the structure. $F^{(2)}$ terms are the smallest contribution and will add a small correction to both of these reflections.[3]

In an analogous way to the helical magnetic structure, we can calculate the circular asymmetry (eq. (5.9)) of the expected reflections of the canted 2-fan using the calculated components of $M^{RES}(\vec{Q})$. Firstly, for the $\vec{Q} = (0, 0, 3)$ reflection the circular asymmetry is of the form,

$$\delta_{(0,0,3)} \approx \frac{2\nu_H Re\big[iF^{(0)}F^{(1)*}\alpha_0 \cos(\theta)(\alpha_2^* \cos(\phi_L) + \alpha_3^* \cos(\phi_S))\big]}{|\alpha_0 F^{(0)}|^2} \tag{5.27}$$

where α_i are complex constants parametrising the relevant phase terms (summations) and are defined in appendix B, ν_H denotes the direction of the applied magnetic field with respect to $\hat{U}_1$, any anisotropy within the $\hat{U}_1\hat{U}_2$ plane is ignored, for our experiment ν_H equals to ± 1. ϕ_L and ϕ_S denote the fan angles of the L and S blocks respectively (fig. 5.2). All other terms take their previously defined definition. For clarity, we have ignored an additional term, $\propto \frac{\nu_H Re(iF^{(1)}F^{(2)*\cdots})}{2\alpha_0|F^{(0)}|^2(1+\cos(2\theta))}$, but it is

[3]This statement is not generally true for all materials and the impact of $F^{(2)}$ terms must be considered on a case-by-case basis.

a much smaller contribution and has the same qualitative features relevant to this thesis (i.e., linear in ν_H) and so can be considered a small correction. Additionally, only terms proportional to $|F^{(0)}|^2$ were included in the denominator as these dominate the scattering cross section. Unlike the helical case, eq. (5.27) shows that the (0,0,3) reflection in the canted 2-fan phase can exhibit circular asymmetry as a result of interference between scattering of charge ($\propto F^{(0)}$) and magnetic ($\propto F^{(1)}$) origin. Importantly, the circular asymmetry is expected to change sign ($\delta \to -\delta$) when the applied magnetic field is switched ($\nu_H \to -\nu_H$).

Secondly, we calculate the predicted circular asymmetry of the $\vec{Q} = (0, 0, 4.5)$ reflection,

$$\delta_{(0,0,4.5)} \approx \frac{-2\lambda Re\left[|F^{(1)}|^2 \sin(\phi_L)\sin(\phi_S)\sin(\theta)\sin(2\theta)\beta_1\beta_2^*\right]}{|F^{(1)}|^2(2\sin^2(\phi_S)\sin(\theta)|\beta_1|^2 + \sin^2(\phi_L)|\beta_2|^2)}, \tag{5.28}$$

where, again, β_i are complex constants parametrising the relevant phase terms (summations) and are defined in appendix B, λ is the previously defined magnetic polarity. We ignore an additional term $\propto \frac{\nu_H Re(iF^{(1)}F^{(2)*\cdots})}{|F^{(1)}|^{2\cdots}}$ as it will add a small correction and is independent of λ. Compared to eq. (5.27) we note that for the (0,0,4.5) reflection the asymmetry arises from purely magnetic scattering. It is sensitive to the magnetic polarity of BSMFO and to first order has no dependence on the applied magnetic field.

5.3 Results and discussion

5.3.1 Zero-field properties

The zero field phase of BSMFO was investigated by mounting the sample in the diffraction chamber in the absence of any magnetic field (electromagnet pole pieces

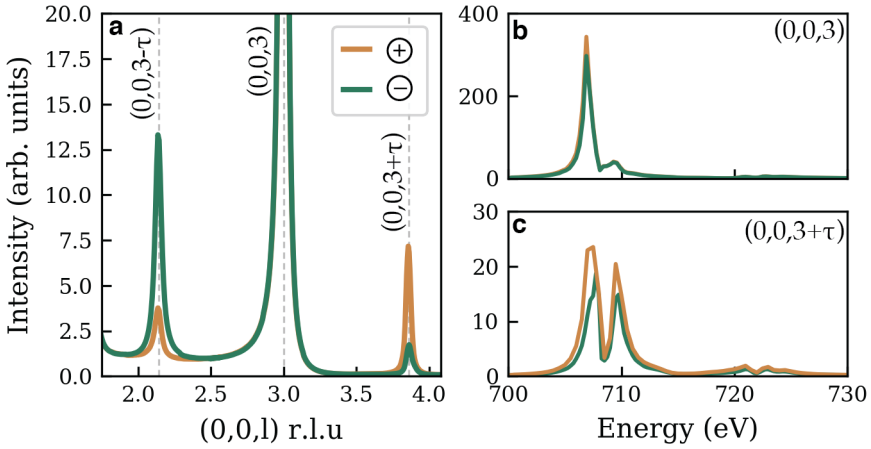


Figure 5.8: l-scan of sample and energy scans of each reflection in zero applied magnetic field. a, l-scan at arbitrary sample position with circular positive (solid green line) and circular negative (solid brown line) incident X-rays. **b-c** Energy scans (fixed $|\vec{Q}|$) on the, b, (0,0,3) reflection and, c, (0,0,3+τ) reflection. The propagation vector (τ) of the helix is ≈ 0.86. Energy scans are recorded with a larger incident beam size compared to the l-scan, their relative intensities cannot, therefore, be compared. Measurements were performed at 300 K.

removed). Scans along the (0,0,l) axis (l-scans) were performed by scanning the $2\theta/\theta$ motor in a specular configuration, changing only the *modulus* ($|\vec{Q}|$) of the scattering vector. The maximum l is limited (primarily by the long-wavelength incident X-rays, ~ 17.5 Å) to ~4.8 r.l.u.

Figure 5.8 displays a (0,0,l) scan performed at room temperature in zero applied magnetic field with circular positive (solid green line) and negative (solid brown line) incident X-rays. Three reflections are observed, a large reflection at the (0,0,3) reciprocal position and two neighbouring ones which index as (0,0,3$\pm\tau_z$) where $\tau_z \approx 0.86$ (see dashed grey lines in fig. 5.8 a). The (0,0,3) reflection exhibits no significant asymmetry under circular light ($I_+ \approx I_-$), whereas the (0,0,3$\pm\tau_z$) reflections exhibit large circular asymmetry, each of opposite sign. These neighbouring reflections can therefore be attributed to the first order magnetic satellites of the helical phase, exhibiting circular asymmetry as predicted by eq. (5.20). The intense central reflection at the (0,0,3) reciprocal position is predominately of charge origin and exhibits no appreciable circular asymmetry, as expected for an incommensurately modulated helical structure (eq. (5.19)).

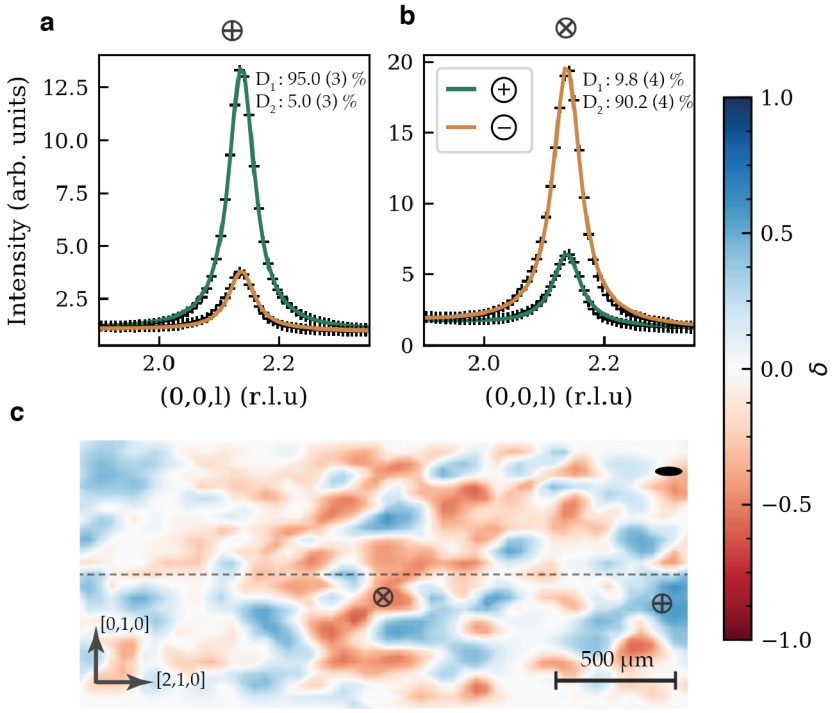


Figure 5.9: Chiral domain structure of the BSMFO single crystal measured in zero applied field at 300 K. a-b, l-scan about the (0,0,3-τ_z) reflection at two locations on the sample, denoted by crosses in c. Solid lines are refined intensities assuming a planar helix (described in section 5.2.3) where the illuminated chiral domain ratio (D_1/D_2 - inset text) is freely refined at each position. **c,** Spatially resolved circular asymmetry (color) of the (0,0,3-τ_z) satellite reflection, the solid black ellipse (top right) represents the spatial resolution of the measurement. The data has been smoothed to aid visualisation.

These (0,0,l) scans were performed with an incident X-ray energy of 707.48 eV, on resonance with the Fe L_3 absorption edge [136]. This energy was determined by performing an energy scan (constant $\vec{Q}$ as the incident X-ray energy is varied) over both the (0,0,3) and (0,0,3+τ_z) reflections, shown in fig. 5.8 b and c respectively. Both of these scans display a large, ∼100-fold, enhancement of the scattering intensity (in fact, 'off resonance' the (0,0,3+τ_z) reflection is not visible) at an energy of ∼707 eV. A smaller enhancement in the signal is also observed at approximately 722 eV, corresponding to the Fe L_2 absorption edge. Several of these scans were performed and an energy of 707.48 eV was found to give the largest average enhancement in the signal and was therefore used throughout the duration of the experiment.

The large circular asymmetry of the first order magnetic satellites (fig. 5.8 a) indicate that this measurement was performed in a region where the two chiral domains are unequally represented, if they occurred in equal proportion the circular asymmetry

would vanish. This suggests that the chiral domains have a sufficient mean area for a domain imbalance to be represented under the X-ray beam footprint (∼250 × 250 µm^2). To investigate the morphology of the chiral domain structure we spatially resolved the circular asymmetry (δ, defined in section 5.2.3) of the (0,0,3-τ_z) reflection over the extent of the sample, displayed in fig. 5.9 c, the lateral resolution (grey ellipse) is approximately 160 × 50 µm^2. Clear contrast in the measured circular asymmetry is observed on length scales (several hundred microns) larger than this resolution across the sample.

l-scans were then performed in two regions of opposite circular asymmetry (fig. 5.9 a and b) with either positive or negative circularly polarised incident X-rays. Each scan was fit with the theoretical scattering intensity for a helical magnetic structure (solid lines in fig. 5.9 a and b). The peak profile is approximated as a Lorentzian and the peak widths, centres and background are tied between scans performed at the same position. The intensity of the reflection is determined by a global scale factor, the ratio of the two chiral domains populations (D_1/D_2) and the predicted scattering amplitude for the helical structure (as determined by eq. (5.6)). The refined domain ratios: D_1: 95.0(3) %, D_2: 5.0(3) % in the first position and D_1: 9.8(4) %, D_2: 90.2(4) % in the second position, confirm that the observed contrast is fully consistent with the chiral domain structure of a planar helix; the slight deviation from a monodomain chiral state at each position can be attributed to either the X-ray beam sampling a neighbouring chiral domain or the presence of a domain boundary parallel to the surface normal of the sample.

Across the extent of the sample two chiral domains are approximately equally populated (46.7%, $\delta < 0$ and 53.4%, $\delta > 0$). The general morphology of the map features large perimeter, interconnected domains with a width typically no larger than 300 µm. The chiral domain structure of two single crystals of the isomorphic hexaferrite $Ba_{0.5}Sr_{1.5}Zn_2Fe_{12}O_{22}$, one with a freshly cleaved surface and the other with a comparitively rough surface, was previously imaged by Hiraoka *et. al* using a similar RXD technique [123, 127]. They observed that chiral domains in the cleaved crystal

were comparatively larger (on the order of 500 µm) than those in the 'rough' crystal. Furthermore, in the latter, chiral domains displayed a tendency to be clamped at defects, cracks and steps in the crystal [123]. Despite our sample being cleaved in ambient conditions, its domain morphology more closely reflects that of the 'rough' crystal studied by Hiraoka *et. al.* The surface of our sample features a series of sharp 'steps' which arise during the cleaving process and it is plausible that these features play a dominant role in controlling the domain structure of our sample [137].

It is worth noting that resonant X-ray diffraction, performed at soft energies, is sensitive only to the very surface of the sample (for hexaferrites the penetration depth of ∼700 eV X-rays is approximately 40nm [123]) and we must consider if our results represent the bulk of the sample. Since, the probed volume represents approximately 10 unit cells and the measured propagation vector of the helical phase is consistent with that measured by bulk-sensitive diffraction techniques (chapter 4) it is likely our results reflect the bulk properties of the sample.

Estimating $\frac{|F^{(1)}|}{|F^{(2)}|}$

As discussed in section 5.2.3 an incommensurate magnetic structure produces two magnetic satellites, the intensity of which is proportional to either $|F^{(1)}|^2$ or $|F^{(2)}|^2$. Therefore, by comparison of the two reflections intensities we can estimate the relative magnitudes of these two constants [52]. Using our previously computed values of the resonant scattering amplitude the intensity of first and second order satellites for σ-incident X-rays, with no polarisation analysis of the scattered X-ray beam are given by,

$$I_{\vec{\tau}} = \frac{|F^{(1)}|^2 \cos^2(\theta_1)(\sum_n e^{i(\vec{Q}\pm\vec{\tau})\cdot\vec{d}_n \pm i\phi_n})^2}{4} \tag{5.29}$$

$$I_{2\vec{\tau}} = \frac{|F^{(2)}|^2 (1+\sin^2(\theta_2))(\sum_n e^{i(\vec{Q}\pm 2\vec{\tau})\cdot\vec{d}_n \pm i2\phi_n})^2}{16}, \tag{5.30}$$

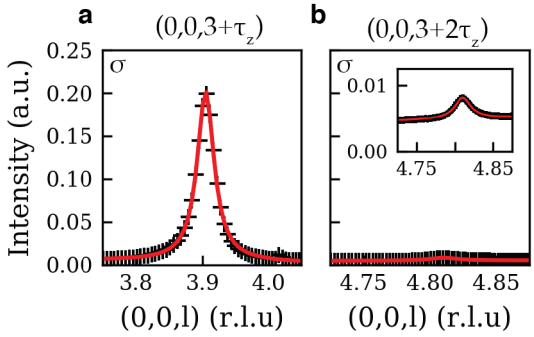


Figure 5.10: l-scans of the 1st and 2nd order magnetic satellite reflections with σ incident light. a, Over the $(0, 0, 3+\tau_z)$ reflection and **b,** the $(0, 0, 3+2\tau_z)$. Inset shows the same reflection but on a zoomed y-scale. Solid red lines are Lorentzian fits to the data. Measurements were performed at 300 K in the absence of an applied magnetic field.

which performing the summations gives,

$$\frac{|F^{(1)}|}{|F^{(2)}|} \approx 0.935\sqrt{\frac{I_{\vec{\tau}}}{I_{2\vec{\tau}}}}. \tag{5.31}$$

Figure 5.10 displays l-scans in the vicinity of the $(0, 0, 3 + \tau_z)$ and $(0, 0, 3 + 2\tau_z)$ reflection. As well as the 1st order reflection (fig. 5.10 a), we also observe the 2nd (fig. 5.10 b) order reflection, with a significantly weaker intensity. Inputting the integrated intensity of both reflections (obtained by fitting Lorentzian profiles to each reflection) into eq. (5.31) we find that $\frac{|F^{(1)}|}{|F^{(2)}|} \approx 5.5$, putting an upper bound on the value of $|F^{(2)}|$ with respect to $|F^{(1)}|$.

5.3.2 Field induced phases

Having investigated the chiral domain structure of the zero field phase of BSMFO we now discuss the circular asymmetry (δ) of each reflection observed in the polar (magnetic field-induced) canted 2-fan phase. While the zero field phases of the Y-type hexaferrites have been extensively studied by resonant X-ray microdiffraction [20, 123, 127, 128, 135], there has been little study of their field induced counterparts.

We begin by discussing the observed scattering intensity under linearly polarised incident X-rays, which will prove essential in interpreting the circular asymmetry

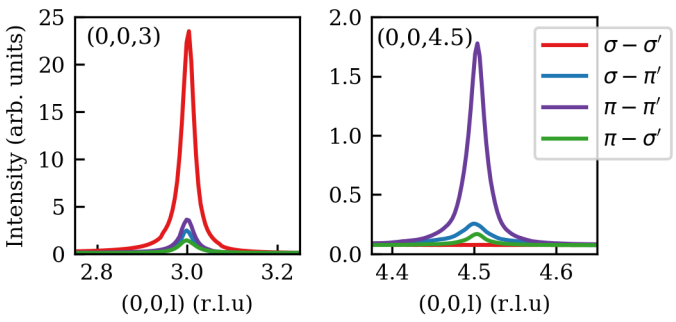


Figure 5.11: l-scans, at 40 K, of each observed reflection in the field induced phase. A magnetic field of 250 mT was applied parallel to the [2,1,0] direction. Colour represents the reflection measured in each linear polarisation channel (see inset legend) for the, **a**, the (0,0,3) and, **b**, (0,0,4.5) reflections. This measurement (by the lack of scattering in the $\sigma - \sigma'$ channel) confirms the purely magnetic origin of the scattering at the (0,0,4.5) position.

of each observed reflection of the canted 2-fan structure. We then discuss circular asymmetry of each reflection, highlighting the parameters of the magnetic structure it is sensitive too, and conclude by investigating the magnetoelectric effect observed in BSMFO: the complete reversal of its electric polarisation by inversion of the applied magnetic field [11, 80].

Phase characterisation

The sample was mounted in the diffraction chamber orientated as previously described in section 5.3.1 but with the addition of the electromagnet to the sample stage. The sample was cooled, in zero applied magnetic field, to ∼40 K at which a magnetic field of 250 mT was applied to the sample parallel to the [2,1,0] direction. Our previous characterisation of BSMFO (chapters 3 and 4) has shown that this field is sufficient to fully stabilize the canted 2-fan magnetic structure.

At 250 mT only three reflections are accessible within the (severely restricted) Ewald sphere: the (0,0,1.5), (0,0,3) and the (0,0,4.5) reflections. In the following we discuss only the (0,0,3) and (0,0,4.5) reflections, which are sufficient to encompass each component of the canted 2-fan structure [91].

Figure 5.11 displays l-scans over the (0,0,3) and (0,0,4.5) reciprocal lattice positions

in each of the four linear polarisation channels. At the (0,0,3) position (fig. 5.11 a) the dominant scattering process is clearly of charge-origin, scattering most intensely in the $\sigma - \sigma'$ channel. However, weak intensity in both the rotated channels ($\sigma - \pi'$ and $\pi - \sigma'$) confirm the presence of magnetic scattering at this location, this is the only scattering process which can rotate the polarisation of incident X-rays.

Conversely, for the (0,0,4.5) reflection (fig. 5.11 b) the largest scattering intensity is in the $\pi - \pi'$ channel. Intensity is observed in every other channel *except* for the $\sigma - \sigma'$ channel. Importantly, the lack of any appreciable scattering in this polarisation channel demonstrates that this reflection is of *pure magnetic origin* and its properties must, therefore, be linked entirely to the magnetic structure of BSMFO.

The importance of this classification becomes apparent when considering that there is a precedent for the commensurate reflections of the Y-type hexaferrites to be attributed to mixed charge and magnetic scattering [128]. The (0,0,4.5) reflection in $Ba_{1.3}Sr_{0.7}CoZnFe_{11}AlO_{22}$ (arising because of the alternating longitudinal structure, not discussed in this thesis [128]) was found to exhibit non-zero circular asymmetry (δ) - it was proposed (despite not being supported with polarisation analysis of scattered X-rays) that this asymmetry arises as a result of interference between charge and magnetic scattering. For the (0,0,4.5) of BSMFO, this clearly cannot be the case.

Circular asymmetry measurements

Having discussed the qualitative nature of the scattering in each linear polarisation channel we now discuss, in analogy to section 5.3.1, the properties of these reflections under circularly polarised incident X-rays. Figure 5.12 a and d, display the spatially resolved circular asymmetry (δ) of the (0,0,3) and (0,0,4.5) reflections in a magnetic field of -250 mT at 40 K. Converse to the zero field situation, the (0,0,3) reflection (fig. 5.12 a) displays a large, spatially uniform asymmetry, approximately equal to

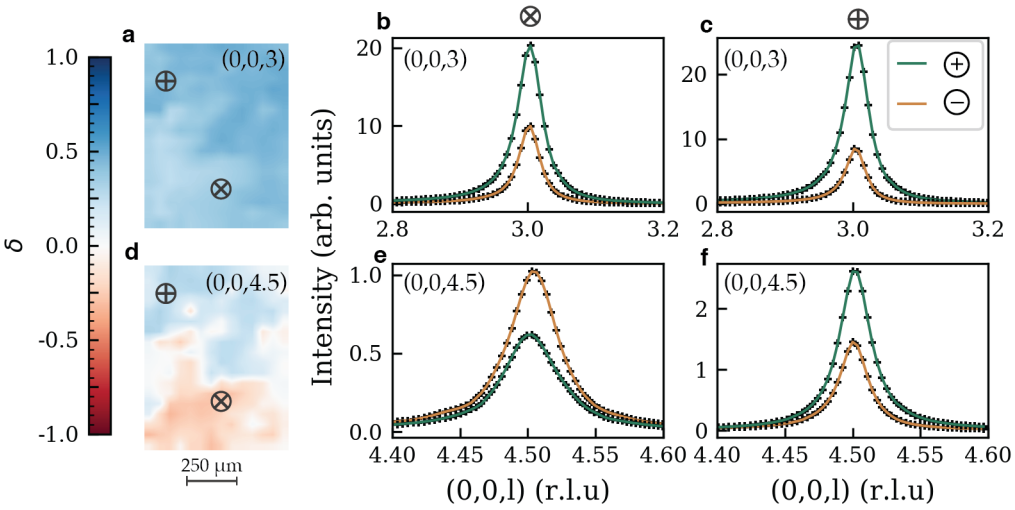


Figure 5.12: Circular asymmetry measurements on the two observed reflections in the canted 2-fan phase at 40 K with μ_0H = -250 mT. a-c, The (0,0,3) reflection and **d-f,** the (0,0,4.5) reflection. a and d are the spatially resolved circular asymmetry maps of the (0,0,3) and (0,0,4.5) reflections respectively, colour represents the measured local asymmetry (left hand colour bar). The two positions on the sample are indicated by crosses and the respective measurements are shown in each column (b,e and c,f). Solid green lines represents circular positive incident X-rays and solid brown line circular negative incident X-rays.

$\delta = 0.39 \pm 0.07$ (where the error denotes the standard deviation of the asymmetry measured across the sample). Conversely, the (0,0,4.5) reflection (fig. 5.12 d) displays two regions of distinct circular asymmetry with equal magnitude ($\delta \approx 0.15$) but opposite in sign. To confirm these observations, we performed l-scans in each of these regions (crosses in panels b,c and e,g of fig. 5.12) with a 50 μm incident beam. They confirm that the (0,0,3) exhibits large, spatially homogeneous circular asymmetry ($I_+ > I_-$, fig. 5.12 b,c) and the circular asymmetry of the (0,0,4.5) reflection is opposite in sign between the two positions (positions with both $I_+ > I_-$ or $I_+ < I_-$ are observed).

Physically, the circular asymmetry on each reflection can be understood considering the magnetic structure of the canted 2-fan structure and with reference to our previous polarisation analysis (see fig. 5.11). Scattering at the (0,0,3) reciprocal point has contributions both from charge ($M_{\sigma\sigma'}$ and $M_{\pi\pi'}$) and magnetic origin ($M_{\sigma\pi'}$ and $M_{\pi\sigma'}$) which under circularly polarised incident X-rays can interfere as described by eq. (5.27), resulting in a non-zero circular asymmetry.

Qualitatively, the circular asymmetry on the (0,0,3) reflection is sensitive to the projection of $\vec{\tau} = (0, 0, 0)$ (ferrimagnetic) components of the magnetic structure into the scattering plane and is expected to change sign on inversion of the applied magnetic field ($\nu_H = 1 \rightarrow -1$ in eq. (5.27)). Its sensitivity to the projection of the structure into the scattering plane means it could, for example, be used to measure the ferrimagnetic domain structure of BSMFO at high temperatures. In fact, interference between scattering of charge and magnetic origin has previously been used to image the ferrimagnetic domain structure of $HoFe_2$. On resonance with the Ho L_3 absorption edge ($\sim$ 8 keV) the spatially resolved circular asymmetry of the (0,0,4) reflection[4] demonstrated contrast, with a morphology that was consistent with the crystals ferrimagnetic domain structure measured with MFM [138].

Having previously confirmed the absence of charge scattering at the (0,0,4.5) reciprocal point (fig. 5.11), the circular asymmetry of this reflection cannot arise from the same mechanism and must have purely magnetic origin. From inspection of eq. (5.9) we can see that the minimum condition for circular asymmetry of magnetic origin is two orthogonal ($\vec{\tau} = (0, 0, 1.5)$) components, one of which is parallel to $\hat{U}_2$, π out-of-phase with each other (in the canted 2-fan structure this is parallel to $\hat{U}_3$). Thus, in an analogous way to a helical structure, the *cycloidal component* of the 2-fan structure (fig. 5.1 b) can exhibit circular asymmetry. Our calculations (eq. (5.28)) showed this to be the case: the circular asymmetry of the (0,0,4.5) reflection is proportional to the structures magnetic polarity (λ) and, in a way analogous to the incommensurate helical reflections, the (0,0,4.5) reflection is sensitive to the 'sense-of-rotation' of the magnetic structure. Therefore, the observed contrast in fig. 5.12 d must arise because of regions of opposite magnetic polarity ($\lambda = \pm 1$). Furthermore, in the spin-current model of magnetically induced polarisation, $\vec{\lambda}$ is directly coupled to the direction of electric polarisation ($\vec{P}$), such that these regions of contrast also represent *polar* domains. Because no electrical bias was applied to the sample, an equal number of polar domains are expected, as reflected in the

[4]The (0,0,4) reflection in $HoFe_2$ has both charge and magnetic contributions.

observed distribution (fig. 5.12).

5.3.3 Magnetic polarity memory

Unlike the (0,0,3) reflection, the predicted circular asymmetry of the (0,0,4.5) reflection does not explicitly depend on the direction of the applied magnetic field (eq. (5.28)). However, if the domains observed in fig. 5.12 are a consequence of the regions of distinct magnetic polarity we predict that they must change sign on inversion of the applied magnetic field, because the electric polarisation (proportional to $\vec{\lambda}$) of our BSMFO samples switches (fig. 5.4) when the applied magnetic field is inverted.

Figure 5.13 shows the spatially resolved circular asymmetry of each observed reflection at key fields as the applied magnetic field is switched. Initially, the sample was zero field cooled to 40 K and the chiral domain structure of the helical phase mapped (fig. 5.13 e), in this virgin state the (0,0,3) reflection exhibited no circular asymmetry (fig. 5.13 a). Following this, a -250 mT was applied and the circular asymmetry of the canted 2-fan reflections were spatially resolved, the results of which being previously discussed in fig. 5.12: the (0,0,3) reflection exhibits spatially homogeneous circular asymmetry and the (0,0,4.5) reflection displays two regions of contrast, equal in magnitude.

On returning to zero applied magnetic field (fig. 5.13 c,g,k), the system enters into a mixed helix / 2-fan state (previously discussed in chapter 4). The (0,0,3) exhibits weak circular asymmetry and the incommensurate helical reflection displays circular asymmetry (fig. 5.13 g), but with no apparent spatial correlation to either the ZFC helical state (fig. 5.13 e) or to the magnetic polarity domains formed on field application (fig. 5.13 j). The magnetic polarity domains themselves (fig. 5.13 k) appear to have changed in some regions, but not in others.

Finally, a 250 mT magnetic field was applied, where the incommensurate reflection again vanishes, leaving just the (0,0,3) and (0,0,4.5) reflections (fig. 5.13 d,h,l). In

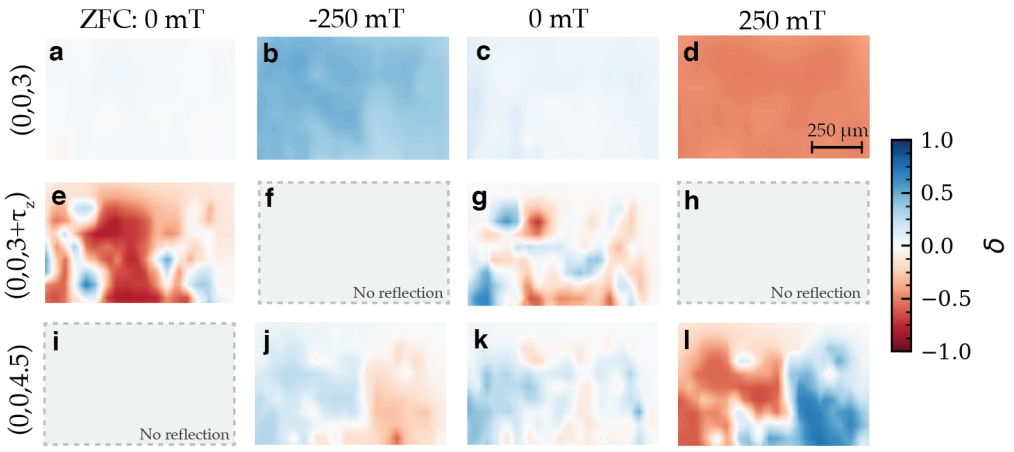


Figure 5.13: Spatially resolved circular asymmetry as function of applied magnetic field. a-d, Circular asymmetry (δ) of the (0,0,3) reflection, **e-h,** the incommensurate helical reflection and **i-l,** the (0,0,4.5) reflection. The incommensurate helical reflection only exists in a narrow low-field region and is severely broadened after magnetic field application. These maps have been arbitrarily rotated relative to fig. 5.12. All maps share a common color scale (far right) and are over the same area of the sample. Maps were only performed when a reflection was visible.

this state, the circular asymmetry of the (0,0,3) has changed sign (as predicted by eq. (5.27)) confirming that interference between charge and magnetic scattering is indeed the origin of its circular asymmetry. The circular asymmetry of the (0,0,4.5) has also changed sign on a *pixel-by-pixel* basis: the local magnetic polarity has switched sign - consistent with our observation of the coupled nature of $\vec{P}$ and the applied magnetic field (fig. 5.4).

These results represent the first measurement of magnetic polarity domains in a Y-type hexaferrite and confirm that the magnetic polarity is coupled to the applied magnetic field. Interestingly the results do not agree with the currently proposed mechanism (see fig. 5.5) explaining this reversal. In this model, proposed by S. Ishiwata *et. al* [77], there must be a direct correlation between the high field magnetic polarity domain structure and the zero field chiral one, this is not apparent from our results (i.e., compare fig. 5.13 e and j). Therefore, the helical regions of the sample likely play only a passive role in the polarity switching process. The lack of agreement with this model means that we must further investigate the mechanism for the magnetic polarity reversal.

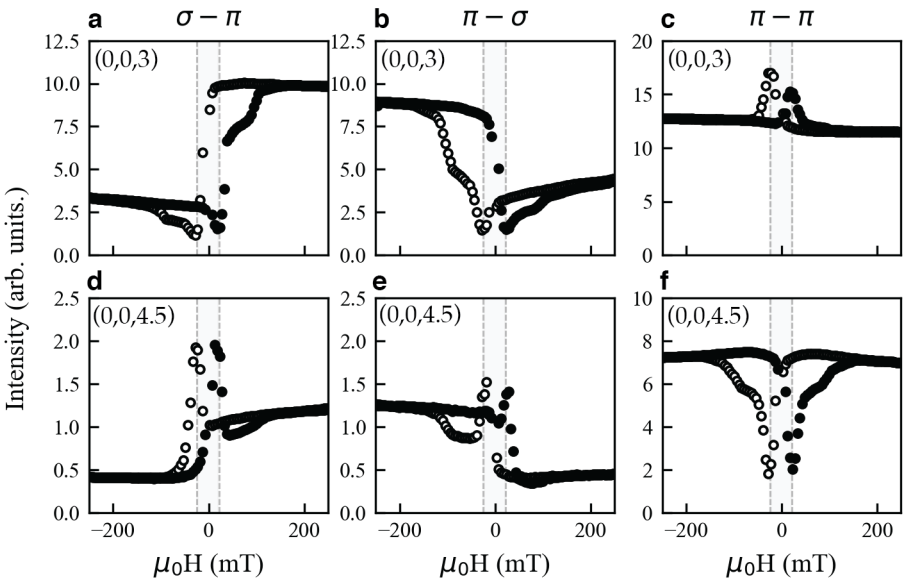


Figure 5.14: Measured intensity in each linear polarisation channel as the applied magnetic field is rapidly changed. a-c, for the (0,0,3) reflection. **d-f,** for the (0,0,4.5) reflection. Each data set is the average of five independent field sweeps highlighting the reproducibility of the data. The field was swept at 6.25 mT s^{-1}. Hollow circles display decreasing field sweeps and solid circles increasing sweeps. Dashed grey lines highlight features associated with the magnetic polarity switching and are at the same field position for all channels.

Mechanism of magnetic polarity reversal

In this section, the mechanism of magnetic polarity switching is investigated by measuring the scattering intensity of the (0,0,3) and (0,0,4.5) reflections in a given linear polarisation channel while rapidly sweeping the applied magnetic field. Such dynamic polarisation analysis allows us to track how orthogonal components of the magnetic structure (as given by the elements of the resonant scattering amplitude, eq. (5.5)) evolve as the magnetic field is inverted.

A 250 mT magnetic field was applied parallel to [2,1,0] at 40 K and the diffractometer was set to the relevant Bragg condition and polarisation channel. A large incident X-ray beam (∼200 × 100 µm^2) was used for these measurements. The reflection intensity was *continuously* monitored as the magnetic field was swept to -250 mT and subsequently back to 250 mT at 6.25 mT s^{-1}. This process was repeated multiple times for each polarisation channel and averaged, the results of which are displayed in fig. 5.14.

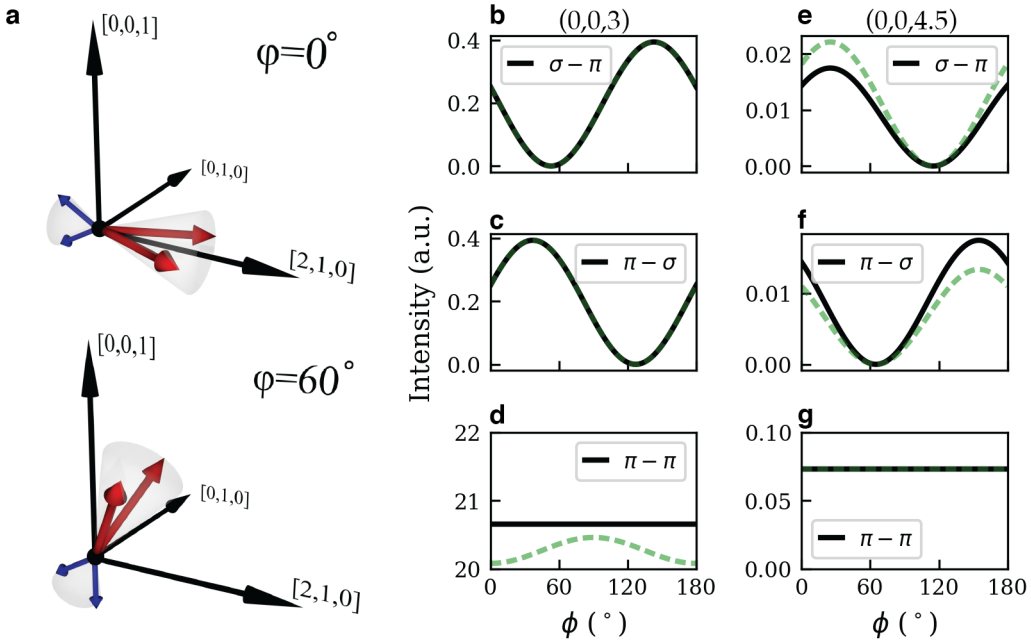


Figure 5.15: Simulated scattering intensity for a canted 2-fan as it is rotated about [0,1,0] direction. a, Graphic outlining the transformation, red arrows represent L spin blocks and blue S spin blocks. **b-d,** Predicted scattering intensity of the (0,0,3) reflection for the $\sigma - \pi'$, $\pi - \sigma'$ and $\pi - \pi'$ channels respectively as the magnetic structure is rotated. **e-g,** Predicted scattering intensity of the (0,0,4.5) reflection for the $\sigma - \pi'$, $\pi - \sigma'$ and $\pi - \pi'$ channels respectively as the magnetic structure is rotated. ϕ parametrises the rotation and is measured between [2,1,0] and the axis of the 'cone'. Solid lines are calculations including $F^{(0)}$ and $F^{(1)}$ terms only and dashed green lines are calculations including $F^{(2)}$ additionally, assuming the upper bound value of $|F^{(2)}| = \frac{1}{6}|F^{(1)}|$.

In the high field limit ($|\mu_0 H| > 100$ mT) the scattering intensity is approximately independent of the applied magnetic field, although the measured intensity is different for anti-parallel magnetic fields of equal magnitude. In the low field limit, where the magnetic polarity switching must occur, we see transient increases in the scattering intensity in some polarisation channels (dashed grey lines in fig. 5.14 c,d,e) and decreases in others (dashed grey lines in fig. 5.14 a,b,f), all of which are coincident in magnetic field (~23 mT). Notably, for scans (not shown) performed in discrete field steps (sweep rate ~0.1 mT s^{-1}) these features are significantly less prominent and are, therefore, associated with the *dynamic* polarity switching of the magnetic structure.

To test the switching process of $\vec{\lambda}$, we calculate the scattering intensity of the canted 2-fan structure under various transformations which invert the magnetic polarity

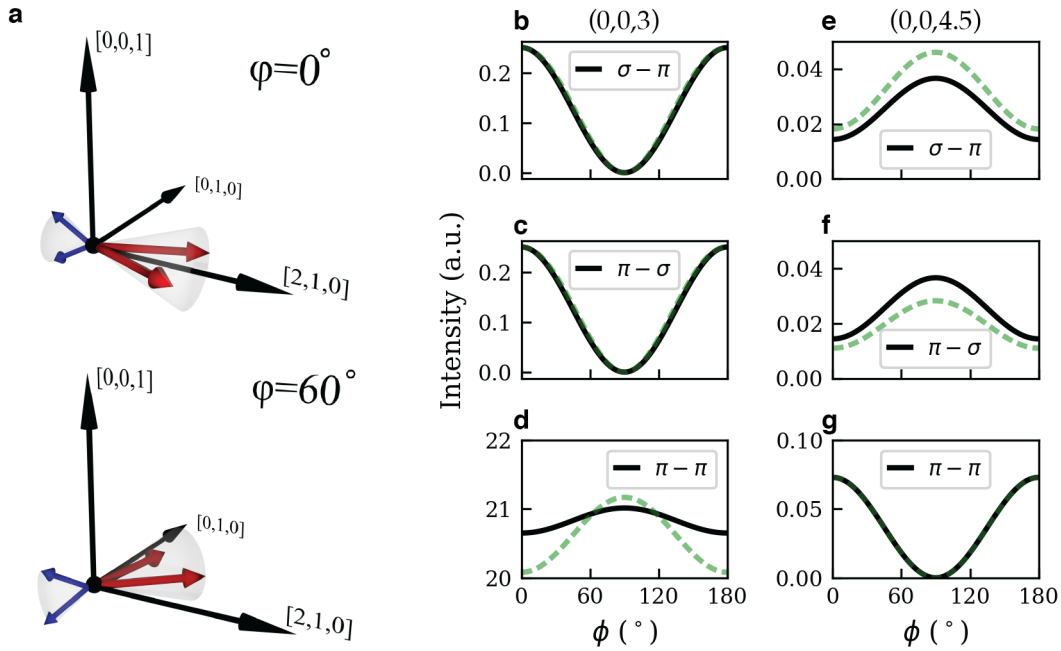


Figure 5.16: Simulated scattering intensity for a canted 2-fan as it is rotated about the [0,0,1] direction. a, Graphic outlining the transformation, red arrows represent L spin blocks and blue S spin blocks. **b-d,** Predicted scattering intensity of the (0,0,3) reflection for the $\sigma - \pi'$,$\pi - \sigma'$ and $\pi - \pi'$ channels respectively as the magnetic structure is rotated. **e-g,** Predicted scattering intensity of the (0,0,4.5) reflection for the $\sigma - \pi'$,$\pi - \sigma'$ and $\pi - \pi'$ channels respectively as the magnetic structure is rotated. ϕ parametrises the rotation and is measured between [2,1,0] and the axis of the 'cone'. Solid lines are calculations including $F^{(0)}$ and $F^{(1)}$ terms only and dashed green lines are calculations including additional $F^{(2)}$ terms, assuming the upper bound value of $|F^{(2)}| = \frac{1}{6}|F^{(1)}|$.

and qualitatively compare their features to the low-field regions of fig. 5.14. Firstly, we consider the predicted scattering intensity as the structure is coherently rotated about the [0,1,0] direction as explained by S. Ishiwata *et. al* - see fig. 5.15 [77]. In these calculations $\phi = 0° \rightarrow \phi = 180°$ corresponds to complete reversal of the magnetic structure and refers to the high field limit of our data ($|\mu_0 H| > 100$ mT), above which we assume the magnetic structure is invariant to the magnetic field [20]. We assume $\phi_L = \phi_S = 45°$ and $|F^{(0)}| = 1$, $|F^{(1)}| = 0.2$ and $|F^{(2)}| = 0.0333$, where $|F^{(2)}|$ is an approximate upper bound. These were chosen as they qualitatively reflect the data but we remark that changing these parameters does not effect the results of this discussion, being essentially scaling factors between different processes/channels.

The results of these calculations (fig. 5.15) demonstrate a distinctive dependence of

the scattering intensity as the structure is rotated. They show that while inclusion of $F^{(2)}$ (dashed green lines) terms could have an observable effect they are not (as expected) the dominate process and generally only add a small correction to the scattering. Furthermore, as the value of $|F^{(2)}|$ used in these calculations represents an upper bound, the relevant contributions could be even smaller. Thus, in the following, we primarily discuss $F^{(0)}$ and $F^{(1)}$ terms in the scattering, with reference to $F^{(2)}$ terms where relevant.

The calculations show little correlation with the low-field switching regions of our experiment (fig. 5.14). For example, when measured in $\pi - \pi'$ channel both the (0,0,3) and (0,0,4.5) reflections are predicted to be largely invariant to rotations of the structure (ϕ), with only a small increase of the (0,0,3) reflection expected as a result of $F^{(2)}$ terms (fig. 5.15 d and g). In fact, we observe a significant increase of the (0,0,3) reflection (dashed grey lines in fig. 5.14 c) and a decrease in the intensity of the (0,0,4.5) reflection (dashed grey lines in fig. 5.14 f) when measured in the $\pi - \pi'$ channel.

In the rotated channels a sinusoidal dependence of the intensity is expected with an initial increase (decrease) in $\sigma - \pi'$ and a respective decrease (increase) in the $\pi - \sigma'$ channel. In our measurements, however, we see that the channels share qualitatively the same behaviour (i.e., both $\pi - \sigma'$ and $\sigma - \pi'$ either increase or decrease in intensity, see fig. 5.14 d and e), in clear disagreement with the predicted behaviour.

The lack of qualitative agreement between our results and calculations, supported by our circular asymmetry maps (fig. 5.13), conclusively demonstrate that magnetic polarity reversal cannot occur via a coherent rotation of the magnetic structure about [0,1,0] and must, therefore, occur by a different mechanism [77].

Another transformation which inverts the magnetic polarity of BSMFO is a coherent rotation of the magnetic structure about [0,0,1], outlined in fig. 5.16 a. Physically, this model is motivated by the planar anisotropy of the Y-type hexaferrites [80],

which favours the alignment of the spins in the $\hat{U}_1\hat{U}_2$ plane. The defining characteristic of these calculations (fig. 5.16 b-g) are the presence of a maximum or a minimum in the scattering intensity at the same rotation angle (ϕ) in each polarisation channel. This is indeed what we observe; the maximum and minimum scattering intensity for both reflections in all channels occur at the same magnetic field value (see dashed grey lines in fig. 5.14) with the qualitatively correct form for each channel.

Importantly, the qualitative results discussed here are largely independent of BSMFOs magnetic structure, i.e., a coherent rotation about the [0,0,1] direction of magnetic structures related to the hexaferrite block model would demonstrate qualitatively similar features. We can therefore confirm that the magnetic polarity of BSMFO is switched by a coherent rotation of the magnetic structure about the [0,0,1] direction.

Adjustments to the block model

In the following we discuss the high-field regions of our measurements. In each rotated polarisation channel, the observed scattering intensity are not necessarily equal for anti-parallel magnetic fields of the same magnitude (see fig. 5.17 and fig. 5.18 respectively). In the block approximation of the canted 2-fan used thus far, this asymmetry is not reproduced, even when $F^{(2)}$ terms are included. For example compare, $\phi = 0$ and $\phi = 180°$ in fig. 5.16 e or f and, more explicitly, the dashed, coloured lines of fig. 5.17 and fig. 5.18. The measured intensity difference for anti-parallel magnetic fields is large ($\sim$50 % of the mean intensity) and only occurs in the rotated channels ($\pi - \pi'$ is approximately flat). It is therefore unlikely to be an experimental artefact. The large difference is likely a result of a $F^{(1)}$ terms in the scattering amplitude, indicating that amendments to the canted 2-fan magnetic structure are required.

Due to the large number of parameters needed for any model, it will be impossible

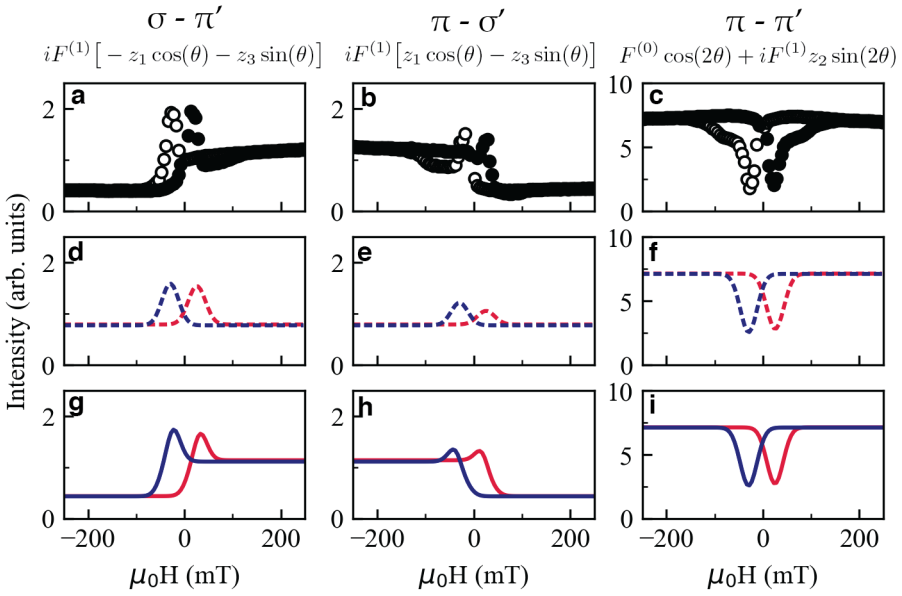


Figure 5.17: Intensity of the (0,0,4.5) reflection as a function of field. a-c, Measured experimental data while sweeping the field at 6.25 mT s^{-1}. **d-f,** Calculated scattering intensity (see main text) for the canted 2-fan structure within the block model. **g-i,** Calculated scattering intensity for the 'minimal' model. Both models assume a coherent rotation of the magnetic structure about the [0,0,1] direction. Columns (left to right) denote measurements in the $\sigma-\pi'$, $\pi-\sigma'$ and $\pi-\pi'$ polarisation channels respectively. Text in the top row denotes the components of the magnetic structure each channel is sensitive to.

to refine the full magnetic structure, so we discuss a minimal model to explain our data including (the dominant) $F^{(0)}$ and $F^{(1)}$ terms only. The intensity of a reflection measured in a given linear polarisation channel is proportional to the square of the relevant component of the scattering amplitude, $I_{i,j} \propto |M^{RES}(\vec{Q})_{i,j}|^2$. In turn the components of the scattering amplitude depend on the Fourier transform of the spin density, described in eq. (5.5).

We represent this Fourier transform of the spin density by z_j (an arbitrary complex number, see eq. (5.5))[5] and express it as,

$$z_j = |z_j|e^{i\phi_j}, \tag{5.32}$$

where ϕ_j is an arbitrary phase. The components of z_j, $j = \{1, 2, 3\}$ corresponds to moments parallel to $\hat{U}_1$, $\hat{U}_2$ and $\hat{U}_3$ directions respectively.

[5] $z_j = \sum_j m_j e^{i\vec{Q}\cdot\vec{r}_j}$.

Firstly, we discuss the (0,0,4.5) reflection, sensitive to $\vec{\tau}_2 = (0, 0, 1.5)$ components of the magnetic structure. In the rotated polarisation channels the intensity of the (0,0,4.5) reflection can be parametrised by,

$$I_{\sigma\pi'/\pi\sigma'} = |z_1|^2 \cos^2(\theta) + |z_3|^2 \sin^2(\theta) \pm 2|z_1||z_3| \cos(\Delta\phi) \cos(\theta) \sin(\theta), \qquad (5.33)$$

where $z_{1,3}$ are complex numbers which encompass all the scale factors and summations included in the calculations of the resonant scattering amplitude (eq. (5.5)) and arise from components of the magnetic moments parallel to $\hat{U}_1$ and $\hat{U}_3$ respectively, θ is the Bragg angle of the (0,0,4.5) reflection. $\Delta\phi = \phi_1 - \phi_3$ is the phase difference between the two complex ($z_{1,3}$) numbers. In the block approximation only z_3 is non-zero - arising from the antiferromagnetic alignment ($\vec{\tau}_2 = (0, 0, 1.5)$) of the S spin blocks. This structure cannot, therefore, exhibit a difference in intensity for anti-parallel magnetic fields as this requires (from inspection of eq. (5.33)) both a z_1 and z_3 component. Furthermore, since we have confirmed that the magnetic polarity switches via a coherent rotation around the [0,0,1] direction the z_3 component is expected to be invariant on field inversion. From eq. (5.33) we note that a change in intensity is only observed on magnetic field inversion if the final term changes sign. This occurs for π change in the value of $\Delta\phi$ and because z_3 is expected to be invariant on magnetic field inversion (ϕ_3 does not change), this must correspond to an inversion of the z_1 component of the magnetic structure (ϕ_1 is incremented by $\pm\pi$). Therefore, to explain this data there must be an additional component of the magnetic structure, parallel to $\hat{U}_1$, which changes sign on magnetic field inversion.

To demonstrate this, we additionally parametrise the scattering intensity,

$$I_{\sigma\pi'/\pi\sigma'} = |z_3|^2 \Big(\cos^2(\theta) + \alpha_1^2 \sin^2(\theta) \pm 2\alpha_1 \cos(\Delta\phi) \cos(\theta) \sin(\theta) \Big), \qquad (5.34)$$

where $\alpha_1 = \frac{|z_1|}{|z_3|}$ and the relative phase between the z_1 and z_3 components is $\Delta\phi$. A global scaling factor is incorporated in $|z_3|^2$ such that $|z_3|^2 \rightarrow S$. We can use the

Reflection	Parameter	Block	Minimal Model
(0,0,3)	S	9.88	8.73
	α_1	0	0.51
	α_2	—	—
	$\Delta\phi$	—	3.5°
(0,0,4.5)	S	0.95	0.91
	α_1	0	0.50
	α_2	3.57	3.66
	$\Delta\phi$	—	0.0°

Table 5.1: Parameters of our fit. Solid lines indicate insensitivity to the relevant parameter (rows). The two columns represent the parameters within the block model and the minimal model required to explain the data.

same approach for the $\pi - \pi'$ channel to get,

$$I_{\pi\pi} = |z_3|^2 \alpha_2^2 \sin^2(2\theta) \tag{5.35}$$

where $\alpha_2 = \frac{|z_2|}{|z_3|}$. We can then fit these parametrised intensities to our experimental data, as show in fig. 5.17. We add the switching behaviour, as previously described, by approximating the switching as a convolution of a Gaussian and a cosine function of (freely refined) arbitrary parameters to visually demonstrate how the switching would manifest itself. The Gaussian convolution simulates that not all the sample switches at once. The dashed lines in fig. 5.17 show our fits for the canted 2-fan magnetic structure within the block model (the parameters of the fit are displayed in table 5.1), where there is clearly no asymmetry.

Using the result of the block model refinement as starting parameters we now allow α_1 to freely refine, introducing a z_1 component with a $\vec{\tau}_2 = (0, 0, 1.5)$ modulation. Introduction of this component allows the experimental data to be reproduced with high accuracy (solid lines in fig. 5.17). The value of α_1 (table 5.1) is equal to 0.51, showing an appreciable z_1 component. This, however, does not necessarily mean that a large correction to the block model needs to be applied: z_3 is already small (arising from the S blocks) so only a small z_1 component is needed: for example, arising from a small twisting of the spins within the L block.

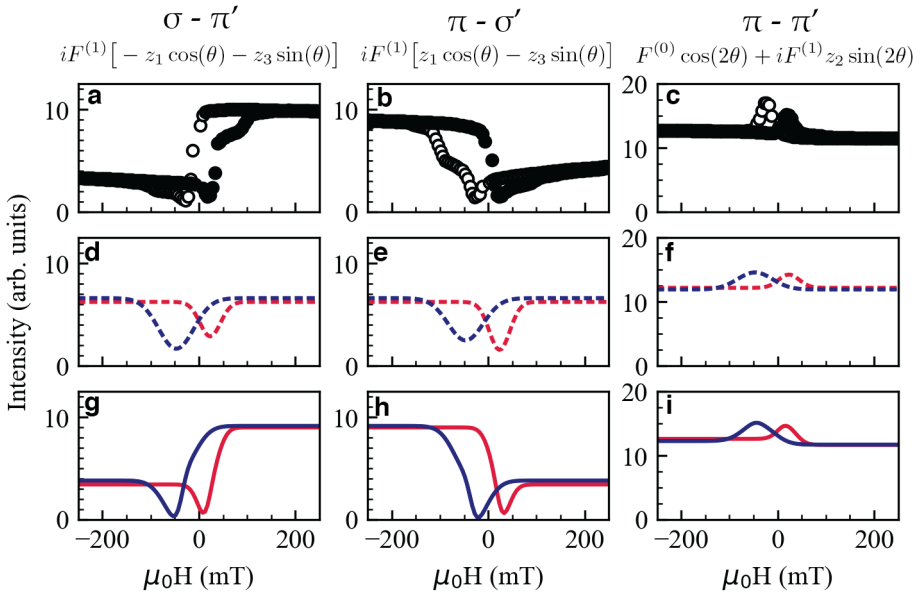


Figure 5.18: Intensity of the (0,0,3) reflection as a function of field. a-c, Measured experimental data while sweeping the field at 6.25 mT s^{-1}. **d-f,** Calculated scattering intensity (see main text) for the canted 2-fan structure. **g-i,** Calculated scattering intensity for the 'minimal' model. Both models assume a coherent rotation of the magnetic structure about c. Columns (left to right) denote measurements in the $\sigma - \pi'$, $\pi - \sigma'$ and $\pi - \pi'$ polarisation channels respectively. Text in the top row denotes the components of the magnetic structure each channel is sensitive to.

Next we discuss the (0,0,3) reflection, where we again parametrise the scattering intensity,

$$I_{\sigma\pi'/\pi\sigma'} = |z_1|^2\left(\cos^2(\theta) + \alpha_1^2\sin^2(\theta) \pm 2\alpha_1\cos(\Delta\phi)\cos(\theta)\sin(\theta)\right) \tag{5.36}$$

$$I_{\pi\pi'} = |z_1|^2\left(\alpha_2^2\sin^2(2\theta) + C\right) \tag{5.37}$$

now $\alpha_1 = \frac{|z_3|}{|z_1|}$, $\alpha_2 = \frac{|z_2|}{|z_1|}$ and C, a constant, describes the strength of the charge scattering. The (0,0,3) reflection is sensitive to $\vec{\tau}_1 = (0,0,0)$ components of the magnetic structure. In the block model the only component is parallel to $\hat{U}_1$ (the ferrimagnetic component of the structure) so an additional component, parallel to $\hat{U}_3$ is required to explain the intensity 'step' observed in our data. For this reflection the z_1 component must change sign on inversion of the magnetic field (apparent, for example, from magnetometry) and the z_3 component must be invariant to field

inversion to reproduce our data.

We refine the block model, dashed lines in fig. 5.18, which highlights the qualitative features of this model. Using the results of this refinement as starting parameters, we refine α_1 and find that an appreciable z_3 component is required to explain our data. This component maybe related to the $\vec{\tau}_1 = (0, 0, 0)$ component of the longitudinal conical magnetic structure observed in the absence of an applied magnetic field [80].

To summarise, these results show that even including terms up to $F^{(2)}$ we need to consider additional components to the canted 2-fan block approximation to explain our experimental results. We can identify that these additional components are a $\vec{\tau}_1$=(0,0,0) component $\parallel$ to $\hat{U}_3$, invariant on field inversion and a $\vec{\tau}_2$=(0,0,1.5) component $\parallel$ to $\hat{U}_1$, that switches on inversion of the applied magnetic field.

Potential models

There are a large number of models (owing to the number of free parameters) which could well-describe our experimental data (figs. 5.17 and 5.18) and we are unable to conclusively discriminate between these models using our results (or any of those currently published). In this section, we hypothesis further on possible models, which could be tested with additional experimentation.

Firstly at a high level, the additional magnetic structure likely takes the form of additional structure *within* the L and S blocks. This may take the form of a different orientation of the octahedrally and tetrahedrally coordinated Fe sites, owing to their different local anisotropies, or be the result of a 'twisting' of the blocks away from their collinear arrangement. There is, in fact, evidence of this within the zero field helix phase, where spins at the L/S block interface are observed to deviate from the collinear spin arrangement of the block [16]. No study has ever been able to resolve such features in the field induced phases, however, because of the increased complexity of studying these commensurate phases. Although, if the field induced phases possess such a twisting of the blocks, it could be manufactured to produce

'steps' in the data as seen in figs. 5.17 and 5.18 and is a plausible explanation of our data.

Secondly, we comment on if the magnetic field was not applied parallel to the $\hat{U}_2$ direction. It can be shown that any arbitrary field misalignment cannot reproduce our data, as it will only introduce the observed 'steps' for the (0,0,4.5) reflection, but not for the (0,0,3) reflection.

To fully resolve the magnetic structure of the canted 2-fan phase additional experimentation is required, which will likely take the form of a single crystal neutron diffraction experiment utilizing a single-wavelength neutron source. The results presented in this chapter, however, provide initial constraints any future model must be consistent with.

5.4 Conclusions

To conclude, we have performed a resonant X-ray diffraction experiment, with an *in-situ* magnetic field, to investigate the microscopic mechanisms of the magnetoelectric effect observed in BSMFO. By polarisation analysis of the scattered X-ray beam we have been able to determine the nature (charge or magnetic) of each observed reflection, this knowledge was used to demonstrate that RXD is sensitive to the magnetic polarity of the canted 2-fan structure. We spatially resolved the magnetic polarity domain structure of BSMFO as a function of applied magnetic field and found that $\vec{\lambda}$ was coupled to the direction of the applied magnetic field, a result consistent with our bulk magnetocurrent measurements.

We investigated the microscopic mechanisms of this coupling by performing dynamic polarisation analysis of the scattered X-rays. Our results proved inconsistent with the currently proposed model of polarity switching. To explain our results we proposed a new model of magnetic polarity reversal, consisting of a coherent rotation of the magnetic structure about the [0,0,1] direction.

Furthermore, we discovered that additional components of the magnetic structure are required to explain the observed reflection intensities of the canted 2-fan state. This likely takes the forms of additional structure within the spin blocks, such as a twisting of the blocks away from their collinear alignment. A model of this magnetic structure, meeting this requirements, could be investigated by performing a single crystal neutron diffraction experiment and is a suggested future experiment.

Having demonstrated the ability of RXD to spatially resolve the magnetic polarity (and hence electrical polar domains) of the Y-type hexaferrites, the next natural extension to this project is to incorporate an electric field into this experiment. In this way the coupling of the magnetic polarity domains with an electric field can be tested, giving greater insights into the magnetoelectric effects of this system.

RXD of the magnetoelectric phases of Y-type hexaferrites will likely become an increasingly important technique if they are to ever be developed toward application. Any realistic application will require the deposition of Y-type hexaferrite thin films, and soft RXD (unlike non-resonant X-ray and neutron scattering) can still provide significant sensitivity to the magnetic order equal to that of bulk specimens, its penetration depth being of the order of 10 nm.

6 | Observation of magnetic vortex pairs in an α-Fe_2O_3/Co heterostructure

In this chapter we discuss the magnetic domain morphology of a coupled α-Fe_2O_3/Co /Al heterostructure imaged using vector-mapped X-ray photoemission microscopy (X-PEEM), revealing an unprecedented network of vortices in the antiferromagnetically ordered α-Fe_2O_3 layer. These vortices imprint, by exchange proximity, into the adjacent Co layer such that the vortex network and their topological properties are fully realised in the ferromagnetic layer. The persistence of these vortices at ambient conditions is consistent with the Kibble-Zurek mechanism, first conceived in the context of cosmology, which describes the formation and preservation of topological defects at a symmetry breaking phase transition [139, 140]. We exploit the topological nature of our vortices to control the domain structure of our heterostructure by inducing mass vortex - antivortex annihilation.

This work represents one of the first observations of antiferromagnetic vortices in a laterally extended system and first appeared in the publication F. Chmiel, *et al.* [141].

6.1 Introduction

Developing the ability to control ferroic domains and their boundaries is a fundamental pre-requisite to implementing new technologies based on these materials. In chapter 5 we spatially resolved the magnetic polarity of the magnetoelectric $Ba_{0.5}Sr_{1.5}Mg_2Fe_{12}O_{22}$ using resonant X-ray diffraction. Importantly, we demonstrated that the magnetic polarity (coupled to the electric polarisation) can be switched with an applied magnetic field, an effect of functional interest [11, 77]. We found the magnetic polarity domains formed irregular morphologies which, with the exception of basic geometric shapes, is a typical configuration for most ordered ferroics [123, 142, 143]. The study of domains in such systems is primarily motivated by the need to control and remove (i.e. prepare into a mono-domain state) domains to tune the macroscopic properties of the system [130, 144].

In recent years, the advent of technologies enabling imaging at the nanoscale have transformed our knowledge of domain topologies [32]. We have discovered that domain boundaries can host emergent properties absent from the domains themselves [145, 146], and have seen domains organising themselves into striking configurations well beyond the trivial, irregular patterns of chapter 5 [30, 147, 148]. Arguably the system which best captures the interest surrounding novel domain topologies and their functionality are the hexagonal manganites (h-$RMnO_3$).

In 2010 Transmission Electron Microscopy (TEM) and scanning probe microscopy were used to image the ferroelectric domain structure of the hexagonal manganite $YMnO_3$, shown in fig. 6.1 b, where the two ferroelectric domains are realised by opposite contrast (dark/light) in the TEM image. Domains meet at several positions across the sample at which the TEM contrast cyclically alternates about these points: the ferroelectric domains configure themselves in so-called 'cloverleafs', visually similar to the Schlieren textures observed in liquid crystals [30,150]. The detailed configuration of these cloverleafs can be understood by considering the structural

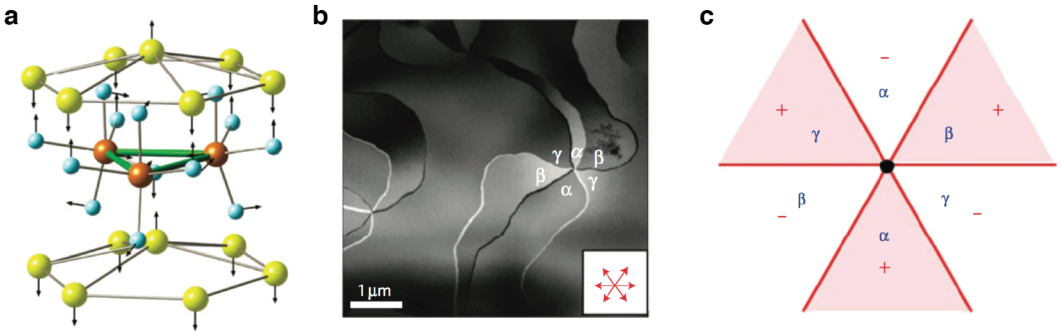


Figure 6.1: Structural anti-phase and ferroelectric domains of $YMnO_3$. **a,** Graphic showing the structural distortion in $YMnO_3$ for a single anti-phase and ferroelectric domain. Y^{3+}, Mn^{3+} and O^{2-} ions are coloured yellow, brown and blue respectively. **b,** TEM dark-field image of ferroelectric domain structure of $YMnO_3$, anti-phase domains do not show any contrast in dark-field TEM images [149]. **c,** Classification of the 'cloverleaf' domain structure in terms of the polarisation state and structural anti-phase domain, colour highlights the possible contrast observable with dark-field TEM. Reprinted/adapted by permission from Springer Customer Service Centre GmbH: Springer Nature, Nature Materials [30].

distortion (known as trimerisation) which induces the improper ferroelectricity in $YMnO_3$. This distortion (fig. 6.1 a) results from a tilting of the MnO_5 polyhedra causing a displacement of the Y^{3+} ions, with two thirds of the Y^{3+} ions distorting up and one third down, causing a net polarisation parallel to c. The three distinct choices of origin for the structural distortion means that there are three possible anti-phase domains (APDs, conventionally labelled α, β, γ), each with two degenerate ferroelectric polarisation states, determined by whether the MnO_5 polyhedra tilting is 'in' or 'out' [151]. The system therefore exhibits six independent domains ($\alpha^{\pm}$, $\beta^{\pm}$, $\gamma^{\pm}$) which can be assigned a periodic arrangement (a vortex) around the 'cloverleaf' core as illustrated in fig. 6.1 c, where antiphase and ferroelectric domains are locked (i.e. there are no boundaries of the form α^{+}/β^{+}) [30].

Following this initial observation the structural vortices have been observed with a range of techniques [32, 152–156], where studies were motivated both by the multifunctional nature of the hexagonal manganites (they are multiferroic) [89, 157] and the details of the domain topologies themselves. Focus was primarily given to the implications of the *topological* nature of the vortices, including the evolution of the vortex networks at the structural phase transition and their respective scaling

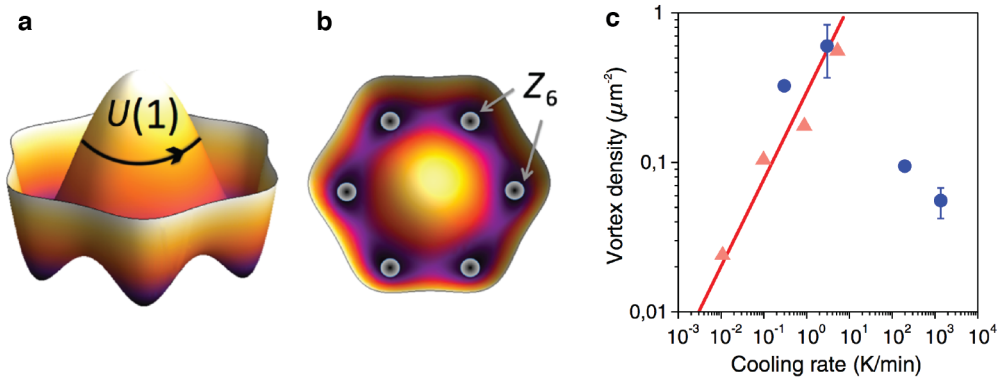


Figure 6.2: Landau free energy landscape of the hexagonal manganites and Zurek scaling of vortex density. a and b, Free energy of $YMnO_3$. At high energy the energy is independent of the MnO_5 polyhedra tilt angle (see main text) and the system thus has continuous U(1) symmetry. At lower energy the symmetry reduces to the sixfold discrete Z_6 symmetry. **c,** Vortex density as a function of cooling time after thermal annealing of the crystal above T_c, red triangles are experimental data from S. Chae *et al.* and the solid red line vortex density from the Zurek mechanism [158]. Note the 'anti-Kibble Zurek' scaling for high quenching rates. Figures adapted from S. Griffin *et al,* [151].

behaviours, discussed in the following.

Topology of vortices in $YMnO_3$

S. Griffin *et al.* showed that the structural phase transition in $YMnO_3$ displayed appropriate symmetry breaking characteristics to be consistent with the Kibble-Zurek mechanism, originally conceived in the context of cosmology to describe the formation of cosmic-strings [139, 151]. The Kibble mechanism describes the formation of topological defects near to a symmetry-breaking phase transition ($T \gtrapprox T_c$) and requires a change in symmetry across the phase transition that corresponds to a non-trivial homotopy group [139]. Near to the phase transition the free energy landscape of $YMnO_3$ is independent of the angle of the MnO_5 polyhedra tilt such that full rotational symmetry is broken when the polyhedra initially tilt, corresponding to U(1) symmetry of the free energy, see fig. 6.2 a [159]. Borrowing the methods of homotopy theory, S. Griffin *et al.* showed that the symmetry of the order parameter can be used to assess the topological properties of the transition. For the case of U(1) symmetry it was shown that the relevant homotopy group ($\pi_k(S^1)$) is non-trivial (i.e. not the identity) [160] and indeed produces one-dimensional topological

defects such as vortex cores [151].

The persistence of these topological defects (vortex cores) at ambient temperatures ($T << T_c$) depends on the quenching rate through the symmetry breaking phase transition and is described by a power law dependence as outlined in the Zurek mechanism [140]. The mechanism has been extensively tested in the hexagonal manganites and shown to be largely consistent with the Zurek mechanism, see for example fig. 6.2 c [151,161,162]. The results are particularly promising as they help to corroborate the universality of the Kibble-Zurek mechanism to all systems of the same homotopy group - independent of the nature of the topological defects (i.e. strings or vortex cores).

Topological domain structures and defects in magnetism

Converse to the large number of condensed matter systems exhibiting topologically rich structural domain configurations [31, 32, 156, 163], there are significantly fewer examples of vortex domains in magnetic materials. In magnetic materials topological physics is usually employed in the context of skyrmions, a topological spin texture of significant functional interest [4]. In 'classic' magnetic configurations (antiferromagnets and ferromagnets) vortices are only ever observed transiently or when geometrically constrained in a nanodot [164–166]. Ferromagnetic vortices are the most accessible topological structure, but long range dipole-dipole interactions inhibit the formation of a vortex, unless the system is spatially confined [165]. There are, however, already several proposed routes to functional application (i.e. in magnetic memories) of ferromagnetic vortices because they can be controlled and read electrically [10].

Vortices in antiferromagnetic materials have only previously been observed when imprinted from a ferromagnetic nanodot and never in an extended system [29, 167]. By developing a vector-mapped XMLD-PEEM technique, we have imaged the real space domain configuration of the archetypal antiferromagnet α-Fe_2O_3, revealing

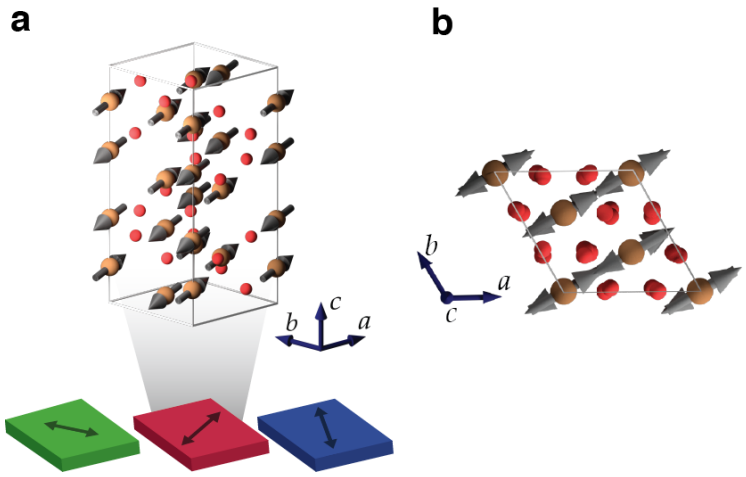


Figure 6.3: Magnetic structure of α-Fe_2O_3 between 250 K and 946 K. a, Perspective view of the hexagonal unit cell for spins in one of the three antiferromagnetic domains. **b** Orthographic view along c demonstrating the orientation of Fe moments in the ab plane, space group $C2/c$.

an unprecedented network of vortices analogous to those observed in $YMnO_3$. Our results show that even the simplest magnetic structures have the potential to host topologically interesting domain structures. We begin by introducing the magnetic order in α-Fe_2O_3 and discussing the behaviour of the magnetic structure at its paramagnetic-antiferromagnetic phase transition.

6.1.1 Crystal and magnetic structure of α-Fe_2O_3

α-Fe_2O_3, often referred to as hematite due to its striking red colour,[1] crystallizes in the corundum structure, $R\bar{3}c1'$, with lattice parameters (in the hexagonal setting) at room temperature of $a = 5.038(2)$ Å and $c = 13.772(12)$ Å [168, 169]. It orders antiferromagnetically at (T_N) 946 K (fig. 6.3) with the Fe^{3+} spins being ferromagnetically coupled in the basal (0001) plane and antiferromagnetically stacked along c, breaking the 3-fold rotation axis of the crystal structure (magnetic space group $C2/c$). This phase is particularly notable because it was one of the earliest known weakly ferromagnetic (WF) antiferromagnets; possessing a spontanenous magnetisation of $\sim$0.004 μ_B per Fe site [170–172], originating from a small canting of the spins, within the basal plane, induced by the antisymmetric part of the anisotropic

[1] 'Hematite' is derived from the Greek for blood

superexchange interaction [17, 18].

We expect domains of the antiferromagnetic order parameter to form at T_N, where individual domains are related by the lost symmetry elements of the parent structure: $R\bar{3}c1'$. For the antiferromagnetic ordering in α-Fe_2O_3 the relevant lost symmetry elements are the 3-fold rotation axis and temporal inversion. Three domains related by a 120° rotation about c (orientational domains) and their time inversion partners (anti-phase domains) are possible, such that six unique domains are expected in total.

Landau free energy of the antiferromagnetic phase transition

The paramagnetic to antiferromagnetic ordering transition in α-Fe_2O_3 is second order: the order parameter grows continuously from zero at the transition temperature. We can thus use a Taylor expansion of the (Landau) free energy in the antiferromagnetic order parameter to inform us about the free energy landscape at the transition [173]. To construct the Taylor expansion we must use the 2-dimensional irreducible representation Γ^{3+} of space group $R\bar{3}c$. For an antiferromagnet we can use the staggered magnetisation as the order parameter,

$$\vec{L} = \vec{m_1} - \vec{m_2}, \tag{6.1}$$

where $\vec{m_i}$ are the sublattice magnetisations. The Landau free energy is invariant under temporal inversion ($\vec{L} \rightarrow -\vec{L}$) so it must only contain even powers of the order parameter, therefore the relevant invariant polynomials are [174],

$$
\begin{aligned}
2^{\text{nd}} \text{ order} &: a^2 + b^2, \\
4^{\text{th}} \text{ order} &: a^4 + 2a^2b^2 + b^2, \\
6^{\text{th}} \text{ order} &: a^6 - 6a^4b^2 + 9a^2b^4, \\
&\quad a^6 + 3a^4b^2 + 3a^2b^4 + b^6.
\end{aligned}
$$

We can take $a = L_x$ and $b = L_y$ and define,

$$a = Q\cos(\theta), \tag{6.2}$$

$$b = Q\sin(\theta), \tag{6.3}$$

where $Q^2 = a^2 + b^2$ and, physically, θ denotes the (azimuthal) orientation of the staggered magnetisation. That is far below the transition (large Q) θ equals to 0, $\pm\frac{\pi}{3}$, $\pm\frac{2\pi}{3}$ and π, where anti-phase domains are related by a π shift in θ. In this limit the free energy landscape has Z_6 symmetry (six degenerate minimum energy states) as in the hexagonal manganites, see fig. 6.2 b.

Using this formalism, the free energy (up to 6^{th} order) is given by,

$$
\begin{aligned}
\Delta F = A(T - T_N)Q^2 + B(T_N)Q^4 + Q^6\big\{C_1(T_N) \\
+ \frac{C_2(T_N)}{2}(\cos(6\theta) + 1)\big\} + \cdots,
\end{aligned} \tag{6.4}
$$

where A, B, C are constants (with the exception of A, temperature independent). Taking the limit of small Q (i.e. approaching the transition) we see that the free energy becomes independent of θ, the direction of the antiferromagnetic spins. The lower order terms thus dominate and the free energy landscape therefore approaches

U(1) symmetry at the phase transition. Importantly the free energy landscape of α-Fe_2O_3 is phenomenologically equivalent to that of $YMnO_3$ (fig. 6.2 a and b) and in the same way, the U(1) symmetry of the free energy for small values of the order parameter implies the antiferromagnetic transition α-Fe_2O_3 can be proliferated by the formation of topological defects, as in the Kibble mechanism, the density of which persisting at ambient conditions to be determined by Zurek scaling [140].

6.1.2 Imaging magnetic domains

A plethora of experimental techniques have been developed to image the real-space configuration of a system's magnetisation at a microscopic level. This development has been driven by a technological need to understand the microscopic domain geometry of functional materials because of the impact the domain configuration can have on a systems macroscopic properties, apparent, for example, in soft ferromagnets where domains (regions of saturated magnetisation, not necessarily parallel to the magnetisation in other domains) can result in a vanishing bulk magnetisation in zero applied magnetic field.

Ferromagnetic domains

Magnetic Force Microscopy (MFM) is one of the most widely used tools today to image, in real space, magnetic domains in ferromagnets [175–177]. It is a non-contact variation on Atomic Force Microscopy (AFM) which scans a magnetised tip near the surface of the system under study to measure the local stray field (through the magnetostatic interaction between tip and field). Because the measured stray field does not uniquely determine a magnetisation configuration, quantitative information about the samples magnetisation can be difficult to extract. Despite this drawback, its ability to routinely achieve spatial resolutions below 10 nm has made it an invaluable technique in understanding the magnetic behaviour of ferromagnets at the microscopic level [178].

Optical techniques, based on the magneto-optical Kerr effect (MOKE, the rotation of the plane of polarisation of light as it reflects from a magnetic media) [179], have the advantage of being sensitive directly to the samples magnetisation, but its resolution (being diffraction limited) cannot rival that of MFM: even under optimal conditions it only approaches a spatial resolution of ∼100 nm [180].

X-ray microscopes utilizing the X-ray Magnetic Dichroism effect (XMCD), first used to image ferromagnetic domains in 1993 [66, 68], have the unique advantage of elemental sensitivity: it relies upon a large resonant enhancement of the signal coincident with an absorption edge of the magnetic ion being probed. The effect is largest when a core electron is excited into a magnetically polarised band, for which the relevant absorption edges (for the first row of transition metals) are the $L_{2,3}$ edges, where a core $2p$ electron is excited into the spin polarised $3d$ state. Additionally, the elemental sensitivity of XMCD can be used to image 'buried' layers in heterostructures composed of layers featuring different magnetic ions, for example as deployed in spin valves used in hard disk read heads and MRAM [181–183].

Antiferromagnetic domains

Many of the aforementioned techniques prove ineffective when imaging domains of antiferromagnetically ordered materials. Magnetic force microscopy, Kerr magnetometry and XMCD-PEEM are all sensitive to either the magnetisation of the probed volume or the local stray field, both of which are vanishingly small for antiferromagnets. There are, however, circumstances where careful application of these techniques can be used to indirectly measure AFM domains. For example, *magnetoelectric* antiferromagnets (such as Cr_2O_3) [21, 83] famously exhibit a symmetry protected, non-zero, boundary magnetisation at their surfaces [184]. This boundary magnetisation is directly coupled to the antiferromagnetic order parameter and is anti-parallel between anti-phase domains (APDs) of the bulk antiferromagnet. In a seminal experiment, Wu *et al.* used XMCD-PEEM to measure the boundary magnetisation of the archetypal magnetoelectric Cr_2O_3, indirectly imaging the

APD structure of the bulk antiferromagnet. Using its magnetoelectric properties they subsequently controlled the antiferromagnetic domain structure of Cr_2O_3, the effects of which were directly reflected in real-space images of the boundary magnetisation [29].

These techniques, however, are not suitable for imaging the domain topology of a general antiferromagnet, the compensated nature of the structure yielding vanishingly small signals. While a range of complementary techniques have been developed to image antiferromagnetic domains (such as Second Harmonic Generation and nitrogen-vacancy magnetometry) [185, 186], arguably the most widely applicable is that of X-ray Magnetic Linear Dichroism PhotoEmission Electron Microscopy (XMLD-PEEM). Whereas the XMCD effect is sensitive to the average magnetisation of the probed region ($\langle\vec{M}\rangle$) XMLD is sensitive to its square ($\langle\vec{M}^2\rangle$) and can thus be used to image compensated magnetic structures, such as antiferromagnets [69, 187].

While a weaker effect than XMCD, XMLD can be easily employed alongside XMCD-PEEM (as performed in this chapter) to image the domain structure of adjacent antiferromagnetic and ferromagnetic layers, of relevance to the community studying the exchange bias effect [188]. While there exists a standard technique for realising a full vector map (the spatial distribution of the magnetisation) of a ferromagnet using XMCD-PEEM (see section 6.2.2) there is no such standard for achieving this for antiferromagnets using XMLD-PEEM. By tracking the XMLD signal for small regions of their (AFM) $LaFeO_3$ sample Hallsteinsen *et al.* showed the average antiferromagnet spin direction within this area could be determined, but did not perform it for the all general positions [74]. In this work we extend this technique and show how it can be used to construct a full vector-map of an antiferromagnet in general.

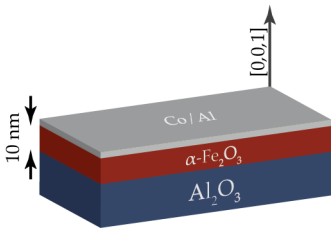


Figure 6.4: Graphic outlining design of our heterostructure. The system is constructed on a c-Al_2O_3 substrate, where a 10 nm α-Fe_2O_3 layer is deposited by RF sputtering, upon which a 1 nm layer of Co is deposited. Finally a 1 nm layer of Al caps the heterostructure.

6.2 Experimental details

6.2.1 Growth of α-Fe_2O_3/Co heterostructure

Films of α-Fe_2O_3 were deposited on polished c-Al_2O_3 single crystals by Radio Frequency (RF) magnetron sputtering, Al_2O_3 was used as a substrate because of its low mismatch ($\sim$5.3 %) with α-Fe_2O_3. The films were deposited using a stoichiometric α-Fe_2O_3 sputtering target at 500°C with an Ar:O_2 ratio of 3:2 and a chamber pressure of 400 mT. Metal layers (Co or Al) were then deposited by DC magnetron sputtering at room temperature. The ferromagnetic Co layer was used to investigate how it coupled to the adjacent α-Fe_2O_3 layer whereas an Al layer was included to both passivate the surface (protecting the Co layer from oxidation) and to electrically ground the sample such that electrons emitted during the photoemission process could be replenished. Films of various thickness's were grown, however, for the X-ray photoemission study presented in this chapter films were of the composition: α-Fe_2O_3 (10 nm) / Co (1 nm) / Al (1 nm).[2]

Film characterisation

The epitaxial relation of the film and substrate was confirmed using a Rigaku SmartLab X-ray diffractometer. Figure 6.5, displays characterisation of an example film,

[2] α-Fe_2O_3 films for this study were grown by J. Schad and C-B. Eom at the University of Wisconsin.

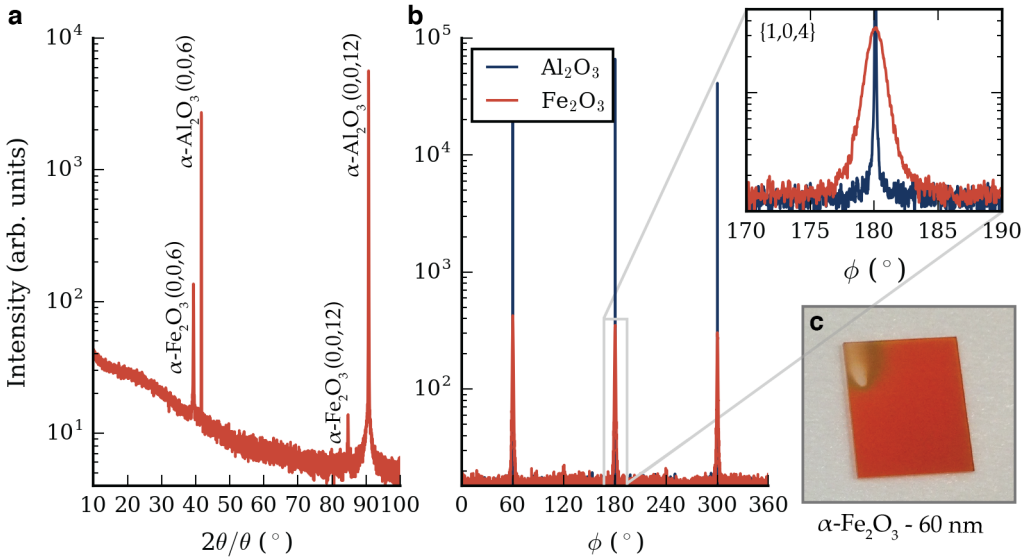


Figure 6.5: Lab-based characterisation of α-Fe_2O_3 films. **a,** Coupled $2\theta/\theta$ scan along the (0,0,1) reciprocal direction of the substrate for a 30 nm thick film. **b,** 'ϕ' scan of the {1,0,4} reflections for Al_2O_3 and α-Fe_2O_3, performed by rotating around c with $|\vec{Q}|$ fixed for the respective reflection. Inset: highlights one of the {1,0,4} reflections for both substrate and film, confirming the in-plane epitaxy. **c,** Photograph of a 60 nm α-Fe_2O_3 film.

a coupled $2\theta/\theta$ scan along the $(0,0,l)$ reciprocal direction of the substrate is used to confirm the out-of-plane epitaxy of the film. A rocking curve of a particular α-Fe_2O_3 reflection can be used to quantify the mosaicity of the film - typically rocking curves of the (0,0,6) reflection of our α-Fe_2O_3 films had a full-width-half maximum less (FWHM) than 0.5° (and as low as 0.06°) confirming a strong orientational preference of the α-Fe_2O_3 layer. In-plane epitaxy is investigated (fig. 6.5 b) by performing a fixed $|\vec{Q}|$ scan of the {1,0,4} reflections of both the film and substrate, where the sample is rotated around c while in the Bragg condition for the respective {1,0,4} reflection. Each of the three {1,0,4} reflections of the α-Fe_2O_3 layer are coincident in direction with a substrate reflection, confirming a good level of in-plane epitaxy. Conversely, if the measured intensity was independent of ϕ the α-Fe_2O_3 layer would have no preferred orientation within the plane of the substrate. Characteristically, thick α-Fe_2O_3 films (d> 20 nm) are bright red (fig. 6.5 c) in colour and thinner films are a ruddy brown, see for example the sample edge in fig. 6.5 c.

The Co layer was characterised by longitudinal magneto-optical Kerr Microscopy

(L-MOKE). It was confirmed to be ferromagnetic with a coercive field of 8 mT, no L-MOKE signal was observed for an isolated α-Fe_2O_3 film confirming the signal arose from the Co layer and not the weak ferromagnetic moment of α-Fe_2O_3.

6.2.2 X-ray PhotoEmission Electron Microscopy

In this section we discuss the practical implementation of X-ray Photoemission Electrion Microscopy (X-PEEM), for a discussion of the relevant theory please see chapter 2. We use X-PEEM as it uniquely allows us to image the magnetic order of the α-Fe_2O_3 and Co layers independently at sub-micron length scales.

Experimental set-up

X-PEEM measurements were performed at the Nanoscience beamline (I06), Diamond Light Source (Didcot, UK). Practically, a sample is mounted in the ultra-high vacuum PEEM chamber with its surface electrically grounded, such that photoemitted electrons can be replenished [189]. The sample is mounted on a translatable manipulator capable of rotating about the films surface normal ([0,0,1]) within an angular range of 180°. Incident X-rays illuminate the sample at 16° grazing incidence, their energy is controlled by two APPLE II undulators and can be tuned between 80 and 2100 eV [132]. The X-ray polarisation (controlled by the same undulators) can be set to either circular polarisation state or to any arbitrary linear polarisation.

While under illumination with incident X-rays secondary electrons from any photoemission from the sample are recorded using an Elmitec SPELEEM-III microscope. Image contrast is achieved by taking multiple images with different incident beam properties. Typically, one takes images at two distinct incident energies or polarisations and calculates the image asymmetry (dichroism),

$$\delta = \frac{I_1 - I_2}{I_1 + I_2}, \tag{6.5}$$

where I_i are the respective images. Sensitivity to the magnetic order is gained by using the X-ray Magnetic Circular Dichroism (XMCD) or X-ray Magnetic Linear Dichroism (XMLD) effects, described in chapter 2.

The X-ray dichroism signal (particularly in the case of XMLD) is relatively weak, such that the photoemission from the sample must be recorded for extended periods of time: as a crude rule of thumb, sufficiently high signal-to-noise is generally achieved with counting times of 3600 seconds for XMLD-PEEM and 300 seconds for XMCD-PEEM. As the sample and X-ray beam invariably move during measurement a set of images with short counting times (10 seconds) are recorded and individually processed to correct for these effects and subsequently averaged.

Data reduction and preparation

Data reduction is performed using Igor Pro (WaveMetrics, Lake Oswego, OR, USA). Initially undesirable sample translation is corrected for (the net translation during the measurement procedure can be as severe as 500 nm), after which the set of individual images are averaged and corrected for optical distortions in the Igor Software: an affine transformation is performed to minimize the distortion by visual inspection. The final image is exported as a TIFF and all the following analysis is performed in Python using home-developed analysis tools.

Each X-PEEM image is smoothed (by convolution of a 2D gaussian with a FWHM of 30 nm) and a 4^{th} order polynomial background is subtracted. This background reflects the spurious movement of the X-ray beam during the measurement which can introduce a non-uniform background at the edges of an image. Continuing with the analysis without performing this background correction does not change the qualitative results of any analysis, but reduces the usable area of the images.

We record images, processed in such a way, at several incident X-ray directions to extract the vector map of the magnetisation of either the Co or Fe layer using XMCD or XMLD-PEEM respectively, as discussed in the following.

XMCD-PEEM

Magnetic vector maps of the ferromagnetic Co overlayer are constructed by imaging the X-ray circular asymmetry, δ, at two orthogonal incident X-ray directions[3] and utilizing the anisotropy of the XMCD effect,

$$\delta_{XMCD} \propto \langle \vec{M} \rangle \cdot \hat{\sigma}, \tag{6.6}$$

where $\langle \vec{M} \rangle$ is the average magnetisation of the probed region and $\hat{\sigma} = \sigma \hat{k}$ is the X-ray helicity ($\sigma = \pm 1$) [190, 191]. Experimentally, δ is measured using incident light of both helicities and two energies,

$$I_{pc} = \frac{I_{pc,E_1}}{I_{pc,E_2}} - 1, \tag{6.7}$$

$$I_{nc} = \frac{I_{nc,E_1}}{I_{nc,E_2}} - 1, \tag{6.8}$$

$$\delta = \frac{I_{pc} - I_{nc}}{I_{pc} + I_{nc}}. \tag{6.9}$$

In the case of Co, the two incident energies are the maxima of the L_3 edge, $E_1 = 777$ eV, and a (pre-edge) value, $E_2 = 770$ eV. By normalising the images recorded on the L_3 (sensitive to the magnetic order) maxima by an image recorded with a pre-edge energy (insensitive to the magnetic order) one minimizes spurious image contrast arising due to differences in the polarisation channels and/or small variations in the X-ray beam as a function of time [192].

To determine the local magnetisation, to within a global scale factor, the intensity of

[3] In chapter 2 we showed this was proportional to the XMCD effect.

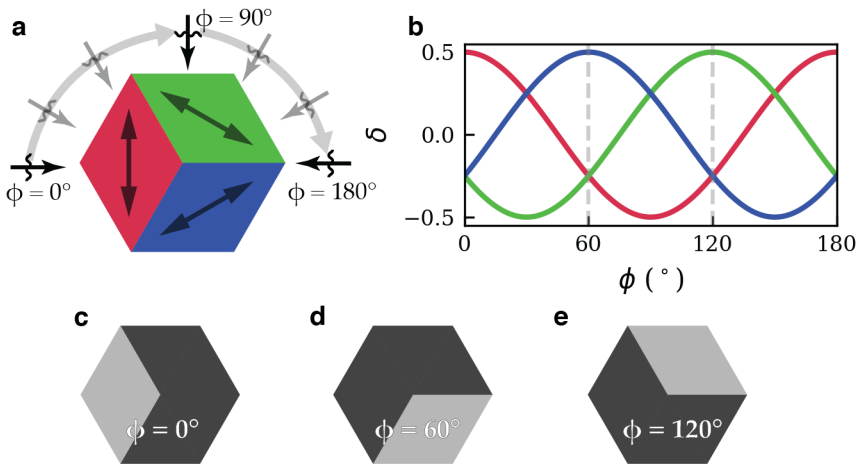


Figure 6.6: Graphic demonstrating the anisotropy of the XMLD effect. a, Arbitrary domain pattern, double-headed arrows denote the direction of the antiferromagnetic spin axis in each domain (colour). Black arrows illustrate rotation of the incident X-ray direction (ϕ). **b,** Angular dependence of measured 'XMLD' signal (δ) for each domain (denoted by colour). **c-e,** Example of contrast observed, for fictional domain configuration shown in a, using X-PEEM for three incident X-ray directions ($\phi = 0°, 60°, 120°$ respectively), highlighting the degeneracy of the XMLD signal.

the XMCD signal is measured with two orthogonal ($\hat{k_1} \parallel \hat{x} : \phi = 0$ and $\hat{k_2} \parallel \hat{y} : \phi = \frac{\pi}{2}$) incident X-rays directions,

$$\langle \vec{M} \rangle \propto \delta_0 \hat{x} + \delta_{\frac{\pi}{2}} \hat{y}, \tag{6.10}$$

where the orthogonal unit vectors $\hat{x}$ and $\hat{y}$ are defined by $\hat{k}$ at 0 and $\frac{\pi}{2}$ radians respectively. Therefore, in XMCD-PEEM only two asymmetry images are required to fully resolve the in-plane magnetisation distribution of a ferromagnetically ordered system.

XMLD-PEEM

To determine the full magnetisation vector map of $\alpha-Fe_2O_3$ we must utilize the XMLD effect to obtain contrast sensitive to the AFM spin direction. This effect has a different angular dependence compared to XMCD because linearly polarised photons posses only axiality. For our experimental geometry the anisotropy of the XMLD signal is of the form,

$$\delta_{XMLD} = A + B(3\cos^2(\theta) - 1)\langle \vec{M}^2 \rangle, \tag{6.11}$$

where A and B are constants describing the size of the absorption edge and XMLD effect respectively. θ is the angle between the incident X-ray polarisation direction (for horizontally polarised X-rays) and the antiferromagnetic spin direction within the plane of the sample [141, 187, 193].

Experimentally, one records X-PEEM images with either horizontally or vertically polarised linear X-rays. For spins lying in the plane of the sample, horizontally polarised X-rays are sensitive to the XMLD effect (and thus the magnetisation) whereas vertically polarised X-rays are insensitive to the direction of magnetisation, they can therefore be used to normalise the X-PEEM images [193]. In an analogous way to XMCD we calculate,

$$I_{LH} = \frac{I_{LH,E_1}}{I_{LH,E_2}} - 1,$$
$$I_{LV} = \frac{I_{LV,E_1}}{I_{LV,E_2}} - 1.$$

where E_1 and E_2 are two incident X-ray energies on resonance (optimized to maximize the XMLD signal).

The asymmetry, δ, is then calculated,

$$\delta = \frac{I_{LH} - I_{LV}}{I_{LH} + I_{LV}}.$$

To compensate for the weakness and degeneracy (fig. 6.6) of the XMLD effect we image the samples asymmetry at multiple incident X-ray directions and then fit the expected angular dependence of XMLD on a pixel by pixel basis, allowing us to extract θ. Figure 6.6 outlines this method by showing the dependence of the XMLD

for a fictional domain configuration as the azimuthal direction of incident X-rays is changed. Notably any two domains of arbitrary orientation will always exhibit degenerate contrast at a minimum of two X-ray directions, demonstrated in fig. 6.6 c-e.

6.3 Results and discussion

6.3.1 In-situ film characterisation

Prior to imaging the domain structure of our heterostructure, we performed several characterisation measurements *in-situ* to the PEEM chamber. While varying the incident X-ray beam energy we recorded the total photoemission from the sample in a 20 µm diameter area. The total photoemission is proportional to the number of absorbed photons and so these measurements represent an indirect measure of the X-ray absorption spectra (XAS) of our system. Figure 6.7 displays the results of these measurements in the proximity of the $L_{2,3}$ edges of both Co and Fe. Between 770 and 805 eV (fig. 6.7 a) we observe two large increases in photo-absorption, whose maxima are coincident with the expected energies of $L_{2,3}$ absorption edges of Co 778 eV and 793 eV respectively [136]. Neither the L_3 or L_2 edge display evidence of additional structure (a result of crystal field-splitting, for example see fig. 6.7 c) suggesting the Co layer is metallic [194]. Importantly we observe dichroism when the photo-absorption is measured with incident light of opposite helicities - confirming the presence of a large XMCD effect in our Co layer.

For incident X-ray energies inclusive of the Fe $L_{2,3}$ edges (fig. 6.7 c) we again see two large increases in photo-absorption, with peak absorption at energies corresponding to the Fe L_3 (707 eV) and L_2 (720 eV) edges [136]. Compared to the spectra about the Co edges (fig. 6.7 a) we see significant 'splitting' of each absorption edge, which arises due to the crystal field of the Fe^{3+} environment [194]. The qualitative form of this spectra indicates that the (vast majority of) Fe sites are oc-

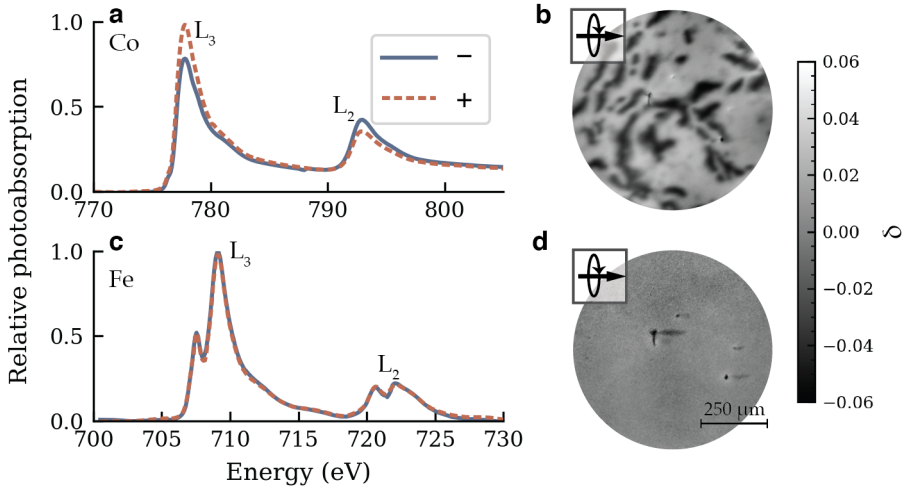


Figure 6.7: Properties of α-Fe_2O_3 / Co heterostructure illuminated with circularly polarised X-rays. a and c, Total photoemission (proportional to the net photoabsorption) for a 20 µm diameter area recorded as a function of incident X-ray energy with positive (dashed lines) and negative (solid lines) circular polarisation. The pre-edge photoemission has been subtracted for clarity and the signal normalised to the maximum of the L_3 edge. **b and d,** XMCD-PEEM images, at the same sample position, b, using energies corresponding to the Co L_3 edge and d, at the Fe L_3 edge, see main text for details.

tahedrally coordinated, as expected in $\alpha-Fe_2O_3$, as opposed to being either metallic or tetrahedrally coordinated; which would occur, for example, in other iron oxides (i.e. Fe_3O_4) [187, 194]. No appreciable difference in photoabsorption with incident light of opposite helicities is observed: there is no XMCD effect at these energies, consistent with the compensated, antiferromagnetic order of $\alpha-Fe_2O_3$.

To further investigate the XMCD effect in our heterostructure we recorded XMCD-PEEM images of our sample with a field-of-view of 10 µm using incident energies corresponding to the Co L_3 edge (E_1 = 777 eV, E_2 = 770 eV) or Fe L_3 edge (E_1 = 708 eV, E_2 = 700 eV) using the methodology outlined in section 6.2.2. The image sensitive to the Co layer (fig. 6.7 b) exhibits dichroism with regions of opposite sign, corresponding to different orientations of the Co magnetisation with respect to the incident X-ray direction. Conversely, for the Fe image (fig. 6.7 d) no XMCD is observed and the dichorism, with the exception of small structural defects (used in the alignment of the sample), is zero and homogeneous, confirming that within our experimental limitations the $\alpha-Fe_2O_3$ layer has no net magnetisation.

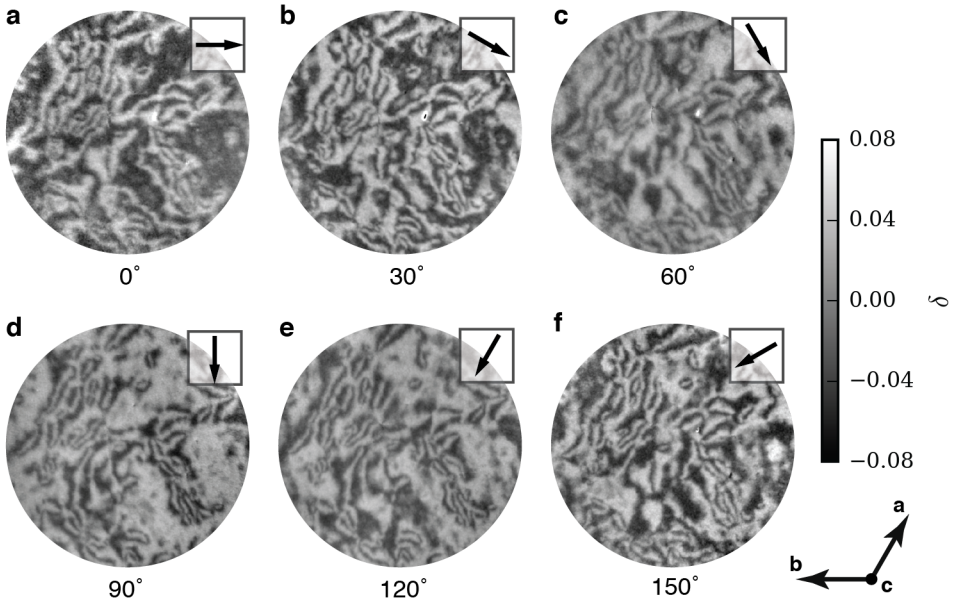


Figure 6.8: Raw XMLD-PEEM images of α-Fe_2O_3 layer. XMLD images as a function of incident X-ray direction (denoted by inset arrow for each panel) recorded at the Fe L_3 edge. The orientation of the α-Fe_2O_3 layer is displayed by the axes in the bottom right corner, each image is to the same scale where the field-of-view is approximately 10 µm.

These results confirm that we can use XMCD-PEEM (outlined in section 6.2.2) to image the magnetisation distribution of the Co layer but not the antiferromagnetically ordered α-Fe_2O_3 layer, for which we must turn to the higher order XMLD effect.

6.3.2 XMLD-PEEM vector map of α-Fe_2O_3

$\alpha-Fe_2O_3$ is known to exhibit a relatively large XMLD effect, historically used to characterise its spin-flop transition (known as the Morin transition) [195,196]. While the morphology of the antiferromagnetic domain structure has been measured, both in MBE grown thin films and in single crystals [197, 198], no experiment has taken advantage of the anisotropy of the XMLD signal (see fig. 6.6) to fully resolve the magnetisation configuration of α-Fe_2O_3, previous results can thus only ever provide a partial insight into the true domain morphology.

To construct a vector map of the antiferromagnetic domain structure, we take advantage of the anisotropy of the XMLD signal. Experimentally, we measure six

XMLD-PEEM images (see section 6.2.2 for details of the experimental procedure) of the α-Fe_2O_3 layer as the incident X-ray direction is rotated about the films surface normal. These images, shown in fig. 6.8, show an appreciable XMLD effect[4] with different values of dichroism, evident in dark / light regions, across the sample. As the incident X-rays direction is rotated (fig. 6.8 a-f) the measured contrast also changes, consistent with the expectation of there to be a set (i.e. more than two) of antiferromagnetic domains. From the raw data we cannot absolutely determine the antiferromagnetic spin direction within these domains, however, regions of dark contrast in fig. 6.8 are domains with the spin direction more parallel to the incident X-ray direction (inset black arrows) and lighter regions are those with the spin direction less parallel to the incident X-rays. We can also comment on the general domain morphology: there are both large area domains, $\sim$1 µm in width, but also elongated domains with a narrow width ($\sim$0.5 µm) and several microns in length, furthermore, these narrow domains appear to converge at several points on the sample.

To determine the antiferromagnetic spin direction in the α-Fe_2O_3 layer, we fit the angular dependence of the XMLD signal (eq. (6.11)) with the antiferromagnetic spin axis (θ) as a free parameter at each pixel in the image. While a single pixel covers $\sim$10 x 10 nm^2 area, the resolution is practically limited by movement of the sample during measurement and uncompensated optical distortions and is of the order of 100 nm. The measured dichroism, as a function of the incident X-ray direction (ϕ), is shown for a set of pixels in fig. 6.9 a. The variation of each pixel can be generally well described with the expected form of the XMLD signal (solid coloured lines). By extracting the fitted antiferromagnetic spin direction (θ) for each pixel we can construct a false colour map, as displayed in fig. 6.9 b, where colour represents the direction of the antiferromagnetic spin axis (parallel to the staggered magnetisation) in the *ab* plane of the sample. Colours (red:'R', green:'G', blue:'B') highlight the directions of the three antiferromagnetic domains as allowed by symmetry, parallel

[4]Generally, this contrast can also be caused by charge anisotropy, but in our geometry (3-fold axis surface normal) this term is vanishing.

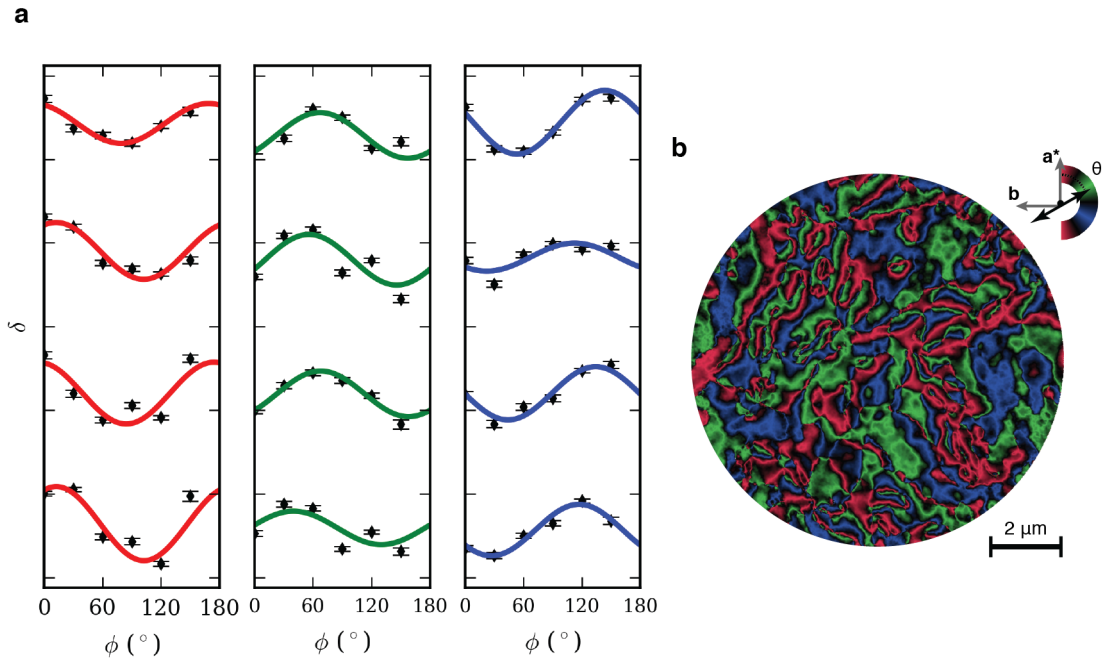


Figure 6.9: Construction of α-Fe_2O_3 vector map. a, Angular dependence of asymmetry of different individual pixels in the α-Fe_2O_3 XMLD maps. Each asymmetry dependence is arbitrarily shifted along the y-axis. From left to right the columns correspond to pixels within the R (red), G (green), and B (blue) domains. **b,** Resultant XMLD vector map of the α-Fe_2O_3 where color represents the direction of the antiferromagnetic spin axes.

to the mirror planes of space group $C2/c$ and related by the lost three-fold axis (R ∥ [2,1,0], B ∥ [1,2,0] and G ∥ [-2,1,0]). Black regions show areas of the sample which deviate from these three directions and primarily highlight domain walls, where the finite resolution of our experiment means neighbouring domains are simultaneously sampled. By binning the measured AFM spin axis of each pixel to the nearest axis allowed by symmetry we find that the three domains are approximately equally populated: 31.8% is red, 33.9% blue and 34.3% is green, as expected for a system grown without external bias.

As well as large area domains (i.e. right of fig. 6.9 b) the domains also form an intricate structure at a sub-micron scale. A prominent feature of this structure is the presence of 'pinch-points' between AFM domains of the same orientation, as shown in detail in fig. 6.10. About these points the domains are typically arranged in a (6-fold) periodic configuration, alternating as either R-G-B-R-G-B or R-B-G-R-B-G clockwise around their common core - examples of which are outlined in the insets of fig. 6.10.

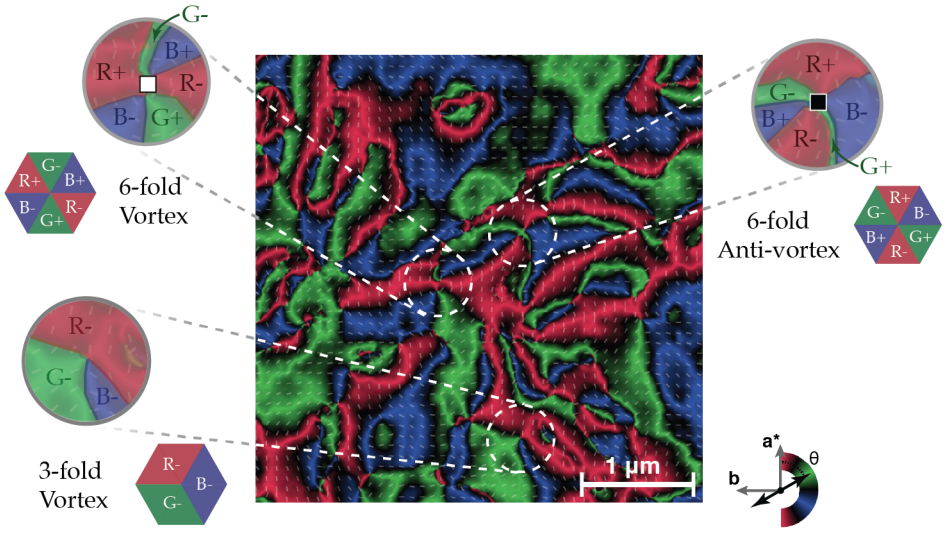


Figure 6.10: Types of domain meeting points in α-Fe_2O_3 layer. Main panel displays the α-Fe_2O_3 antiferromagnetic domain structure as determined by vector-mapped XMLD-PEEM. Color represents the direction of the antiferromagnetic axis (bottom right) on a pixel by pixel basis and white bars the average antiferromagnetic axis direction for a ten square pixel region. Inset figures highlight examples of different meeting points of the orientational / time inversion domains, in analogy with the structural trimerisation domains observed in $YMnO_3$ [30].

This network of points and periodic domain configurations (vortices) is remarkably similar to the cloverleaf ferroelectric domain patterns observed in the hexagonal manganite $YMnO_3$, discussed in section 6.1, pointing towards a common phenomenology in completely different contexts. Importantly, we have shown (section 6.1) that the potential energy surface of α-Fe_2O_3 approaches the continuous U(1) symmetry in the limit of a small order parameter (i.e. at T_N) and, in the same way as the structural vortices in $YMnO_3$, the phase transition can be proliferated by the formation of topological defects [32]. Topological defects (vortices) will therefore form by statistical necessity when crossing the paramagnetic - antiferromagnetic phase transition and in the Kibble-Zurek mechanism the number of vortices/anti-vortices surviving at ambient conditions will depend on the quenching rate through the symmetry breaking phase transition [140].

In analogy with the structural/ferroelectric vortices observed in $YMnO_3$ and with our knowledge of the free energy landscape of α-Fe_2O_3 our vector mapped XMLD-PEEM image of α-Fe_2O_3 can be straightforwardly interpreted: pinch-points are the

loci of anti-phase domains, where the AFM order parameter has the same orientation but changes sign across the boundary. Although XMLD is insensitive to the sign of the AFM order parameter (i.e. anti-phase domains have the same projection on the incident X-ray direction), by analogy with $YMnO_3$ and the Z_6 symmetry of the α-Fe_2O_3 free energy, we can classify our periodic domain pattern as antiferromagnetic *vortices* (R-G′-B-R′-G-B′) and *anti-vortices* (R-B′-G-R′-B-G′), with primes denoting time inversion, see insets of fig. 6.10. Importantly, the antiferromagnetic vortices and anti-vortices are topologically distinct (i.e. they cannot be transformed into one another by continuous deformations) and have a winding number of $\pm$ 1 respectively [199].

In fig. 6.10 we see that the vortices form relatively dense networks, there are closely bounded pairs of '6-fold' vortices as well as lower order '3-fold' vortices: in total there are approximately 40 instances of 6-fold vortices over the full field-of-view of our measurement. Thus far, vortices in AFM structures have only been created in geometrically confined, nanoscale heterostructures by imprinting from ferromagnetic vortices [167,200], and have never before been observed in a laterally unconfined system. These vortices are therefore a novel topological defect in a magnetic system and represent an entirely magnetic analogue to the $YMnO_3$ structural vortices, offering an opportunity to study Kibble-Zurek scaling in another condensed matter system to investigate the universality of this mechanism [139, 140].

6.3.3 Coupled domain structure of α-Fe_2O_3/Co heterostructure

Having observed a topologically rich network of antiferromagnetic vortices in our α-Fe_2O_3 layer, we now consider the effect this configuration has on the adjacent (ferromagnetically ordered) Co layer. Exchange proximity in layered antiferromagnets/ferromagnets heterostructure is an integral part of modern studies of magnetism as it has numerous applications. It can be used, for example, in proposed

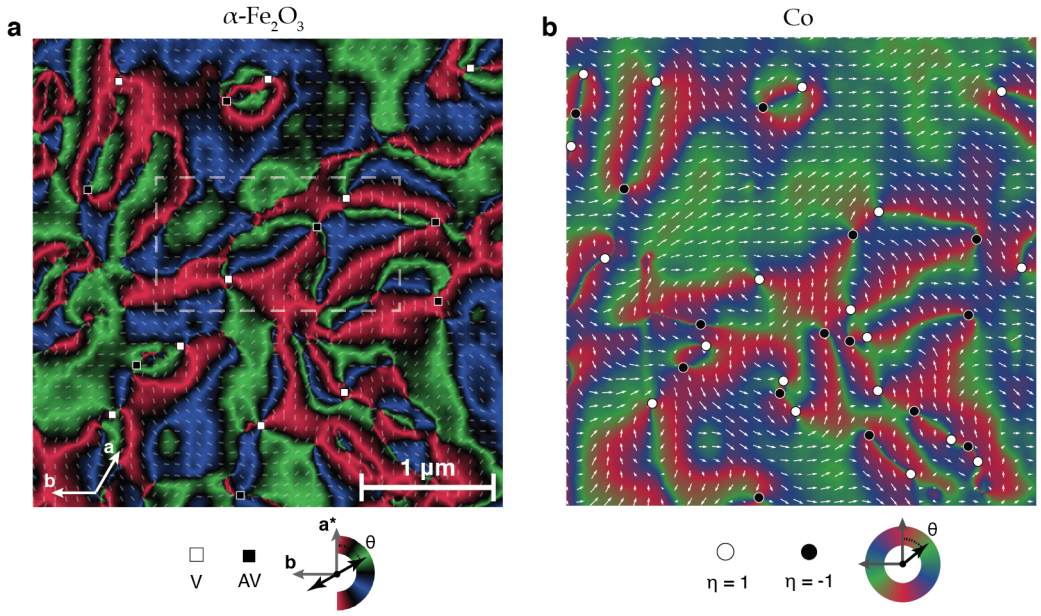


Figure 6.11: Magnetic domain structure of α-Fe_2O_3 / Co heterostructure. a, α-Fe_2O_3 antiferromagnetic domain structure as determined by vector - mapped XMLD-PEEM. White (black) squares indicate the approximate centre of identified vortex (anti-vortex) cores. White bars display the measured antiferromagnetic axis for a ten square pixel region; color represents the angle of the antiferromagnetic axis for each pixel measured clockwise from a*. The dashed box shows outlines the region of interest used in fig. 6.12. **b,** Co spin vector map determined from XMCD-PEEM, white (black) circles are topological defects with a winding number of 1 (-1). White arrows show the local in-plane spin orientation of the Co film for a ten square pixel region and colour the angle of the spin, for each pixel, measured clockwise from a*. Both images were recorded at the same position on the sample.

devices where an antiferromagnetic multiferroic is coupled to an adjacent ferromagnet [201]. The antiferromagnet can be efficiently controlled (for example with electric fields via a magnetoelectric effect) and the state of the coupled ferromagnet can be easily read; generally, reading the state of an antiferromagnet is significantly harder. For our system it is essential to study the degree of coupling between the antiferromagnet and ferromagnet, such that the potential applications of this antiferromagnetic vortex network can be understood.

To image the real space magnetisation distribution of the Co layer we used XMCD-PEEM, as described in section 6.2.2. Whereas XMLD is sensitive only to the axis of magnetisation, XMCD is sensitive to its absolute direction: the result of our XMCD measurement is a vector field of the *in-plane* Co magnetisation. The measured magnetisation of the Co layer is displayed in fig. 6.11 b. It shows that the Co

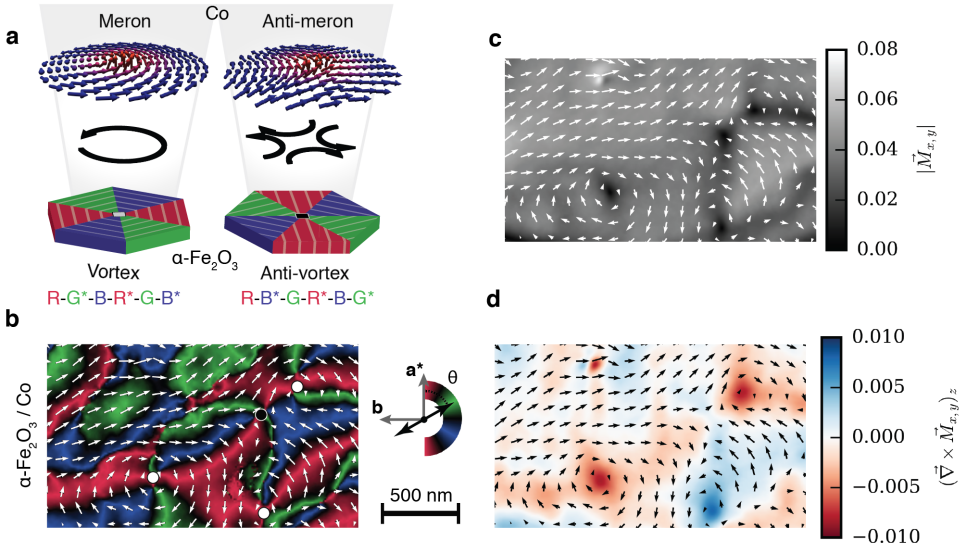


Figure 6.12: Topological defects in α-Fe_2O_3 and Co. **a,** Graphic demonstrating coupling between α-Fe_2O_3 (anti-)vortices and Co (anti-)merons. **b,** Combined ferromagnetic (white arrows) and antiferromagnetic (colour) α-Fe_2O_3 / Co film domain structure for a small area of our film, shown by the dashed box in fig. 6.11 a. White (black) circles show topological defects with a winding number of +1(-1). **c** Measured magnitude of Co magnetisation in the sample plane. **d,** $\hat{z}$ component of the curl of the Co vector map.

layer is textured at a sub-micron scale (colour and arrows), the magnetisation tends to align parallel to the α-Fe_2O_3 spin direction (compare fig. 6.11 a and b) such that the two maps show a strikingly similar morphology and are clearly strongly coupled. Noticeably, antiferromagnetic vortices and antivortices in the α-Fe_2O_3 layer are directly imprinted into the Co layer, such that all features in the α-Fe_2O_3 layer are reproduced in the Co layer with identical topological properties (see for example fig. 6.12 a).

To characterise the Co layer and its coupling to α-Fe_2O_3 we further analyse a small area featuring a prominent vortex / anti-vortex pair (dashed box in fig. 6.11) in detail. Figure 6.12 overlays the Co magnetisation (arrows) in this region onto the false colour map of the α-Fe_2O_3 antiferromagnetic spin axis. This shows that Co vortex cores are precisely aligned with the centre of the α-Fe_2O_3 vortices within the resolution of our measurement and share a common topology, i.e. white circles in fig. 6.12 show Co *vortices* (winding number equal to +1) which align with α-Fe_2O_3

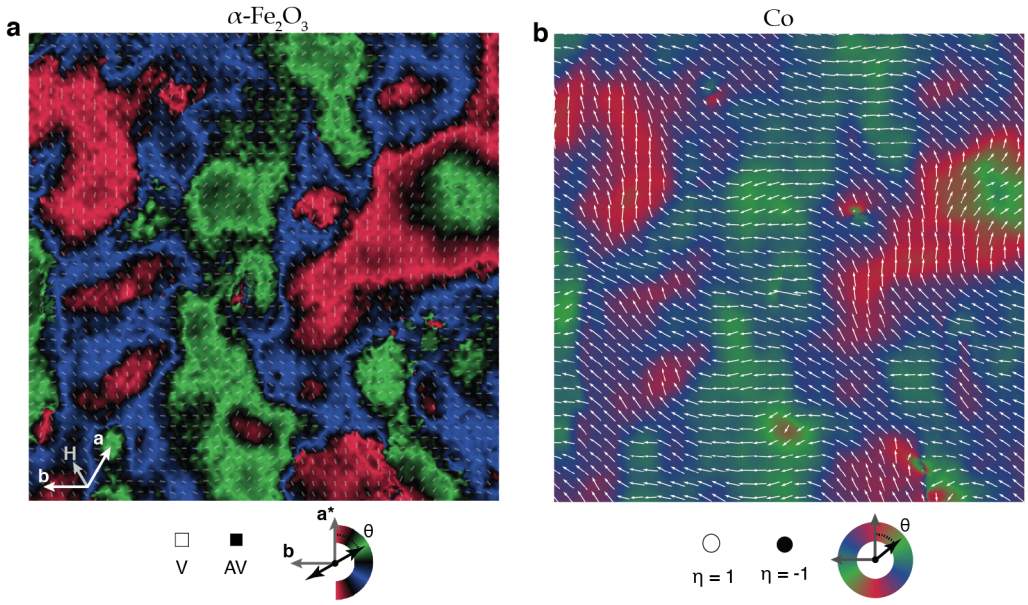


Figure 6.13: Domain structure of α-Fe_2O_3 / Co heterostructure post application of in-plane (100 mT) magnetic field. a, α-Fe_2O_3 antiferromagnetic domain structure, after fig. 6.11. White (black) squares indicate the approximate centre of identified vortex (anti-vortex) cores. White bars display the measured antiferromagnetic axis for a ten square pixel region; color represents the angle of the antiferromagnetic axis for each pixel measured clockwise from a*. **b,** Co spin vector map determined from XMCD-PEEM, white (black) circles are topological defects with a winding number of 1 (-1). White arrows show the local in-plane spin orientation of the Co film for a ten square pixel region and color the angle of the spin, for each pixel, measured clockwise from a*. Images were recorded at the same sample location as in fig. 6.11.

vortices.

Numerical differentiation of the Co magnetisation allows us to plot the spatial variation of the curl of the magnetisation ($(\vec{\nabla} \times \vec{M}_{x,y})_z$ - fig. 6.12 d). This map highlights vortices with opposite vorticity, with clockwise vortices having a negative curl and anti-clockwise having a positive curl. Anti-vortices are characterised by an alternation of the sign of the curl in each sector. Calculating the magnitude of the Co magnetisation ($|M_{x,y}|$ - displayed in fig. 6.12 b) highlights the vortex cores, where we see a reduction in the magnitude of the measured magnetisation at the centre of the vortex. The size of the vortex cores (obtained by fitting a 2D gaussian to the magnitude map and extracting the FWHM, fig. 6.12 b) is approximately 100 nm and appears to be limited by the resolution of our experiment. In ferromagnetic vortices, even with strong planar anisotropy, the magnetisation at the core often points out of the vortex plane at its core to satisfy unfavourable exchange [166].

The observed reduction in the magnitude of the in-plane magnetisation is consistent with such a situation, although it shoudl be noted that resolution effects at the core could produce a similar effect. This evidence and comparison with similar ferromagnetic vortices [166], does suggest that an out-of-plane moment is present at the core - raising the possibility that the vortices in the Co layer are actually merons/antimerons (fig. 6.12 a) as opposed to planar vortices [202]. Historically, stable merons were only previously observed in geometrically confined structures, such as nanodots [165, 203], and this observation could lead the way to engineering structures in a laterally unconfined device by imprinting from an adjacent antiferromagnetic layer.

The geometry of our device will still clearly play a role in the stability of these structures. While laterally unconfined (the heterostructure has a surface area of 5 $\times$ 5 mm^2) the Co layer is extremely thin - nominally 1 nm. Exchange anisotropy with the antiferromagnet is an interfacial effect and is therefore independent of the thickness of the Co layer. The energy associated with magnetic dipole-dipole interactions (favouring a parallel alignment of the Co spins) will, however, increase with the thickness of the Co film, such that these interactions would be the dominant contribution for a thicker Co film. In this limit we expect the Co layer to be topologically trivial, essentially ignoring the α-Fe_2O_3 layer. Conversely, the Kibble mechanism describing the formation of vortices in the antiferromagnetic layer is expected to be independent of the thickness of the α-Fe_2O_3 layer, we should therefore be able to observe antiferromagnetic vortices in bulk single crystal specimens if appropriately prepared.

6.3.4 Vortex annihilation

Topological defects are invariant under continuous deformations and are therefore considered protected by topology [204]. Being the case a single topological defect, i.e. a vortex core, will be intrinsically stable to external perturbation. However, pairs of

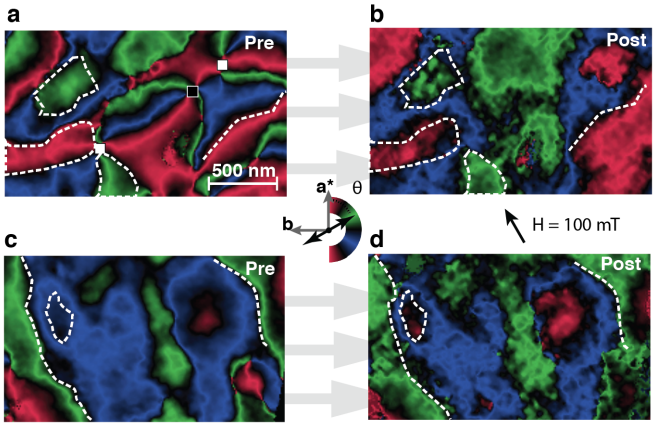


Figure 6.14: Vortex annihilation with *ex-situ* applied magnetic field. a-d, Measured α-Fe_2O_3 domain configuration in two different regions of the sample before, **a** and **c**, and after, **b** and **d**, application of a 100 mT magnetic field parallel to [1,1,0] (solid black arrow).

topological defects with equal and opposite winding number (i.e. vortex/anti-vortex pairs) can annihilate if the energy causing them to be kinematically arrested can be overcome. If the network of vortices observed in our α-Fe_2O_3/Co heterostructure truly reflects topological domain configurations (consistent with the Kibble-Zurek mechanism) they must exhibit such topological stability.

To test this, we applied a 100 mT magnetic field parallel to [1,1,0] *ex-situ* to the PEEM chamber.[5] Following the application of the magnetic field we vector mapped both the α-Fe_2O_3 and Co layers using XMLD- and XMCD-PEEM as previously described.

Figure 6.13 displays these measurements in the same position on the sample as the pre-field measurement (fig. 6.11). The post-field domain morphology of the α-Fe_2O_3 layer is dramatically altered: the surface is now dominated by large area domains and all 6-fold vortices have been removed. The Co spins (fig. 6.13 b) still align parallel to the α-Fe_2O_3 spin direction, re-affirming the strongly coupled nature of the film: the Co relaxes from its field polarised state to align parallel to the α-Fe_2O_3 spin direction at every position on our sample.

[5]Regions exposed to the X-ray beam (∼30 µm in width) have a very thin layer of carbon deposited on them, resulting in a change of work function of the sample. We can use this change to find the *exact* 10 µm region imaged prior to field application.

By comparing regions featuring vortices in the pre-field measurement to those absent of them, we can investigate the mechanism of this change. Figure 6.14 a shows a region featuring a vortex / anti-vortex pair which is clearly removed following the application of the magnetic field (fig. 6.14 b) such that the α-Fe_2O_3 layer is left in a topologically trivial state. Conversely, domains not involved in vortices (fig. 6.14 c and d) are insensitive to the field application and show no significant changes, highlighted by dashed white lines in fig. 6.14 c and d. These observations demonstrate that the dramatic change in domain topology was clearly caused by annihilation of vortex and anti-vortex pairs en-mass. By extension, it confirms the topological nature of the vortices as (in the low energy limit) re-configurations of the domain topology can only occur by vortex/anti-vortex annihilation [32].

The topological stability of the antiferromagnetic vortices shows promise for their potential incorporation into magnetic memory devices. It could, for example, be exploited by isolating vortices and using them to store information. A theoretical device could be based on similar proposed 'vortex-core' memories utilizing a cross-point architecture [205], where a regular array of antiferromagnetic vortices would imprint into a ferromagnetic layer where information could be stored in either the polarity of the core or vortex chirality. Such a device could even offer a rapid, irreversible wipe feature to destroy all stored information by inducing mass vortex/anti-vortex annihilation.

6.4 Conclusions

To summarise, we used a novel vector-mapping technique to image the domain structure of the archetypal antiferromagnetic α-Fe_2O_3, revealing an unexpectedly topologically rich antiferromagnetic domain configuration. We showed, by analogy with the structural vortices in $YMnO_3$, that our antiferromagnetic vortices are consistent with topological defects seeded by the Kibble mechanism [139]. The vortices are directly imprinted onto an adjacent ferromagnetic layer, which in future could

offer a convenient way of indirectly measuring the antiferromagnetic vortex network by measuring the ferromagnetic layer with one of the many accessible lab-based techniques (such as MFM). We took advantage of the topological stability of these objects to control the domain morphology of our heterostructure by inducing mass vortex / anti-vortex annihilation.

As well as their potential incorporation into future memory devices, reliant on the successful engineering of the antiferromagnetic vortices, our results offer a further opportunity to test the universality of Kibble-Zurek scaling. The natural extension of this project is to prepare a set of films, annealed at high temperatures and quenched through T_{N} at different rates, after which we would expect to observe a variation in the vortex density as described by the Zurek scaling mechanism [140]. Such experiments on the hexagonal manganites have shown good agreement with Zurek scaling at moderate quenching speeds, although at high quenching speeds 'anti-Kibble-Zurek' scaling is observed and not fully understood [162], showing the need for a greater diversity of systems to test this mechanism in.

7 | Conclusions

To conclude, we have presented our experimental studies on two functional magnetic iron oxide systems, single crystals of $Ba_{0.5}Sr_{1.5}Mg_2Fe_{12}O_{22}$ (BSMFO) and a α-Fe_2O_3 thin film incorporated into a magnetic heterostructure. The overarching theme of this work is in understanding the different magnetic orders of these functional systems at length scales over several orders of magnitude. The long term motivation is that the understanding developed in this work will eventually lead to the development of novel magnetic memory devices utilizing the magnetic orders of these systems.

In chapter 3 we showed that partial Sr substitution of the Ba sites in $Ba_2Mg_2Fe_{12}O_{22}$ dramatically increases its helical ordering temperature (T_H). Optimally, we increased T_H from 195 K to approximately 390 K. This high helical ordering temperature meets the minimum requirements for a functional Y-type hexaferrite device and motivated us to study the magnetic phase diagram of the optimal compound (BSMFO) in detail.

Magnetometry was used to construct the most detailed magnetic phase diagram of a Y-type hexaferrite studied to date and enabled us to identify the metamagnetic phases of BSMFO. Comparison of our phase diagram to that of the Sr-free compound allowed us to hypothesise on the magnetic order of each phase [78]. Magnetocurrent measurements were performed, confirming that BSMFO was indeed magnetoelectric at low temperatures. The poor insulating properties of our Y-type single crystal samples, however, prevented us from directly confirming whether the high temperature

phases were polar. In addition to this, these measurements showed that our BSMFO samples exhibited the large magnetoelectric effect (magnetic field inversion of the electric polarisation) which has drawn interest to this class of compounds [11, 77].

In chapter 4 we took advantage of the different sensitivities of non-resonant X-ray and neutron diffraction to magnetic order, to further interrogate our phase classification. We found that the zero field phase was characterised by an incommensurate propagation vector and that all the field-induced phases were modulated commensurately with the crystallographic lattice, consistent with the known magnetic fan structures of the Y-type hexaferrites [91]. By measuring the set of propagation vectors characterising each phase, we identified the magnetic order of each phase within the block model of the Y-type hexaferrites.

Following the classification of the magnetic phase diagram of BSMFO we performed a resonant X-ray diffraction (RXD) experiment, focussing on the magnetoelectric phase of BSMFO. Our calculations demonstrated that RXD is sensitive to the magnetic polarity of BSMFO and we spatially resolved the magnetic polarity domain configuration of our BSMFO single crystal; the first time this has been achieved in a Y-type hexaferrite. We found that the magnetic polarity is coupled to the direction of the applied magnetic field: it losslessly switches when the magnetic field is reserved. We proposed a microscopic model for this switching, a coherent rotation of the magnetic structure about the [0,0,1] direction. This mechanism, by virtue of the coupled nature of the electric polarisation and magnetic polarity, also explains the switching of the electric polarisation when the magnetic field is reversed. Our model is at odds with the previously proposed mechanism for the polarity switching [77], but our investigation was the first study supported by diffraction experiments sensitive to the switching process [11, 77]. The sensitivity of RXD to the magnetic polarity of Y-type hexaferrites demonstrated in this chapter is likely to be used in future studies, particularly as it is well suited for the study of thin films (it is approximately surface sensitive), since this is the geometry which must be utilized if Y-type hexaferrites are to be developed for application.

Finally, in chapter 6 we developed a vector-mapped X-ray photoemission electron microscopy technique to study the magnetic domain configuration of a coupled α-Fe_2O_3/Co heterostructure. Our technique allowed us to observe an unprecedented network of antiferromagnetic vortices and anti-vortices in the α-Fe_2O_3 layer which were found to imprint, by exchange proximity, into the ferromagnetically ordered Co layer. This vortex network appears consistent with the Kibble-Zurek mechanism, describing the formation of topological defects at a symmetry-breaking phase transition and their persistence to ambient conditions [139, 140], familiar in a structural analogue in the hexagonal manganites [30]. We demonstrated the control of our vortex/anti-vortex network by taking advantage of their topological nature and induced mass vortex/anti-vortex annihilation by application of a magnetic field. As well a being an ideal magnetic system to test the universality of the Kibble-Zurek mechanism, these vortices maybe suitable for integration into magnetic memory devices; their topological stability making them robust to small external perturbation. Additionally, the vector-mapping technique demonstrated in this chapter could have a wide range of application in the study of the magnetic domain structures of spintronic devices which feature an antiferromagnetic layer.

A | X-ray scattering calculations

In this chapter we present the tools for calculating the scattering intensity of X-rays from crystalline materials.

Incident polarisation matrix

The general density matrix, ρ, describing the polarisation of the incident X-ray beam can be expressed as a summation of the unit matrix ($\mathbb{1}$) and the Pauli matrices, [41, 206]

$$\rho = \frac{1}{2}(\mathbb{1} + \vec{P} \cdot \vec{\sigma}), \tag{A.1}$$

where $\vec{P} = [P_1, P_2, P_3]$ is the Poincairé -Stokes representation of the polarisation and $\vec{\sigma} = [\sigma_1, \sigma_2, \sigma_3]$ are the Pauli matrices.[1] In the Poincairé -Stokes representation P_3 describes linear polarisation along two orthogonal direction normal to the direction of propagation of light, P_2 is the mean helicity of the beam and P_1 describes linear polarisation polarisation 45° from the $P_3 = 1$ axis. [41]

Using the Poincairé -Stokes representation we can then calculate the density matrix for light of arbitrary polarisation,

$$\rho = \frac{1}{2}\begin{pmatrix} 1 + P_3 & P_1 - iP_2 \\ P_1 + iP_2 & 1 - P_3 \end{pmatrix}. \tag{A.2}$$

[1] Note $\vec{P}$ is not a real space vector.

We can then calculate the relevant density matrices for the incident polarisation states used in this experiment, for σ-incident light $\vec{P} = [0, 0, 1]$,

$$\rho_\sigma = \frac{1}{2}\begin{pmatrix} 1 & 0 \\ 0 & 0 \end{pmatrix}.$$

For π-incident $\vec{P} = [0, 0, -1]$,

$$\rho_\pi = \frac{1}{2}\begin{pmatrix} 0 & 0 \\ 0 & 1 \end{pmatrix},$$

and for circular incident, $\vec{P} = [0, \pm 1, 0]$,

$$\rho_{+/-} = \frac{1}{2}\begin{pmatrix} 1 & -\mp i \\ \pm i & 1 \end{pmatrix}.$$

Post-scatter analyser

Practically, to perform polarisation analysis of the scattered X-ray beam the beam is directed to undergo a secondary scattering event with a (near-perfect) single crystal (such as Ge). The polarisation dependence of Thomson scattering (as described in chapter 5) is then used to analyse the polarisation state of the outgoing X-ray beam. The matrix describing the analyser is given by,

$$D(\eta) = \begin{pmatrix} \cos^2(\eta) + \sin^2(\eta)\cos^2(2\theta_M) & \cos(\eta)\sin(\eta)(\cos^2(2\theta_M) - 1) \\ \cos(\eta)\sin(\eta)(\cos^2(2\theta_M) - 1) & \sin^2(\eta) + \cos^2(\eta)\sin^2(2\theta_M) \end{pmatrix}$$

where η is the polarisation analyser angle (defining the orientation of the scattering plane of the secondary diffraction event) θ_M is the 'miscut' (or Bragg) angle of the analyser crystal used and is ideally equal to 45°. For example, to measure only π polarised scattered X-rays one sets $\eta = 90°$, such that the secondary (analysing)

scattering plane is orthogonal to the experimental scattering plane. With $\theta_M = 45°$,

$$D(\eta) = \begin{pmatrix} 0 & 0 \\ 0 & 1 \end{pmatrix}. \tag{A.3}$$

B | Defined constants

In this chapter we present the constants used in our resonant X-ray scattering calculations.

$$\alpha_0 = \sum_n^{} e^{i\vec{Q}\cdot\vec{d}_n}, \tag{B.1}$$

$$\alpha_1 = \sum_n^{L} e^{i(\vec{Q}+2\vec{\tau}_2)\cdot\vec{d}_n+2i\phi_n} + e^{i(\vec{Q}-2\vec{\tau}_2)\cdot\vec{d}_n-2i\phi_n} - 2e^{i\vec{Q}\cdot\vec{d}_n}, \tag{B.2}$$

$$\alpha_2 = \sum_n^{L} e^{i\vec{Q}\cdot\vec{d}_n+i\phi_{\pi,n}}, \tag{B.3}$$

$$\alpha_3 = \sum_n^{S} e^{i\vec{Q}\cdot\vec{d}_n+i\phi_{\pi,n}}, \tag{B.4}$$

$$\alpha_4 = \sum_n^{L} e^{i\vec{Q}\cdot\vec{d}_n}, \tag{B.5}$$

$$\alpha_5 = \sum_n^{S} e^{i\vec{Q}\cdot\vec{d}_n}, \tag{B.6}$$

$$\alpha_6 = \sum_n^{S} e^{i(\vec{Q}+2\vec{\tau}_2)\cdot\vec{d}_n+i(\phi_n+\phi_{\pi,n})} + e^{i(\vec{Q}-2\vec{\tau}_2)\cdot\vec{d}_n-i(\phi_n-\phi_{\pi,n})} + 2e^{i\vec{Q}\cdot\vec{d}_n}, \tag{B.7}$$

$$\beta_1 = \sum_n^{S} e^{i(\vec{Q}+\vec{\tau}_2)\cdot\vec{d}_n+i\phi_n} + e^{i(\vec{Q}-\vec{\tau}_2)\cdot\vec{d}_n-i\phi_n}, \tag{B.8}$$

$$\beta_2 = \sum_n^{L} e^{i(\vec{Q}+\vec{\tau}_2)\cdot\vec{d}_n+i\phi_n} - e^{i(\vec{Q}-\vec{\tau}_2)\cdot\vec{d}_n-i\phi_n}, \tag{B.9}$$

$$\beta_3 = \sum_n^{L} e^{i(\vec{Q}+\vec{\tau}_2)\cdot\vec{d}_n+i(\phi_n+\phi_{\pi,n})} - e^{i(\vec{Q}-\vec{\tau}_2)\cdot\vec{d}_n-i(\phi_n-\phi_{\pi,n})}. \tag{B.10}$$

Bibliography

[1] Spaldin, N. A. Fundamental materials research and the course of human civilization. *VSH-Bulletin* (2017).

[2] Nobelprize.org. The Nobel Prize in Physics (2000).

[3] Gutfleisch, O. *et al.* Magnetic materials and devices for the 21st century: stronger, lighter, and more energy efficient. *Advanced Materials* **23**, 821–842 (2011).

[4] Fert, A., Reyren, N. & Cros, V. Magnetic skyrmions: advances in physics and potential applications. *Nature Reviews Materials* **2**, 17031 (2017).

[5] Eerenstein, W., Mathur, N. & Scott, J. F. Multiferroic and magnetoelectric materials. *Nature* **442**, 759–765 (2006).

[6] Parkin, S. S. P., Hayashi, M. & Thomas, L. Magnetic domain-wall racetrack memory. *Science* **320**, 190–194 (2008).

[7] Childress, J. R. & Fontana Jr, R. E. Magnetic recording read head sensor technology. *Comptes Rendus Physique* **6**, 997–1012 (2005).

[8] Yamada, K. *et al.* Electrical switching of the vortex core in a magnetic disk. *Nature Materials* **6**, 270–273 (2007).

[9] Mühlbauer, S. *et al.* Skyrmion lattice in a chiral magnet. *Science* **323**, 915–919 (2009).

[10] Nakano, K. *et al.* All-electrical operation of magnetic vortex core memory cell. *Applied Physics Letters* **99**, 262505 (2011).

[11] Zhai, K. *et al.* Giant magnetoelectric effects achieved by tuning spin cone symmetry in Y-type hexaferrites. *Nature Communications* **8**, 519 (2017).

[12] Pauli, W. Über den Zusammenhang des Abschlusses der Elektronengruppen im Atom mit der Komplexstruktur der Spektren. *Zeitschrift für Physik* **31**, 765–783 (1925).

[13] Blundell, S. *Magnetism in condensed matter.* Oxford University Press (2003).

[14] Smit, J. & Wijn, H. Ferrites. *Philips Technical Library* **278** (1959).

[15] Khomskii, D. *Transition metal compounds.* Cambridge University Press (2014).

[16] Utsumi, S., Yoshiba, D. & Momozawa, N. Superexchange interactions of $(Ba_{1-x}\ Sr_x)_2Zn_2Fe_{12}O_{22}$ system studied by neutron diffraction. *Journal of the Physical Society of Japan* **76**, 034704 (2007).

[17] Dzyaloshinsky, I. A thermodynamic theory of 'weak' ferromagnetism of antiferromagnets. *Journal of Physics and Chemistry of Solids* **4**, 241–255 (1958).

[18] Moriya, T. Anisotropic superexchange interaction and weak ferromagnetism. *Physical Review* **120**, 91–98 (1960).

[19] Momozawa, N. & Yamaguchi, Y. Field-induced commensurate intermediate phases in helimagnet $(Ba_{1-x}Sr_x)_2Zn_2Fe_{12}O_{22}$ (x= 0.748). *Journal of the Physical Society of Japan* **62**, 1292–1304 (1993).

[20] Hearmon, A. J. *et al.* Magnetic fan structures in $Ba_{0.5}Sr_{1.5}Zn_2Fe_{12}O_{22}$ hexaferrite revealed by resonant soft X-ray diffraction. *Physical Review B* **88**, 174413 (2013).

[21] Astrov, D. The magnetoelectric effect in antiferromagnetics. *Soviet Physics JETP* **11**, 708–709 (1960).

[22] Newnham, R. E. *Properties of materials: anisotropy, symmetry, structure.* Oxford University Press (2005).

[23] Nan, C.-W., Bichurin, M., Dong, S., Viehland, D. & Srinivasan, G. Multiferroic magnetoelectric composites: Historical perspective, status, and future directions. *Journal of Applied Physics* **103**, 031101 (2008).

[24] Kimura, T. Spiral magnets as magnetoelectrics. *Annual Review of Material Research* **37**, 387–413 (2007).

[25] Katsura, H., Nagaosa, N. & Balatsky, A. V. Spin current and magnetoelectric effect in noncollinear magnets. *Physical Review Letters* **95**, 057205 (2005).

[26] Fan, F. *et al.* Ferroelectric domain switching investigation of $BiFeO_3$ thin film on $Pt/Ti/SiO_2/Si$ (1,1,1) substrate. *Applied Surface Science* **258**, 7412–7416 (2012).

[27] Chu, Y.-H. *et al.* Domain control in multiferroic $BiFeO_3$ through substrate vicinality. *Advanced Materials* **19**, 2662–2666 (2007).

[28] Wu, J.-C., Huang, H., Lai, C.-H. & Wu, T.-h. Monodomain configurations due to bias effect in NiO/NiFe microstructures. *Journal of Applied Physics* **87**, 4948–4950 (2000).

[29] Wu, N. *et al.* Imaging and control of surface magnetization domains in a magnetoelectric antiferromagnet. *Physical Review Letters* **106**, 087202 (2011).

[30] Choi, T. *et al.* Insulating interlocked ferroelectric and structural antiphase domain walls in multiferroic $YMnO_3$. *Nature Materials* **9**, 253–258 (2010).

[31] Oh, Y. S., Luo, X., Huang, F.-T., Wang, Y. & Cheong, S.-W. Experimental demonstration of hybrid improper ferroelectricity and the presence of abundant charged walls in $(Ca,Sr)_3Ti_2O_7$ crystals. *Nature Materials* **14**, 407–413 (2015).

[32] Huang, F.-T. & Cheong, S.-W. Aperiodic topological order in the domain configurations of functional materials. *Nature Reviews Materials* **2**, 17004 (2017).

[33] Kittel, C., McEuen, P. & McEuen, P. *Introduction to solid state physics*, volume 8. Wiley, New York (1996).

[34] Hammond, C. & Hammond, C. *The Basics of Cristallography and Diffraction*, volume 214. Oxford University Press (2001).

[35] Radaelli, P. *Symmetry in crystallography: Understanding the international tables*. Oxford University Press (2011).

[36] Friedrich, W., Knipping, P. & von Laue, M. Sitzungsberichte der Mathematisch-Physikalischen Classe der Königlich-Bayerischen Akademie der Wissenschaften zu München (1912).

[37] Nobelprize.org. The Nobel Prize in Physics (1914).

[38] Bragg, W. & Bragg, W. The X-ray spectrometer. *Nature* **94**, 199–200 (1914).

[39] Bragg, W. L. & Gibbs, R. E. The structure of α and β quartz. *Proceedings of the Royal Society of London A* **109**, 405–427 (1925).

[40] Winick, H. Synchrotron radiation sources–present capabilities and future directions. *Journal of Synchrotron Radiation* **5**, 168–175 (1998).

[41] Blume, M. & Gibbs, D. Polarization dependence of magnetic X-ray scattering. *Physical Review B* **37**, 1779–1789 (1988).

[42] Hannon, J., Trammell, G., Blume, M. & Gibbs, D. X-ray resonance exchange scattering. *Physical Review Letters* **61**, 1245–1248 (1988).

[43] Warren, B. E. *X-ray Diffraction*. Dover Publications (1969).

[44] Zachariasen, W. H. *Theory of X-ray Diffraction in Crystals*. Dover Publications (2004).

[45] Debye, P. Interferenz von röntgenstrahlen und wärmebewegung. *Annalen der Physik* **348**, 49–92 (1913).

[46] Waller, I. On the effect of thermal motion on the interference of X-rays. *Zeitschrift für Physik* **17**, 398–408 (1923).

[47] Brown, P., Fox, A., Maslen, E., O'Keefe, M. & Willis, B. Intensity of diffracted intensities. In *International Tables for Crystallography Volume C: Mathematical, Physical and Chemical tables*, 554–595. Springer (2006).

[48] Low, F. E. Scattering of light of very low frequency by systems of spin $\frac{1}{2}$. *Physical Review* **96**, 1428–1432 (1954).

[49] Blume, M. Magnetic scattering of X rays. *Journal of Applied Physics* **57**, 3615–3618 (1985).

[50] Lovesey, S. W. & Collins, S. P. *X-ray scattering and absorption by magnetic materials*. Oxford University Press (1996).

[51] Gibbs, D. *et al.* Polarization and resonance properties of magnetic X-ray scattering in holmium. *Physical Review Letters* **61**, 1241–1244 (1988).

[52] Hill, J. & McMorrow, D. Resonant exchange scattering: Polarization dependence and correlation function. *Acta Crystallographica Section A: Foundations of Crystallography* **52**, 236–244 (1996).

[53] Landau, L. D., Pitaevskii, L. P., Lifshitz, E. M. & Berestetskii, V. B. *Relativistic quantum theory*. Pergamon (1971).

[54] Konya, T. X-ray thin-film measurement techniques. *The Rigaku Journal* **25**, 1–8 (2009).

[55] Park, N.-G. Perovskite solar cells: an emerging photovoltaic technology. *Materials Today* **18**, 65–72 (2015).

[56] Westneat, M. W., Socha, J. J. & Lee, W.-K. Advances in biological structure, function, and physiology using synchrotron X-ray imaging. *Annual Review of Physiology* **70**, 119–142 (2008).

[57] Mobilio, S., Boscherini, F. & Meneghini, C. *Synchrotron Radiation*. Springer (2016).

[58] Lovesey, S. W. *Theory of neutron scattering from condensed matter*. Clarendon Press (1984).

[59] Egelstaff, P. A. *Thermal neutron scattering*. Academic Press (1965).

[60] Sivia, D. S. *Elementary scattering theory: for X-ray and neutron users*. Oxford University Press (2011).

[61] Sears, V. F. Neutron scattering lengths and cross sections. *Neutron News* **3**, 26–37 (1992).

[62] Johnson, R. D. *Magnetism in crystalline rare-earth compounds*. Ph.D. thesis, Durham University (2011).

[63] Brown, P. Magnetic form factors. *International Tables for Crystallography* **C**, 454–461 (2006).

[64] Schneider, C. M. & Schönhense, G. Investigating surface magnetism by means of photoexcitation electron emission microscopy. *Reports on Progress in Physics* **65**, 1785–1839 (2002).

[65] Scholl, A. Applications of photoemission electron microscopy (PEEM) in magnetism research. *Current Opinion in Solid State and Materials Science* **7**, 59–66 (2003).

[66] Schütz, G. *et al.* Absorption of circularly polarized X-rays in iron. *Physical Review Letters* **58**, 737–740 (1987).

[67] Thole, B. T., Van der Laan, G. & Sawatzky, G. A. Strong magnetic dichroism predicted in the $M_{4,5}$ X-ray absorption spectra of magnetic rare-earth materials. *Physcal Review Letters* **55**, 2086–2088 (1985).

[68] Stohr, J. *et al.* Element-specific magnetic microscopy with circularly polarized X-rays. *Science* 658–661 (1993).

[69] Scholl, A. *et al.* Observation of antiferromagnetic domains in epitaxial thin films. *Science* **287**, 1014–1016 (2000).

[70] Bhatti, S. *et al.* Spintronics based random access memory: A review. *Materials Today* **20**, 530–548 (2017).

[71] Zabel, H. Magnetic heterostructures: examples and perspectives. *Philosophical Magazine B* **80**, 293–306 (2000).

[72] Als-Nielsen, J. & McMorrow, D. *Elements of modern X-ray physics.* John Wiley & Sons (2011).

[73] Waterfield Price, N. *Domains and functionality in multiferroic $BiFeO_3$ films.* Ph.D. thesis, University of Oxford (2017).

[74] Hallsteinsen, I. *et al.* Magnetic domain configuration of (111)-oriented $LaFeO_3$ epitaxial thin films. *Applied Physics Letters Materials* **5**, 086107 (2017).

[75] Alders, D. *et al.* Magnetic X-ray dichroism study of the nearest-neighbor spin-spin correlation function and long-range magnetic order parameter in antiferromagnetic NiO. *Europhys. Lett.* **32**, 259–265 (1995).

[76] Taniguchi, K., Abe, N., Ohtani, S., Umetsu, H. & Arima, T.-H. Ferroelectric polarization reversal by a magnetic field in multiferroic Y-type hexaferrite $Ba_2Mg_2Fe_{12}O_{22}$. *Applied Physics Express* **1**, 031301 (2008).

[77] Ishiwata, S., Taguchi, Y., Murakawa, H., Onose, Y. & Tokura, Y. Low-magnetic-field control of electric polarization vector in a helimagnet. *Science* **319**, 1643–1646 (2008).

[78] Sagayama, H. *et al.* Two distinct ferroelectric phases in the multiferroic Y-type hexaferrite $Ba_2Mg_2Fe_{12}O_{22}$. *Physical Review B* **80**, 180419 (2009).

[79] Kida, N. *et al.* Electric-dipole-active magnetic resonance in the conical-spin magnet $Ba_2Mg_2Fe_{12}O_{22}$. *Physical Review B* **80**, 220406 (2009).

[80] Ishiwata, S. *et al.* Neutron diffraction studies on the multiferroic conical magnet $Ba_2Mg_2Fe_{12}O_{22}$. *Physical Review B* **81**, 174418 (2010).

[81] Scott, J. Data storage: Multiferroic memories. *Nature Materials* **6**, 256–257 (2007).

[82] Bibes, M. & Barthélémy, A. Multiferroics: Towards a magnetoelectric memory. *Nature Materials* **7**, 425–426 (2008).

[83] Dzyaloshinskii, I. On the magneto-electrical effects in antiferromagnets. *Soviet Physics JETP* **10**, 628–629 (1960).

[84] O'Dell, T. Magnetoelectrics-a new class of materials. *Electronics and Power* **11**, 266–267 (1965).

[85] Fiebig, M. Revival of the magnetoelectric effect. *Journal of Physics D: Applied Physics* **38**, 123–152 (2005).

[86] Kenzelmann, M. *et al.* Magnetic inversion symmetry breaking and ferroelectricity in $TbMnO_3$. *Physical Review Letters* **95**, 087206 (2005).

[87] Grössinger, R., Duong, G. V. & Sato-Turtelli, R. The physics of magnetoelectric composites. *Journal of Magnetism and Magnetic Materials* **320**, 1972–1977 (2008).

[88] Khomskii, D. Trend: Classifying multiferroics: Mechanisms and effects. *Physics* **2**, 20 (2009).

[89] Cheong, S.-W. & Mostovoy, M. Multiferroics: a magnetic twist for ferroelectricity. *Nature Materials* **6**, 13–20 (2007).

[90] Kimura, T. *et al.* Magnetic control of ferroelectric polarization. *Nature* **426**, 55–58 (2003).

[91] Kimura, T. Magnetoelectric hexaferrites. *Annual Review of Condensed Matter Physics* **3**, 93–110 (2012).

[92] Aminoff, G. Über ein neues oxydisches Mineral aus Långban. (Magnetoplumbite). *Geologiska Föreningen i Stockholm Förhandlingar* **47**, 283–289 (1925).

[93] Ings, J., Simmins, J. & May, J. Fabrication of thin bulk ceramics for microwave circulator applications. Technical report, American Ceramic Society, Westerville, OH (United States) (1995).

[94] Sugimoto, M. The past, present, and future of ferrites. *Journal of the American Ceramic Society* **82**, 269–280 (1999).

[95] Pullar, R. C. Hexagonal ferrites: a review of the synthesis, properties and applications of hexaferrite ceramics. *Progress in Materials Science* **57**, 1191–1334 (2012).

[96] Kohn, J., Eckart, D. & Cook, C. F. Crystallography of the hexagonal ferrites. *Science* **172**, 519–525 (1971).

[97] Tokunaga, Y. *et al.* Multiferroic M-type hexaferrites with a room-temperature conical state and magnetically controllable spin helicity. *Physical Review Letters* **105**, 257201 (2010).

[98] Kitagawa, Y. *et al.* Low-field magnetoelectric effect at room temperature. *Nature Materials* **9**, 797–802 (2010).

[99] Okumura, K. *et al.* Magnetism and magnetoelectricity of a U-type hexaferrite $Sr_4Co_2Fe_{36}O_{60}$. *Applied Physics Letters* **98**, 212504 (2011).

[100] Sui, X., Cheong, B.-k., Laughlin, D. E. & Kryder, M. H. Growth of perpendicular barium hexaferrite thin film media on a Pt underlayer for high density

perpendicular magnetic recording. *Journal of The Magnetics Society of Japan* **18**, 319–322 (1994).

[101] Hirose, S., Haruki, K., Ando, A. & Kimura, T. Mutual control of magnetization and electrical polarization by electric and magnetic fields at room temperature in Y-type $BaSrCo_{2-x}Zn_xFe_{11}AlO_{22}$ ceramics. *Applied Physics Letters* **104**, 022907 (2014).

[102] Hirschner, J. *et al.* Spin Seebeck effect in Y-type hexagonal ferrite thin films. *Physical Review B* **96**, 064428 (2017).

[103] Momozawa, N., Nagao, Y., Utsumi, S., Abe, M. & Yamaguchi, Y. Cation distribution and helimagnetic structure of the $Ba_2(Zn_{1-x}Mg_x)_2Fe_{12}O_{22}$ system as revealed by magnetization measurements and neutron diffraction. *Journal of the Physical Society of Japan* **70**, 2724–2732 (2001).

[104] Knížek, K., Novák, P. & Küpferling, M. Electronic structure and conductivity of ferroelectric hexaferrite: Ab initio calculations. *Physical Review B* **73**, 153103 (2006).

[105] Hiraoka, Y., Nakamura, H., Soda, M., Wakabayashi, Y. & Kimura, T. Magnetic and magnetoelectric properties of $Ba_{2-x}Sr_xNi_2Fe_{12}O_{22}$ single crystals with Y-type hexaferrite structure. *Journal of Applied Physics* **110**, 033920 (2011).

[106] Bai, Y., Zhou, J., Gui, Z. & Li, L. Magnetic properties of Cu, Zn-modified Co_2Y hexaferrites. *Journal of Magnetism and Magnetic Materials* **246**, 140–144 (2002).

[107] Chang, H. *et al.* Al doping effect on magnetic phase transitions of magnetoelectric hexaferrite $Ba_{0.7}Sr_{1.3}Zn_2(Fe_{1-x}Al_x)_{12}O_{22}$. *Physical Review B* **85**, 064402 (2012).

[108] Lee, H. B. *et al.* Heliconical magnetic order and field-induced multiferroicity of the Co_2 Y-type hexaferrite $Ba_{0.3}Sr_{1.7}Co_2Fe_{12}O_{22}$. *Physical Review B* **86**,

094435 (2012).

[109] Bai, Y., Xu, F., Qiao, L. & Zhou, J. Effect of Mn doping on physical properties of Y-type hexagonal ferrite. *Journal of Alloys and Compounds* **473**, 505–508 (2009).

[110] Jalli, J. *et al.* Magnetic and microwave properties of ferrimagnetic Zr-substituted $Ba_2Zn_2Fe_{12}O_{22}$ (Zn-Y) single crystals. *Journal of Applied Physics* **109**, 07A509 (2011).

[111] Collomb, A., Muller, J. & Fournier, T. Magnesium location in the barium-magnesium-iron Y-type hexagonal ferrite. *Materials Research Bulletin* **28**, 621–627 (1993).

[112] Momozawa, N., Yamaguchi, Y., Takei, H. & Mita, M. Magnetic structure of $(Ba_{1-x}Sr_x)_2Zn_2Fe_{12}O_{22}$ (x= 0–1.0). *Journal of the Physical Society of Japan* **54**, 771–780 (1985).

[113] Kimura, T., Lawes, G. & Ramirez, A. Electric polarization rotation in a hexaferrite with long-wavelength magnetic structures. *Physical Review Letters* **94**, 137201 (2005).

[114] Nakamura, S., Tsunoda, Y. & Fuwa, A. Mössbauer study on Y-type hexaferrite $Ba_2Mg_2Fe_{12}O_{22}$. *Hyperfine Interactions* **208**, 49–52 (2012).

[115] Dzyaloshinskii, I. Thermodynamic A. *Journal of Physics and Chemisty of Solids* (1958).

[116] Bai, Y., Zhou, J., Gui, Z. & Li, L. The effect of Sr substitution on phase formation and magnetic properties of Y-type hexagonal ferrite. *Journal of the American Ceramic Society* **88**, 318–323 (2005).

[117] Wu, W. *et al.* Multiferroic nanoregions and a memory effect in cupric oxide. *Physical Review B* **81**, 172409 (2010).

[118] Beilsten-Edmands, J. *et al.* Polarization memory in the nonpolar magnetic ground state of multiferroic $CuFeO_2$. *Physical Review B* **94**, 144411 (2016).

[119] Wang, F., Shen, S.-P. & Sun, Y. Magnetoelectric memory effect in the Y-type hexaferrite $BaSrZnMgFe_{12}O_{22}$. *Chinese Physics B* **25**, 087503 (2016).

[120] Lee, H. B. *et al.* Heliconical magnetic order and field-induced multiferroicity of the Co_2 Y-type hexaferrite $Ba_{0.3}Sr_{1.7}Co_2Fe_{12}O_{22}$. *Physical Review B* **86**, 094435 (2012).

[121] Chapon, L. C. *et al.* WISH: The new powder and single crystal magnetic diffractometer on the second target station. *Neutron News* **22**, 22–25 (2011).

[122] Von Dreele, R., Jorgensen, J. T. & Windsor, C. Rietveld refinement with spallation neutron powder diffraction data. *Journal of Applied Crystallography* **15**, 581–589 (1982).

[123] Hiraoka, Y. *et al.* Spin-chiral domains in $Ba_{0.5}Sr_{1.5}Zn_2Fe_{12}O_{22}$ observed by scanning resonant Xray microdiffraction. *Physical Review B* **84**, 064418 (2011).

[124] Wilkins, S. *et al.* Direct observation of orbital ordering in $La_{0.5}Sr_{1.5}MnO_4$ using soft X-ray diffraction. *Physical Review Letters* **91**, 167205 (2003).

[125] Staub, U. *et al.* Orbital and magnetic ordering in $La_{0.5}Sr_{1.5}MnO_4$ studied by soft X-ray resonant scattering. *Physical Review B* **71**, 214421 (2005).

[126] Wadati, H. *et al.* Origin of the large polarization in multiferroic $YMnO_3$ thin films revealed by soft-and hard-X-ray diffraction. *Physical Review Letters* **108**, 047203 (2012).

[127] Hiraoka, Y., Tanaka, Y., Oura, M., Wakabayashi, Y. & Kimura, T. The effect of field cooling on a spin-chiral domain structure in a magnetoelectric helimagnet $Ba_{0.5}Sr_{1.5}Zn_2Fe_{12}O_{22}$. *Journal of Magnetism and Magnetic Materials* **384**, 160–165 (2015).

[128] Ueda, H. *et al.* Magnetic structure and effect of magnetic field on its domain structure in magnetoelectric $Ba_{1.3}Sr_{0.7}CoZnFe_{11}AlO_{22}$. *Applied Physics Letters* **109**, 182902 (2016).

[129] Johnson, R. *et al.* X-ray imaging and multiferroic coupling of cycloidal magnetic domains in ferroelectric monodomain $BiFeO_3$. *Physical Review Letters* **110**, 217206 (2013).

[130] Waterfield Price, N. *et al.* Electrical switching of magnetic polarity in a multiferroic $BiFeO_3$ device at room temperature. *Physical Review Applied* **8**, 014033 (2017).

[131] Beale, T. *et al.* RASOR: An advanced instrument for soft X-ray reflectivity and diffraction. *Review of Scientific Instruments* **81**, 073904 (2010).

[132] Wang, H. *et al.* Complete polarization analysis of an APPLE II undulator using a soft X-ray polarimeter. *Journal of Synchrotron Radiation* **19**, 944–948 (2012).

[133] Pradhan, P., Majhi, A. & Nayak, M. Optical performance of W/B4C multilayer mirror in the soft X-ray region. *Journal of Applied Physics* **123**, 095302 (2018).

[134] Waterfield Price, N. *et al.* Coherent magnetoelastic domains in multiferroic $BiFeO_3$ films. *Physical Review Letters* **117**, 177601 (2016).

[135] Mulders, A. M. *et al.* Circularly polarized soft X-ray diffraction study of helical magnetism in hexaferrite. *Physical Review B* **81**, 092405 (2010).

[136] Elam, W., Ravel, B. & Sieber, J. A new atomic database for X-ray spectroscopic calculations. *Radiation Physics and Chemistry* **63**, 121–128 (2002).

[137] Palmer, S., Baruchel, J., Drillat, A., Patterson, C. & Fort, D. Influence of the purity on the domains and the elastic constants in the helimagnetic phases of Ho and Tb. *Journal of Magnetism and Magnetic Materials* **54**, 1626–1628 (1986).

[138] Pollmann, J. *et al.* Characterization of a microfocused circularly polarized X-ray probe. *Review of Scientific Instruments* **71**, 2386–2390 (2000).

[139] Kibble, T. W. B. Topology of cosmic domains and strings. *Journal of Physics A: Mathematical and General* **9**, 1387–1398 (1976).

[140] Zurek, W. H. Cosmological experiments in superfluid helium? *Nature* **317**, 505–508 (1985).

[141] Chmiel, F. *et al.* Observation of magnetic vortex pairs at room temperature in a planar α-Fe_2O_3/Co heterostructure. *Nature Materials* **17**, 581–585 (2018).

[142] Wei, X.-K. *et al.* Ferroelectric translational antiphase boundaries in nonpolar materials. *Nature Communications* **5**, 3031 (2014).

[143] Wu, W. *et al.* Formation of pancakelike Ising domains and giant magnetic coercivity in ferrimagnetic $LuFe_2O_4$. *Physical Review Letters* **101**, 137203 (2008).

[144] Gruverman, A., Auciello, O. & Tokumoto, H. Imaging and control of domain structures in ferroelectric thin films via scanning force microscopy. *Annual Review of Materials Science* **28**, 101–123 (1998).

[145] Meier, D. *et al.* Anisotropic conductance at improper ferroelectric domain walls. *Nature Materials* **11**, 284–288 (2012).

[146] Seidel, J. *et al.* Domain wall conductivity in La-doped $BiFeO_3$. *Physical Review Letters* **105**, 197603 (2010).

[147] Horibe, Y. *et al.* Color theorems, chiral domain topology, and magnetic properties of Fe_xTaS_2. *Journal of the American Chemical Society* **136**, 8368–8373 (2014).

[148] Huang, F.-T. *et al.* Domain topology and domain switching kinetics in a hybrid improper ferroelectric. *Nature Communications* **7**, 11602 (2016).

[149] Tanaka, M. & Honjo, G. Electron optical studies of barium titanate single crystal films. *Journal of the Physical Society of Japan* **19**, 954–970 (1964).

[150] Nehring, J. & Saupe, A. On the Schlieren texture in nematic and smectic liquid crystals. *Journal of the Chemical Society, Faraday Transactions 2* **68**, 1–15 (1972).

[151] Griffin, S. M. *et al.* Scaling behavior and beyond equilibrium in the hexagonal manganites. *Physical Review X* **2**, 041022 (2012).

[152] Liang, L., Wu, H., Li, L. & Zhu, X. Characterization of multiferroic domain structures in multiferroic oxides. *Journal of Nanomaterials* **2015**, 1–8 (2015).

[153] Wu, X. *et al.* Low-energy structural dynamics of ferroelectric domain walls in hexagonal rare-earth manganites. *Science Advances* **3** (2017).

[154] Lilienblum, M. *et al.* Ferroelectricity in the multiferroic hexagonal manganites. *Nature Physics* **11**, 1070–1073 (2015).

[155] Geng, Y. *et al.* Direct visualization of magnetoelectric domains. *Nature Materials* **13**, 163–167 (2014).

[156] Chae, S. *et al.* Self-organization, condensation, and annihilation of topological vortices and antivortices in a multiferroic. *Proceedings of the National Academy of Sciences* **107**, 21366–21370 (2010).

[157] Ramesh, R. & Spaldin, N. A. Multiferroics: progress and prospects in thin films. In *Nanoscience And Technology: A Collection of Reviews from Nature Journals*, 20–28. World Scientific (2010).

[158] Chae, S. *et al.* Direct observation of the proliferation of ferroelectric loop domains and vortex-antivortex pairs. *Physical Review Letters* **108**, 167603 (2012).

[159] Artyukhin, S., Delaney, K. T., Spaldin, N. A. & Mostovoy, M. Landau theory of topological defects in multiferroic hexagonal manganites. *Nature Materials*

13, 42–49 (2014).

[160] Kervaire, M. & Milnor, J. Groups of homotopy spheres. i. In *Topological Library: Part 2: Characteristic Classes and Smooth Structures on Manifolds*, 11–48. World Scientific (2010).

[161] Chae, S. *et al.* Evolution of the domain topology in a ferroelectric. *Physical Review Letters* **110**, 167601 (2013).

[162] Meier, Q. N. *et al.* Global formation of topological defects in the multiferroic hexagonal manganites. *Physical Review X* **7**, 041014 (2017).

[163] Huang, F.-T. *et al.* Topological defects at octahedral tilting plethora in bi-layered perovskites. *npj Quantum Materials* **1**, 16017 (2016).

[164] Eggebrecht, T. *et al.* Light-induced metastable magnetic texture uncovered by in situ lorentz microscopy. *Physical Review Letters* **118**, 097203 (2017).

[165] Cowburn, R. P., Koltsov, D. K., Adeyeye, A. O., Welland, M. E. & Tricker, D. M. Single-domain circular nanomagnets. *Physical Review Letters* **83**, 1042–1045 (1999).

[166] Shinjo, T., Okuno, T., Hassdorf, R., Shigeto, K. & Ono, T. Magnetic vortex core observation in circular dots of permalloy. *Science* **289**, 930–932 (2000).

[167] Sort, J. *et al.* Imprinting vortices into antiferromagnets. *Physical Review Letters* **97**, 067201 (2006).

[168] Blake, R. L., Hessevick, R., Zoltai, T. & Finger, L. Refinement of the hematite structure. *American Mineralogist* **51**, 123–129 (1966).

[169] Pauling, L. & Hendricks, S. B. The crystal structures of hematite and corundum. *Journal of the American Chemical Society* **47**, 781–789 (1925).

[170] Néel, L. & Pauthenetm, R. C. R. *Academy of Sciences Paris* **234**, 2712–2174 (1952).

[171] Nathans, R., Pickart, S., Alperin, H. & Brown, P. Polarized-neutron study of hematite. *Physical Review* **136**, 1641–1647 (1964).

[172] Hill, A. *et al.* Neutron diffraction study of mesoporous and bulk hematite, α-Fe_2O_3. *Chemistry of Materials* **20**, 4891–4899 (2008).

[173] Landau, L. & Lifshitz, E. Statistical physics, vol. 5. *Course of Theoretical Physics* **30** (1980).

[174] Hatch, D. M. & Stokes, H. T. Invariants: program for obtaining a list of invariant polynomials of the order-parameter components associated with irreducible representations of a space group. *Journal of Applied Crystallography* **36**, 951–952 (2003).

[175] Martin, Y. & Wickramasinghe, H. K. Magnetic imaging by 'force microscopy' with 1000 Å resolution. *Applied Physics Letters* **50**, 1455–1457 (1987).

[176] Saenz, J. *et al.* Observation of magnetic forces by the atomic force microscope. *Journal of Applied Physics* **62**, 4293–4295 (1987).

[177] Freeman, M. & Choi, B. Advances in magnetic microscopy. *Science* **294**, 1484–1488 (2001).

[178] Hartmann, U. Magnetic force microscopy. *Annual Review of Materials Science* **29**, 53–87 (1999).

[179] Williams, H., Foster, F. & Wood, E. Observation of magnetic domains by the Kerr effect. *Physical Review* **82**, 119–120 (1951).

[180] Argyle, B. E. & McCord, J. G. New laser illumination method for kerr microscopy. *Journal of Applied Physics* **87**, 6487–6489 (2000).

[181] Hempstead, R., Krongelb, S. & Thompson, D. Unidirectional anisotropy in nickel-iron films by exchange coupling with antiferromagnetic films. *IEEE Transactions on Magnetics* **14**, 521–523 (1978).

[182] Parkin, S. *et al.* Magnetically engineered spintronic sensors and memory. *Proceedings of the IEEE* **91**, 661–680 (2003).

[183] Brüssing, F. *et al.* Magnetization and magnetization reversal in epitaxial Fe/Cr/Co asymmetric spin-valve systems. *Physical Review B* **85**, 174409 (2012).

[184] Belashchenko, K. D. Equilibrium magnetization at the boundary of a magnetoelectric antiferromagnet. *Physical Review Letters* **105**, 147204 (2010).

[185] Fiebig, M., Fröhlich, D., Sluyterman v. L, G. & Pisarev, R. Domain topography of antiferromagnetic Cr_2O_3 by second-harmonic generation. *Applied Physics Letters* **66**, 2906–2908 (1995).

[186] Rondin, L. *et al.* Magnetometry with nitrogen-vacancy defects in diamond. *Reports on progress in physics* **77**, 056503 (2014).

[187] Arenholz, E., van der Laan, G., Chopdekar, R. V. & Suzuki, Y. Anisotropic X-ray magnetic linear dichroism at the Fe $L_{2,3}$ edges in Fe_3O_4. *Physical Review B* **74**, 094407 (2006).

[188] Nogués, J. & Schuller, I. K. Exchange bias. *Journal of Magnetism and Magnetic Materials* **192**, 203–232 (1999).

[189] Dhesi, S. *et al.* The nanoscience beamline (I06) at Diamond Light Source. In *AIP Conference Proceedings*, volume 1234, 311–314. AIP (2010).

[190] Stöhr, J. & Siegmann, H. C. *Magnetism: from fundamentals to nanoscale dynamics*, volume 152. Springer Science & Business Media (2007).

[191] van der Laan, G. Applications of soft X-ray magnetic dichroism. In *Journal of Physics: Conference Series*, volume 430, 012127. IOP Publishing (2013).

[192] Scholl, A., Ohldag, H., Nolting, F., Stöhr, J. & Padmore, H. A. X-ray photoemission electron microscopy, a tool for the investigation of complex magnetic structures. *Review of Scientific Instruments* **73**, 1362–1366 (2002).

[193] Stöhr, J. *et al.* Images of the antiferromagnetic structure of a NiO (100) surface by means of X-ray magnetic linear dichroism spectromicroscopy. *Physical Review Letters* **83**, 1862–1865 (1999).

[194] van der Laan, G. & Kirkman, I. The $2p$ absorption spectra of $3d$ transition metal compounds in tetrahedral and octahedral symmetry. *Journal of Physics: Condensed Matter* **4**, 4189–4204 (1992).

[195] Kuiper, P., Searle, B. G., Rudolf, P., Tjeng, L. H. & Chen, C. T. X-ray magnetic dichroism of antiferromagnet Fe_2O_3: the orientation of magnetic moments observed by Fe $2p$ X-ray absorption spectroscopy. *Physical Review Letters* **70**, 1549–1552 (1993).

[196] Gota, S., Gautier-Soyer, M. & Sacchi, M. Magnetic properties of Fe_2O_3 (0001) thin layers studied by soft X-ray linear dichroism. *Physical Review B* **64**, 224407 (2001).

[197] Bezencenet, O., Bonamy, D., Belkhou, R., Ohresser, P. & Barbier, A. Origin and tailoring of the antiferromagnetic domain structure in α-Fe_2O_3 thin films unraveled by statistical analysis of dichroic spectromicroscopy (X-ray photoemission electron microscopy) images. *Physical Review Letters* **106**, 107201 (2011).

[198] Williams, H. J., Sherwood, R. & Remeika, J. P. Magnetic domains in α-Fe_2O_3. *Journal of Applied Physics* **29**, 1772–1773 (1958).

[199] Cheng, S. *et al.* Topologically allowed nonsixfold vortices in a sixfold multiferroic material: Observation and classification. *Physical Review Letters* **118**, 145501 (2017).

[200] Wu, J. *et al.* Direct observation of imprinted antiferromagnetic vortex states in CoO/Fe/Ag(001) discs. *Nature Physics* **7**, 303–306 (2011).

[201] Heron, J., Schlom, D. & Ramesh, R. Electric field control of magnetism using $BiFeO_3$-based heterostructures. *Applied Physics Reviews* **1**, 021303 (2014).

[202] Senthil, T., Vishwanath, A., Balents, L., Sachdev, S. & Fisher, M. P. Deconfined quantum critical points. *Science* **303**, 1490–1494 (2004).

[203] Wintz, S. *et al.* Topology and origin of effective spin meron pairs in ferromagnetic multilayer elements. *Physical Review Letters* **110**, 177201 (2013).

[204] Han, M.-G. *et al.* Ferroelectric switching dynamics of topological vortex domains in a hexagonal manganite. *Advanced Materials* **25**, 2415–2421 (2013).

[205] Yu, Y.-S., Jung, H., Lee, K.-S., Fischer, P. & Kim, S.-K. Memory-bit selection and recording by rotating fields in vortex-core cross-point architecture. *Applied Physics Letters* **98**, 052507 (2011).

[206] Fano, U. Description of states in quantum mechanics by density matrix and operator techniques. *Reviews of Modern Physics* **29**, 74–93 (1957).